



Detection of absorbed neutrons through determination of rhenium content in tungsten with laser induced fast pulse discharge

B.D. Stankov ^a, I. Traparić ^a, M. Gavrilović Božović ^b, M. Ivković ^{a,*}

^a Institute of Physics Belgrade, Pregrevica 118, 11080, Belgrade, Serbia

^b Faculty of Engineering, Department of Electrical Engineering and Computer Science, Sestre Janjić 6, 34000, Kragujevac, Serbia

ARTICLE INFO

Keywords:

Laser-induced breakdown spectroscopy (LIBS)
Rhenium detection
Tungsten materials
Neutron absorption
Fast pulse discharge (FPD)
Fusion reactor diagnostics
Material transmutation

ABSTRACT

The diagnostics of the first wall of future fusion reactors provides a major source of information about the state of the machine and the expected lifetime of the first wall components. As the absorption of neutrons can cause induced radioactivity of the first wall tiles and produce significant structural changes to material, it is of the essence to monitor the amount of absorbed neutrons. One possibility to monitor them is via nuclear transmutation reaction where tungsten absorbs neutron and creates rhenium core. Therefore by assessing the amount of rhenium present in the material, information about neutron irradiation conditions can be deduced. Hence in this work, in order to assess the concentration of rhenium, Laser Induced Breakdown Spectroscopy (LIBS) combined with Fast Pulse Discharge (FPD) was used. The main achievement of this work is the amplification of line intensity and signal to noise ratio compared to the classical LIBS setup at reduced pressure which enables detection of Re in samples with less than 0.1% of Re. With synergistic use of LIBS and FPD, ie. Laser Induced Fast Pulse Discharge (LIFPD), significantly enhanced Limit Of Detection (LOD) is obtained compared to the previously reported results. This result is of particular importance since only small amounts of rhenium are expected to be found in the first wall tiles, therefore making this approach suitable for this type of diagnostics.

1. Introduction

The advancement of nuclear fusion technology presents the prospect of a sustainable energy source, but it also imposes significant challenges regarding materials science and engineering. The first wall of fusion reactors, which directly absorbs neutron radiation arising from fusion reactions, plays a critical role in ensuring the reactor's structural integrity and operational efficiency. Tungsten is a leading candidate for future fusion reactors due to its high melting temperature (3422 °C), low sputter yield and high thermal conductivity (~170 W/m/K at room temperature), and low tritium retention [1,2].

Research on tungsten materials, particularly in the context of nuclear fusion, has surged, largely driven by the ITER project, leading to an increase in publications about tungsten's interactions with irradiation and plasma. Extensive studies have been conducted on neutron irradiation-induced defect formation and recovery in tungsten, offering well-characterized data crucial for understanding its properties [3].

While tungsten shows considerable potential as an armor and blanket material, it is predicted to undergo substantial transmutation under fusion neutron irradiation [4–6]. According to [7], W in the first wall

substantially transmutes to Re followed by Os for the water cooled blanket. Noda et al. show a small reduction in W content is seen in the W armor as neutron fluence increases, while concentrations of Re, Ta and Os rise with fluence. In the transmutation processes induced by neutron irradiation, approximately 4% of W transmutes to Re for the W armor of all blankets, irrelevant of the blanket composition, after 10 MWy/m² irradiation. At contrast, there is significant transmutation of W at the first wall position. Rhenium concentration surpasses that of tungsten at approximately 30 MWy/m², as illustrated in [7].

This transformation not only alters the material properties but also impacts the reactor's performance and safety. Precise measurement of Re concentrations is essential to understand the extent of transmutation, which influences the alloying behavior of tungsten and its capacity to maintain structural integrity under extreme conditions. Furthermore, the induced radioactivity associated with rhenium isotopes, particularly ¹⁸⁶Re, necessitates accurate quantification to assess potential safety concerns related to long-term radioactivity in reactor components. Consequently, comprehensive knowledge of Re concentrations in tungsten facilitates enhanced material optimization and ensures the reliability of fusion reactors in both operational and safety contexts [7].

* Corresponding author.

E-mail address: ivke@ipb.ac.rs (M. Ivković).

In addition to rhenium being a product of tungsten transmutation after heavy neutron irradiation, the tungsten-rhenium (W-Re) alloy is very important. Adding rhenium can improve some of the drawbacks of pure tungsten, such as its low ductility at room temperature and low recrystallization temperature, leading to better overall performance as structural material in fusion reactors [8]. With idea of W-Re alloy being PFM, experiments on deuterium permeation and retention were conducted in Bo-Yu Wu et al. [9] using tungsten-rhenium samples with 3% and 25% rhenium to analyze how rhenium affects hydrogen isotope transport in tungsten. The results indicate that adding rhenium increases the D diffusion coefficient but decreases D permeability, with the diffusion coefficients for both W-3 % Re and W-25 % Re being similar, while permeability declines as Re content increases. Therefore, the detection of Re in W is important as W-Re alloy might be used as plasma facing material whose properties are largely influenced by the percentage of Re present in the material. This, on the other hand, can be closely correlated with the neutron irradiation conditions, see e.g. [10] where calculated Re contents for different neutron fluences assigned to different DPA (displacement per atom) levels are given in tabular form. Graph of predicted Re concentration under fusion DPA conditions based on the fission reactor irradiation data on pure W and W-Re alloys can be found in [11].

Detecting small percentages of rhenium in tungsten is critical for several reasons relevant to fusion reactor materials. The addition of just 5% rhenium can reduce thermal conductivity and diffusivity to half that of pure tungsten [8,12]. Furthermore, a drift in the temperature reading of a W-Re thermocouple will occur due to precipitation and compositional changes during irradiation [13]. Therefore, it is important to study the effects of compositional changes due to transmutation on the physical properties of W upon neutron irradiation, which is usually done through complex calculations and numerical simulations [14,15], while experimentally the information about the degree of transmutation could be assessed through accurate and sensitive determination of Re percentage in material. In [10] measurement on solid transmutations with glow discharge optical emission spectroscopy system equipped with dual interferometry system showed an excellent agreement with the results of numerical calculations. On the other hand, the authors state that the GD-OES data collection lasted at least 5 minutes, and they could not be performed in situ, or real time.

Laser Induced Breakdown Spectroscopy (LIBS) technique can provide a fast and reliable estimation of element content in the first wall of fusion reactor. It was already applied in a range of different studies related to the estimation of retained fuel in the first wall and for depth profile analysis of plasma facing components (PFCs) materials or thin film coatings relevant for PFC materials. Maddaluno and collaborators used single pulse LIBS (SP – LIBS) [16], while Colao et al [17] used double pulse LIBS (DP – LIBS) together with Calibration Free LIBS (CF – LIBS) procedure for quantitative assessment of retained fuel. Paris et al [18] studied the fuel retention in different W coatings using SP – LIBS and Nuclear Reaction Analysis (NRA). Bhat et al [19] studied depth profiles of Be coated samples with different percentages of deuterium and seeding gases using SP – LIBS in combination with CF – LIBS to evaluate the impact on fuel retention. Depth profiling using LIBS was also exploited by Feng et al [20], where they estimated lithium penetration depth in Er_2O_3 coatings and its depth concentration by CF – LIBS. The corrosion resistance of Er_2O_3 coating was determined by Li et al [21] using standard LIBS calibration curve technique. Wu et al [22] applied picosecond SP – LIBS in vacuum environment to study the depth distribution of boron in tungsten. Also, Hu et al [23] performed the quantitative analysis with CF – LIBS of deposited impurities on PFCs using a custom developed hand-held portable LIBS device. Van der Meiden et al. [24] demonstrated LIBS as a reliable method for in-situ monitoring of tritium retention and impurity deposition on tungsten plasma-facing components in fusion devices, providing quantitative depth-resolved analysis with high sensitivity. In particular, picosecond LIBS (ps-LIBS) has shown significant advantages for highly

depth-resolved characterization of tungsten PFCs, achieving minimal thermal effects and an ablation rate below 40 nm per pulse, making it well-suited for diagnostic applications [25].

The lowest detection limit regarding Re detection by LIBS, that the authors are aware of, is reported by Ibano et al [26], who used a CF-LIBS to assess the concentration of Re in W-Re alloy. The authors state that relatively weak signal of Re I at 488.9 nm is observed at the right shoulder of a W-I line at 488.7 nm. In theirs experiment a line of Ar II is also present at 488.9 nm and according to the authors its influence on the line of Re cannot be ignored in cases of Re concentrations lower than 0.5 at.%. The authors confirm that the CF-LIBS results align closely with the nominal manufacturer concentration down to 0.5 at.%. However, after 12 years of full DT operation, the tungsten wall in ITER is expected to produce only about 0.18 at.% of Re [27]. Therefore, developing a more sensitive method based on the LIBS in the non-argon atmosphere is essential.

In this work, we investigate the potential enhancement of LIBS sensitivity through its integration with Fast Pulse Discharge (FPD) in a helium atmosphere, termed Laser Induced Fast Pulse Discharge (LIFPD). This approach is anticipated to significantly amplify the resultant spectral signals [28], thereby improving the limit of detection (LOD) for rhenium in predominantly tungsten targets, which is important for assessing absorbed neutron doses and consequent structural changes both in the pure and Re-alloyed tungsten.

In the following Section 2, we discuss the experimental setup of the LIFPD method. Main results of this work are presented and discussed in Section 3 which is organised as follows: Section 3.1 gives thorough description of the optimisation procedure to achieve highest analytical signal, while the achieved signal amplification with the proposed LIFPD setup is discussed in the Section 3.2. Procedure for detection limit determination of trace Re in W is presented in Section 3.3. Finally, our findings are summarized in Section 4 Conclusion. .

2. Experimental setup

The experimental setup of proposed LIFPD method is shown in the Fig. 1.

Laser beam (Nd:YAG Quantel 450, $\lambda = 532$ nm, pulse duration 6 ns, $E = 50$ mJ, 1 Hz) was focused via lens ($f = 12.5$ cm) onto the target that was placed inside the vacuum chamber. Target was rotated to expose the fresh surface on the target for each measurement. After the laser shot, laser induced plasma enters central part of the cross shaped vacuum vessel, where two electrodes were placed and connected to the capacitor battery ($C = 330$ nF). The experiment was optimized in a way that the laser produced plasma triggers the fast pulsed discharge, meaning that the HV level was carefully adjusted to be close to the breakdown voltage in order that the plasma can ignite the discharge. Targets investigated were 95 % W with 5% of Re, 90 % W with 10% of Re and 75 % W with 25% of Re. Thickness of the targets was measured to be 0.6 mm. Light emitted from LIBS plasma, as well as from the fast pulsed discharge, was collected with the collimator and guided through the fiber cable onto the entrance slit of the SOLinstruments MS7504i spectrometer equipped with Andor iStar ICCD camera (model DH734 – 18F – 63, 1024×1024 pixels, 18 mm sensor size). Camera was triggered and gated with the external digital delay generator (DDG) unit (Stanford Research SRS535), which on the other hand was triggered with signal from photodiode that monitors the LIBS plasma. HV was measured with high voltage probe that was attached to the Tektronix TDS2024C digital storage oscilloscope. Current intensity in pulsed arc was measured with Rogowski coil mounted around the current supply cable. The experiment was performed under controlled atmosphere of He gas, with the pressure adjusted in the range from 3 mbar up to 25 mbar. Each spectrum is obtained as accumulation over 10 laser pulses.

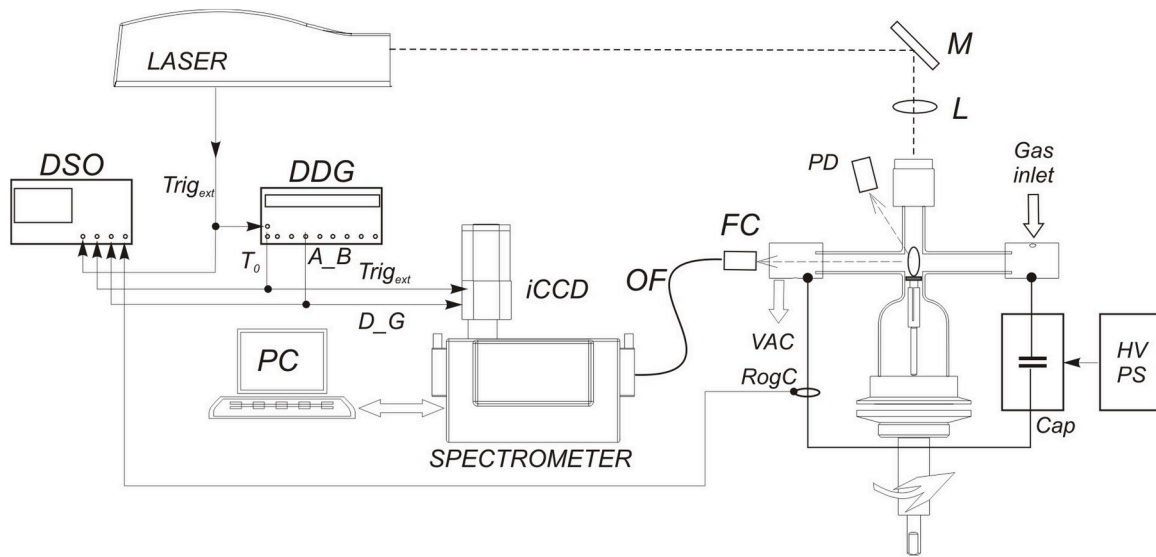


Fig. 1. Experimental setup with interaction chamber for proposed integrated LIFPD. High voltage electrodes are positioned orthogonally to the laser beam propagation direction and charged to the level that fast discharge is formed after laser pulse interaction with the sample.

3. Results and discussion

3.1. Optimization of the experiment

Experimental parameters that were optimized are working pressure inside the discharge tube, discharge voltage, the delay time and gate width of spectra recording with respect to the laser pulse. The optimisation is performed on the target sample consisting of 5 % of Re and 95 % of W.

The influence of ambient gas on the measurements was also carefully evaluated. While argon is noted for its effective performance as an infusing gas in LIBS [26,29], in the case of Rhenium detection it also imposes certain problems due to the spectral lines of Ar overlap the Re lines of interest. Our findings suggest that clear differentiation of the Re I line from tungsten can be obtained in He atmosphere under the optimized conditions within our LIFPD setup, thus avoiding any potential spectral overlaps, which led to the choice of helium as a background gas instead of argon.

For pressures of Helium gas lower than 10 mbar, the temporal reproducibility of the discharge current with respect to the laser pulse was worse than 5 μ s, meaning that the appearance of LIFPD plasma was not temporally reproducible, implying that the experiment must be done at greater pressures. For pressures above 10 mbar, temporal reproducibility was 2 μ s which is acceptable for the application of interest in this paper. In other words, plasma generated by the additional discharge appears with a delay relative to the laser impulse, with a reproducibility of approximately 2 μ s.

The pressure dependence of line intensities belonging to target material is shown in Fig. 2, in the pressure range of 11 mbar to 25 mbar. As can be seen, higher pressure values were preferred to ensure the increase in the intensity of the spectral lines, as well as for temporal reproducibility of the LIFPD. However, pressures exceeding 24 mbar were excluded due to instability in the discharge, which did not occur consistently following each laser pulse, possibly due to the irregular supply of target material particles which propagate at slower speed at increased pressure and experience higher number of collisions moving them out of the LIFPD interaction zone. Consequently, all subsequent measurements were conducted in an atmosphere of 24 mbar of helium, which ensures highest signal enhancement with stable and reproducible LIFPD event.

It is noteworthy that the fast pulse discharge plasma emerges after the LIBS plasma, allowing to assess separately the effects of this

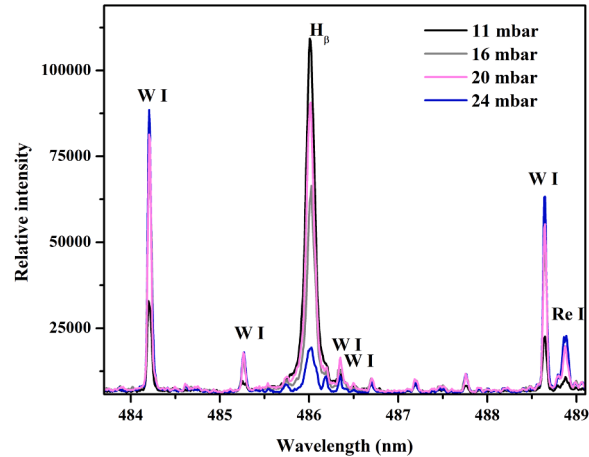


Fig. 2. Pressure optimisation for LIFPD plasma.

additional discharge. This sequence of events was assured with the proper combination of discharge voltage and gas pressure. It is concluded that the voltage of 420 V in combination with the pressure of 24 mbar leads to appearance of LIFPD plasma 7 μ s after the ending of LIBS plasma. Spectra recorded from LIBS plasma for different delay time and gate width are represented in Fig. 3. From Fig. 3 it can be concluded that the LIBS plasma does not persist longer than 20 μ s.

In the present study, the main task was to achieve a stable and reproducible FPD event triggered by the LIBS plasma. All working parameters, including laser energy, spot size, pressure etc were adjusted in that respect. The critical parameter to achieve this reproducibility was laser fluence achieved on the target in combination with suitable working pressure. Namely, laser fluence needed to be sufficiently high to ablate enough sample material to induce LIFPD event and create strong spectral emission of the elements of interest, but on the other hand sufficiently low to avoid explosive boiling of tungsten. Considering previous works regarding tungsten irradiation with Nd:YAG lasers [30, 31], to achieve this with the fixed laser energy of 50 mJ used here, the optimal spot size was determined to be 1 mm. The ablation rate was not studied since the target was constantly rotated, potentially creating overlapping spots which may hamper accurate profilometry measurements.

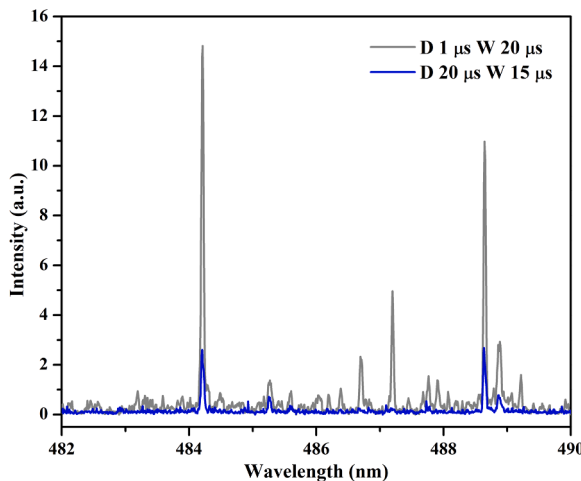


Fig. 3. Typical LIBS spectra obtained from different stages of plasma temporal evolution. Respective delays and gate widths are shown in the figure.

For the LIFPD plasma signal recordings, two options were considered: the first one was to trigger the camera at the maximum of the current signal, and the second is to trigger the camera 2 μ s before the current signal. As the illustration of triggering scheme, oscilloscope signals are shown in Fig. 4.

The signal enhancement for lines of Re in the case of triggering on the current maximum is almost negligible. When the camera is triggered 2 microseconds before the current signal (Fig 4), the amplification of the signal in the resultant spectra (Fig 5) is almost 5 times for the tungsten line and almost 10 times for the Re I 488.91 nm line compared to the LIBS signal. Based on these significant analytical signal enhancements, this gating scheme was adopted as optimal and used in all subsequent measurements. Two current maxima are appearing (see Fig 4) because the pulsed plasma source is not critically damped, i.e. plasma impedance and external circuit impedance are not matched.

After the selection of the pressure, voltage, and the delay time, the gate width was adjusted accordingly. The gate width for the recording of FPD was set to compensate the temporal irregularity of FPD plasma appearance by $\pm 2\mu$ s. The gate width was therefore chosen as the duration of LIFPD current signal plus additional 4 μ s. For that reason the gate width was set to be 23 μ s. Temporal evolution of LIBS and LIFPD plasma is presented in Fig. 5.

To summarize the optimization process, it was determined that the optimal gas for the experiment is helium, with a pressure of 24 mbar. Optimal voltage is 420 V. At this pressure and voltage, the ideal

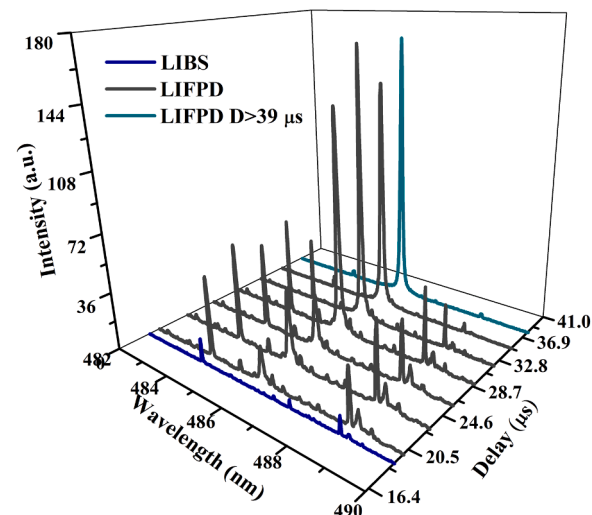


Fig. 5. Temporal evolution of LIBS and LIFPD.

triggering scheme involves initiating camera recording 2 μ s prior to the current signal. The gate width is configured to match the duration of the current pulse, with an additional 4 microseconds added to accommodate the temporal irregularities associated with the discharge plasma's appearance, leading to gate width of 23 μ s.

Electron temperature in LIFPD was estimated from the ratio of intensities of WI 484.381 nm and WI 488.689 nm lines, using the formula:

$$\frac{I_1}{I_2} = \frac{g_1 A_1 \lambda_2 e^{\frac{E_2 - E_1}{k_B T_e}}}{g_2 A_2 \lambda_1}$$

Measured relative intensity ratio corresponds to the excitation temperature of 12 000 K. Having this estimation in mind, we determined of electron density. For this purpose, the hydrogen H β line was used. As a first step, the FWHM was measured to be 0.133 nm. Instrumental width was measured to be 0.025 nm and from Doppler broadening was determined from the formula:

$$\Delta\lambda = 7.16 \times 10^{-7} \cdot \lambda_0 \cdot \sqrt{\frac{T}{M}}$$

to be 0.036 nm. The deconvolution formula [32,33] was used to determine the Stark component from the total FWHM:

$$w_s = \left(w_m^{1.4} - w_{D,I}^{1.4} \right)^{1/1.4}$$

When calculated, Stark width is estimated to be 0.11 nm. Finally, using the formula [32,34]:

$$\log N_e = 22.578 + 1.478 \times \log w_s - 0.144 \times (\log w_s)^2 - 0.1265 \times \log T_e$$

The electron density was estimated to be $3.2 \times 10^{14} \text{ cm}^{-3}$. Since the electron density is estimated to be $3.2 \times 10^{14} \text{ cm}^{-3}$, Stark broadening of the spectral lines is negligible. Furthermore, as this work was performed at low pressures, van der Waals broadening is also negligible.

3.2. Comparison of analytical capabilities of LIBS vs LIFPD

The main objective of this work was to obtain signal amplification with application of LIFPD compared to conventional LIBS. This predicted line intensity amplification is reasonable assumption since LIFPD is much stronger spectral light source than LIBS plasma.

The achieved results regarding signal amplification are shown in the Fig. 6. Optimal camera delay to capture the LIFPD signal with the best SNR is 23 μ s after LIBS plasma, where the highest SNR was achieved. This SNR is three times higher than the one obtained with the pure LIBS, while the line intensity itself is almost 5 times increased. This

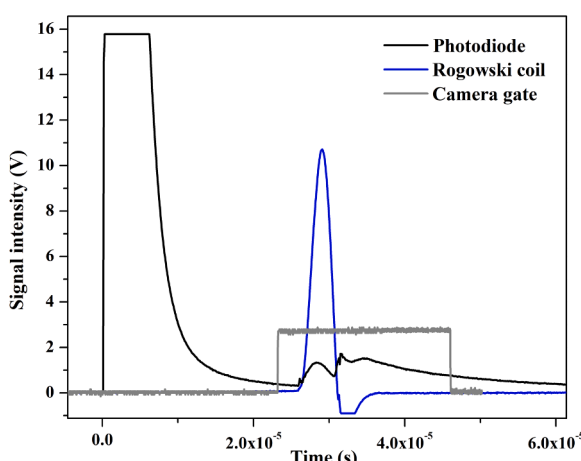


Fig. 4. Triggering and gating of the iCCD camera.

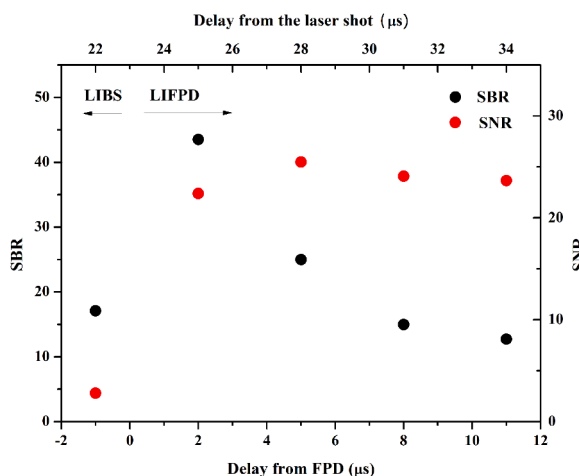


Fig. 6. SBR (Signal to Background Ratio) and SNR (Signal to Noise Ratio) for LIBS and LIFPD plasma as a function of camera delay. The trigger of the camera set 2 μ s before the current pulse is regarded as 0 μ s.

result bears significant importance for the analysis of the first wall of fusion reactors in terms of absorbed neutrons, since predicted concentrations of material of interest, i.e. Re, are expected to be quite low.

The possibility of target ablation via the discharge and its subsequent influence on the intensity of rhenium lines in the spectrum was also examined, as illustrated in the Fig. 7. The discharge was operated in pulsed mode, employing a sequence of 10 accumulated pulses, with the voltage set at 600 V to facilitate a pulsed discharge without the requirement for laser initiation. In the absence of the initial LIBS plasma, no spectral lines from the target material were detected in the pure FPD spectrum; the dominant feature observed was the H_{β} line. However, upon activation of the laser, well-resolved lines corresponding to the target material emerged, exhibiting significantly stronger intensities compared to the pure LIBS signal. This indicates that the primary source of material in the discharge is laser ablation, with contributions from sputtering and ablation due to FPD being negligible in this context. In the absence of the initial LIBS plasma, no spectral lines from the target material were detected in the pure FPD spectrum; instead, the dominant feature was the H_{β} line. This H_{β} line appears as an impurity since hydrogen is absent from both the working gas and the target material. Its presence is attributed to traces of water vapor on the walls of the discharge tube. Notably, the LIBS plasma, due to its significantly smaller size, does not induce moisture evaporation from the tube walls between the electrodes, thereby there are no hydrogen lines in the spectra.

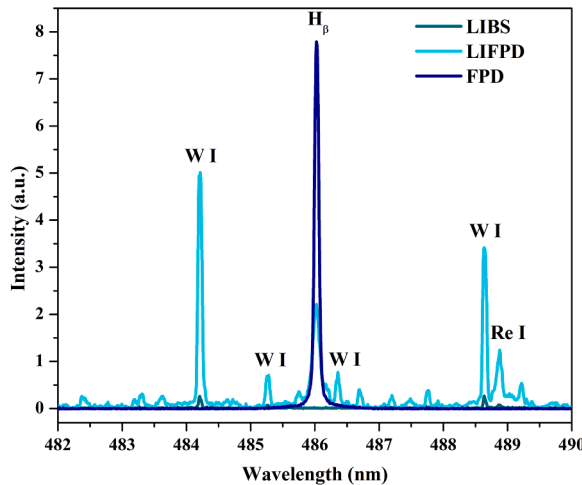


Fig. 7. LIBS, LIFPD and FPD spectra compared.

3.3. Detection threshold of trace Re in W

In this section, we present the calculation of the detection limit (LOD) as the smallest quantity of analyte that can be confidently identified in a sample, along with the quantification limit (LOQ), defined as the smallest quantity that can be reliably quantified, both with the proposed LIFPD approach and standard LIBS setup. The calculations were performed using the formulas: $LOD = 3 \times \sigma / S$ and $LOQ = 10 \times \sigma / S$, where S represents the slope of the calibration curve and σ denotes the standard deviation of the spectral recordings.

The spectra were recorded using the LIFPD setup described in the experimental section, with an optimized set of parameters: pulse energy of 50 mJ, a spot diameter of 1 mm, 10 accumulations per recording, and a gain of 100. The delay time was set to 23 μ s, accompanied by a gate time width of 23 μ s.

Integral intensities of the Re I lines were determined by approximating them with Lorentzian functions, which is appropriate given the negligible contribution of Doppler broadening at temperatures around 10,000. Specifically, the Doppler broadening was calculated to be 1.54 pm for Re I at 488.91 nm and 1.5 pm for WI at 488.69 nm. The Lorentzian profile effectively captures the predominant collisional and natural broadening in this temperature range. The selected line is well-suited for the range of Re concentrations considered in this study.

To evaluate the minimum measurable concentration of rhenium (Re) in relation to experimental error, we employed the Re I line at 488.9 nm recorded from three samples with known concentrations, Fig. 8.

The intensity of this spectral line was plotted against the known concentration of Re to generate a calibration curve, as depicted in Fig. 9. The standard deviation was determined as the average of eight measurements from a target mixture composed of 95% tungsten (W) and 5% rhenium (Re), yielding a value of 308.34.

A linear relationship was established between the intensities of the Re I line at 488.91 nm and the Re concentration, as illustrated in Fig. 9. This finding indicates that the intensity ratio can serve as a reliable indicator of Re concentration in the analyzed samples. The calibration curve's prediction error, calculated as the Root Mean Square Error (RMSE), was found to be 11,354, with a normalized RMSE value of 5.68%. These results demonstrate the robustness of the calibration curve and its potential for accurately quantifying Re concentrations in various applications.

The calculated values for LOD and LOQ were found to be 0.068% (680 ppm or 0.067% at.) and 0.23% (or 2300 ppm or 0.227% at.), respectively. These results represent a significant improvement over previous reports, which indicated a detection limit of approximately 0.5 at.% [21]. This enhancement in sensitivity is crucial for applications requiring precise quantification of trace amounts of rhenium, potentially

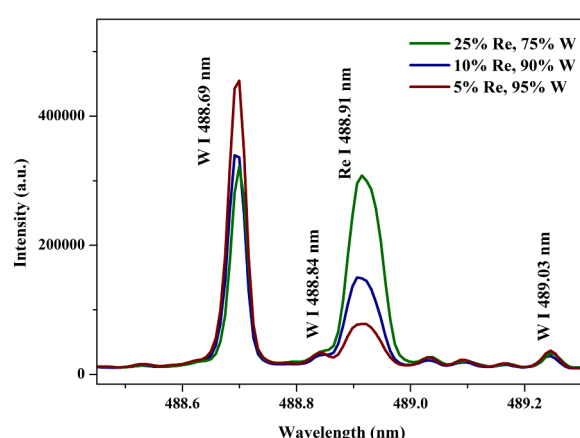


Fig. 8. WI and Re I lines recorded from LIFPD from three samples with known concentrations.

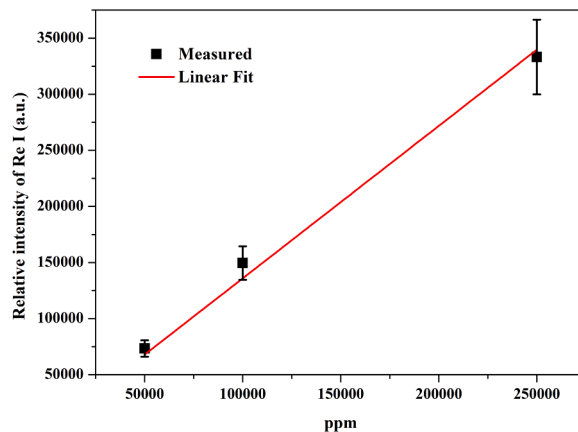


Fig. 9. Calibration curve for determination of LOD for Rhenium in LIFPD.

expanding its applicability in various fields such as materials science and analytical chemistry.

The spectra were also recorded using the standard LIBS setup, with an optimized set of parameters: pulse energy of 50 mJ, a spot diameter of 1 mm, 10 accumulations per recording, and a gain of 150. The delay time was set to 1 μ s, accompanied by a gate time width of 15 μ s.

This is done in order to compare the two methods. For LIBS analysis the standard deviation was calculated to be 260, and the Slope of calibration curve was 0.3701, leading to the value of LOD of 2106 ppm or 0.21%, which is again fairly good result. However, it must be noted that the quality of the fitting is not nearly as good as is in the case of the results obtained with the LIFPD setup. The possible reason is that for the standard LIBS setup, spectra obtained with only 10 accumulations are usually not good enough in terms of reproducibility due to the changes in the amount of ablated material per shot, plasma target shielding for subsequent pulses, more pronounced background in the spectra etc. In addition, the calibration curve in the Fig. 10 is not passing through the coordinate origin as it should, so this additionally speaks in the favour of better reproducibility and higher accuracy of concentration determination with the LIFPD approach.

4. Conclusion

This investigation successfully demonstrates the feasibility of utilizing Laser Induced Breakdown Spectroscopy (LIBS) in conjunction with Fast Pulse Discharge (FPD) to detect low concentrations of rhenium in tungsten samples. Our findings reveal that the proposed method significantly amplifies the spectral signal, achieving a threefold increase in the signal-to-noise ratio and nearly five times greater intensity compared to the conventional LIBS techniques. This amplification is particularly crucial given the anticipated low levels of rhenium resulting from neutron transmutation reactions within the first wall of fusion reactors.

Our experimental approach involved analysis of various tungsten-rhenium alloy specimens, leading to a threshold detection limit of 0.067 at. %. This marks a substantial improvement over previous studies, which reported a detection limit of approximately 0.5 at.% [26].

Our findings indicate that the optimized conditions within our FPD-enhanced LIBS setup enable clear differentiation of the Re I line from tungsten in Helium, thus circumventing potential spectral overlaps caused by the ambient gas.

The LIFPD approach outlined in this research holds promise for enhanced diagnostics of fusion reactor components, allowing for precise monitoring of absorbed neutron levels through the quantification of rhenium. It provides a valuable tool for assessing the integrity and longevity of structural materials in fusion reactors under operational conditions. Future studies should aim to further refine this methodology

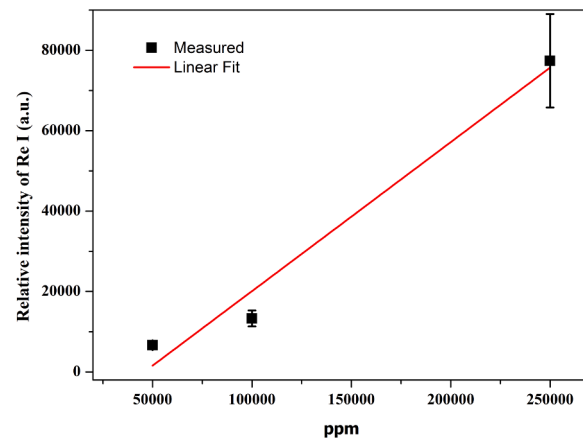


Fig. 10. Calibration curve for determination of LOD for Rhenium in LIBS.

and explore its application in real-time monitoring environments, thereby contributing to the development of safer and more efficient fusion energy systems. This approach is suitable for post-mortem analysis (between experimental campaigns); however, the authors are currently working on a measuring device that will enable the application of this method for real-time in situ measurements (without demounting the components in tokamak).

Additionally, the results of this paper have shown that a standard LIBS setup based on Nd:YAG laser can be successfully applied to quantitative analysis of W/Re composition materials relevant to fusion technology.

Further investigations will focus on optimizing the measurement conditions and exploring the applicability of this method to other analytes, thereby broadening the scope of this analytical technique.

CRediT authorship contribution statement

B.D. Stankov: Investigation, Formal analysis, Writing – original draft. **I. Traparić:** Investigation, Formal analysis, Writing – review & editing. **M. Gavrilović Božović:** Writing – original draft, Formal analysis. **M. Ivković:** Writing – review & editing, Supervision, Conceptualization, Methodology, Funding acquisition.

Declaration of competing interest

The authors declare that they have no known competing financial interests or personal relationships that could have appeared to influence the work reported in this paper.

Acknowledgements

The research was funded by the Ministry of Science, Technological Development and Innovations of the Republic of Serbia, Contract numbers: 451-03-68/2022-14/200024, 451-03-66/2024-03/200107 and supported by the Science Fund of the Republic Serbia, Grant no. 7753287 “NOVA2LIBS4fusion”. The authors thank Stanko Milanovic for technical assistance in preparation and setting up the experiment.

Data availability

Data will be made available on request.

References

- [1] H. Bolt, V. Barabash, W. Krauss, J. Linke, R. Neu, S. Suzuki, N. Yoshida, ASDEX Upgrade Team, Materials for the plasma-facing components of fusion reactors, *J. Nucl. Mater.* 329–333 (2004) 66–73, <https://doi.org/10.1016/j.jnucmat.2004.04.005>.

- [2] V. Philippss, Tungsten as material for plasma-facing components in fusion devices, *J. Nucl. Mater.* 415 (Issue 1) (2011) S2–S9, <https://doi.org/10.1016/j.jnucmat.2011.01.110>. Supplement.
- [3] M. Rieth, R. Doerner, A. Hasegawa, Y. Ueda, M. Wirtz, Behavior of tungsten under irradiation and plasma interaction, *J. Nucl. Mater.* 519 (2019) 334–368, <https://doi.org/10.1016/j.jnucmat.2019.03.035>.
- [4] L.R. Greenwood, F.A. Garner, Transmutation of Mo, re, W, Hf, and V in various irradiation test facilities and STARFIRE, *J. Nucl. Mater.* 212–215 (1994) 635–639, [https://doi.org/10.1016/0022-3115\(94\)90136-8](https://doi.org/10.1016/0022-3115(94)90136-8).
- [5] C.B.A. Forty, G.J. Butterworth, J.-Ch. Sublet, Burnup of some refractory metals in a fusion neutron spectrum, *J. Nucl. Mater.* 212–215 (1994) 640–643, [https://doi.org/10.1016/0022-3115\(94\)90137-6](https://doi.org/10.1016/0022-3115(94)90137-6).
- [6] T. Noda, M. Fujita, Effect of neutron spectra on the transmutation of first wall materials, *J. Nucl. Mater.* 233–237 (1996) 1491–1495, [https://doi.org/10.1016/S0022-3115\(96\)00108-0](https://doi.org/10.1016/S0022-3115(96)00108-0).
- [7] T. Noda, M. Fujita, M. Okada, Transmutation and induced radioactivity of W in the armor and first wall of fusion reactors, *J. Nucl. Mater.* 258–263 (1998) 934–939, [https://doi.org/10.1016/S0022-3115\(98\)00088-9](https://doi.org/10.1016/S0022-3115(98)00088-9). Get rights and content.
- [8] M. Fujitsuka, B. Tsuchiya, I. Mutou, T. Tanabe, T. Shikama, Effect of neutron irradiation on thermal diffusivity of tungsten–rhenium alloys, *J. Nucl. Mater.* 283–287 (2000) 1148, [https://doi.org/10.1016/S0022-3115\(00\)00170-7](https://doi.org/10.1016/S0022-3115(00)00170-7).
- [9] Bo-Yu Wu, Yu-Ping Xu, Yi-Ming Lyu, Xiao-Chun Li, Xiang Geng b, Shou-An Puyang, Xin Shen, Xin-Dong Pan, Hai-Shan Zhou, Guang-Nan Luo, Effects of rhenium content on the deuterium permeation and retention behavior in tungsten, *J. Nucl. Mater.* 565 (2022) 153709, <https://doi.org/10.1016/j.jnucmat.2022.153709>.
- [10] Y. Katoh, L.L. Snead, L.M. Garrison, X. Hu, T. Koyanagi, C.M. Parish, P. D. Edmondson, M. Fukuda, T. Hwang, T. Tanaka, A. Hasegawa, Response of unalloyed tungsten to mixed spectrum neutrons, *J. Nucl. Mater.* 520 (2019) 193–207, <https://doi.org/10.1016/j.jnucmat.2019.03.045>.
- [11] A. Hasegawa, M. Fukuda, S. Nogami, K. Yabuuchi, Neutron irradiation effects on tungsten materials, *Fusion Eng. Des.* 89 (2014) 1568–1572, <https://doi.org/10.1016/j.fusengdes.2014.04.035>.
- [12] T. Tanabe, C. Eamchotchawalit, C. Busabok, S. Taweethavorn, M. Fujitsuka, T. Shikama, Temperature dependence of thermal conductivity in W and W–Re alloys from 300 to 1000 K, *Mater. Lett.* 57 (2003) 2950–2953, [https://doi.org/10.1016/S0167-577X\(02\)01403-9](https://doi.org/10.1016/S0167-577X(02)01403-9).
- [13] R.K. Williams, F.W. Wiffen, J. Bentley, J.O. Stiegler, Irradiation induced precipitation in tungsten based, W–Re alloys, *Metall. Trans. A* 14A (April) (1983) 655–666, <https://doi.org/10.1007/BF02643781>.
- [14] T. Hwang, A. Hasegawa, K. Tomura, N. Ebisawa, T. Toyama, Y. Nagai, M. Fukuda, T. Miyazawa, T. Tanaka, S. Nogami, Effect of neutron irradiation on rhenium cluster formation in tungsten and tungsten–rhenium alloys, *J. Nucl. Mater.* 507 (2018) 78–86, <https://doi.org/10.1016/j.jnucmat.2018.04.031>.
- [15] A. Hasegawa, M. Fukuda, K. Yabuuchi, S. Nogami, K. Ibano, D. Nishijima, Y. Ueda, R.P. Doerner, Neutron irradiation effects on the microstructural development of tungsten and tungsten alloys, *J. Nucl. Mater.* 522 (2019) 324–328, <https://doi.org/10.1016/j.jnucmat.2019.10.047>.
- [16] G. Maddaluno, S. Almaviva, L. Caneve, F. Colao, V. Lazic, L. Laguardia, P. Gasior, M. Kubkowska, FTU team, Detection by LIBS of the deuterium retained in the FTU toroidal limiter, *Nucl. Mater. Energy* 18 (2019) 208–211, <https://doi.org/10.1016/j.nme.2018.12.029>.
- [17] F. Colao, et al., LIBS experiments for quantitative detection of retained fuel, *Nucl. Mater. Energy* 12 (2017) 133–138, <https://doi.org/10.1016/j.nme.2017.05.010>.
- [18] P. Paris, I. Jögi, K. Piip, M. Passoni, D. Dellasega, E. Grigore, WM. Arnoldbik, H. van der Meiden, In-situ LIBS and NRA deuterium retention study in porous W–O and compact W coatings loaded by Magnum-PSI, *Fusion Eng. Des.* 168 (2021) 112403, <https://doi.org/10.1016/j.fusengdes.2021.112403>.
- [19] P.G. Bhat, et al., LIBS depth profiling of Be-containing samples with different gaseous impurity concentrations, *Nucl. Mater. Energy* 37 (2023) 101549, <https://doi.org/10.1016/j.nme.2023.101549>.
- [20] S. Feng, C. Ke, Y. Chen, H. Zhang, Y. He, Y. Zhao, CF-LIBS analysis in depth profile of lithium corrosion resistance of Er_2O_3 coatings prepared by sol-gel method, *Fusion Eng. Des.* 170 (2021) 112506, <https://doi.org/10.1016/j.fusengdes.2021.112506>.
- [21] Y. Li, C. Ke, X. Liu, F. Gou, X. Duan, Y. Zhao, Analysis liquid lithium corrosion resistance of Er_2O_3 coating revealed by LIBS technique, *Fusion Eng. Des.* 136 (2018) 1640–1646, <https://doi.org/10.1016/j.fusengdes.2018.07.001>.
- [22] H. Wu, R. Yi, A. Houben, S. Brezinsek, M. Rasinski, C. Li, G. Sergienko, Y. Liang, T. Dittmar, H. Ding, Study of spectral features and depth distributions of boron layers on tungsten substrates by ps-LIBS in a vacuum environment, *Nucl. Mater. Energy* 41 (2024) 101812, <https://doi.org/10.1016/j.nme.2024.101812>.
- [23] Z. Hu, X. Bai, H. Wu, R. Hai, F. Ding, M. Imran, C. Li, H. Ding, G.N. Luo, Quantitative analysis of impurities deposited on the Plasma-Facing components of EAST tokamak using a portable LIBS device, *Nucl. Mater. Energy* 41 (2024) 101785, <https://doi.org/10.1016/j.nme.2024.101785>.
- [24] H.J. van der Meiden, S. Almaviva, J. Butikova, V. Dwivedi, P. Gasior, W. Gromelski, A. Hakola, X. Jiang, I. Jögi, J. Karhunen, M. Kubkowska, M. Laan, G. Maddaluno, A. Marin-Roldán, P. Paris, K. Piip, M. Pisarcík, G. Sergienko, M. Veis, P. Veis, S. Brezinsek and the EUROfusion WP PFC, Monitoring of tritium and impurities in the first wall of fusion devices using a LIBS based diagnostic, 61 (2021) 125001 (14pp) doi [10.1088/1741-4326/ac31d6](https://doi.org/10.1088/1741-4326/ac31d6).
- [25] Dongye Zhao, Ding Wu, Jannis Oelmann, Sebastijan Brezinsek, Qingmei Xiao, Rongxing Yi, Laizhong Cai, Hongbin Ding, Highly depth-resolved characterization of fusion-related tungsten material based on picosecond laser-induced breakdown spectroscopy, *J. Anal. At. Spectrom.* 35 (12) (2020) 2867–2879, <https://doi.org/10.1039/D0JA00340A>.
- [26] K. Ibano, D. Nishijima, Y. Ueda, R.P. Doerner, LIBS measurement of trace tantalum and rhenium in tungsten for in-situ diagnostic of nuclear transmutation, *J. Nucl. Mater.* 522 (2019) 324–328, <https://doi.org/10.1016/j.jnucmat.2019.05.030>.
- [27] M.R. Gilbert, J.-C. Sublet, Neutron-induced transmutation effects in W and W–alloys in a fusion environment, *Nucl. Fusion* 51 (2011) 043005, <https://doi.org/10.1088/0029-5515/51/4/043005>.
- [28] M. Vinić, M. Ivković, Laser ablation initiated fast discharge for spectrochemical applications, *Hem. Ind.* 68 (3) (2014) 381–388, <https://doi.org/10.2298/HEMIND130314065V>.
- [29] D. Nishijima, Y. Ueda, R.P. Doerner, M.J. Baldwin, K. Ibano, Laser-induced breakdown spectroscopy measurement of a small fraction of rhenium in bulk tungsten, *Spectrochim. Acta Part B At. Spectrosc.* 141 (2018) 94–98, <https://doi.org/10.1016/j.sab.2018.01.013>.
- [30] J. Liu, D. Wu, X. Hu, S. Liu, H. Wu, R. Hai, C. Li, H. Ding, Study of spectral intensity of the laser ablated tungsten plasma and ablation mass at various laser spot sizes and laser fluence in vacuum environment, *Spectrochim. Acta Part B At. Spectrosc.* 199 (2023) 106569, <https://doi.org/10.1016/j.sab.2022.106569>.
- [31] M. Ivkovic, J. Savovic, B.D. Stankov, M. Kuzmanovic, I. Traparic, LIBS depth-profile analysis of W/Cu functionally graded material, *Spectrochim. Acta Part B At. Spectrosc.* 213 (2024) 106874, <https://doi.org/10.1016/j.sab.2024.106874>.
- [32] N. Konjević, M. Ivković, N. Sakan, Hydrogen balmer lines for low electron number density plasma diagnostics, *Spectrochim. Acta Part B At. Spectrosc.* 76 (2012) 16–26, <https://doi.org/10.1016/j.sab.2012.06.026>.
- [33] D.E. Kelleher, Stark broadening of visible neutral helium lines in a plasma, *J. Quant. Spectrosc. Radiat. Transf.* 25 (1981) 191–220.
- [34] A. Cernichowski, J. Chapelle, Use of the 447 nm He I line to determine electron concentrations, *J. Quant. Spectrosc. Radiat. Transf.* 33 (1985) 427–436.



Resolving studies of Balmer alpha lines relevant to the LIBS analysis of hydrogen isotope retention



I. Traparic ^a, D. Rankovic ^b, B.D. Stankov ^a, J. Savovic ^c, M. Kuzmanovic ^b, M. Ivkovic ^{a,*}

^a Institute of Physics, University of Belgrade, 11080 Belgrade, Serbia

^b Faculty of Physical Chemistry, University of Belgrade, 11158 Belgrade, Serbia

^c Vinca Institute of Nuclear Sciences, University of Belgrade, 11000 Belgrade, Serbia

ARTICLE INFO

Keywords:

Hydrogen isotopes
Balmer alpha lines
LIBS, hydrogen isotope retention
Plasma-facing components

ABSTRACT

Utilizing Laser-Induced Breakdown Spectroscopy (LIBS) for detecting deuterium and tritium retention in fusion devices poses a significant challenge due to the experimental limitations in resolving hydrogen isotope Balmer alpha lines (H_{α} , D_{α} , and T_{α}). This study utilizes the Rayleigh criterion to distinguish T_{α} and D_{α} lines by determining the maximum line widths and corresponding plasma parameters. Experimental validation was performed through LIBS analysis of heavy water-doped graphite/silica gel targets in both argon and helium atmospheres to assess the predicted plasma parameters and line profile shapes. The optimization of laser pulse energy, gas pressure, delay, and gate times aimed at achieving fully resolved lines based on the intensity, width, and the dip between deuterium and hydrogen Balmer alpha lines. By fine-tuning these experimental parameters, the study successfully achieved a dip of less than 10 % between the H_{α} and D_{α} lines with a satisfactory signal-to-noise ratio, demonstrating the feasibility of fully resolving the T_{α} and D_{α} lines. These findings underscore the potential of LIBS in enhancing the detection of deuterium and tritium retention in fusion devices.

1. Introduction

Resolving the challenges surrounding energy production stands at the forefront of modern science and technology. Nuclear fusion is a clean and sustainable energy production that holds the promise of addressing global energy demands. A fusion reactor uses deuterium (D) and tritium (T) as fuels to produce inert gas helium, high-speed neutrons, and vast amounts of energy without producing long-lived radioactive waste. Despite its immense potential, the complexity and costliness of fusion reactors necessitate collaborative efforts on an international scale, exemplified by the joint endeavor to construct the International Thermonuclear Experimental Reactor (ITER) among participating nations such as the EU, USA, Japan, Russia, China, India, and South Korea [1].

The development and maintenance of nuclear fusion reactors are vital to sustain the promise of clean and efficient energy production. Amidst the complex operational challenges faced by fusion reactors, attention must be given to the impact on plasma-facing components (PFCs), exposed to various stresses, requiring meticulous material composition monitoring and particularly critical hydrogen isotope retention studies. In a nuclear fusion reactor, PFC faces intense plasma radiation, thermal loads, and neutron fluxes, leading to structural

material damage. Thermal loads may cause re-crystallization, cracks, melting, and dust formation. Plasma exposure leads to sputtering, hydrogen isotope retention, and helium-induced morphology changes. Potential defects and transmutations may appear under neutron action. Because of this, in-situ real-time material analysis is essential to prevent an unexpected failure. Monitoring hydrogen isotope retention in PFCs is particularly important as it may affect fuel efficiency, plasma density, and the density of neutral hydrogen in the plasma boundary, essential for the safe operation of nuclear fusion installations [2]. Consequently, hydrogen isotope retention studies play a key role in PFC diagnostics [2–6].

Numerous research papers focus on various methodologies for PFC characterization [7,8]. Two currently significant techniques for the ex-situ characterization of fusion-relevant materials are accelerator-based Ion Beam Analysis (IBA) and Thermal Desorption Spectroscopy (TDS) [3,9–13]. IBA encompasses setups like Nuclear Reaction Analysis (NRA) and Elastic Recoil Detection Analysis (ERDA) crucial for quantifying light isotopes due to their sensitivity and selectivity. Additionally, TDS offers insights by analyzing demounted (from the reactor) material samples using a quadrupole mass spectrometer with an enclosed ion source to evaluate hydrogen isotope desorption behavior. However, TDS

* Corresponding author.

E-mail address: ivke@ipb.ac.rs (M. Ivkovic).

cannot provide information on the depth distribution of fuel concentrations. Radiofrequency Glow Discharge Spectrometry (RF-GDOES) proves effective for depth profiling of PFCs, as demonstrated in studies such as the analysis of deuterium in tungsten [2].

Laser Induced Breakdown Spectroscopy holds a prominent position among techniques applied for PFCs analysis within fusion devices. Its analytical capabilities have been extensively documented in many books and review articles [14–20]. LIBS is a minimally invasive non-contact technique suitable for multi-element analysis, including depth profiling, without requiring sample preparation. The technique is adaptable for vacuum or low-pressure gas environments and excels in remote in situ analysis. Notably, LIBS allows for on-site analysis without the need to dismantle or cut samples from the reactor, reducing costs and eliminating issues related to PFC replacement due to structural non-uniformity. Moreover, LIBS offers versatility in analyzing various reactor components beyond those that are easily disassembled. Review articles [21–23] provide an overview of the current state of LIBS development for fusion applications. Various LIBS systems were used for diverse characterization objectives, such as identifying elemental composition, depth profiling, deposited layer thickness, or spatial analysis. The efficiency of LIBS as a remote online diagnostics tool was demonstrated by analyzing multilayer structures, simulating the surface of a PFC covered with deposited impurity layers [24]. Specifically tailored LIBS configurations optimized for vacuum operation showcased promising results, including a compact system integrated onto the robotic arm of the Frascati Tokamak Upgrade (FTU) for ITER-relevant sample analysis [25], demonstrating improved spectral resolution in double-pulse (DP-LIBS) over single-pulse (SP-LIBS) configurations. Notably, the exceptional sensitivity of LIBS to lighter elements has been found application in hydrogen isotope retention investigations [26–35]. At Experimental Advanced Superconducting Tokamak (EAST) [26], a remote in situ laser-induced breakdown spectroscopic (RIS-LIBS) system has been developed for the determination of PFC composition (fuel retention, impurity deposition, and deposited layer thickness) [26]. Isotope lines D_α and H_α were identified but only partially resolved. The limit of detection of H/D was estimated to be about 200 ppm in the lithium layer on the first wall [27] applied LIBS for in-situ probing of D retention and Li deposition on a W-PFC surface after being exposed to D plasmas in a tokamak. Deuterium retention inside both pure and lithiated tungsten was investigated, and it was found that the D_α and H_α signals of lithiated W are significantly more intense than those of pure W. LIBS was also applied for in-situ diagnostics of the Li-H/D co-deposition on the first wall of EAST [28]. The results showed that the D_α and H_α signal intensities disappeared after the third laser shot, which was explained by the greater depth of the nanosecond laser ablation than the thickness of the deposited impurity layer. Additionally, femtosecond laser filamentation-induced breakdown spectroscopy combined with chemometrics methods was used to quantify deuterium content in water samples [29]. Filamentation was found to suppress spectral broadening, and well-resolved peaks of H_α and D_α were obtained. Burger et al. [30] studied the segregation of species and spectral line broadening in D₂O-H₂O plasma produced by single- and double-pulse nanosecond laser ablation in air. It was found that species segregation for laser-produced plasma formed in the air does not significantly impact the ability to distinguish D_α and H_α Balmer lines for the SP-LIBS and DP-LIBS. Fantoni et al. [31] studied the resolving of H_α and D_α lines using double pulse configuration with Nd:YAG lasers having energy of 170 mJ at 1.06 μm to irradiate, in vacuum, Mo target co-deposited with W, Al, and D using vacuum arc deposition method. With a 300 ns delay between pulses, H_α and D_α lines are almost resolved according to the Rayleigh criteria, thus enabling line intensity determination using fitting with Pseudo Voigt functions.

Kautz et al. [32,33] obtained an even better resolution by using fs Ti-sapphire laser (800 nm, 35 fs, 5 mJ) to irradiate H and D loaded Zircaloy-4 targets. In 10 Torr of He, using a gate of 2 μs, FWHM of hydrogen lines from 0.08 to 0.05 nm was obtained for delays from 1 to 26 μs [33]. Using

an ns laser and different pressures of Ar, a slightly greater FWHM was obtained. Later [34], using the same fs laser irradiation of the Zircaloy-4 target with incorporated D or T in 26 Torr of Ar, the hydrogen Balmer alpha lines are clearly resolved from the D_α or T_α. Lowering gas pressure, the line width goes even below 0.08 nm, but the line intensity drops even faster, thus limiting the possibility for resolving D_α from T_α.

Recently [35], the analysis of the parameters influencing resolving and recordings of the fully resolved D_α and H_α lines are obtained in 30 Torr of Ar at delays of 60 μs, but without indicating other experimental conditions.

Achieving direct Laser-Induced Breakdown Spectroscopy (LIBS) analysis of hydrogen isotopes remains a formidable challenge due to the high electron density in laser-induced plasma, intensifying Stark broadening and hindering the clear distinction of closely spaced spectral lines of different H isotopes.

This research aims to enhance the resolution and sensitivity of LIBS for detecting hydrogen isotopes in fusion-relevant materials. The initial focus involved a theoretical exploration to ascertain the maximum line widths for resolving hydrogen Balmer alpha D_α and T_α lines and to determine their real intensity. Parameters such as maximum temperature, electron number density, and instrumental width in conjunction with peak intensity ratios were meticulously assessed. In addition, the influence of the applied approximations on maximum line widths was evaluated.

The experimental verification of obtained results, i.e., generation of plasma condition necessary to resolve hydrogen isotopes Balmer lines, was performed using an earlier proposed [36] CO₂ laser-based LIBS under a low-pressure helium and argon atmosphere. Different graphite targets incorporated with heavy water (D₂O) were analyzed, including the silica gel-doped wet graphite targets.

2. Theoretical considerations

In this section, the requirements for resolving Balmer alpha lines of hydrogen isotopes were analyzed and calculated. Special attention was devoted to calculating the requirements for resolving the tritium Balmer alpha line. This is necessary since tritium control and retention studies are critical for the safety operation of fusion power plants due to the possibility of tritium permeation into the coolant and the difficulties associated with its recovery [37].

However, as tritium is radioactive and its determination is experimentally challenging, laboratory studies of hydrogen retention primarily rely on analyzing deuterium content. A key parameter in applying isotopically resolved LIBS for retention studies is the relation between line broadening and the isotopic shifts. Compared to other Balmer series lines, the Balmer alpha lines, besides being the most intense visible hydrogen line, have lesser Stark broadening than isotopic shifts, so they are commonly selected for hydrogen retention studies. Namely, H_β and D_β lines cannot be resolved under typical LIBS plasma conditions ($N_e = 10^{22} \text{ m}^{-3}$ and $T_e = 10.000 \text{ K}$) since the isotopic shift for the Balmer beta H_β - D_β lines is 0.13 nm [38], while the Stark widths of these lines are 1 nm (according to the computer simulation (CS) calculations [39]). Contrary, under the same plasma conditions, the Stark width of the Balmer alpha lines is 0.23 nm [39], while the isotopic shift for H_α - D_α is 0.18 nm and 0.23 nm for H_α - T_α [38]. The main task of our research was to enhance the sensitivity of LIBS for the detection of hydrogen isotopes. For that purpose, optimal plasma conditions must be found under which hydrogen lines broadening is reduced, peak separation improved, and emission signal increased.

2.1. Determination of the critical FWHM for resolving hydrogen isotope lines

The first step in the analysis was to determine the limiting values of the spectral line widths necessary for resolving the H-D-T lines. From the spectroscopic point of view, lines are resolved if they fulfill the Rayleigh

criterion [29]. Therefore, the theoretical analysis of the overall line profiles (when all three isotopes are present in plasma) was performed to determine the maximum width of spectral lines that satisfy the Rayleigh criterion.

It is shown that the fitting of the hydrogen Balmer series lines with one, two, 4, 6, or seven Lorentzian excellent matches theoretical Stark profiles [40]. This and the fact that fitting the overall hydrogen profiles with one or sum of the Voigt function [40–42] also gives an excellent matching is a clear consequence of the fine structure of these lines. Since each fine structure component can be presented by the Voigt function, the resulting overall profile also has the Voigt shape [43]. Of course, such an approximation can be applied only above the fine structure limit [44]. On the contrary, it is unclear how such a fitting with several Voigt profiles can be easily applied for electron number density diagnostics.

Therefore, in many applications hydrogen profiles were fitted with a single Voigt profile. Determination of the full half width at half maximum, FWHM by such fitting procedure is adequate and is used in this work. On the contrary, deconvolution to determine Stark contribution by equalizing it with Lorentzian contribution to the overall line width may lead to significant errors [45]. More details about this approximation in determining electron density will be discussed in Section 2.3.

First, H_α , D_α , and T_α spectral lines, having the same intensity and line width, were generated using the Voigt approximation, which treats each peak as a sum of fractional contributions of the Gaussian and Lorentzian shapes:

$$w_V = 0.5346 \cdot w_L + \sqrt{0.2169 \cdot w_L^2 + w_G^2} \quad (1)$$

where w_V , w_L , and w_G are the full width at half maximum (FWHM) of the Voigt, Lorentz, and Gaussian profiles, respectively [46].

The Gaussian contribution is taken as the combination of the instrumental (w_i) and the Doppler broadening (w_D) [47]:

$$w_G = \sqrt{w_D^2 + w_i^2} \quad (2)$$

$$w_D = 7.16 \times 10^{-7} \lambda (T/M)^{1/2} \quad (3)$$

where T and M are the temperature and mass of the radiating atom in atomic mass units, and λ is the central wavelength in nm.

The estimated maximum line width (critical FWHM) for which the hydrogen isotope lines can be resolved is shown in Fig. 1. According to Rayleigh's criterion, assuming that the hydrogen isotope line intensities are the same, the critical FWHM to separate the H_α peak from the blended D_α/T_α lines is 0.18 nm (Fig. 1a), and 0.054 nm to resolve the D_α

from T_α line (Fig. 1b). It should be stressed that even when D_α/H_α line pair is resolved, the information about T_α may be lost entirely. In addition, if one wants to resolve D_α/T_α line pair, the dip between the D_α and H_α lines should be 10 % or less of the smaller line peak intensity.

Resolved deuterium and hydrogen lines were obtained in LIBS spectra of samples with different deuterium concentrations, confirming that the critical FWHM for H_α/D_α line separation is attainable [29–36]. It is much harder to attain the minimum peak width necessary to separate the $D_\alpha - T_\alpha$ line pair. In addition, the critical FWHM for resolving lines depends on the assumed peak intensities' ratio, R . Dependence of, determined, (critical for D_α and T_α lines resolving according to the Rayleigh criterion) FWHM dependance on a line intensity ratio in the range from 0.1 to 1 is presented in Table 1. The critical FWHM depends on the assumed ratio between D_α and T_α line intensities, R , regardless of which line is more intense, i.e., there was no difference between critical FWHM values obtained for intensity ratios of 0.5 and 2. Therefore, Table 1 presents only the values for intensity ratios between 0.1 and 1. To simplify procedure for critical FWHM determination, lines were approximated by Voigt profiles using the same line width for all lines.

As illustrated in Table 1, the determined critical FWHM of Voigt profiles for resolving D_α and T_α lines go from 0.027 to 0.054 nm, depending on the line intensity ratio. The results in Table 1 suggest that as the intensity ratio between these two lines decreases, it becomes more challenging to resolve D_α and T_α lines experimentally.

The dependence of determined critical FWHM on the assumed ratio of peak intensities of the Balmer alpha lines can be, besides in Table 1, presented by eq. (4), which enables easy calculation of the maximum FWHM necessary for resolving studied lines, for the estimated value of R :

$$FWHM_{cr} = 0.0599 - 0.0388 \times \exp(-1.765 \times R) \quad (4)$$

2.2. Critical plasma parameters for resolving hydrogen isotope lines

Resolving hydrogen isotope lines requires detecting a spectral signal at reduced electron density with corresponding narrower line widths. In other words, plasma parameters (T and N_e) must be optimized to ensure the conditions necessary to decrease electron density without a

Table 1
Critical FWHM for resolving D_α and T_α for different intensity ratios.

Line intensity ratio (R)	0.1	0.3	0.5	0.67	0.8	1
Critical FWHM	0.027	0.038	0.044	0.047	0.050	0.054

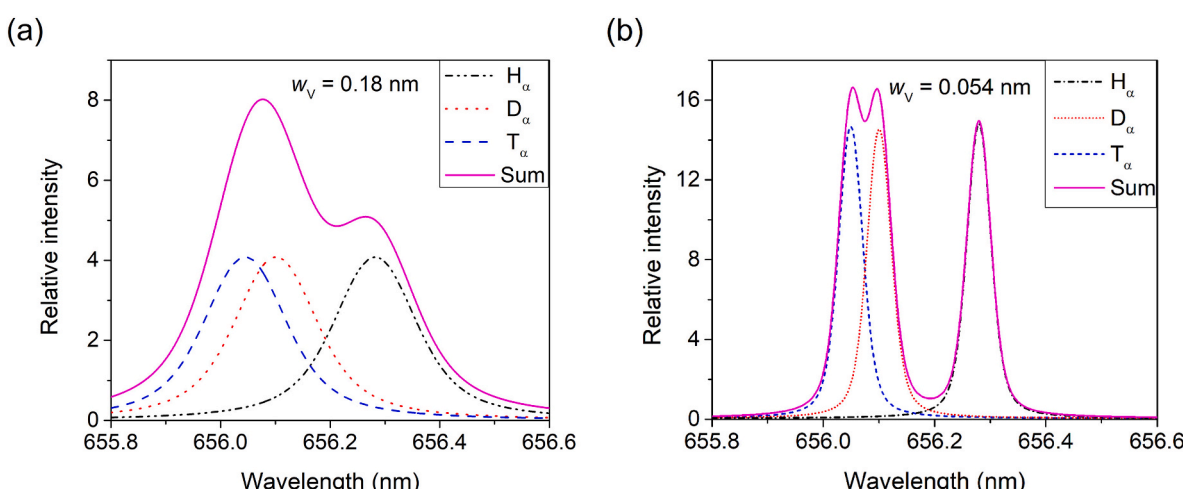


Fig. 1. Voigt approximation of hydrogen spectral lines having equal line widths and intensities and critical FWHM for resolving (a) H_α and D_α and (b) D_α and T_α peaks.

significant decrease in light emission intensity.

Electron density from the width of the H_{α} can be determined using different approaches since much work was devoted to studying this line. For example, it is shown [48] that using Griem theory, there is a considerable difference between electron densities determined from Balmer alpha and Balmer beta line widths. Having in mind the high accuracy of the H_{β} line theory, electron density can be determined using the correction factor between theories of the H_{α} and H_{β} widths.

In this work, according to the approximation that the Stark profile of the H_{α} line at electron densities greater than 10^{21} m^{-3} is close to Lorentzian [45], the eq. (1) was used to obtain Stark broadening contribution to overall line width, assuming $w_L = w_S$. Then, eq. (5) [39] was used to calculate N_e :

$$N_e [\text{m}^{-3}] = 10^{23} \cdot (w_s [\text{nm}] / 1.098)^{1.47135} \quad (5)$$

Fig. 2 shows the maximum values of plasma parameters (T and N_e), under which critical FWHM for T_{α} , D_{α} resolving is obtained, estimated for different values of the instrumental FWHM parameter, w_i . Plasma parameters were calculated for two critical line width values corresponding to two values of R spectral line intensity ratios. Upon approaching the limit value of $N_e = 1.2 \times 10^{21} \text{ m}^{-3}$ as shown in **Fig. 2a**, it becomes impossible to obtain the parameters (T and w_i) required to resolve both the D_{α} and T_{α} , when $R = 1$. Additionally, it is observed that for an electron density of approximately $4 \times 10^{20} \text{ m}^{-3}$ and temperature less than 6000 K, (corresponding to LIBS plasma at later evolution times), the instrumental FWHM should be less than 0.027 nm to resolve the T_{α} and D_{α} lines. Also, with equal peak intensities, if the temperature is higher than 10,000 K and N_e greater than $4 \times 10^{20} \text{ m}^{-3}$, the instrumental width must be smaller than 0.02 nm. As shown in **Fig. 2b**, for an N_e lower than $1 \times 10^{20} \text{ m}^{-3}$ and a minimal instrumental width of less than 0.01 nm, the temperature cannot exceed 3000 K.

2.3. Validity of approximations used for simulation of line profiles

Several approximations were used to determine critical, i.e., maximal FWHM and plasma parameters necessary to resolve hydrogen isotope Balmer alpha lines. Therefore, the validity of these approximations and their influence on determined parameters will be analyzed.

2.3.1. Approximation of line profiles with Voigt function

The validity check of the Voigt approximation, in the determination of the plasma conditions required for resolving studied lines, was performed by comparing estimated parameters with those obtained using

the Computer Simulation model of hydrogen spectral line profiles (CS tables) given by Gigosos et al. [39]. Previous studies [45] have confirmed the validity of approximating hydrogen Balmer alpha line shapes using the Voigt function. Conversely, determining the width by fitting hydrogen lines with the Voigt function, even by fixing the Gaussian contribution to the line width, can lead to significant errors at low electron densities. Therefore, the calculation of plasma parameters was performed using relation (5) [39,45] to improve their accuracy.

The difference in calculated values for the instrumental width $w_i = 0.01 \text{ nm}$, and $w_i = 0.027 \text{ nm}$ respectively, (0.027 CS and 0.01 CS), was illustrated in **Fig. 2 a,b**, respectively. Error bars, included for these data in **Fig. 2**, indicate uncertainty of used formula. The slight variation between these values can be attributed to the contribution of a Doppler broadening mechanism because Voigt profiles were generated assuming identical widths of all three lines. For example, in the Voigt approximation, all three lines have a width of 0.054 nm, whereas the precise values are 0.0598 nm for H_{α} , 0.052 nm for D_{α} , and 0.049 nm for T_{α} .

2.3.2. Consistency in the assumption of the same stark widths and shifts

Different Stark widths of Balmer alpha lines of hydrogen and deuterium were reported [49]. The author measured the Stark-broadened line profiles of H_{α} and D_{α} in a wall-stabilized argon arc at an electron density of $N_e = 1.4 \times 10^{22} \text{ m}^{-3}$ and found the half width of D_{α} to be about 15 % smaller than the width of H_{α} . It was found that only about 5 % of the measured 15 % difference between the experimental H_{α} and D_{α} profiles can be explained by differences in Doppler widths and inaccuracies in reproducing the exact electron density, while the major portion ($\approx 10 \%$) must be attributed to ion dynamic effects. In reference [49], for the evaluation of N_e through the Stark broadening of the D_{α} line, the numerical factor of 0.9 was introduced in relation (5) to account for the reduced Stark broadening of the D_{α} compared to the H_{α} line.

Our study of the necessary conditions for resolving the H_{α} , D_{α} , and T_{α} peaks assumed the same values for FWHM of these lines. Therefore, the impact of disregarding the influence of the reduced mass on the line profile was examined using CS tables [39]. The analysis was performed for four values of a reduced mass of 0.5, 0.8, 1, and 2, corresponding (in case of equal gas and electron temperatures) to different plasma compositions: pure hydrogen, hydrogen-helium, hydrogen-argon, and a mixture of argon with deuterium or all three hydrogen isotopes, respectively. It was concluded that ion dynamics affects the line shapes, resulting in the observed difference in line widths. As a result, observed differences could impact the precision of estimated widths and plasma conditions for separating D_{α} and T_{α} peaks in the studied range of densities. Namely, according to the CS simulation results, a dip between

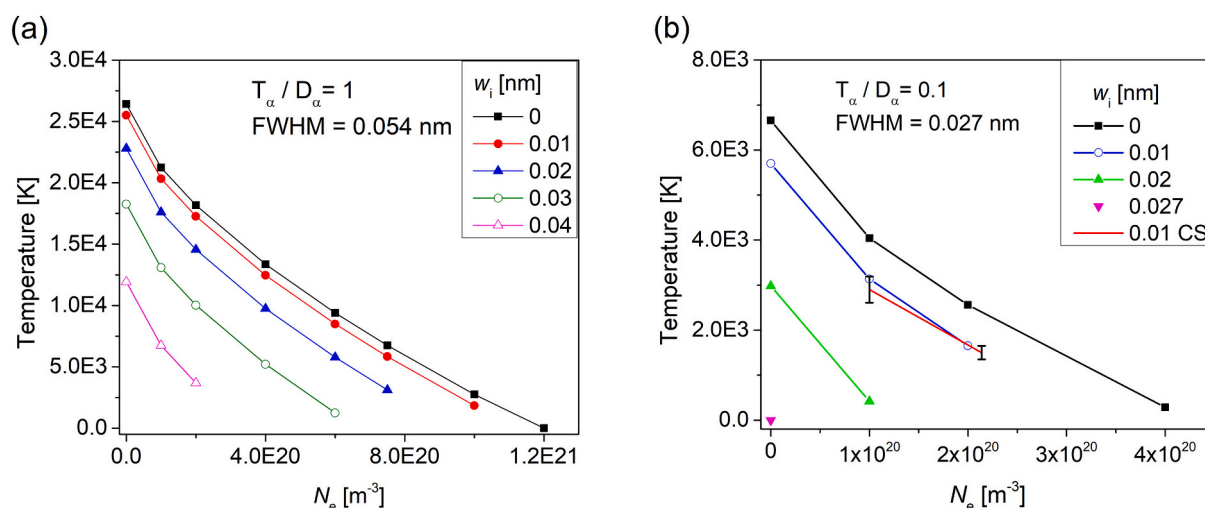


Fig. 2. Relationship of the maximal electron temperature versus the electron density corresponding to different values of the instrumental FWHM calculated for two critical line width values: a) critical FWHM = 0.054 nm, $T_{\alpha}/D_{\alpha} = 1$, and b) critical FWHM = 0.027 nm, $T_{\alpha}/D_{\alpha} = 0.1$.

lines increases with the increase of the reduced mass, which positively influences the conditions for resolving the hydrogen isotope lines. But, neglecting the influence of reduced mass on the line shapes by analyzing theoretical profiles for pure hydrogen only loosen the criteria for maximal FWHM for other μ . In addition, the hydrogen and deuterium spectral line profiles analyzed and experimentally tested in this work correspond to plasma with a simultaneous presence of hydrogen isotopes. On the contrary, in reference [49], measurements were performed for two experimental conditions (with a small percentage of the H or D added to Ar) having different reduced masses, which caused the stated difference in the hydrogen and deuterium line width.

3. Experimental methods and materials

Requirements for line resolution, analyzed in Chapter 2, were experimentally tested using the LIBS setup described in Section 3.1. Emission spectra were recorded using the spectrometer, the resolution of which is analyzed in Section 3.2. The selection of targets and their preparation procedures are described in Section 3.3. To verify the requirements for plasma parameters estimated in Chapter 2, temperature and electron number density diagnostics were performed. These results are described in Section 3.4.

3.1. Experimental setup

The breakdown on a solid target was generated using the modified carbon dioxide TEA laser (Tachisto 215G) operated at 10.6 μm , with a repetition rate of 1 Hz. The duration of the main laser pulse was 80 ns with a tail lasting 2 μs (see inset in Fig. 3). The targets were placed within the vacuum chamber mounted on the x-y table (Isel-automation 230,510). The chamber was vacuumed and filled with a continuous argon or helium gas flow at the desired pressure. The laser beam was focused perpendicular to the target surface using a ZnSe lens (L , $f_1 = 100$ mm), as illustrated in Fig. 3. Fast imaging was conducted through a lateral window of the vacuum chamber, capturing the plasma image and projecting it onto the entrance slit of a spectrometer. This process utilized an optical fiber settled at 15 degrees and equipped with a collimator (SolarLas PS2) for precise light transmission. For recordings of line shapes, a spectrometer (Sol Instruments MS7504i) was employed, outfitted with an iCCD camera (Andor Technology, model DH734I-18F-63 featuring 1024×1024 pixels, with a size of $13 \times 13 \mu\text{m}$ and an 18 mm diameter intensifier). The iCCD was controlled using a pulse generator (DG-535, Stanford Research Systems), triggered optically by the occurrence of plasma on the target. A fast photodiode (PD) oriented towards the target was utilized to convert the light signal into electrical

and trigger the DDG. Line shape recordings were performed with full vertical binning and different gate widths at various delay times. The acquisition gate width was varied between 15 ns and 70 μs . If not stated otherwise, the gate time was 5 μs . The shorter acquisition widths at earlier delays were favorable for tracking fast-changing plasma. Signals were recorded over ten accumulations to mitigate the influence of shot-to-shot variations.

3.2. Instrument selection and determination of instrumental profile

The initial step in experimental evaluation of the criteria for resolving hydrogen isotope Balmer alpha lines involved examining the spectrometer's resolution, i.e., determining the instrumental half-width. Namely, the instrumental half-width must be smaller than the values shown in Table 1. The shape and width of the instrumental profile of the MS 7504i spectrometer were determined by measuring radiation from the Ne pen lamp. The instrumental width (diffraction grating with 1800 grooves/mm and a 15 μm wide entrance slit of spectrometer) was determined to be $w_i = 0.03$ nm. Thus, it was concluded that the spectrometer was suitable for resolution studies of hydrogen isotope Balmer alpha lines.

3.3. Preparation and testing of targets

The second task was selecting and preparing the targets that could serve as substitutes for the hydrogen isotope-enriched components of the plasma fusion reactor. The material selected for the present study was graphite because of its importance for fusion technology [50,51]. Two preparation procedures were used to obtain graphite targets with embedded D₂O. In the first case, a controlled amount of the D₂O was applied with a micropipette to the surface of a tablet made from spectroscopically pure graphite powder. In this way, graphite targets with a gradient concentration of hydrogen along the sample thickness were produced. These targets were suitable for depth analysis of hydrogen retention, i.e., recording LIBS spectra in which the intensity ratio of hydrogen over deuterium Balmer alpha lines changes with the number of laser shots.

In the second case, tablets were made from graphite powder doped with D₂O and mixed with silica gel (SiO₂). The silica gel was added to prevent a decrease in water content during vacuuming. Before mixing with D₂O-doped graphite, SiO₂ was ground to a fine powder and dried in an oven at 110 °C for 20 h to eliminate previously accumulated moisture. The best consistency of the tablets was achieved by mixing the graphite and silica gel powders in the proportion of 3:1. After pressing (10 tons hydraulic press for 30 min), the tablets were dried at 120 °C for

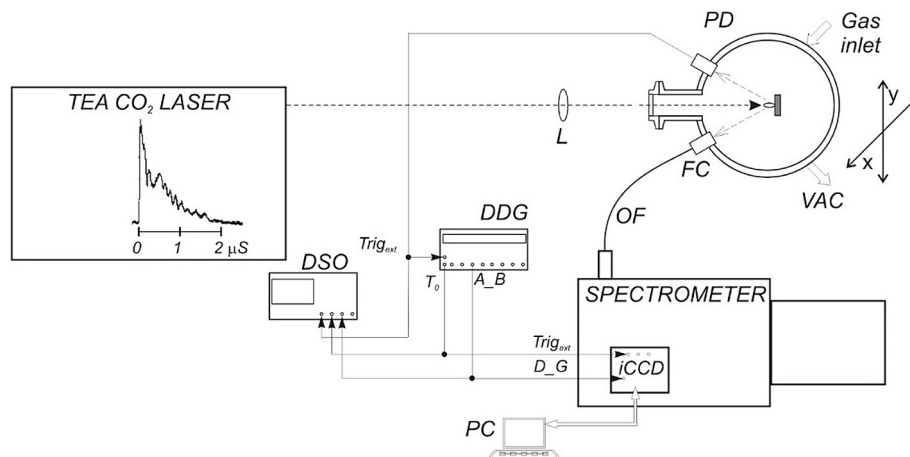


Fig. 3. Experimental setup: L-lens, PD-photodiode, OF-optical fiber, FC-focusing collimator, VAC-vacuum outlet, DSO-digital storage oscilloscope and DDG-digital delay generator.

6 h and stored in a desiccator to prevent moisture absorption. Targets prepared with this procedure had a homogeneous water distribution, as confirmed by LIBS spectra. The intensity ratio of the H_α and C II lines remained almost unchanged with increasing number of applied laser shots. The heavy water-doped graphite/silica gel targets were used in all further experiments.

3.4. Plasma diagnostics

The plasma parameter measurements were conducted to experimentally validate the conclusions drawn from the results depicted in Fig. 2. Electron number density was evaluated from the measurement of wavelength separation (s) between peaks of allowed ($2p\ 3P^0 - 4d\ 3D$) and forbidden ($2p\ 3P^0 - 4d\ 3F^0$) component of the He I 447.1 nm line, using the relation (6) [52], with T_e in K, s in nm and N_e in m^{-3} :

$$\log_{10}(N_e) = 21.5 + \log_{10} \left[\left(\frac{s}{0.1479} \right)^{b(T_e)} - 1 \right]$$

$$b(T_e) = 1.46 \times \frac{8380}{T_e^{1.2}} \quad (6)$$

From the spectra presented in Fig. 4 a, the separation between peaks was determined: $s = 0.206$ nm for shorter delay/gate times (0.5 μ s / 5 μ s) and 0.155 nm for longer delay/gate times (5.5 μ s / 50 μ s). The estimated N_e for shorter and longer delay/gate times were 2.5×10^{21} and $2.7 \times 10^{20} m^{-3}$, respectively.

In addition, N_e was determined from the parameters of the He I 492.2 nm line ($2p\ ^1P_0 - 4d\ ^1D$) with forbidden component ($2p\ ^1P^0 - 4f\ ^1F^0$ and $2p\ ^1P^0 - 4p\ ^1P^0$) using the relation (7) [53], with T_e in K, s in nm, and N_e in m^{-3} :

$$\log_{10}(N_e) = 21.3065 + \left(\frac{1}{0.8766} \right) \log_{10} \left[\left(\frac{s}{0.131187} \right)^{b(T_e)} - 1 \right]$$

$$b(T_e) = 1.25 + \frac{994}{T_e} \quad (7)$$

Using the separation values $s = 0.203$ nm and 0.146 nm determined from Fig. 4 b, the calculated electron number density was $N_e = 1.5 \times 10^{21}$ and $2.2 \times 10^{20} m^{-3}$ for shorter and longer delay/gate times, respectively. From data presented in Fig. 4, for separation between forbidden (F) and allowed (A) components ($s = 0.203$ nm and 0.146 nm) and their intensities ratios ($F/A = 0.196$ and 0.044) the following N_e values were obtained by interpolation of the data according to unified theory (BCS) [54]: 2.03×10^{21} , 3×10^{20} , 1.5×10^{21} and $3.66 \times 10^{20} m^{-3}$, which are in reasonable agreement with values obtained from the calculations based on approximative formulas [52,53].

The gas temperature was determined by comparing the synthetic and

recorded spectra of the sequence $\Delta\nu = 0$ of the C_2 molecule Swann system at 515 nm. Fig. 5a shows a part of the $\Delta\nu = 0$ sequence of the C_2 molecule Swann system spectrum, obtained in an Ar atmosphere at reduced pressure (10 millibars) between the band heads (0–0) and (1–1). Spectra were obtained with different delay times (5, 10, and 15 μ s), with a gate of 5 μ s. As can be seen from the picture, the resolution of the spectrograph and the plasma conditions allow for obtaining spectra with a well-developed rotational structure, where the lines of the R and P branches are well-separated. Due to the decrease of plasma temperature with time, the band intensities obtained for different delay times decrease rapidly with increasing time. In general, the emission of molecular bands is characteristic of the peripheral plasma parts and/or later times of development of the laser-induced plasma: with increasing temperature, the intensity of the emission increases, but at the same time, the concentration of molecules decreases due to dissociation. The maximum emission intensity of the Swan system is usually reached at a temperature around 6700 K [55].

When the rotational structure of molecular band spectra is well resolved, it can be used to determine the temperature of heavy particles. The (0–0) band of the Swan system is very suitable for that purpose: the C_2 molecule has a sufficiently high dissociation energy (6.2 eV) and a sufficiently low excitation energy (2.4 eV) to obtain very intense spectra, and on the other hand, the structure of the energy levels is such that the components of rotational structures can also be separated using a medium-resolution spectrograph. Fig. 5 b shows a detail of the C_2 band spectrum synthesized for different temperatures, with a Gaussian profile corresponding to the instrumental profile of the spectrograph. The Pgopher program [56] was used to synthesize the spectra. The intensity ratio of R components and band head does not depend on temperature, so both synthesized and experimental spectra can be normalized to the intensity of the R component. This way of normalization is better than normalization using the (0–0) band head because of its potential self-absorption. As shown in Fig. 5 b, the intensity ratios of the R and P components of the (0–0) band strongly depend on temperature, so they can be used to estimate plasma temperature.

By comparing the normalized experimental and synthesized spectra, the temperature was estimated for different delay times: for a delay of 5 μ s, a temperature value of 5000 K was determined, with an error of 10 %. With the delay time increase, a clear trend of temperature decrease was observed, from 4500 K for a delay of 10 μ s to a temperature of about 3500 K for a delay of 20 μ s. The intensities were significantly lower for delay times longer than 10 μ s, considerably increasing the determination error.

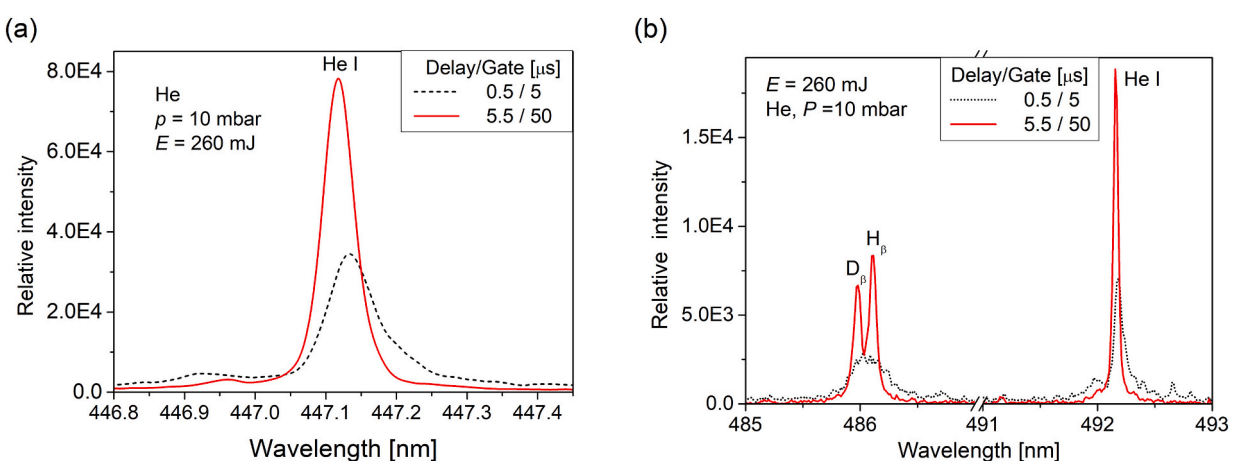


Fig. 4. Examples of the N_e diagnostics: (a) Shape of the He I line at 447.1 nm and (b) Shapes of the hydrogen isotope Balmer beta lines and He I line at 492.2 nm.

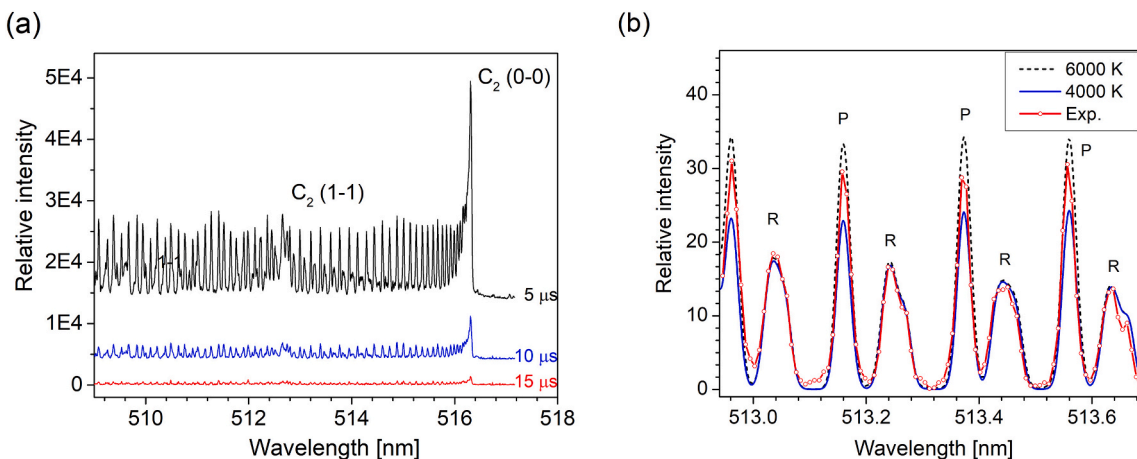


Fig. 5. (a) Experimentally obtained spectra of the Swan band ($\Delta v = 0$ sequence) for different delay times. (b) Synthesized normalized spectra for temperatures of 4000 and 6000 K and experimental spectrum for a delay time of 5 μ s (part of the (0-0) band).

4. Results

The analysis outlined in Chapter 2 has shown that a necessary requirement for resolving hydrogen isotope lines is employing a spectroscopic instrument with minimal instrumental width and generating plasma with parameters (N_e and T) falling within the limits indicated in Fig. 2. The LIBS operation is commonly performed in air and spectral lines are recorded with some delay period to the laser pulse, to avoid the influence of continuum radiation, i.e., acquisition starts when lines of the studied elements appear in spectra and last, until their intensity becomes comparable to noise.

Typical temperature and electron number density values for laser-induced plasmas are around $T = 15,000$ K and $N_e = 10^{23} \text{ m}^{-3}$ (or above) [14–20]. The value of N_e is almost two orders of magnitude greater than the values shown in Fig. 2. The plasma induced by Nd:YAG laser in Ar at reduced pressure is characterized by a lower N_e but still far above the values required to resolve the Balmer alpha line. For example, the H _{α} line measured in tungsten plasma induced in He atmosphere at 10 mbar had FWHM of around 0.5 nm [57], i.e., almost ten times greater than requested for resolving studied lines. In LIBS detection of hydrogen in molybdenum within mixtures of argon and nitrogen at atmospheric pressure it is observed that the width of the H _{α} line decreases (for the same delay), with shorter duration of plasma, i.e., emission intensities decrease faster than in pure argon [58]. The resolving of the H _{α} and D _{α} was obtained using double-pulsed LIBS (with ps and fs lasers) or laser-induced filamentation LIBS. However, the line widths were too wide to resolve D _{α} and T _{α} , like the line profiles shown in Fig. 1a.

Resolving D _{α} and T _{α} lines is the most critical task for LIBS analysis of hydrogen isotope retention, bearing in mind that the isotope shift

between D _{α} and T _{α} is 0.0598 nm, while between H _{α} and D _{α} is 0.1785 nm. The targets used in this study did not contain tritium. Nonetheless, the analysis presented in Section 2 (Fig. 1 b) demonstrates that when the H _{α} and D _{α} are distinctly resolved, and the dip between these lines accounts for less than 10 % of the intensity of the smaller peak, the requirements for resolving D _{α} and T _{α} are met.

In this work, we investigated the potential of LIBS based on TEA CO₂ laser for obtaining well-resolved hydrogen Balmer alpha lines. Experimental parameters were optimized by recording LIBS spectra of heavy water-doped graphite/silica gel targets under different experimental conditions. Three laser energies were used in this study, namely 260 mJ, 320 mJ and 420 mJ. Targets were irradiated in Ar and He atmosphere at different gas pressures (3–80 mbar), and spectra were recorded with variable delay (0.5–15 μ s) and gate times (5–50 μ s).

The characteristic dependence of the line profiles on delay time at He pressure of 30 mbar are shown in Fig. 6 a, and on He gas pressure at a delay of 15 μ s in Fig. 6 b. Each spectrum is a sum of 10 accumulated laser shots applied at the same spot on the target.

Based on Fig. 6, it can be inferred that ionized carbon lines start to emerge in the spectra during the initial phase of plasma evolution and persist for less than 5 μ s. It should be stressed that the width of the C II lines (3 s ²S - 3p ²P⁰) at 657.8 nm and 658.29 nm, recorded at the beginning of the plasma evolution, was 0.033 nm, which confirms that w_i is equal to or slightly less than the stated value. In addition, since the overall width is not greater than the instrumental width, we may conclude that the contribution of the other line-broadening mechanisms was negligible. Further, in the time window 0.5 μ s – 5 μ s, the N_e value was around 10^{21} m^{-3} since a Stark width of these lines, according to theory [59], is around 0.1 nm at $N_e = 10^{23} \text{ m}^{-3}$.

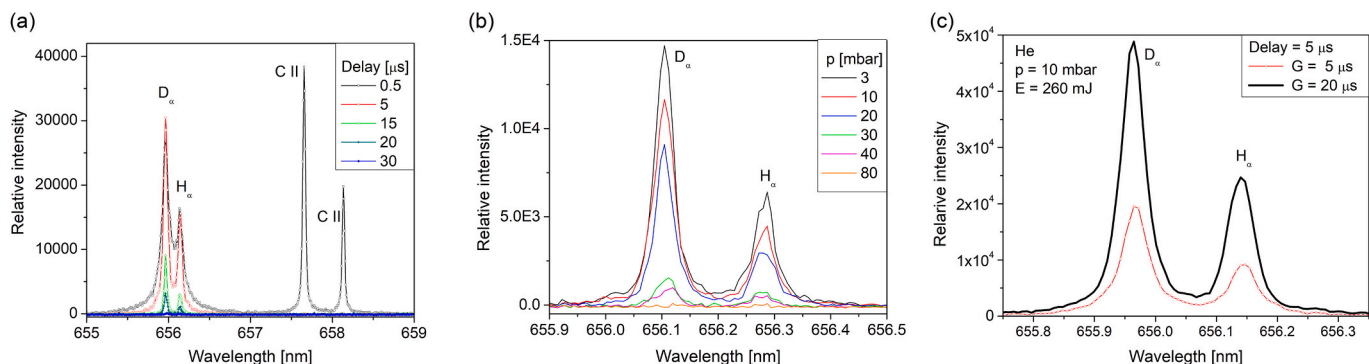


Fig. 6. Variation of line shapes: (a) with delay time at He pressure of 30 mbar and (b) on gas pressure at a delay of 15 μ s. The influence of gate time on spectra (c) recorded in He at 10 mbar. All spectra were recorded using the laser energy of 260 mJ. Gate time for (a) and (b) was 5 μ s. Delay for (c) was 5 μ s.

After a few microseconds, the spectral lines of surrounding gas (He or Ar) and those of hydrogen become more pronounced, thus enabling adequate resolving of the Balmer alpha line from the closely spaced spectral lines of the target material. This fact is significant for studying hydrogen isotope retention in tungsten targets because the presence of the spectral line of W I at 656.32 nm or Be II line at 656.45 nm can make it difficult to separate it from the hydrogen Balmer alpha line. Furthermore, the Balmer alpha lines were not fully resolved at short delay times, see Fig. 6 a, indicating a preference for analysis at delays longer than 15 μs . Fig. 6 also shows that the dip between H_α and D_α lines decreases with increasing pressure. For pressure higher than 10 mbar, lines are fully resolved. Unfortunately, the intensities of Balmer lines diminish swiftly as the pressure and delay times increase. Hence, the primary objective of this study was to identify experimental parameters where line intensities significantly exceed the noise level and fulfill conditions required for resolution. As the plasma evolves, the line width decreases, indicating improved resolution. However, this decrease in width is accompanied by a decrease in intensity, which presents a drawback. Therefore, when the line width aligns with the instrumental resolution, the remaining signal can be captured by widening the gates for data collection. As an illustration, the spectra recorded in He at 10 mbar, using laser energy of 260 mJ and delay time of 15 μs for gate values of 20 μs and 5 μs , are shown in Fig. 6c.

In argon, under the same experimental conditions as for He gas, the intensity and shape of the hydrogen isotope Balmer alpha lines are considerably different due to the changes in electron number density, electron temperature, and different temporal and space evolution of plasma. The recorded line shapes for a laser energy of 420 mJ and a gate time of 5 μs are shown in Fig. 7a for various delay times.

Considerably greater electron number densities are obtained in LIBS with Ar compared to He. Consequently, the resolution of lines at the beginning of the plasma evolution is of poorer quality (Fig. 7a). However, plasma emission in Ar lasts longer, and for longer time delays (at 50 μs) well-resolved lines of sufficient intensity can also be obtained, see Fig. 7a. The line shapes obtained under same laser energy and gate time parameters, but under varying pressure, are depicted in Fig. 7b, for delay time of 0.5 μs .

As a figure of merit, which will clearly describe the quality of resolving of hydrogen lines, the dip between lines seems to be the most appropriate. The dip was defined as the minimum intensity between lines (presented as a percentage of the lowest peak intensity). Considering that determining the line widths requires fitting, it is clear that dip is a more adequate parameter. Namely, a dip may, without any other procedure, give a reasonable estimate of how far one is from the optimal conditions for resolving not only the H_α and D_α line, but also for resolving the deuterium and tritium Balmer alpha lines. Fig. 8 shows the

dependence of the dip between hydrogen isotope lines versus studied parameters: laser energy, gas type and pressure, and delay times. For comparison, the line widths are also shown in the same figure.

In Fig. 8, it is evident that the dip value's dependency on gas pressure and laser energy is most notable during the initial stages of plasma evolution. However, as delay times progress, the line width approaches or matches the instrumental width, leading to dip changes among lines comparable to the measurement uncertainty. It is plausible to infer that employing a spectrometer of higher resolution would yield smaller dip and FWHM values, particularly at longer delays.

In argon (Ar), the dip increases with both pressure and laser energy due to the higher electron number density, resulting in an increase in the Stark width of the spectral line. Conversely, when using helium (He) as the surrounding gas, the increment in electron density is less pronounced, leading to a dip that remains nearly unaffected by changes in pressure and laser energy, under studied conditions.

Hydrogen isotope retention studies depend not only on resolving Balmer alpha lines but also on studied line peak intensities. Therefore, we presented the results for lines fitting in the form of peak intensity versus determined FWHM for all experimental parameters. In Fig. 9, gas pressure was used as a parameter, while data for various delay times are presented and labeled for each data point. On the same graph, the critical FWHM value of 0.054 nm (Chapter 2) for resolving D and T Balmer alpha lines having equal intensities is presented as a thick vertical line. The experimental points on the left side of the vertical line display plasma parameters where the line separation was deemed satisfactory. The vertical dotted line presents the value of the minimal instrumental width of the spectrometer. The red arrow indicates the data point for which optimal intensity and resolution of spectral lines were obtained.

Fig. 9 shows that resolved hydrogen isotope Balmer alpha lines can be obtained in both gases, but the line's intensity and signal-to-noise ratios is better in He than in Ar. In addition, at various line peak intensities, the dip between studied D_α and H_α lines is less than 10 % (see Fig. 8), i.e., line widths much less than 0.054 nm (see Fig. 9) can be obtained, which guarantees, according to the analysis presented in Chapter 2, resolving of D_α and T_α lines. At optimal conditions for resolving lines, the intensity is much lower than at the beginning of plasma evolution, see Fig. 10a, but still adequate for determining their intensities with high accuracy, see Fig. 10b.

5. Conclusion

This study examined the resolution of hydrogen isotope Balmer alpha lines, a crucial aspect for tritium retention investigations using LIBS. Key highlights of the study included determining the critical line

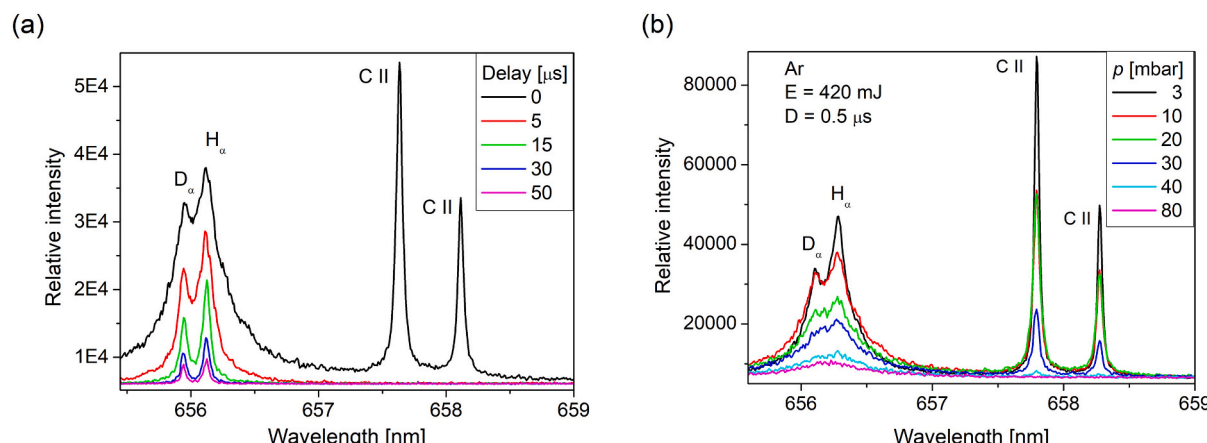


Fig. 7. Figure (a) illustrates the variation of line shapes with delay time at an argon pressure of 10 mbar, while figure (b) shows the influence of gas pressure at a delay of 0.5 μs . The laser energy and gate time used for these measurements were 420 mJ and 5 μs , respectively.

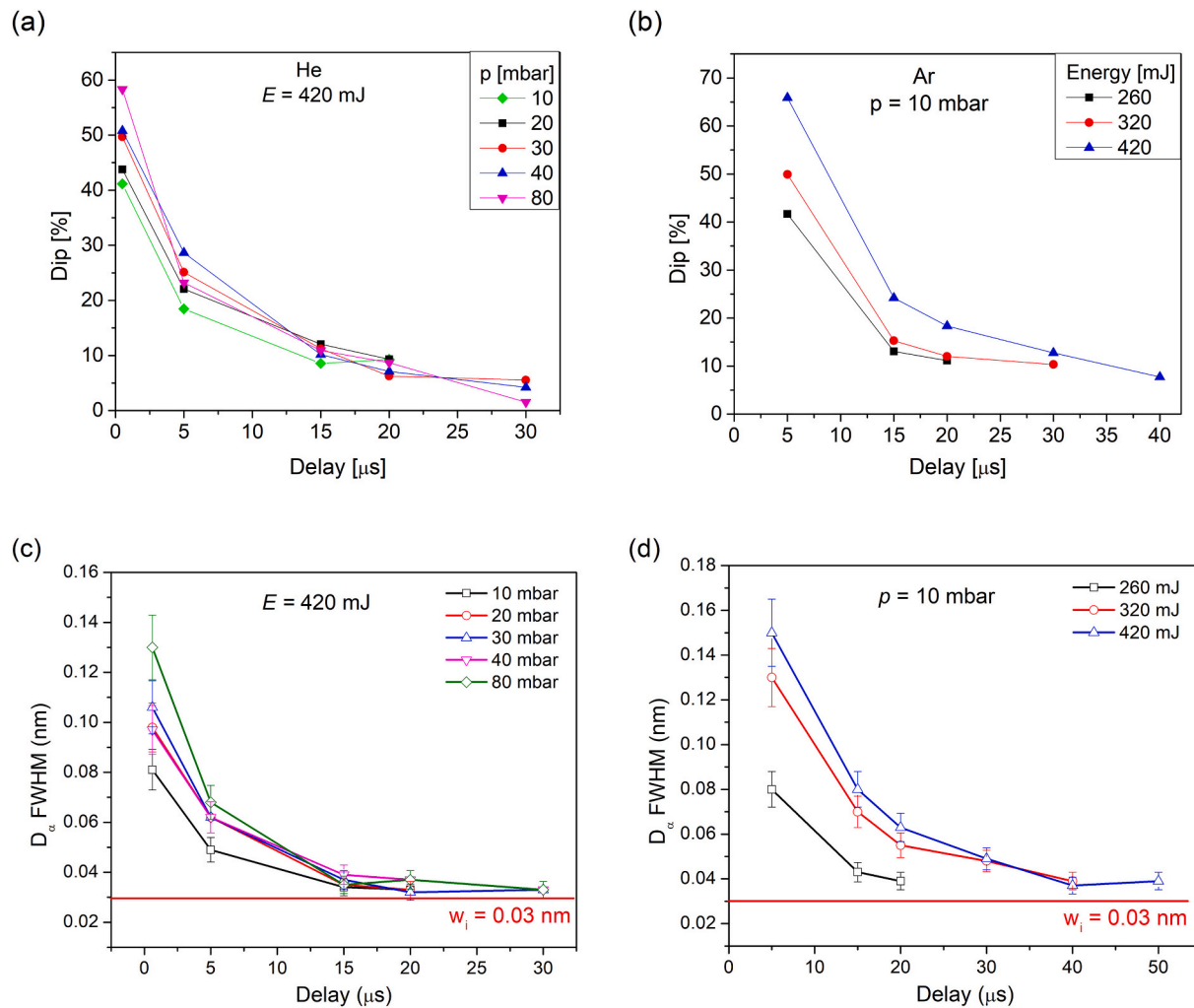


Fig. 8. Dip between H_α and D_α lines expressed in the percentage of the lower peak intensity versus delay for a different: (a) He gas pressure, (b) laser energy in Ar at 10 mbar. FWHM of the H_α and D_α lines at conditions: c) same as a) and d) same as b). All data are recorded using a gate time of 5 μs.

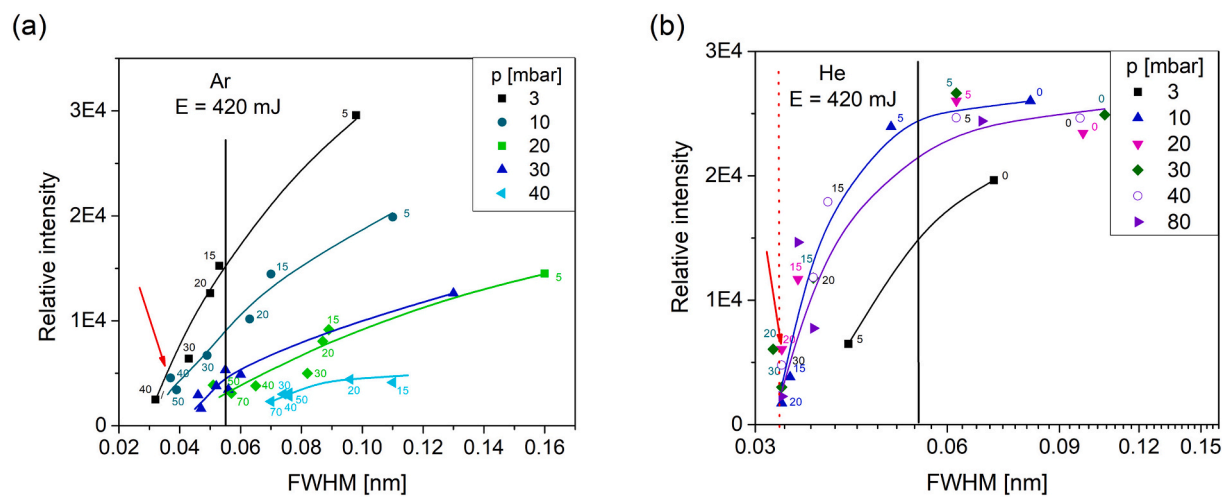


Fig. 9. Dependence of spectral line peak intensity on FWHM for different gas pressures of (a) Ar and (b) He at laser energy 420 mJ. A vertical line represents the maximum spectral line width (0.054 nm) for resolving D_α and T_α with equal peak intensity. Labels represent the values of delay time for each data point.

width (FWHM_{cr}) for resolving deuterium (D_α) and tritium (T_α) lines by applying Rayleigh criteria and Voigt profile approximations for hydrogen lines. The estimated FWHM_{cr} ranged between 0.054 nm for

equal peak intensities ($R = 1$) and 0.027 nm for $R = 0.1$. An approximate formula for calculating FWHM_{cr} dependency on R was proposed. The study emphasized that fulfilling necessary conditions for resolving D_α

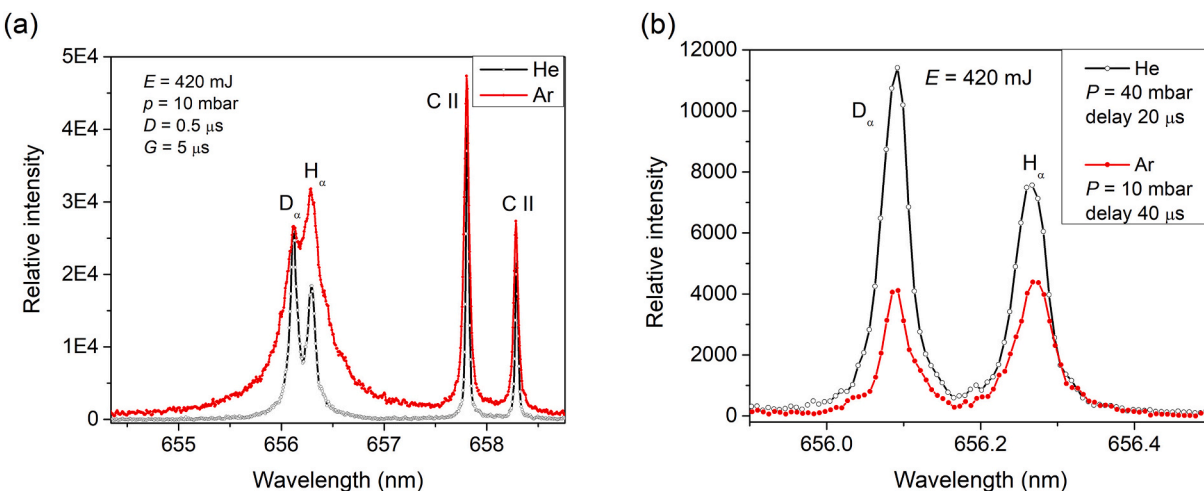


Fig. 10. Comparison of the Balmer alpha line shapes at (a) the beginning of the plasma evolution and at (b) optimal conditions: for He at 40 mbar at a delay 20 μ s and for Ar at 10 mbar at a delay 40 μ s.

and T_α required full resolution of H_α and D_α lines while ensuring the dip between these lines was less than 10 % of the smaller peak intensity.

Experimental validation of the determined conditions essential for resolving T_α and D_α was conducted using a LIBS setup employing a TEA CO₂ laser and recording plasma emission through an iCCD camera mounted on the spectrometer's exit slit with an instrumental width of 0.03 nm. Tests on hydrogen isotope retention in plasma-facing components were carried out using graphite samples doped with heavy water (D₂O) mixed with silica gel. Plasma parameters were assessed by determining electron number density from the separation between peaks of He I components and inferring temperature from the measured and synthetic segments of the C₂ molecule sequence $\Delta\nu = 0$. In the time frame of 0.5 μ s – 5 μ s, the electron number density was approximately 10^{21} m^{-3} , with plasma temperature around 5000 K and 3500 K for delays of 5 μ s and 20 μ s, respectively.

Spectra of hydrogen and deuterium Balmer alpha lines were obtained using different laser energies under varying experimental conditions in Ar or He atmospheres, impacting line resolution differently. Optimal conditions for plasma induced in He and Ar were identified concerning laser energy, gas pressure, and delay times, resulting in better intensities and signal-to-noise ratios. Resolving D_α and H_α lines with a dip below 10 % of the smaller peak intensity under optimal conditions showcased the potential for obtaining fully resolved T_α and D_α lines in both gas atmospheres.

Enhancement of the line intensities by using longer gate times (for recordings when at given delay time, the line width approaches instrumental width) is demonstrated.

CRediT authorship contribution statement

I. Traparic: Writing – review & editing, Investigation, Formal analysis. **D. Rankovic:** Investigation, Formal analysis. **B.D. Stankov:** Investigation, Formal analysis. **J. Savovic:** Writing – review & editing, Visualization, Formal analysis. **M. Kuzmanovic:** Writing – review & editing, Formal analysis. **M. Ivkovic:** Writing – review & editing, Writing – original draft, Supervision, Methodology, Conceptualization.

Declaration of competing interest

The authors declare that they have no known competing financial interests or personal relationships that could have appeared to influence the work reported in this paper.

Data availability

Data will be made available on request.

Acknowledgements

The research was funded by the Ministry of Science, Technological Development and Innovations of the Republic of Serbia, Contract numbers: 451-03-68/2022-14/200024 and 451-03-65/2024-03/200146, and supported by the Science Fund of the Republic Serbia, Grant no. 7753287 “NOVA2LIBS4fusion”. This work was carried out under the project: “Laser induced breakdown spectroscopy for determination of LHD wall composition” (NIFS21KLPF087) within the agreement between NIFS and the University of Belgrade. The authors thank Stanko Milanovic for technical assistance in preparation and setting up the experiment.

References

- [1] Fusion Energy and ITER. https://research-and-innovation.ec.europa.eu/research-area/energy/fusion-energy_en, 2024.
- [2] L. Qiao, X. Zhang, R. He, H. Zhang, E. Fu, P. Wang, Experimental measurement of deuterium concentration and depth profiling in tungsten by radio frequency glow discharge optical emission spectroscopy, Spectrochim. Acta Part B At. Spectrosc. 173 (2020) 105975, <https://doi.org/10.1016/j.sab.2020.105975>.
- [3] C. Cupak, E. Pitthan, M.V. Moro, M. Fellinger, D. Premetzhofer, F. Aumayr, Retention of deuterium in beryllium: a combined investigation using TDS, ERDA and EBS, Nucl. Mater. Energy. 33 (2022) 101249, <https://doi.org/10.1016/j.nme.2022.101249>.
- [4] M. Yajima, S. Masuzaki, N. Yoshida, M. Tokitani, T. Otsuka, Y. Oya, Y. Torikai, G. Motojima, Investigation on tritium retention and surface properties on the first wall in the large helical device, Nucl. Mater. Energy. 27 (2021) 100906, <https://doi.org/10.1016/j.nme.2021.100906>.
- [5] J. Roth, E. Tsitrone, T. Loarer, V. Philippss, S. Brezinsek, A. Loarte, G.F. Counsell, R. P. Doerner, K. Schmid, O.V. Ogorodnikova, R.A. Causey, Tritium inventory in ITER plasma-facing materials and tritium removal procedures, Plasma Phys. Control. Fusion. 50 (2008) 103001, <https://doi.org/10.1088/0741-3335/50/10/103001>.
- [6] A.P. Zakharov, A.E. Gorodetsky, V.K. Alimov, S.L. Kanashenko, A.V. Markin, Hydrogen retention in plasma-facing materials and its consequences on tokamak operation, J. Nucl. Mater. 241–243 (1997) 52–67, [https://doi.org/10.1016/S0022-3115\(97\)80030-X](https://doi.org/10.1016/S0022-3115(97)80030-X).
- [7] L. Cai, Z. Wang, C. Li, X. Huang, D. Zhao, H. Ding, Development of an in situ diagnostic system for mapping the deposition distribution on plasma facing components of the HL-2M tokamak, Rev. Sci. Instrum. 90 (2019), <https://doi.org/10.1063/1.5082630>.
- [8] W. Gonzalez, W. Biel, P. Mertens, M. Tokar, O. Marchuk, C. Linsmeier, Conceptual studies on spectroscopy and radiation diagnostic systems for plasma control on DEMO, Fusion Eng. Des. 146 (2019) 2297–2301, <https://doi.org/10.1016/j.fusengdes.2019.03.176>.
- [9] M. Rubel, P. Petersson, E. Alves, S. Brezinsek, J.P. Coad, K. Heinola, M. Mayer, A. Widdowson, The role and application of ion beam analysis for studies of plasma-facing components in controlled fusion devices, Nucl. Instruments Methods Phys.

- Res. Sect. B Beam Interact. with Mater. Atoms. 371 (2016) 4–11, <https://doi.org/10.1016/j.nimb.2015.09.077>.
- [10] M. Mayer, S. Möller, M. Rubel, A. Widdowson, S. Charisopoulos, T. Ahlgren, E. Alves, G. Apostolopoulos, N.P. Barradas, S. Donnelly, S. Fazinić, K. Heinola, O. Kakuee, H. Khodja, A. Kimura, A. Lagoyannis, M. Li, S. Markelj, M. Mudrinic, P. Petersson, I. Portnykh, D. Premetzhofer, P. Reichart, D. Ridikas, T. Silva, S. M. Gonzalez de Vicente, Y.Q. Wang, Ion beam analysis of fusion plasma-facing materials and components: facilities and research challenges, Nucl. Fusion 60 (2020) 025001, <https://doi.org/10.1088/1741-4326/ab5817>.
- [11] Y. Oya, H. Fujita, C. Hu, Y. Uemura, S. Sakurada, K. Yuyama, X. Li, Y. Hatano, N. Yoshida, H. Watanabe, Y. Nobuta, Y. Yamauchi, M. Tokitani, S. Masuzaki, T. Chikada, Effect of impurity deposition layer formation on D retention in LHD plasma exposed W, Nucl. Mater. Energy. 9 (2016) 84–88, <https://doi.org/10.1016/j.nme.2016.07.005>.
- [12] V.K. Alimov, M. Yajima, S. Masuzaki, M. Tokitani, Analysis of mixed-material layers deposited on the toroidal array probes during the FY 2012 LHD plasma campaign, Fusion Eng. Des. 147 (2019) 111228, <https://doi.org/10.1016/j.fusengdes.2019.06.001>.
- [13] Y. Oya, C. Hu, H. Fujita, K. Yuyama, S. Sakurada, Y. Uemura, S. Masuzaki, M. Tokitani, M. Yajima, Y. Hatano, T. Chikada, Development of H, D, T simultaneous TDS measurement system and H, D, T retention behavior for DT gas exposed tungsten installed in LHD plasma campaign, Fusion Sci. Technol. 71 (2017) 351–356, <https://doi.org/10.1080/15361055.2017.1291039>.
- [14] A.W. Miziolek, V. Palleschi, I. Schechter, eds. Laser-Induced Breakdown Spectroscopy (LIBS), Cambridge University Press, Cambridge, 2006, <https://doi.org/10.1017/CBO9780511541261>.
- [15] D.A. Cremers, L.J. Radziemski, Handbook of laser-induced breakdown spectroscopy, Wiley (2013), <https://doi.org/10.1002/9781118567371>.
- [16] P.J. Singh, S.N. Thakur (Eds.), Laser-Induced Breakdown Spectroscopy, Elsevier, 2020, <https://doi.org/10.1016/C2018-0-03938-9>.
- [17] R. Noll, Laser-Induced Breakdown Spectroscopy, Springer Berlin Heidelberg, Berlin, Heidelberg, 2012, <https://doi.org/10.1007/978-3-642-20668-9>.
- [18] S. Musazzi, U. Perini, eds. Laser-Induced Breakdown Spectroscopy, Springer, Berlin Heidelberg, Berlin, Heidelberg, 2014, <https://doi.org/10.1007/978-3-642-45085-3>.
- [19] D.W. Hahn, N. Omenetto, Laser-induced breakdown spectroscopy (LIBS), part I: review of basic diagnostics and plasma–particle interactions: still-challenging issues within the analytical plasma community, Appl. Spectrosc. 64 (2010) 335A–336A, <https://doi.org/10.1366/000370210793561691>.
- [20] D.W. Hahn, N. Omenetto, Laser-induced breakdown spectroscopy (LIBS), part II: review of instrumental and methodological approaches to material analysis and applications to different fields, Appl. Spectrosc. 66 (2012) 347–419, <https://doi.org/10.1366/11-06574>.
- [21] C. Li, C.-L. Feng, H.Y. Oderji, G.-N. Luo, H.-B. Ding, Review of LIBS application in nuclear fusion technology, Front. Phys. 11 (2016) 114214, <https://doi.org/10.1007/s11467-016-0606-1>.
- [22] G.S. Maurya, A. Marín-Roldán, P. Veis, A.K. Pathak, P. Sen, A review of the LIBS analysis for the plasma-facing components diagnostics, J. Nucl. Mater. 541 (2020) 152417, <https://doi.org/10.1016/j.jnucmat.2020.152417>.
- [23] H.J. van der Meiden, S. Almaviva, J. Butikova, V. Dwivedi, P. Gasior, W. Gromelski, A. Hakola, X. Jiang, I. Jögl, J. Karhunen, M. Kubkowska, M. Laan, G. Maddaluno, A. Marín-Roldán, P. Paris, K. Piip, M. Pisarcík, G. Sergienko, M. Veis, P. Veis, S. Brezinsek, T. EUROfusion WP PFC team, Monitoring of tritium and impurities in the first wall of fusion devices using a LIBS based diagnostic, Nucl. Fusion 61 (2021) 125001, <https://doi.org/10.1088/1741-4326/ac31d6>.
- [24] S. Almaviva, L. Caneve, F. Colao, R. Fantoni, G. Maddaluno, Remote-LIBS characterization of ITER-like plasma facing materials, J. Nucl. Mater. 421 (2012) 73–79, <https://doi.org/10.1016/J.JNUCMAT.2011.11.050>.
- [25] S. Almaviva, L. Caneve, F. Colao, V. Lazic, G. Maddaluno, P. Mosetti, A. Palucci, A. Reale, P. Gasior, W. Gromelski, M. Kubkowska, LIBS measurements inside the FTU vessel mock-up by using a robotic arm, Fusion Eng. Des. 157 (2020) 111685, <https://doi.org/10.1016/j.fusengdes.2020.111685>.
- [26] D. Zhao, C. Li, Z. Hu, C. Feng, Q. Xiao, R. Hai, P. Liu, L. Sun, D. Wu, C. Fu, J. Liu, N. Farid, F. Ding, G.-N. Luo, L. Wang, H. Ding, Remote in situ laser-induced breakdown spectroscopic approach for diagnosis of the plasma facing components on experimental advanced superconducting tokamak, Rev. Sci. Instrum. 89 (2018), <https://doi.org/10.1063/1.5024848>.
- [27] C. Li, X. Wu, C. Zhang, H. Ding, G. de Temmerman, H.J. van der Meiden, Study of deuterium retention on lithiated tungsten exposed to high-flux deuterium plasma using laser-induced breakdown spectroscopy, Fusion Eng. Des. 89 (2014) 949–954, <https://doi.org/10.1016/J.FUSENGDES.2014.04.071>.
- [28] P. Liu, D.Y. Zhao, L.Y. Sun, C.L. Fu, J.M. Liu, C. Li, R. Hai, C.F. Sang, Z.H. Hu, Z. Sun, J.S. Hu, L. Wang, J.L. Chen, Y.F. Liang, G.N. Luo, H. Ding, In situ diagnosis of Li-wall conditioning and H/D co-deposition on the first wall of EAST using laser-induced breakdown spectroscopy, Plasma Phys. Control. Fusion. 60 (2018) 085019, <https://doi.org/10.1088/1361-6587/ace83>.
- [29] G. Li, H. Hou, P. Ran, Y. Zhao, Z. Zhong, Calibration-free quantitative analysis of D/H isotopes with a fs-laser filament, J. Anal. At. Spectrom. 35 (2020) 1320–1329, <https://doi.org/10.1039/D0JA00062K>.
- [30] M. Burger, P.J. Skrodzki, L.A. Finney, J. Hermann, J. Nees, I. Jovanovic, Isotopic analysis of deuterated water via single- and double-pulse laser-induced breakdown spectroscopy, Phys. Plasmas 25 (2018), <https://doi.org/10.1063/1.5042665>.
- [31] R. Fantoni, S. Almaviva, L. Caneve, F. Colao, G. Maddaluno, P. Gasior, M. Kubkowska, Hydrogen isotope detection in metal matrix using double-pulse laser-induced breakdown-spectroscopy, Spectrochim. Acta B At. Spectrosc. 129 (2017) 8–13, <https://doi.org/10.1016/j.sab.2016.12.008>.
- [32] E.J. Kautz, E.C.E. Rönnebro, A. Devaraj, D.J. Senor, S.S. Harilal, Detection of hydrogen isotopes in zircaloy-4 via femtosecond LIBS, J. Anal. At. Spectrom. 36 (2021) 1217–1227, <https://doi.org/10.1039/D1JA00034A>.
- [33] E.J. Kautz, A. Devaraj, D.J. Senor, S.S. Harilal, Hydrogen isotopic analysis of nuclear reactor materials using ultrafast laser-induced breakdown spectroscopy, Opt. Express 29 (2021) 4936, <https://doi.org/10.1364/OE.412351>.
- [34] S.S. Harilal, A.K. Shaik, E.J. Kautz, A. Devaraj, A.M. Casella, D.J. Senor, Detection of tritium using ultrafast laser-induced breakdown spectroscopy, J. Anal. At. Spectrom. 39 (2024) 699–703, <https://doi.org/10.1039/D3JA00439B>.
- [35] S. Harilal, E.J. Kautz, Analysis of hydrogen and lithium isotopes using laser-induced breakdown spectroscopy, in: C.R. Phipps, V.E. Gruzdev (Eds.), High-Power Laser Ablation VIII, SPIE, 2024, p. 14, <https://doi.org/10.1117/12.3015929>.
- [36] K.H. Kurniawan, T.J. Lie, M.M. Suliyanti, R. Hedwig, M. Pardede, D.P. Kurniawan, Y. Kusumoto, K. Kagawa, Quantitative analysis of deuterium using laser-induced plasma at low pressure of helium, Anal. Chem. 78 (2006) 5768–5773, <https://doi.org/10.1021/ac060633h>.
- [37] C.W. Forsberg, S. Lam, D.M. Carpenter, D.G. Whyte, R. Scarlat, C. Contescu, L. Wei, J. Stempien, E. Blandford, Tritium control and capture in salt-cooled fission and fusion reactors: status, challenges, and path forward, Nucl. Technol. 197 (2017) 119–139, <https://doi.org/10.13182/NT16-101>.
- [38] A. Kramida, Y.Ralchenko, J. Reader, N.A. Team, NIST At. Spectra Database (2024), <https://doi.org/10.18434/T4W30F> (ver. 5.11).
- [39] M.A. Gigosos, M.Á. González, V. Cardeñoso, Computer simulated Balmer-alpha, -beta and -gamma stark line profiles for non-equilibrium plasmas diagnostics, Spectrochim. Acta B At. Spectrosc. 58 (2003) 1489–1504, [https://doi.org/10.1016/S0584-8547\(03\)00097-1](https://doi.org/10.1016/S0584-8547(03)00097-1).
- [40] A. Díaz-Soriano, J.M. Alcaraz-Pelegrina, A. Sarsa, M.S. Dimitrijević, C. Yubero, A simple and accurate analytical model of the stark profile and its application to plasma characterization, J. Quant. Spectrosc. Radiat. Transf. 207 (2018) 89–94, <https://doi.org/10.1016/j.jqsrt.2017.12.027>.
- [41] A. Díaz-Soriano, M.S. Dimitrijević, J.M. Alcaraz-Pelegrina, A. Sarsa, C. Yubero, Simple and analytical function for the stark profile of the H α line and its application to plasma characterization, J. Quant. Spectrosc. Radiat. Transf. 217 (2018) 111–115, <https://doi.org/10.1016/j.jqsrt.2018.05.031>.
- [42] A. Ortiz-Mora, A. Díaz-Soriano, A. Sarsa, M.S. Dimitrijević, C. Yubero, A practical method for plasma diagnosis with Balmer series hydrogen lines, Spectrochim. Acta Part B At. Spectrosc. 163 (2020) 105728, <https://doi.org/10.1016/j.sab.2019.105728>.
- [43] C.O. Laux, T.G. Spence, C.H. Kruger, R.N. Zare, Optical diagnostics of atmospheric pressure air plasmas, Plasma Sources Sci. Technol. 12 (2003) 125–138, <https://doi.org/10.1088/0963-0252/12/2/301>.
- [44] H. Ehrlich, Experimental study of Balmer- α stark broadening, Z. Für Naturforsch. A. 34 (1979) 188–191, <https://doi.org/10.1515/zna-1979-0210>.
- [45] N. Konjević, M. Ivković, N. Sakan, Hydrogen Balmer lines for low electron number density plasma diagnostics, Spectrochim. Acta B At. Spectrosc. 76 (2012) 16–26, <https://doi.org/10.1016/j.sab.2012.06.026>.
- [46] J.J. Olivero, R.L. Longbothum, Empirical fits to the voigt line width: a brief review, J. Quant. Spectrosc. Radiat. Transf. 17 (1977) 233–236, [https://doi.org/10.1016/0022-4073\(77\)90161-3](https://doi.org/10.1016/0022-4073(77)90161-3).
- [47] H.R. Griem, Principles of plasma spectroscopy, in: fast electr. Opt. Meas., Springer Netherlands, Dordrecht, 1986: pp. 885–910. doi:https://doi.org/10.1007/978-94-017-0445-8_34.
- [48] Z. Mijatović, S. Djurović, L. Gavanski, T. Gajo, A. Favre, V. Morel, A. Bultel, Plasma density determination by using hydrogen Balmer H α spectral line with improved accuracy, Spectrochim. Acta Part B At. Spectrosc. 166 (2020) 105821, <https://doi.org/10.1016/j.sab.2020.105821>.
- [49] S. Almaviva, L. Caneve, F. Colao, G. Maddaluno, R. Fantoni, Accessory laboratory measurements to support quantification of hydrogen isotopes by in-situ LIBS from a robotic arm inside a fusion vessel, Spectrochim. Acta Part B At. Spectrosc. 181 (2021) 106230, <https://doi.org/10.1016/j.sab.2021.106230>.
- [50] Y. Yu, J. Hu, Y. Zhao, X. Gao, J. Li, ICRF (ion cyclotron range of frequencies) discharge cleaning with toroidal and vertical fields on east, Plasma Phys. Control. Fusion. 53 (2011) 015013, <https://doi.org/10.1088/0741-3335/53/1/015013>.
- [51] S. Breznsek, C.P. Dhard, M. Jakubowski, Plasma-surface interaction in the stellarator W7-X: conclusions drawn from operation with graphite plasma-facing components, Nucl. Fusion. 62 (2022) 016006, <https://doi.org/10.1088/1741-4326/ac3508>.
- [52] M. Ivković, M.A. Gonzalez, S. Jovićević, M.A. Gigosos, N. Konjević, A simple line shape technique for electron number density diagnostics of helium and helium-seeded plasmas, Spectrochim. Acta B At. Spectrosc. 65 (2010) 234–240, <https://doi.org/10.1016/j.sab.2010.03.003>.
- [53] M. Ivković, M.A. Gonzalez, N. Lara, M.A. Gigosos, N. Konjević, Stark broadening of the He I 492.2 nm line with forbidden components in dense low-temperature plasma, J. Quant. Spectrosc. Radiat. Transf. 127 (2013) 82–89, <https://doi.org/10.1016/j.jqsrt.2013.04.030>.
- [54] A.J. Barnard, J. Cooper, E.W. Smith, Stark broadening tables for He I λ 4922 Å, J. Quant. Spectrosc. Radiat. Transf. 15 (1975) 429–437, [https://doi.org/10.1016/0022-4073\(75\)90062-X](https://doi.org/10.1016/0022-4073(75)90062-X).
- [55] A. de Giacomo, J. Hermann, Laser-induced plasma emission: from atomic to molecular spectra, J. Phys. D. Appl. Phys. 50 (2017) 183002, <https://doi.org/10.1088/1361-6463/aa6585>.
- [56] C.M. Western, PGOPHER: a program for simulating rotational, vibrational and electronic spectra, J. Quant. Spectrosc. Radiat. Transf. 186 (2017) 221–242, <https://doi.org/10.1016/j.jqsrt.2016.04.010>.

- [57] B. Stankov, M. Gavrilovic Bozovic, J. Savovic, M. Ivkovic, Spectroscopic characterization of laser-induced plasma on doped tungsten, in: Publ. Astron. Obs. Belgrade 102, 2022, pp. 239–242. ISBN:978-86-82296-02-7.
- [58] I. Jögi, J. Ristikok, J. Raud, J. Butikova, K. Mizohata, P. Paris, Laser induced breakdown spectroscopy for hydrogen detection in molybdenum at atmospheric pressure mixtures of argon and nitrogen, Fusion Eng. Des. 179 (2022) 113131, <https://doi.org/10.1016/j.fusengdes.2022.113131>.
- [59] N. Larbi-Terzi, S. Sahal-Bréchot, N. Ben Nessib, M.S. Dimitrijević, Stark-broadening calculations of singly ionized carbon spectral lines, Mon. Not. R. Astron. Soc. 423 (2012) 766–773, <https://doi.org/10.1111/j.1365-2966.2012.20968.x>.



Stark spectral line broadening modeling by machine learning algorithms

Irinel Tapalaga¹ · Ivan Traparić^{1,2} · Nora Trklja Boca¹ · Jagoš Purić¹ · Ivan P. Dojčinović¹

Received: 9 February 2021 / Accepted: 11 November 2021

© The Author(s), under exclusive licence to Springer-Verlag London Ltd., part of Springer Nature 2021

Abstract

Various types of electric fields contained in the laboratory and astrophysical plasma cause a Stark broadening of spectral lines in plasma. Therefore, a large number of spectroscopic diagnostics of laboratory and astrophysical plasma are based on experimental and theoretical studies of Stark broadening of spectral lines in plasma. The topic of the present investigation is the Stark broadening caused by free electrons in plasma and its dependence on certain atomic parameters using a new method based on the machine learning (ML) approach. Analysis of empirical data on atomic parameters was done by ML algorithms with more success than it was previously done by classical methods of data analysis. The correlation parameter obtained by artificial intelligence (AI) is slightly better than the one obtained by classical methods, but the scope of application is much wider. AI conclusions are applicable to any physical system while conclusions made by classical analysis are applicable only to a small portion of these systems. ML algorithms successfully identified quantum nature by analyzing atomic parameters. The biggest issue of classical analysis, which is infinite spectral line broadening for high ionization stages, was resolved by AI with a saturation tendency.

Keywords Machine learning · Stark broadening · Atomic data · Plasma physics

1 Introduction

One of the greatest challenges of the modern science is the processing of enormous amounts of data. Two primary goals in this field are how to learn from data and how to make data predictions [37]. Data science and machine learning (ML) have made tremendous progress in the last few decades. Statistical physics have a great contribution to the development and understanding methods in ML [6]. ML algorithms have become very important in the analysis of data in physics and related sciences. ML methods have been shown to be useful in different physical sciences: astrophysics, particle physics, chemical physics, condensed-matter physics, quantum physics. In astrophysics and particle physics experiments such as CMS and ATLAS

at the LHC in CERN, as well as projects such as the Sloan Digital Sky Survey (SDSS), gives enormous amount of data measuring the particle collisions and properties of a billion stars and galaxies [37]. Object classification in astrophysics is very important task [3, 27, 46] whose successful solution enables easier selection of objects according to certain criteria and their further study. Use of ML algorithms enables the solution of numerous problems in the processing of astronomical data and enables the consideration of dependences and correlations that have not been observed before [25, 26, 44, 45]. In one of the most significant modern experiment: observation of the gravitational waves arises from the merger of a binary black hole, ML algorithms are used to clear the noise in the signals of gravitational waves [1, 57]. Large development in the domain of data science, as well as the strengthening of connection to quantum physics, enabled the development of our knowledge of the matter. Namely, atomic physics is a base for the creation of new molecules and advanced materials, as well. The theoretical basis of atomic physics is quantum mechanics. Quantum mechanics has provided a base for successful research of molecular

✉ Nora Trklja Boca
nora@ff.bg.ac.rs

¹ Faculty of Physics, University of Belgrade, Studentski trg 12, Belgrade 11000, Serbia

² Institute of Physics, University of Belgrade, Pregrevica 118, Belgrade 11080, Serbia

physics and condensed matter physics, as well as nuclear physics and particle physics. Consequently, the development of ML algorithms recently has been used to address fundamental questions in the domain of quantum physics [4, 49]. One of the big problems in quantum physics is the inability to solve the Schrödinger equation for multiparticle systems, i.e., inability to obtain appropriate wave functions. In quantum chemistry and chemical physics, ML algorithms are used for analysis and prediction of physical and chemical properties, chemical structures, optimization of reaction parameters and process conditions (a type of reagents, catalysts, concentration, time, temperature), prediction of new reaction design, maximization of the production rate of chemical reactions [2, 9, 18, 29, 59, 60]. In condensed-matter physics and material science, ML has been used to improve the calculation of material properties, as well as a modeling of properties of new materials [10, 12, 19, 43, 58]. Learning techniques can be used for the research of advanced materials: materials for memory devices, solar cells, batteries, sensors, nanoparticle catalysts, supercapacitors, superhard material, etc.

From interconnections between quantum physics and ML, scientific community has huge expectation [4, 8, 23, 24, 32, 33, 35, 38, 49, 54]. There are many current questions about entanglement classification [23], quantum state tomography [54], solving the quantum many-body problem [8, 24]. There are many interesting active ML models with the aim of creation of new quantum experiments [32, 33, 38], as well as quantum machine models [17]. Also, ML can be used to discover physical concepts from new experimental data [28]. ML approaches have been applied to atomic physics. The neural networks can be used as a representation of quantum states [6]. There is a lack of atomic parameters for heavy elements and high ionized atoms. ML can be applied to the classification of heavy atoms energy levels according to their electronic configurations [7, 41]. Learning techniques have been applied for the investigation of atomic processes, like ionization and radiation [6]. Analysis of spectra from stars and quasars, as well as laser-produced and fusion plasma, can be done with the help of ML [40, 45]. The knowledge of atomic parameters is a base for atomic processes modeling. The aim of this research work is to use machine learning algorithms for modeling Stark spectral line broadening.

Stark broadening of spectral lines is a tool for spectroscopic diagnostics of laboratory plasma, as well as astrophysical and fusion plasma. In astrophysics, stark line widths are used for analysis of stellar spectra, investigation of chemical abundances of elements in different stellar objects, opacity calculations. Recently, it has been shown that Stark broadening has a big influence on the uncertainties in the calculation of the solar opacity [34]. Spectral

analysis has a very important role in the physics of fusion plasma, too. Part of the current research in this field is concentrated on the possibility of using various durable materials, (as Mo, Ti, Zr...) for tungsten alloying. During the operation of fusion machines, it is expected that a small amount of these materials would be found in the peripheral regions of confined plasma, because of the spattering process. Stark widths of these atoms and their ions are needed for a detailed spectral analysis and diagnostics.

Stark broadening of spectral lines of neutral atoms and ions is used in science for a number of problems in various physical conditions. Theoretical calculations of the Stark width values usually use one of the models given by Griem et al. [20]; Sahal-Bréchot et al. [47]; Griem [21]; Dimitrijević and Konjević [13]. Recent research indicates the importance and usefulness of searching for possible types of regularities in the framework of a Stark broadening investigation [16, 53, 56]. Still, existing tables with calculated and measured Stark widths have a big lack of data. There is a need for Stark widths data in the wide range of chemical elements, plasma temperature and electron densities. In this paper a correlation between Stark broadening and environment parameters, such as the ionization potential of the upper level of the corresponding transition, electron density and temperature, will be investigated using modern ML algorithms. If this method proves to be accurate enough, the process of calculating the value of stark widths will be significantly accelerated and facilitated.

2 Theoretical background of Stark line broadening

One of the primary deexcitation ways of excited atoms is photon emission. A cumulative signal obtained from a radiating medium (for example plasma) is a spectral line with a small frequency range. Each spectral line emitted by atoms in plasma has a finite frequency range represented as line width. Generally, there are four types of spectral line broadening in plasma. One is a natural line broadening, related with the uncertainty in the energy of the states involved in the transition profile, with line width negligible compared to the other broadening mechanisms. The second is instrumental line broadening which includes the influence of spectral device on a line profile. Doppler broadening is caused by a distribution of velocities of atoms or molecules and depends on plasma temperature. The pressure broadening, which generally depends on pressure (i.e., density of active species) and temperature, results from the interactions of the emitters with neighboring neutral particles (resonant and Van der Waals broadening) and ionized particles (Stark broadening). Natural and instrumental broadening are always present. The existence of other types

of spectral line broadening depends on the plasma conditions. Stark broadening is caused by the free charges which surround the emitters in plasma and produce the local electric field which affects the emission process, giving rise to shifts of the emission wavelengths or changes in the phase of the radiation. This is observed as a phenomenon of broadening and shift of the spectral lines [22]. This effect is determined by the intensity of the local electric field and it depends on the density of charged particles in the plasma (electrons and ions). The influence of free electrons on the line broadening in plasma is much more pronounced than the influence of ions. The topic of the present investigation is the Stark broadening caused by free electrons in plasma using new method based on ML approach.

The general formula for Stark width calculation in the impact approximation, which is appropriate to use in the overwhelming number of cases, is [22]:

$$\omega = N_e \left\langle v \cdot \left(\sigma_{if} + \sum_{i'} \sigma_{ii'} + \sum_{f'} \sigma_{ff'} \right) \right\rangle_{av} \quad (1)$$

The line has a Lorentzian profile whose width is ω , expressed in angular frequencies unit [rad/s]. N_e and v are electron density and velocity, respectively. The average is being over the velocity distribution of perturbing electrons. The cross sections $\sigma_{ii'}$ ($\sigma_{ff'}$) are for inelastic scattering on the initial (final) state of the line,

while σ_{if} is an effective elastic cross section to be calculated essentially from the difference of elastic scattering amplitudes f_i and f_f .

The formula proposed by Griem [22] is very complicated, it cannot be resolved exactly, so it is useful to use different approaches in the calculation. The regularity approach which correlates Stark width of spectral line, ω , expressed in [rad/s], electron density N_e , electron temperature T_e and positive value of electron binding energy on the upper level of the transition, expressed in [eV], is given by Purić and Šćepanović [42] (Eq. 2):

$$\omega = Z_e^k \cdot a \cdot N_e \cdot f(T_e) \cdot \chi^{-b} \quad (2)$$

where $Z_e = 1, 2, 3\dots$ for neutrals, singly charged ions, ... respectively and it represents the rest core charge of the ionized emitter and a , b and k are coefficients independent of electron concentration and ionization potential for a particular transition and the rest core charge of the emitter. In Eq. 2, stark width is expressed in radian per second and this is the only suitable unit to analyze the regularity of Stark broadening. If regularity analysis use wavelengths (λ) and line widths ($\Delta\lambda$) expressed in meters, Eq. 2 should be written as follows:

$$\Delta\lambda = \frac{Z_e^k \cdot a \cdot N_e \cdot f(T_e) \cdot \chi^{-b} \cdot \lambda^2}{2 \cdot \pi \cdot c} \quad (3)$$

In Eq. 3, every transition have its own wavelength, while the other parameters remain unchanged, so regularity can't be seen.

Atoms and ions with the same number of electrons form an isoelectronic sequence. It is expected that spectral series within an isoelectronic sequence show regularity behavior because a wide range of atomic/ionic parameters depend on the electron number. The results obtained by regularity studies have proven to be very precise and this approach has been used in previous papers of our group. In the last decade we have investigated Stark broadening regularities using Eq. 2 within spectral series of individual elements [14, 15, 30, 51, 52], within spectral series of individual isoelectronic sequences [53, 55, 56] and we published one paper with analysis of Stark line broadening regularities within two spectral series of isoelectronic sequences simultaneously: potassium and copper [16]. The present investigation goes one step further and analyses all elements for which there are available data needed for Stark broadening investigation, simultaneously, using machine learning approach. The aim is to find the best possible model which correlates Stark width of spectral line with all available parameters for transition of interest (atomic parameters and environmental parameters).

3 Dataset creation and data cleaning

In order to create our dataset we used two public repositories connected with atomic spectroscopy. First one is Stark B database [48], where the parameters of Stark broadening for different emitters are given. The features taken from this database are: chemical element, ionization stage, upper and lower level of spectral transitions, Stark broadening, the environment temperature and electron density in environment. In the available database, stark widths are expressed in angstroms ($1 \text{ angstrom} = 10^{-10} \text{ m}$). For analysis purpose, angstroms are converted in radian per second [53] (Eq. 4). In the physical sense, radian per second is unit related with energy.

$$\omega = \frac{2\pi \cdot c \cdot \Delta\lambda}{\lambda^2} \quad (4)$$

We also performed data analysis with Stark widths expressed in meters, using machine learning and results have not shown any meaningful trends. This is confirmation that radians per second are suitable unit for machine learning approach, too. When the difference between energy levels of the same multiplet is small compared to the distance to the next level linked by an allowed

transition, all the fine structure lines of the same multiplet have the same width and shift in Stark B database . In that case, the data are given of the multiplet only (w_{mult}) and for an average wavelength of the whole multiplet (λ_{mult}). The width value for a particular line (w_{line}) within a multiplet is obtained from:

$$w_{\text{line}} = \frac{w_{\text{mult}} \cdot \lambda_{\text{line}}^2}{\lambda_{\text{mult}}^2} \quad (5)$$

To ensure better results, we enriched features taken from Stark B database with ones taken from NIST Atomic Spectra database [31]: binding energy of both upper and lower transition levels, ground level energy, total angular momentum quantum number J of both upper and lower transition level, as well as principal n and orbital ℓ quantum numbers and total angular momentum J quantum numbers of upper and lower transition levels.

The algorithm of connecting those two databases to form our own works as described below. For every transition connected with certain chemical element, we take the electronic configuration of both upper and lower levels from Stark B database. Then, we look for that particular element in NIST database and compare the electronic configurations. If they match, then we take the binding energy of those levels,

their principal quantum number n , orbital quantum number ℓ and total angular momentum quantum number J and finally the ionization energy of that atom. The ionization energy is needed for calculation of the so-called upper level ionization potential χ . For practical purposes, we replaced the chemical element name with its atomic number Z and its charge, obtained from periodic system of elements (i.e., instead of Ar+2, we used $Z = 10$ and charge = + 2). For better understanding of the algorithm mentioned above, pseudo code is given in table Algorithm 1 while the complete code can be found at <https://github.com/ivantraparic/StarkBroadeningMLApproach>. After we completed the creation of database, it consisted of 54,236 successfully matched transitions for 53 different emitters.

Then we proceeded with data cleaning. Outliers were detected as those transitions where the energy of upper level is smaller than the energy of lower level, which is physically impossible, thus those lines were removed from the database. Next, we excluded transitions given for temperatures above 150,000 K and electron densities above 10^{18} cm^{-3} , because we are currently not interested in making predictions for those plasma conditions. As a result, this dataset contains 53 emitters and 34,973 spectral lines and follows a normal distribution.

Algorithm 1 Creation of database used in this paper

```

1: for element in elements do
2:   charge, Z  $\leftarrow$  DetermineZAndCharge(element)
3:   elementNIST  $\leftarrow$  FindElementInNIST(element)
4:   ElectronTemperature  $\leftarrow$  electronic temperature from Stark B database
5:   ElectronDensity  $\leftarrow$  electron density from Stark B database
6:   StarkWidth  $\leftarrow$  stark broadening from Stark B database
7:   UpperLevels  $\leftarrow$  upper transition levels from Stark B for element
8:   LowerLevels  $\leftarrow$  lower transition levels from Stark B for element
9:   Levels  $\leftarrow$  levels configuration in NIST database for elementNIST
10:  Upperbindingenergy, Lowerbindingenergy, jupper, jlower, ni, li, nf, lf, chi  $\leftarrow$  Arrays
    for saving found quantities from NIST database
11:  GroundLevel  $\leftarrow$  FindGroundLevel(elementNIST)
12:  for lowerlevel in LowerLevels do
13:    for level in Levels do
14:      if lowerlevel == level then
15:        Lowerbindingenergy, nf, lf, jlower  $\leftarrow$  binding energy
        and associated quantum numbers for that lower level taken from NIST
        upper level ionization potential chi  $\leftarrow$  GroundLevel - Lowerbindingenergy
        break
16:    for upperlevel in UpperLevels do
17:      for level in Levels do
18:        if upperlevel == level then
19:          Upperbindingenergy, ni, li, jupper  $\leftarrow$  binding energy
          and associated quantum numbers for that upper level taken from NIST
          break
20:        if length(Lowerbindingenergy) != length(Upperbindingenergy) then
21:          Error
22:        return
23:      else
24:        for i != length(Lowerbindingenergy) do
25:          Z, ElectronTemperature, ElectronDensity, charge, chi, GroundLevel,
          Upperbindingenergy, jupper, Lowerbindingenergy, jlower, ni, li, nf, lf, StarkWidth
           $\leftarrow$  Insert line i in database

```

Table 1 List of ML algorithms and parameters

Model	Parameters
Linear regression	Normalize: [True, False]
Decision tree regressor	max_depth [3, 5, 10]
Random forest regressor	n_estimators [5, 10, 15, 100]
Gradient boosting regressor	max_depth [3, 5, 10], n_estimators [100, 150, 200]

Table 2 List of ML algorithms and their final score

Model	Best R^2	Parameters
Linear regression	0.38	Normalize: False
Decision tree regressor	0.92	max_depth = 10
Gradient boosting regressor	0.94	max_depth = 10, n_estimators = 150

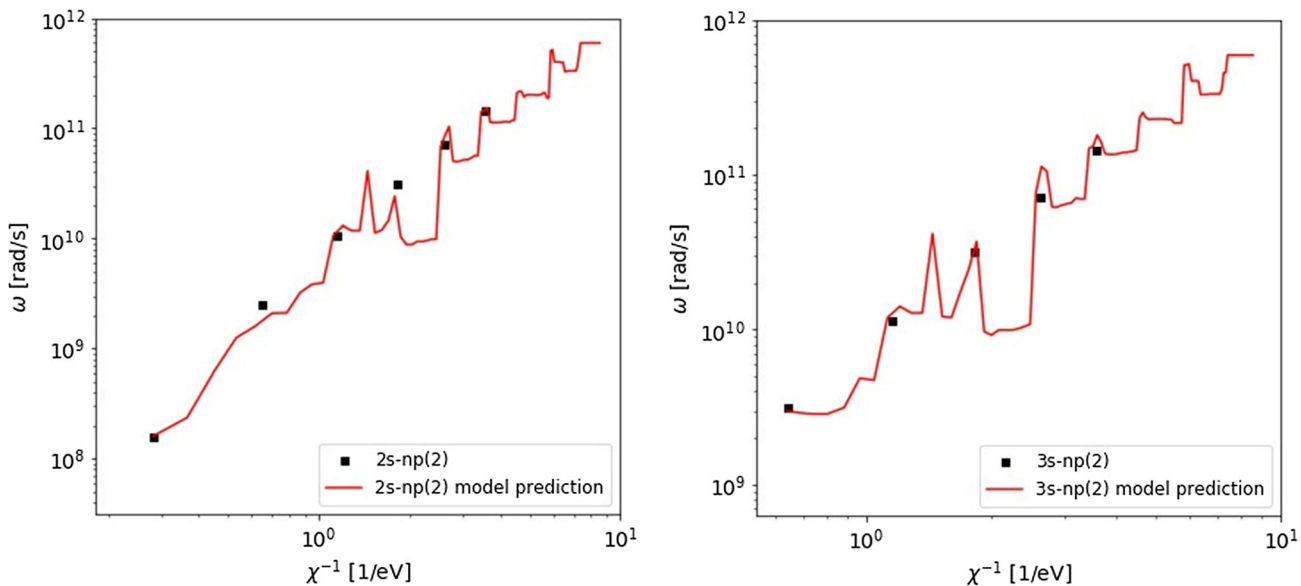
It consisted of 15 columns, 14 of those were our features (atomic number Z , electron temperature, electron density, charge, lower level ionization potential χ , ground level energy, lower level energy, lower level J , upper level energy, upper level J , principal quantum number of lower level n_f , orbital quantum number of lower level ℓ_f , principal quantum number of upper level n_i , orbital quantum number of upper level ℓ_i), and 15th column was our target value ω .

4 Model creation and training

For model creation and training, we used public Python package Sci-kit learn. We created four models, every being Pipeline with two steps. In each object of Pipeline class, the

first step was data scaling using StandardScaler, and in second step we made our predictions with defined model. Considered models were: Linear Regression, Decision Tree Regressor, Random Forest Regressor and Gradient Boosting Regressor. We split the dataset into training and test dataset using train_test_split method, leaving 25% of the data for testing. To find the best model out of four considered, and best parameters for that model, we used ShuffleSplit combined with GridSearchCV. In ShuffleSplit object we set number of splits to 5, and we left 30% of data for testing. In GridSearchCV object we set cross validation to ShuffleSplit object. The values for parameters of models used in GridSearchCV are presented in table 1. Other parameters of the model remained at their default values.

To rank the performance of models, we used best Coefficient of Determination, R^2 , value obtained after

**Fig. 1** Stark widths regularities within 2s-np i 3s-np spectral series of Li 1 ($T = 30,000$ K, $N_e = 10^{20}$ m⁻³)

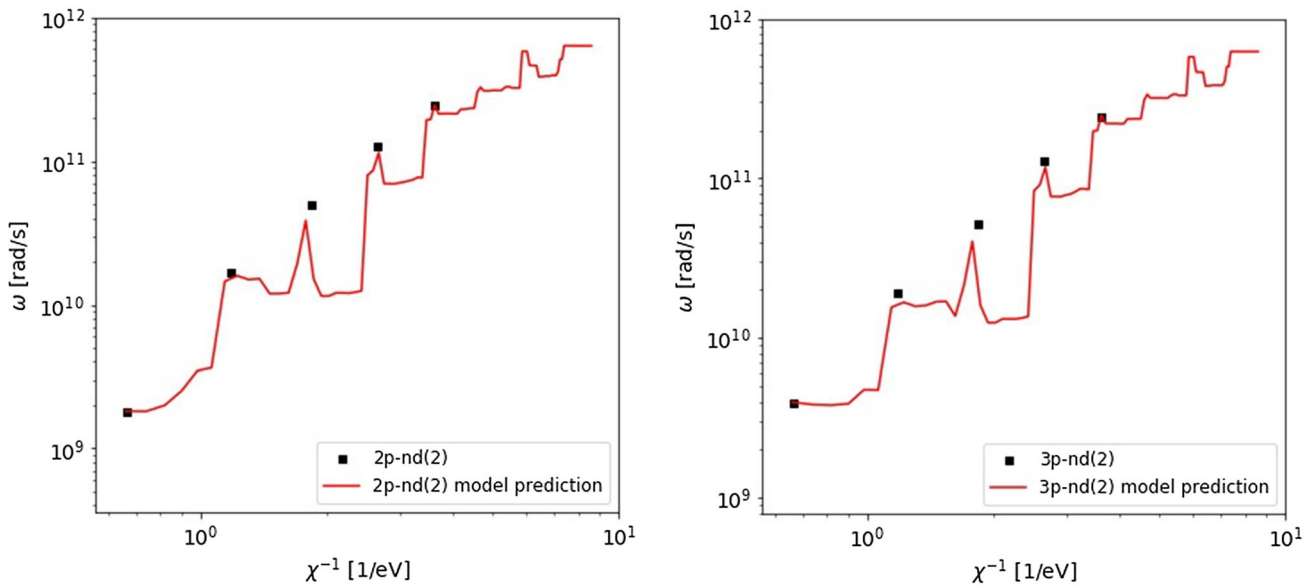


Fig. 2 Stark widths regularities within 2p-nd and 3p-nd spectral series of Li I ($T = 30,000 \text{ K}$, $N_e = 10^{20} \text{ m}^{-3}$)

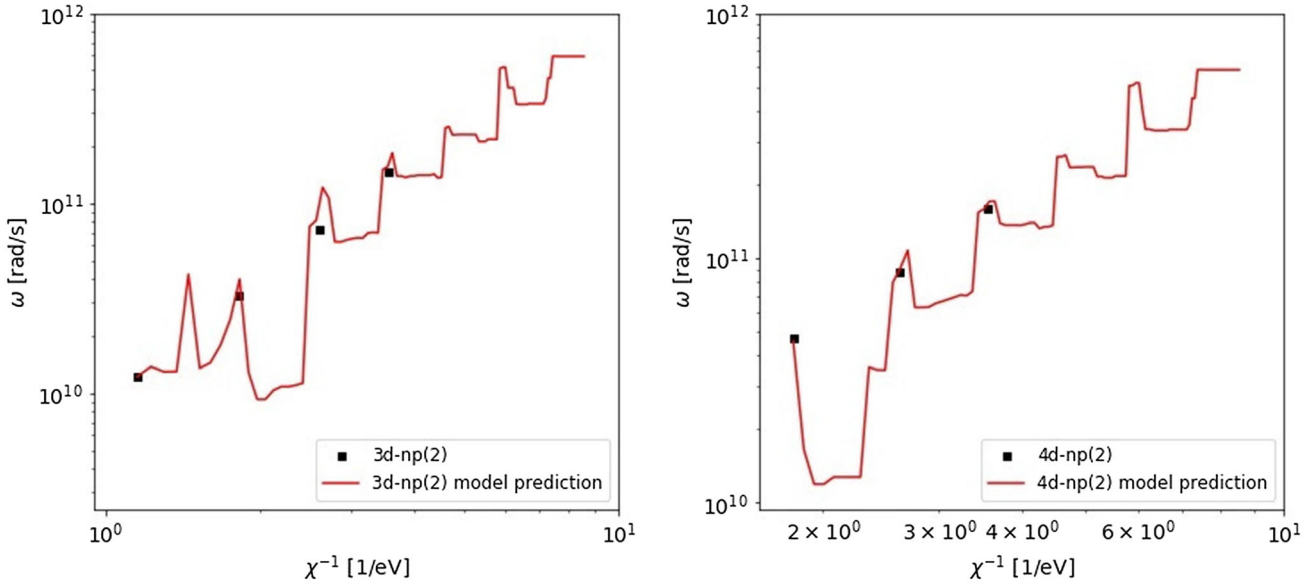


Fig. 3 Stark widths regularities within 3d-np and 4d-np spectral series of Li I ($T = 30,000 \text{ K}$, $N_e = 10^{20} \text{ m}^{-3}$)

GridSearchCV algorithm finished. We have taken the parameters that the algorithm used to score that particular R^2 . As a result, we got that the best R^2 value was for Random Forest Regressor having $R^2 = 0.95$ for n_estimators = 100. The results of other model is given in table 2.

So, our winning model after performing hyper parameter tuning using GridSearchCV was Random Forest Regressor with number of estimators set to 100. Random Forest is a learning method that operates by constructing a large number of decision trees during the training process [5]. It is simple to use and shows high performance for a wide variety of tasks, making it one of the most popular ML

algorithms in different sciences. Random forests are an effective tool in predicting new data, in our case new atomic parameters. It should be emphasized that Breimans paper [5] is cited more about 30,000 times (Web of Science: 36,234, CrossRef: 27,683). In order to check overfitting of the winning model, we did R^2 score check of the model on both training and test datasets. Training R^2 score was 0.98, and test score was $R^2 = 0.95$, so we were sure our model is not overfitting the data.

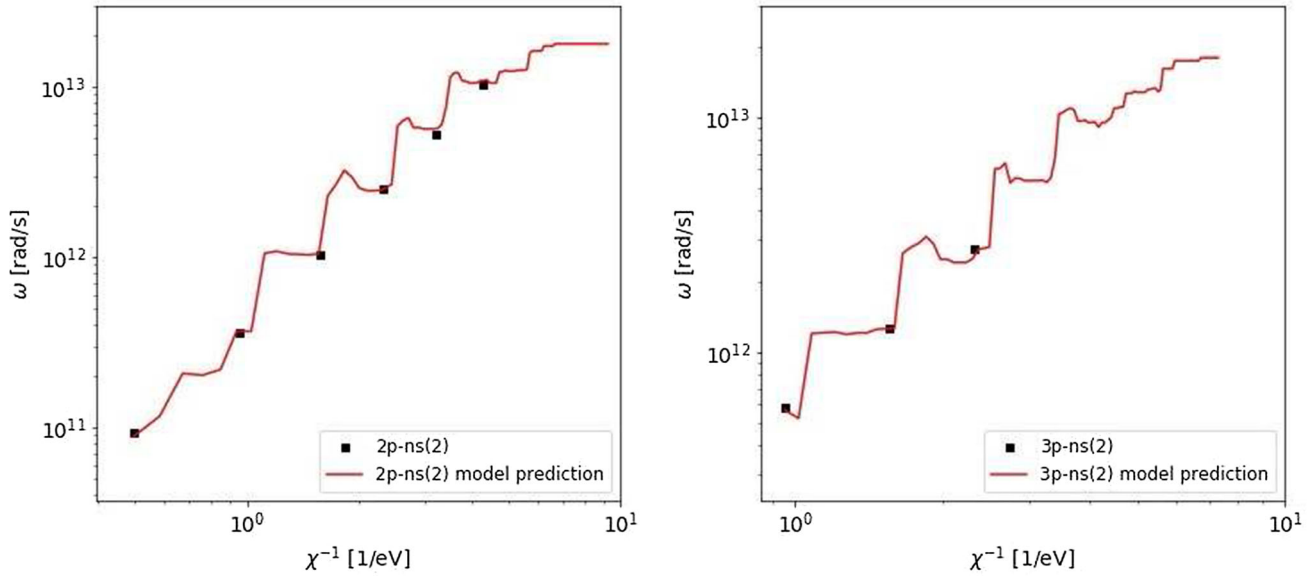


Fig. 4 Stark widths regularities within 2p-ns and 3p-ns spectral series of Li I ($T = 30,000$ K, $N_e = 10^{22} \text{ m}^{-3}$)

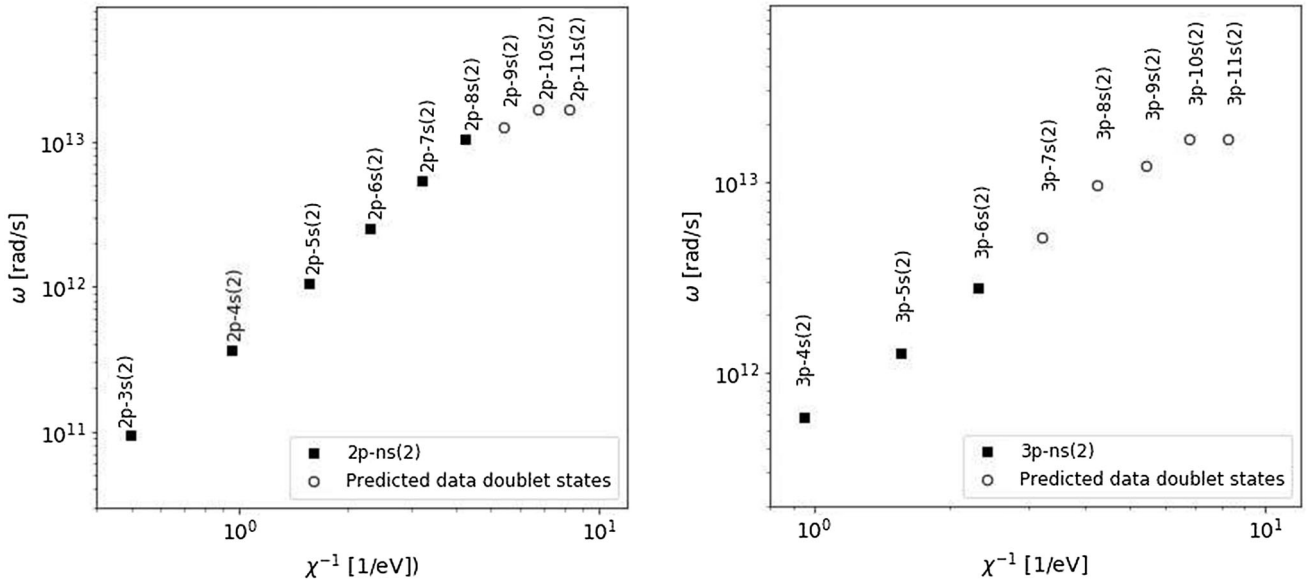


Fig. 5 Stark widths predictions for 2p-ns and 3p-ns spectral series of Li I ($T = 30,000$ K, $N_e = 10^{22} \text{ m}^{-3}$)

5 Results

The Random Forest model is used to calculate Stark broadening data for spectral series within neutral lithium Li I. Calculated stark widths (red lines) for transitions within analyzed series are represented with existing known values of Stark widths data at the same graphs.

Figure 1 shows the dependence of the Stark width (ω) on the reciprocal value of the electron binding energy at the upper level of the transition (χ^{-1}) for 2s-*np* and 3s-*np* transitions within lithium atom at a temperature of $T = 30,000$ K and electron concentration $N_e = 10^{20} \text{ m}^{-3}$.

Figures 2 and 3 show the change in Stark width under the same conditions (temperature $T = 30,000$ K and electron concentration $N_e = 10^{20} \text{ m}^{-3}$), but for 2p-nd and 3p-nd transitions, as well as 3d-*np* and 4d-*np*. A very good description of the atomic structure of lithium, i.e., the values of atomic parameters, can be observed. Interestingly, points 2s-2p and 2p-3d were omitted in our previous analysis [15], while the ML algorithm includes them in the overall analysis and gives excellent agreement with the Stark width value.

Of special importance is the possibility of obtaining the value of stark widths at higher energy levels, for which

these data are not quantitatively calculated. Figure 4 shows the change of Stark widths for the 2p-ns and 3p-ns transitions at a temperature of $T = 30,000$ K and electronic concentration $N_e = 10^{22} \text{ m}^{-3}$. In Fig. 5, the conditions are the same, but the initial values of the Stark width and the values obtained by the ML algorithm are given for higher energy levels of lithium atom. A slight saturation of the values of Stark parameters at higher energy levels can be observed.

The functional dependence obtained using the ML algorithm describes the quantum structure of the energy levels of lithium atoms. From the model lines (red lines), it can be concluded that the model successfully (within the error) indicates the quantum nature of atomic transitions and that other results do not make physical sense, but only jumps.

6 Conclusion

Analysis of spectral data on Stark broadening for 53 different emitters and 34973 lines by ML algorithms was done with more success than it was previously done by classical methods of data analysis. Random forest has scored an average of $R^2 = 0.95$ which makes it an excellent choice for Stark broadening calculations. The correlation parameter obtained by AI is slightly better than the one obtained by classical methods of Stark broadening analysis, but the scope of application is much wider. AI conclusions are applicable to any physical system while conclusions made by classical analysis are applicable only to a small portion of these systems, mostly to ions with low ionization stage. This improves the quality of predictions and enhance a broader usability of results. In fact, these results can be used for any transition and any environment without any restrictions. ML algorithms successfully identified quantum nature by analyzing Stark broadening parameters which can not be done with similar analyses that used classical methods and obtained linear correlation. The biggest issue of the classical analysis is infinite spectral line broadening for high ionization stages and it was successfully resolved by AI with a saturation tendency.

The process of calculating the values of Stark widths, which is used in science for a number of problems in various physical conditions in spectroscopic diagnostics of laboratory plasma, as well as astrophysical and fusion plasma, is significantly accelerated and facilitated with new method based on ML and proposed in the present paper. Using our new proposed model, Stark databases can be significantly improved. For example, Stark broadening calculations can be made for some spectral transitions within W, Ti, Mo and Zr atoms, which are common in

nuclear fusion diagnostics and of interest for spectral analysis in fusion physics [39], as titanium, molybdenum and zirconium are used as alloying materials for tungsten [11, 50]. Lines of Ti are used for astrophysics diagnostics, too [36]. Despite their significance, there is a very big lack of Stark data for these atoms and their ions. There is a lot of missing energy data for higher energy levels for W, Ti, Mo and Zr atoms and their ions. For example, there is no precise value of energy for 6p level for Ti II, so there is no calculated Stark data for transition for which this level is the closest perturbing level. Although very rich in data, NIST database does not have energy values data for all possible excited states of atoms. With standard known methods for Stark width calculation, it is not possible to calculate Stark widths for levels for which energy values of the closest perturbing levels are missing, but ML algorithms enable calculation in these situations, too. In next step, ML predictions and analytic calculations will be compared and ML technique will be used for atomic parameters analyses. Special attention will be paid to spectral lines that are important for fusion and astrophysical research.

Funding The Funding was provided by Ministarstvo Prosvete, Nauke i Tehnološkog Razvoja. This work is financially supported by the Ministry of Education, Science and Technological Development of the Republic of Serbia.

Declarations

Conflict of interest The authors declare that they have no conflict of interest.

References

- Abbott BP, Abbott R, Abbott TD, Abernathy MR, Acernese F, Ackley K, Adams C et al (2016) Observation of gravitational waves from a binary black hole merger. *Phys Rev Lett* 116:061102
- Balabin RM, Lomakina EI (2009) Neural network approach to quantum-chemistry data: accurate prediction of density functional theory energies. *J Chem Phys* 131:074104
- Ball NM, Brunner RJ (2010) Data mining and machine learning in astronomy. *Int J Mod Phys* 19(7):1049–1106
- Bharti K, Haug T, Vedral V, Kwek LC (2020) Machine learning meets quantum foundations: a brief survey. *AVS Quantum Sci* 2:034101
- Breiman L (2001) Random Forests. *Mach Learn* 45:5–32
- Carleo G, Cirac I, Cranmer K, Daudet L, Schuld M, Tishby N, Vogt-Maranto L, Zdeborova L (2019) Machine learning and the physical sciences. *Rev Mod Phys* 91:045002
- Cao X, Liu H, Chen N (1997) Classification of Cm I energy levels using PCA-BPN and PCA-NLM. *Chem Phys* 220:289–297
- Carleo G, Troyer M (2017) Solving the quantum many-body problem with artificial neural networks. *Science* 355:602–606

9. Cova TFGG, Pais AAC (2019) Deep learning for deep chemistry: optimizing the prediction of chemical patterns. *Front Chem* 7:809
10. Carrasquilla J, Melko RG (2017) Machine learning phases of matter. *Nat Phys* 13:431–434
11. Cui Z, Zhang X, Liu Q, Li H, Liu Y, Liu H, Wang X, Huang J, Liu H, Cheng J, Li M (2020) A first-principles study of the mechanical and thermodynamic properties of WTi, WV, W2Zr, WVTi, WVZr alloys. *Fusion Eng Design* 152:111451
12. Deringer VL, Caro MA, Csanyi G (2019) Machine learning interatomic potentials as emerging tools for materials science. *Adv Mater* 1902765:1–16
13. Dimitrijević MS, Konjević N (1980) Stark widths of doubly- and triply-ionized atom lines. *JQSRT* 24:451
14. Dojčinović IP, Tapalaga I, Purić J (2012) Stark parameter regularities of neutral helium lines within different spectral series. *Mon Not R Astron Soc* 419(1):904–912
15. Dojčinović IP, Tapalaga I, Purić J (2013) Stark-width regularities of neutral lithium lines within different spectral series. *Mon Not R Astron Soc* 429(3):2400–2406
16. Dojčinović IP, Trkla N, Tapalaga I, Purić J (2019) Investigation of Stark line broadening within spectral series of potassium and copper isoelectronic sequences. *Mon Not R Astron Soc* 489(3):2997–3002
17. Dunjko V, Wittek P (2020) A non-review of quantum machine learning: trends and explorations. *Quantum Views* 4:32
18. Gastegger M, Behler J, Marquetand P (2017) Machine learning molecular dynamics for the simulation of infrared spectra. *Chem Sci* 8:6924–6935
19. Gavezzotti A (2012) Computational studies of crystal structure and bonding. *Top Curr Chem* 315:1–32
20. Griem HR, Baranger M, Kolb AC, Oertel G (1962) Stark Broadening of Neutral Helium Lines in a Plasma. *Phys Rev* 125:177
21. Griem HR (1968) Semiempirical Formulas for the Electron-Impact Widths and Shifts of Isolated Ion Lines in Plasmas. *Phys Rev* 165:258
22. Griem HR (1974) Spectral line broadening by plasmas. Academic Press, New York
23. Harney C, Pirandola S, Ferraro A, Paternostro M (2020) Entanglement classification via neural network quantum states. *New J Phys* 22:045001
24. Hartmann MJ, Carleo G (2019) Neural-network approach to dissipative quantum many-body dynamics. *Phys Rev Lett* 122:250502
25. Hezaveh YD, Levasseur LP, Marshall PJ (2017) Fast automated analysis of strong gravitational lenses with convolutional neural networks. *Nature* 548:555–557
26. Huerta EA, Allen G, Andreoni I, Antelis JM, Bachelet E, Berrian GB, Bianco FB et al (2019) Enabling real-time multi-messenger astrophysics discoveries with deep learning. *Nat Rev Phys* 1:600–608
27. Ishida EEO, Beck R, González-Gaitán S, de Souza RS, Krone-Martins A, Barrett JW, Kennamer N et al (2019) Optimizing spectroscopic follow-up strategies for supernova photometric classification with active learning. *Mon Not R Astron Soc* 483:2–18
28. Iten R, Metger T, Wilming H, del Rio L, Renner R (2020) Discovering physical concepts with neural networks. *Phys Rev Lett* 124:010508
29. Janet JP, Chan L, Kulik HJ (2015) Accelerating Chemical discovery with machine learning: simulated evolution of spin crossover complexes with an artificial neural network. *J Phys Chem Lett* 9:1064–1071
30. Jevtić D, Dojčinović IP, Tapalaga I, Purić J (2012) Stark width regularities of neutral potassium lines within different spectral series. *Bull Astr Soc India* 40:151–160
31. Kramida A,Ralchenko Y, Reader J, NIST ASD Team (2019) NIST Atomic Spectra Database (version 5.7.1), [Online]. Available: <https://physics.nist.gov/asd> [Tue Mar 24 (2020) National Institute of Standards and Technology. Gaithersburg, MD
32. Krenn M, Gu X, Zeilinger A (2017) Quantum experiments and graphs: Multiparty states as coherent superpositions of perfect matchings. *Phys Rev Lett* 119:240403
33. Krenn M, Malik M, Fickler R, Lapkiewicz R, Zeilinger A (2016) Automated search for new quantum experiments. *Phys Rev Lett* 116:090405
34. Krief M, Feigel A, Gazit D (2016) Line broadening and the solar opacity problem. *Astrophys J* 824(2):98
35. Luchnikov IA, Vintskevich SV, Grigoriev DA, Filippov SN (2020) Machine learning non-Markovian quantum dynamics. *Phys Rev Lett* 124:140502
36. Manrique J, Aguilera JA, Aragon C (2016) Experimental Stark widths and shifts of Ti II spectral lines. *Mon Not R Astron Soc* 462(2):1501–1507
37. Mehta P, Bukov M, Wanga CH, Day AGR, Richardson C, Fisher CK, Schwab DJ, colleagues, (2019) A high-bias, low-variance introduction to Machine Learning for physicists. *Phys Rep* 810:1–124
38. Melnikov AA, Nautrup HP, Krenn M, Dunjko V, Tiersch M, Zeilinger A, Briegel HJ (2018) Active learning machine learns to create new quantum experiments. *Proc Natl Acad Sci USA* 115(6):1221–1226
39. Miškovićova J, Anguš M, van der Meiden H, Veis P (2020) Selection of molybdenum lines by quantitative analysis of molybdenum-zirconium-titanium alloy by CF-LIBS for future fusion applications. *Fusion Eng Des* 153:111488
40. Osterheld AL, Morgan WL, Larsen JT, Young BKF, Goldstein WH (1994) Analysis of spectra from laser produced plasmas using a neural network. *Phys Rev Lett* 73(11):1505–1508
41. Peterson KL (1991) Classification of Cm II and Pu I energy levels using counterpropagation neural networks. *Phys Rev A* 44:126–138
42. Purić J, Šćepanović M (1999) General regularities of stark parameters for ion lines. *Astroph J* 521:490
43. Purja Pun GP, Batra R, Ramprasad R, Mishin Y (2019) Physically informed artificial neural networks for atomistic modeling of materials. *Nat Commun* 10:2339
44. Reis I, Baron D, Shahaf S (2019) Probabilistic random forest: a machine learning algorithm for noisy data sets. *Astronom J* 157(16):1–12
45. Reis I, Poznanski D, Baron D, Zasowski G, Shahaf S (2018) Detecting outliers and learning complex structures with large spectroscopic surveys - a case study with APOGEE stars. *Mon Not R Astron Soc* 476:2117–2136
46. Rohde DJ, Drinkwater MJ, Gallagher MR, Downs T, Doyle MT (2005) Applying machine learning to catalogue matching in astrophysics. *Mon Not R Astron Soc* 360:69–75
47. Sahal-Bréchet S (1969) Impact theory of the broadening and shift of spectral lines due to electrons and ions in a plasma. *Astron Astrophys* 1:91
48. Sahal-Bréchet S, Dimitrijević MS, Moreau N (2020) STARK-B database, [online]. Available: <http://stark-b.obspm.fr> [February 20, 2020]. Observatory of Paris, LERMA and Astronomical Observatory of Belgrade
49. Sarma SD, Deng DL, Duan LM (2019) Machine learning meets quantum physics. *Phys Today* 72(3):48–54
50. Snead LL, Hoelzer DT, Rieth M, Nemith AA (2019) Refractory Alloys: Vanadium, Niobium, Molybdenum, Tungsten. *Struct*

- Alloys for Nucl En App 585–640, Chapter 13. <https://www.sciencedirect.com/science/article/pii/B9780123970466000137>
51. Tapalaga I, Dojčinović IP, Purić J (2011) Stark width regularities within magnesium spectral series. *Mon Not R Astron Soc* 415:503
 52. Tapalaga I, Dojčinović IP, Milosavljević MK, Purić J (2012) Stark Width Regularities within Neutral Calcium Spectral Series. *PASA* 29:20
 53. Tapalaga I, Trkla N, Dojčinović IP, Purić J (2018) Stark width regularities within spectral series of the lithium isoelectronic sequence. *Mon Not R Astron Soc* 474:5479
 54. Torlai G, Mazzola G, Carrasquilla J, Troyer M, Melko R, Carleo G (2018) Neural-network quantum state tomography. *Nat Phys* 14:447
 55. Trkla N, Tapalaga I, Dojčinović IP, Purić J (2018) Stark widths regularities within spectral series of sodium isoelectronic sequence. *New Astr* 59:54
 56. Trkla N, Tapalaga I, Dojčinović IP, Purić J (2019) Stark Widths Regularities Within: ns-np, np-ns, np-nd, nd-np and nd-nf Spectral Series of Potassium Isoelectronic Sequence. *Atoms* 7(4):99
 57. Wei W, Huerta EA (2020) Gravitational wave denoising of binary black hole mergers with deep learning. *Phys Lett B* 800:135081
 58. Westerhout T, Astrakhantsev N, Tikhonov KS, Katsnelson MI, Bagrov AA (2020) Generalization properties of neural network approximations to frustrated magnet ground states. *Nat Commun* 11:1593
 59. Wu J, Shen L, Yang W (2017) Internal force corrections with machine learning for quantum mechanics/molecular mechanics simulations. *J Chem Phys* 147:161732
 60. Zhang P, Shen L, Yang W (2019) Solvation free energy calculations with quantum mechanics / molecular mechanics and machine learning models. *Phys Chem B* 123(4):901–908

Publisher's Note Springer Nature remains neutral with regard to jurisdictional claims in published maps and institutional affiliations.



LIBS depth-profile analysis of W/Cu functionally graded material

M. Ivkovic ^{a,*}, J. Savovic ^b, B.D. Stankov ^a, M. Kuzmanovic ^c, I. Traparic ^a

^a Institute of Physics, University of Belgrade, Belgrade 11080, Serbia

^b Vinca Institute of Nuclear Sciences, University of Belgrade, Belgrade 11000, Serbia

^c Faculty of Physical Chemistry, University of Belgrade, Belgrade 11158, Serbia



ARTICLE INFO

Keywords:

Laser-induced breakdown spectroscopy, LIBS

W/Cu composite

Functionally graded material, FGM

Quantitative analysis

Depth-profile analysis

ABSTRACT

A feature of Laser-Induced Breakdown Spectroscopy (LIBS), the ability to perform depth profiling, has been exploited to analyze a tungsten-copper functionally graded material (FGM), considered a relevant candidate for components in a nuclear fusion reactor. The proposed method relies on establishing correlations between the depth of ablation craters and the number of laser pulses, along with the accompanying LIBS spectra acquired by varying a number of laser pulses. LIBS measurements were performed using a Q-switched Nd:YAG laser at 532 nm with 100 mJ/pulse energy under reduced Ar pressure. The ablation craters were analyzed using optical profilometry. The copper concentration at each specific depth was assessed using a univariate calibration curve constructed with intensity ratios of Cu I 521.82 nm and W I 522.47 nm spectral lines. The calibration samples were pure W and homogenous W/Cu composite samples with different Cu content (10.9% - 35.3%) whose composition was determined by X-ray fluorescence. The proposed method exhibits potential applicability for quantitative analysis of multilayered materials.

1. Introduction

Functionally Graded Materials (FGM) have innovative properties and multifunctional characteristics that conventional homogeneous materials cannot achieve. In its simplest form, FGM consists of a singular material on one surface, a distinct material on the opposing surface, and an intermediary layer characterized by a gradual variation in structure, composition, and morphology spanning micron-level dimensions between the two materials. A desired function can be achieved by selecting the transition profile of FGM. Therefore, the FGM must be classified separately from conventional homogeneous composites and nanocomposite materials [1–3]. The applications of FGM are extensive and include engineering, aerospace, chemical plants, electronics, energy conversion, optics, nuclear energy, and even biomaterials [4,5]. Depending on the application, various properties, such as thermal (expansion coefficient, conductivity, stability, temperature distribution, response under transient heating), electric (conductivity, dielectric properties), elastic (deformation, strength, Young's elastic modulus), or some other can have one-, two- or three-dimensional variation in the fraction of its components.

Due to their distinctive characteristics, materials with property gradation offer significant advantages for application in nuclear fusion

reactors. For example, functionally graded materials are relevant candidates for the interlayer between W plasma-facing components (PFCs) and CuCrZr heat sinks [6–15]. The challenge posed by a substantial difference in the coefficient of thermal expansion between these two materials, resulting in thermal stress on PFC, can be mitigated by introducing a transition layer consisting of a material characterized by a low thermal expansion rate, high thermal conductivity, and favorable thermomechanical properties. Promising candidates for joining layers of W to CuCrZr are W/Cu composites and W/Cu functionally graded composites [13,14]. The suitability of these materials is reflected in the ability to finely tune their macroscopic properties (microstructure and phase distribution) to attain the desired characteristics.

As an in-situ, non-contact, minimally invasive technique sensitive to light elements, with the limit of detection down to ppm (or even to ppb in some cases), laser-induced breakdown spectroscopy (LIBS) is a promising tool for analyzing plasma-facing components in fusion devices [16]. Various LIBS configurations, using either single pulse (SP-LIBS) or double pulse (DP-LIBS), have been used to explore the optimization of the technique for monitoring compositional alterations in PFCs. These changes may arise due to impurity deposition, erosion, or fuel retention [17–23]. Also, the effect of laser parameters (energy and duration of laser pulse, wavelength) and the effect of atmospheric

* Corresponding author.

E-mail address: ivke@ipb.ac.rs (M. Ivkovic).

conditions on the emission, mass ablation, and plasma parameters have been extensively studied [24–27]. LIBS possesses a competitive advantage over alternative techniques designed for in-depth elemental analysis due to its in-situ and remote analysis capability, which is especially important when analysis has to be performed in hostile environments like nuclear reactors.

This paper presents the research findings on the potential of LIBS for in-depth profiling of W/Cu functionally graded material using a medium-resolution spectrometer. A conventional nanosecond LIBS system was used, and the samples were analyzed under the Ar atmosphere at reduced pressure. The proposed method is based on the correlation of the depth of the ablation craters and gathered LIBS spectra for different number of accumulated laser pulses. The ablation craters were analyzed using optical profilometry. The copper content at each depth was estimated from the constructed calibration curve. For concentration calibration, homogenous W/Cu samples whose composition was determined by X-ray fluorescence were used. Subsequently, a univariate calibration curve was developed utilizing the line intensity ratios of Cu I 521.82 nm and W I 522.47 nm lines.

The proposed approach is also amenable to the analysis of elemental composition and the determination of individual layer thickness in multilayered materials.

2. Experimental

2.1. Samples

A set of tungsten-copper alloys W93Cu7, W90Cu10, W80Cu20, W70Cu30, and pure W in the form of tablets (diameter 10 mm, thickness 1 mm) were obtained from HUBEI FOTMA MACHINERY CO LTD, Wuhan, P. R. China. Since W/Cu samples' trade names represent a rough percentage of the main constituents, the precise composition of the samples was determined using X-ray fluorescence (XRF) analysis. These samples were used as calibration samples for LIBS analysis. A W/Cu functionally graded material (W/Cu FGM), i.e., tungsten with a gradient concentration of copper along the sample thickness direction, was used for LIBS depth-profile analysis. A W/Cu FGM sample was a disc with a 6 mm diameter and thickness of 1 mm.

2.2. XRF spectrometry

A portable XRF Niton XL3t970 GOLDD analyzer (Thermo Fisher Scientific) was used to analyze the composition of W/Cu standards. The instrument is equipped with an X-ray tube, working at a maximum of 50 kV, 200 μ A, and a high-performance semi-conductor detector with a resolution of 185 eV. The spot diameter at the measurement point is

about 3 mm. Depending on the application, the analytical range covers up to 30 elements, from sulfur to uranium. The analysis was carried out using a General Metal Mode calibration (includes elemental analysis of Ba, Sb, Sn, In, Cd, Pd, Ag, Mo, Nb, Zr, Se, Bi, Pb, Pt, Br, Au, Hg, Ta, Hf, Zn, Cu, Ni, Co, Fe, Mn, Cr, V, Ti) for a total time of 60 s (30 s Main filter and 15 s for Low and High filters).

2.3. LIBS setup

Fig. 1a shows a sketch of the focusing head for the basic single-pulse LIBS setup used in this work. A setup consists of the laser (1) mounted on the platform (2) movable vertically (0–380 mm) by the column (3) connected to the second fixed platform (4). The focusing head (5) carries a dichroic bending mirror at 45 degrees, a green diode laser (6) for indicating the position of a focal point, and a focusing mirror mount (which has the possibility for fine focal distance adjustment with accuracy of 10 μ m and the range of ± 10 mm). A laser source (1) was Nd:YAG Quantel Q-smart 450 laser ($\lambda = 532$ nm; energy 100 mJ; 6 ns pulses, frequency 10 Hz). The change in the laser energy density was obtained by varying the distance between the sample and lens with a 10 cm focal length.

The shape, position, and size of the laser beam spot on the target were monitored using the endoscopic camera (8) equipped with six white light-emitting diodes for illumination. The camera has a diameter of 7 mm and a 5 m long light guide connected to the computer. The resolution of the camera is 640 \times 480 pixels.

Fiber optic cable ($\varnothing = 400$ μ m) led the plasma emission collected by the light collector, i.e., fiber adapter Solar LS FA-2 (9), to the entrance of the imaging spectrometer Shamrock 303 Andor. The imaging spectrometer was equipped with the ICCD camera Andor iStar DH720. The camera working in full vertical binning mode (FVB) was triggered at various delays and gate times determined by a digital delay generator (SRS DG535) using the signals from the ICCD camera computer interface and Q switch trigger from the laser (controlled by the remote laser controller) by the help of the digital storage oscilloscope and computer software. Spectral sensitivity calibration of a Shamrock spectrometer system with an Andor iStar DH720 ICCD camera was performed with a calibrated tungsten lamp in the 300–800 nm wavelength range. Instrumental width (w_i) was experimentally determined by fitting a profile of the spectral line emitted from a low-pressure mercury lamp. For entrance slit width of 20 μ m, w_i was 0.11 nm.

A small vacuum chamber (based on KF40 Tee, see **Fig. 1b**) carrying target was settled on the carrier (Thorlabs, Pitch and roll platform) (7) with the manually adjustable angle, connected to the Thorlabs XY stepper motor translation stage controlled by the computer. After the chosen number of laser pulses, n , the target position (10) was changed to

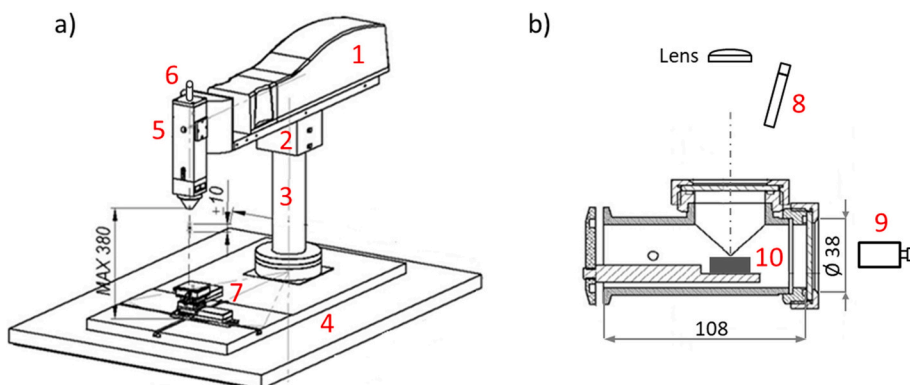


Fig. 1. a) Sketch of the focusing head for the single-pulse LIBS setup showing dimensions and range of the focal point adjustment. Legend: (1) laser, (2) platform, (3) movable column, (4) fixed platform, (5) focusing head, (6) green diode laser, (7) XY translation stage; b) Technical drawing of the vacuum chamber. Legend: (8) endoscopic camera, (9) light collector, i.e., fiber adapter, (10) target. (For interpretation of the references to colour in this figure legend, the reader is referred to the web version of this article.)

expose the “fresh” target surface. The target position was fixed when the task was to determine the ablation depth as a function of the number of applied laser shots. The appropriate gas pressure inside the chamber was adjusted using regulation and needle valves and monitored by the manometer, led to the chamber using appropriate tubing, and evacuated by the vacuum pump. All measurements reported in this work were recorded under reduced Ar pressure.

2.3.1. Profilometry analysis

The Zygo New View 7100 Scanning White Light Interferometer (optical Surface profiler) was used for fast, non-contact 3D measurement of surface morphology. The profilometer’s vertical scan range is 150 μm , with the extended scan range up to 20 mm. Vertical resolution is <0.1 nm, while the lateral resolution is objective dependent and ranges from 0.36 to 9.5 μm . A data scan rate is user-selectable (camera and scan mode dependent) and goes up to 26 $\mu\text{m}/\text{s}$. RMS repeatability is <0.01 nm. The step height accuracy is $\leq 0.75\%$, while repeatability is $\leq 0.1\%$. The profilometer is equipped with the program (Zygo corporation, Metro Pro) that was used for measuring crater depths from two-dimensional (2D) profiles and their three-dimensional (3D) visualization.

3. Results and discussions

3.1. XRF spectroscopy

The composition of the W/Cu calibration standards was determined by XRF analysis. A part of the obtained XRF spectra is presented in Fig. 2. The elemental composition obtained by XRF is summarised in Table 1. Samples also contain trace levels of other elements, such as Ti, Mn, Fe, and Co. The measurement accuracy (element dependent) was typically 2% - 5% of the reported weight percent value. Concentration values obtained by XRF were used to construct the calibration curve.

3.2. LIBS analysis

A critical problem with the application of LIBS for the elemental (quantitative) analysis of W and W-alloys is the low reproducibility of the spectral line intensities caused by different grain sizes in a tungsten structure [28]. The line intensities also depend on grain distribution, causing differences in measured intensities during target irradiation at different angles [29]. In addition, explosive boiling occurs at temperatures greater than critical [30–32]. For example, threshold laser intensity for phase explosion in tungsten under interaction with Nd:YAG laser at 355 nm was estimated to be $6 \times 10^{10} \text{ W cm}^{-2}$ [31].

Our first step was to study the influence of different experimental parameters (e.g., gas pressure, laser energy, beam size, the number of accumulated pulses, and delay time) on the reproducibility of the

Table 1
Results of the XRF analysis of W/Cu calibration samples.

Trade name	Concentration (wt%)*					Other elements
	Cu	W	Zn	Ni	Cr	
W	—	100	—	—	—	—
W93Cu7	10.9	87	1.6	0.47	—	0.03
W90Cu10	12.9	84	1.9	0.56	0.23	0.41
W80Cu20	24.3	72	2.8	0.78	—	0.12
W70Cu30	35.3	59	3.0	1.5	0.11	1.09

measured spectral line intensities. All LIBS measurements reported in this study were done in an argon atmosphere, as it was shown that the inert background gas provides almost uniform spatial distributions of plasma temperature and densities [33,34].

3.2.1. Optimization of the LIBS experimental parameters

The influence of Ar pressure on the spectral emission intensity was studied within the pressure range spanning from vacuum conditions to 1 atm. Fig. 3 shows that, in the analyzed pressure range, the highest signal-to-noise ratio (SNR) of spectral lines was obtained at 10 mbar, hence this pressure was chosen as optimal.

The influence of delay time on the intensity of Cu I 521.82 nm and W 522.47 nm lines is illustrated in Fig. 4 (a), while the SBR and signal-to-noise ratio (SNR) for a copper 521.82 nm line is illustrated in Fig. 4 (b).

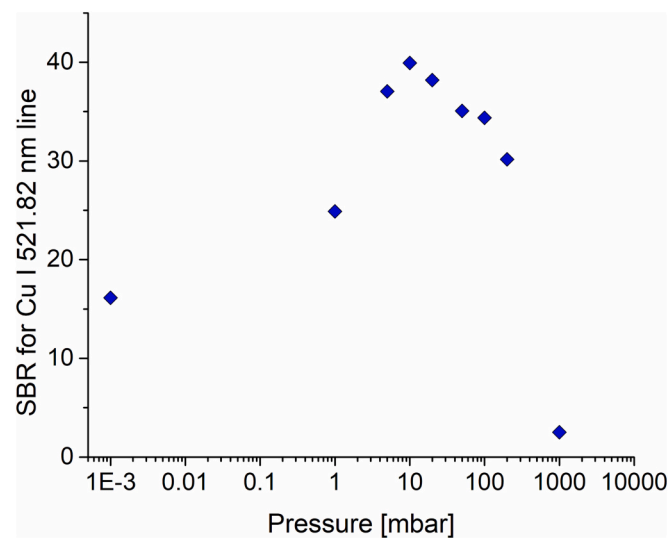


Fig. 3. The influence of Ar pressure on the signal-to-background ratio of Cu 521.82 nm line.

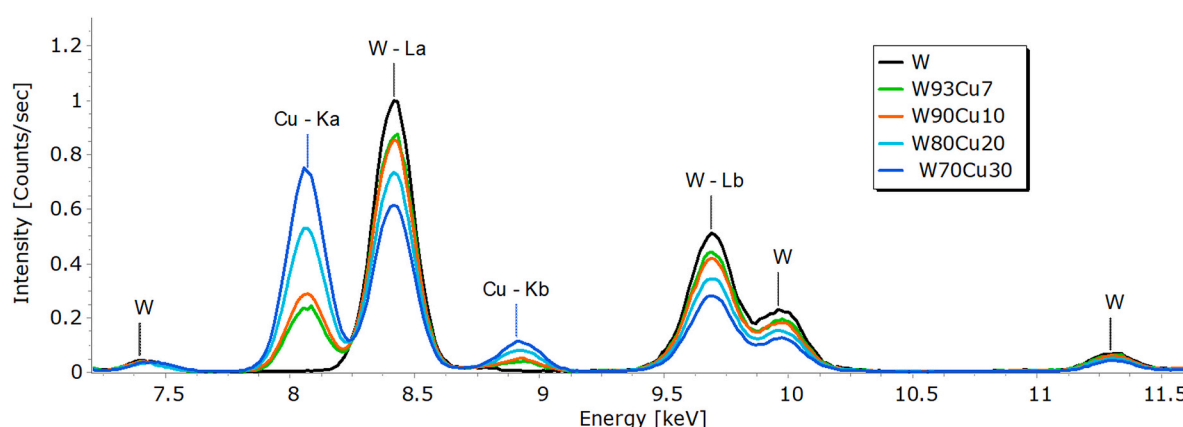


Fig. 2. Segment of the XRF spectra of W and W/Cu samples used as calibration standards for LIBS.

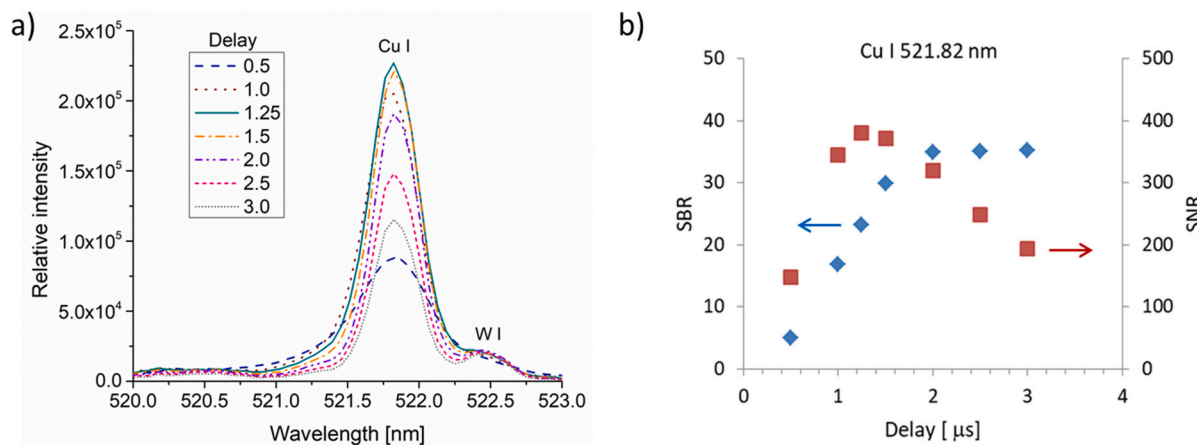


Fig. 4. (a) LIBS spectra of W93Cu7 showing Cu I 521.82 nm and W I 522.47 nm lines recorded for different gate delay times. Laser energy 100 mJ, gate 20 ns, spot diameter 1 mm. Each spectrum represents an average of ten measurements consisting of 10 accumulated consequent laser shots. (b) The SNR and the SBR of Cu 521.82 nm line, as a function of the delay time.

The highest SBR and SNR values were obtained for a delay time of around 1.5–2 μs.

The laser pulse energy threshold required for creating plasma usable for spectrochemical analysis was determined to be 30 mJ. As shown in Fig. 5, the intensity of W and Cu demonstrated a proportional increase with elevated laser energy. Nevertheless, when the beam is focused on the target and the laser energy surpasses 50 mJ, the ratio of line intensities (Cu I 521.82 nm / W I 522.47 nm) remains constant. Uniform evaporation of both components was achieved at energies exceeding 50 mJ, resulting in a constant line intensity ratio at higher laser pulse energies. A laser energy of 100 mJ was chosen for further LIBS measurements to enhance emission intensity, thereby improving the precision of intensity measurements and increasing the ablated mass compared to a pulse energy of 50 mJ (for the same spot diameter).

The spot size required optimization to ensure that the spot diameter remains significantly larger than the sample grain size. The spot size was optimized by adjusting the focus, specifically by varying the lens-to-sample distance to define the surface that would be ablated. Due to the granulation of the material, the minimal preferable spot size should be above 100 μm. A spot size of 1 mm eliminated a problem with inhomogeneous grain size distribution and reduced spectral intensity

fluctuations.

The minimum number of laser shots needed to obtain reproducible spectral line intensities was determined to be 10. For the laser pulse energy of 100 mJ, the spot size of 1 mm, and 100 shots (average of ten measurements of 10 accumulated consequent laser shots), the relative standard deviation of the intensity ratio of the selected Cu and W lines was around 5%.

Because the measured line intensities may vary due to the interaction of the plasma with the crater walls, the plasma confinement, or plasma cooling by the crater walls, the influence of crater depth on the measured LIBS intensity was also investigated. Fig. 6 (a) shows spectra recorded for a sequence (1–800) of laser shots applied to the same spot on the W90Cu10 target. The effect of the crater depth on the intensity of Cu I 521.82 nm and W I 522.47 nm line and Cu/W intensity ratio is shown in Figs. 6 (b-d). The variation of the line intensities is more pronounced than the variation of the Cu/W intensity ratio. After the 100th shot at the same position, the influence on the measured Cu/W intensity ratio is significant, i.e., it decreases with a further increase of the crater depth. A possible explanation for such behavior could be a more significant effect of the changed plasma parameters (caused by crater walls) on the intensity of the line with lower excitation energy.

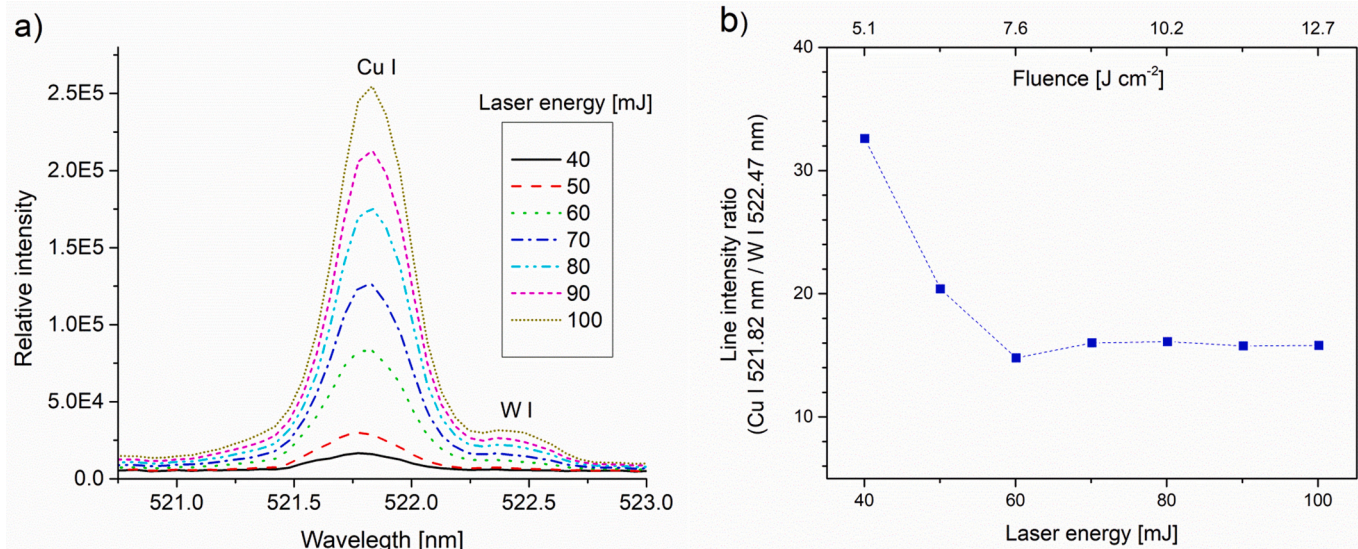


Fig. 5. (a) Effect of laser pulse energy on the LIBS emission of Cu I 521.82 nm and W I 522.47 nm line. (b) The influence of pulse energy and fluence on the Cu/W line intensity ratio. Target W93Cu7; delay 1.5 ms; gate 20 ns; spot diameter 1 mm.

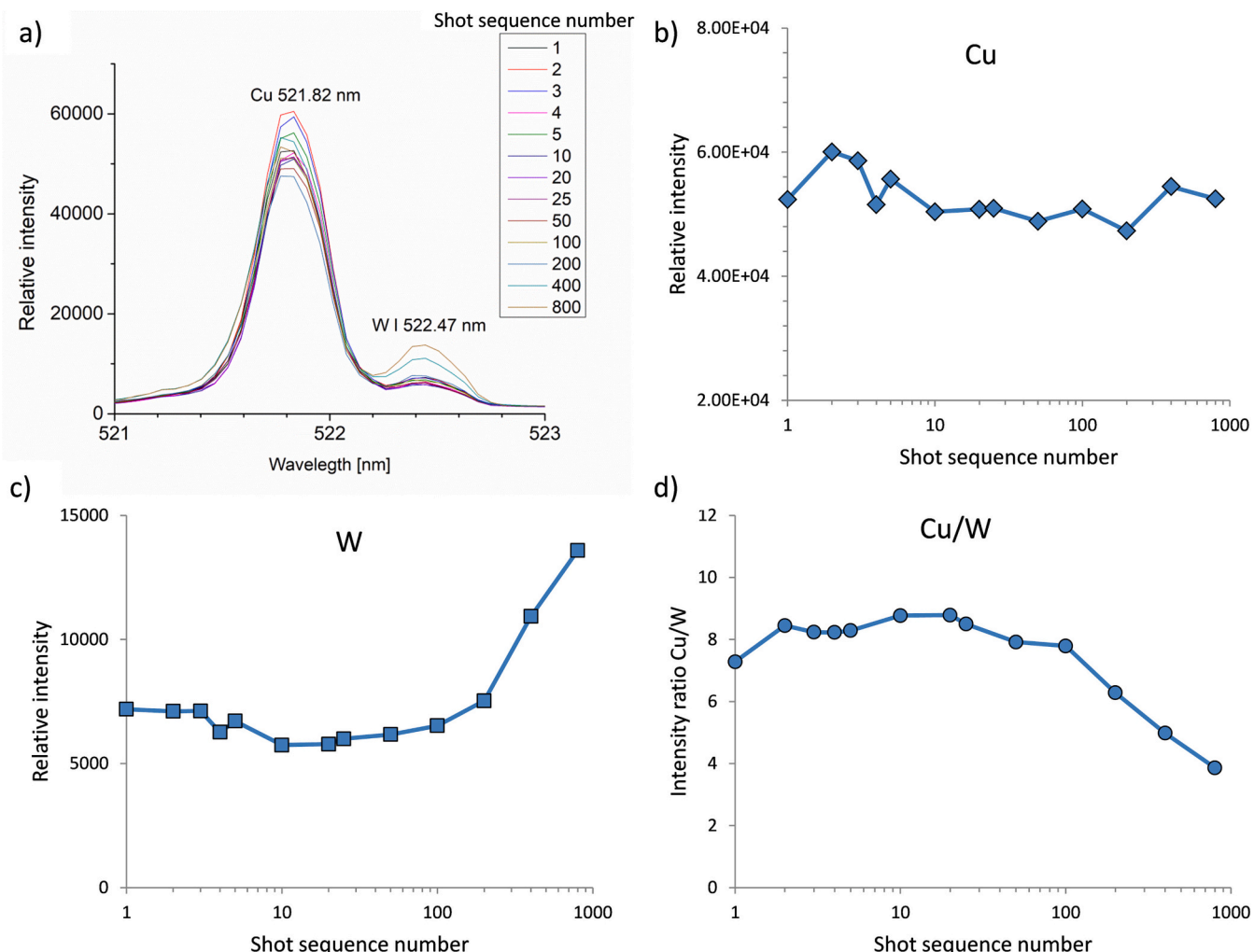


Fig. 6. (a) LIBS spectra recorded for a sequence (1–800) of laser shots applied to the same spot on the W90Cu10 target. (b-d) The effect of the crater depth on the intensity of Cu I 521.82 nm and W I 522.47 nm line and Cu/W intensity ratio.

Therefore, the influence of crater depth on the measured Cu/W intensity ratio was negligible for the number of pulses applied in this work.

3.2.2. Plasma diagnostics

LIBS spectrum recorded for the W70Cu30 sample was used to determine the excitation temperature from the Boltzmann plot of the selected W and Cu spectral lines. In order to cover a large spectral

window (320 nm to 550 nm), several consecutive LIBS spectra were recorded, each covering a spectral portion of about 60 nm. The experimental parameters (laser energy, focusing, delay and gate time, and the number of accumulations) were held constant. Under our experimental conditions, only lines generated by neutral and single ionized W and Cu species can be detected. The list of lines and their spectral parameters (taken from the NIST Atomic Spectral Database [35]) are given in the

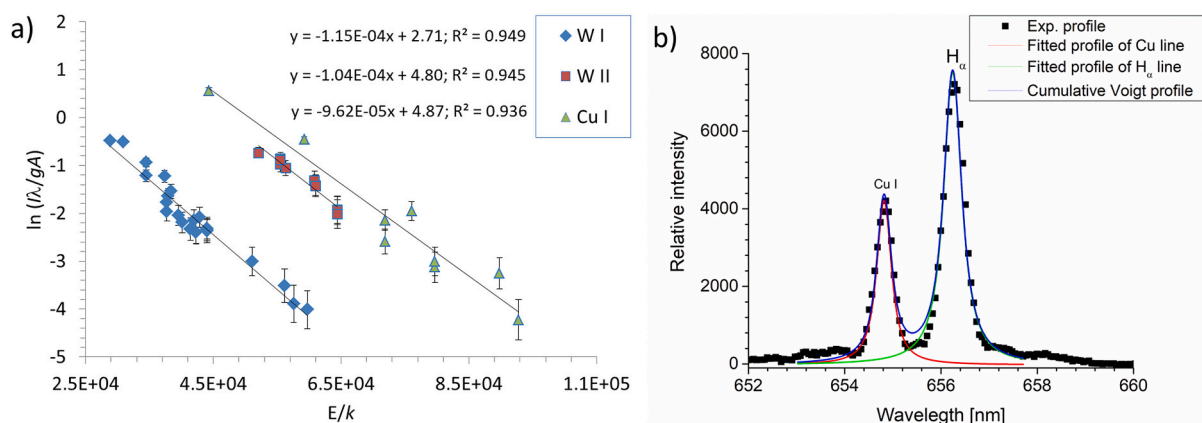


Fig. 7. a) Boltzmann plot of Cu and W spectral lines, and b) Experimental profile of the H α line fitted to a Voigt function.

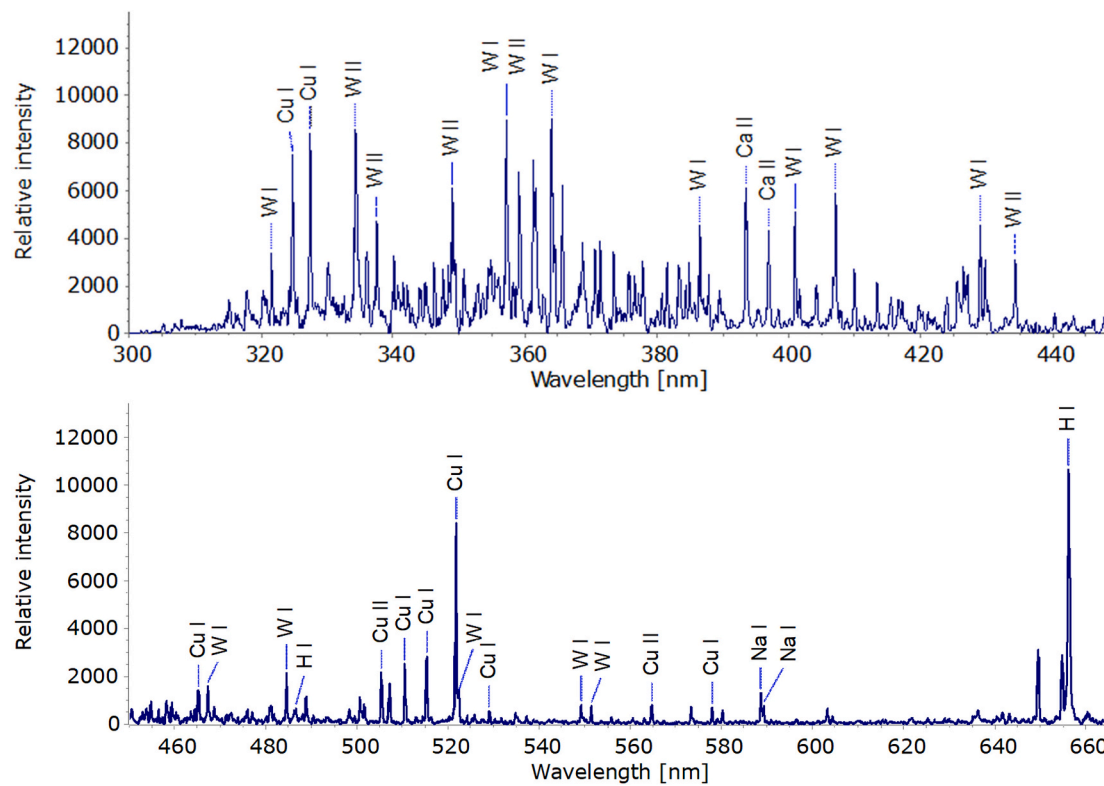


Fig. 8. LIBS spectra of the W93Cu7 alloy sample. Experimental conditions: Nd:YAG pulse energy 40 mJ; wavelength 532 nm; frequency 10 Hz; delay 0.5 μ s; gate 2.5 μ s; 10 mbar argon.

Appendix. The temperatures obtained from Boltzmann plots (Fig. 7a) were 8900 K, 9400 K, and 10,400 K for W I, W II, and Cu I, respectively. A Boltzmann plot using copper ionic lines was omitted because it had poor calculation accuracy of the plasma temperature due to a low number of identified Cu II spectral lines.

The electron number density was determined from the Stark width of the Balmer alpha line of the hydrogen, which is always present in the tungsten as an impurity (Fig. 7b). This line was chosen due to the low Balmer beta line intensity caused by the small amount of hydrogen. The line width was determined under the approximation that the line profile can be described with a Voigt function. The deconvolution of a Voigt function was performed using the Levenberg-Marquardt nonlinear fitting algorithm for minimum squares, with the Gaussian FWHM fixed, assuming that the Lorentzian component, w_L , is due to Stark broadening. The Gaussian fraction (w_G) is assumed to be a combination of the instrumental (w_i) and the Doppler broadening (w_D): $w_G = (w_D^2 + w_i^2)^{0.5} = (0.05^2 + 0.11^2)^{0.5} = 0.12$ nm. To calculate N_e , an approximate formula was used [36,37]:

$$N_e [m^{-3}] = 10^{23} \left(\frac{w_L [nm]}{1.098} \right)^{1.47135}$$

The estimated value of N_e was $2.5 \times 10^{22} \text{ m}^{-3}$.

3.2.3. Univariate calibration

Characteristic spectra of the W/Cu composite sample in the 300–660

nm spectral range are shown in Fig. 8.

The possible influence of self-absorption was checked by comparing the experimental and theoretical ratios of line strengths within multiplets [38]. Based on the results shown in Table 2, it was concluded that the influence of self-absorption on the measured intensities of W and Cu could be neglected.

LIBS spectra of pure W and four W/Cu composite samples (Table 1) were used to construct a calibration curve. The spectra were recorded using the standard LIBS setup described in the experimental section using an optimized set of parameters: pulse energy 100 mJ; spot diameter 1 mm; delay 2 μ s; gate 20 ns; 100 accumulations (average of ten measurements of 10 accumulated consequent laser shots). LIBS spectra of calibration samples are shown in Fig. 9 a.

Because the selected Cu and W lines overlap, integral intensities of these lines were determined using their approximation with Voigt functions. The line fit was performed using the Levenberg-Marquardt nonlinear fitting algorithm for minimum squares, with the Gaussian FWHM fixed ($w_i = 0.11$ nm). The calculated contribution of Doppler broadening was negligible for temperatures around 10,000 K, 0.005 nm for the Cu 521.82 nm line, and 0.003 for the W 522.47 nm line. The selected line pair was suitable for the Cu concentration range considered in this study. For samples with a low concentration of Cu, the intensity ratio of the strongest Cu I line at 324.75 nm with some of the nearby W lines (e.g., W I 320.72 nm) may be used.

A linear relationship was obtained between the Cu I 521.82 nm and

Table 2

Comparison of theoretical and experimental ratios of spectral line intensities.

	Configuration	λ_1 (nm)/ λ_2 (nm)	$R = I_{\lambda_1}/I_{\lambda_2}$ (theor.)	$R = I_{\lambda_1}/I_{\lambda_2}$ (exp.)
W I	5d46s2 - 5d5(6S)6p	413.74 / 407.06	2.11	2.10
		436.48 / 407.06	0.32	0.29
Cu I	3d94s2 - 3d104p	510.55 / 578.21	2.42	2.27
	3d104p - 3d104d	515.32 / 521.82	0.53	0.56

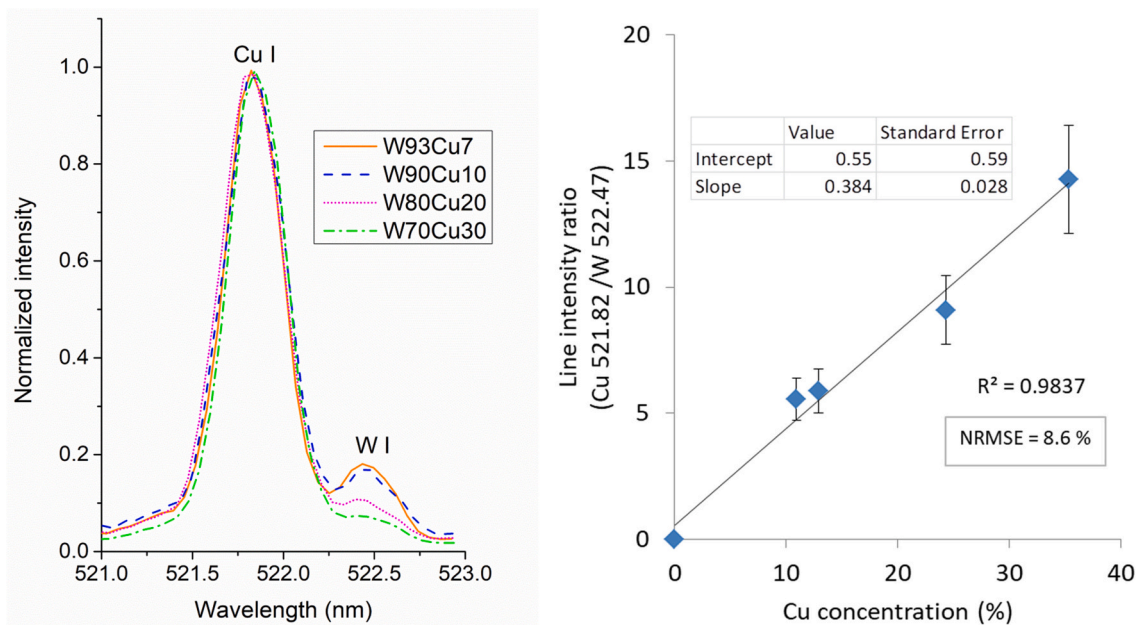


Fig. 9. (a) LIBS spectrum of W/Cu composites; (b) Calibration curve for Cu from the ratio $I_{\text{Cu I}}/I_{\text{W I}}$.

W I 522.46 nm line intensity ratio and the Cu concentration (Fig. 9 b). The calibration curve prediction error, calculated as a Root Mean Square Error (RMSE), was 0.598. The normalized value of the RMSE was 8.6%.

3.3. LIBS depth-profile analysis

A W/Cu functionally graded material (W/Cu FGM), i.e., tungsten with infiltrating copper along the sample thickness direction, was exposed to a variable number of Nd:YAG laser pulses. Time-resolved LIBS spectra were recorded to monitor the corresponding W and Cu spectral line intensity changes. The proposed depth profile analysis method was performed by combining the LIBS spectral analysis with the

results of 3D-optical profilometry used to establish the depth of the ablation craters [39]. Fig. 10 shows 3D surface profiles of craters created on a W/Cu target after the increasing number of laser pulses irradiated the same spot on the target.

Corresponding 2D cross-sectional profiles used to evaluate the depth of the craters are shown in Fig. 11 a. A relationship between the number of laser pulses and crater depths is shown in Fig. 11 b.

As seen in Fig. 11 a, the paraboloid function describes the crater shape well. The volume of a paraboloid is given by $V = 1/2 \pi r^2 h$, where r is the radius of the circular “cap” of the paraboloid and h is the axial height of the paraboloid. In our case, the radius of the surface damaged area was taken as r and the crater depth as h . Using this equation, the

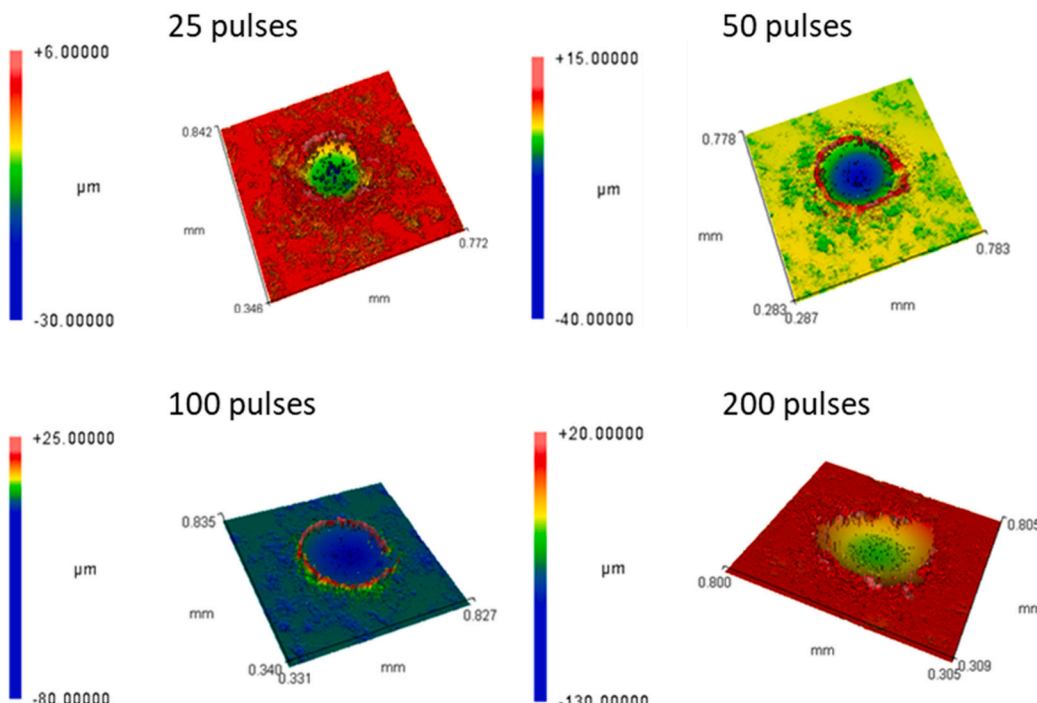


Fig. 10. Surface map of the W/Cu FGM target exposed to a different number of laser pulses.

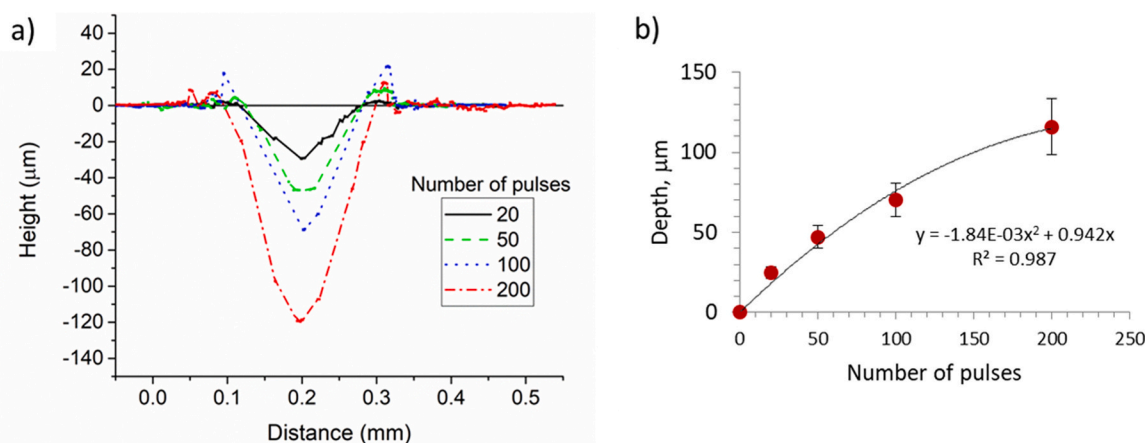


Fig. 11. (a) 2D profile of craters created on W/Cu target by a different number of laser pulses. (b) Crater depth as a function of the number of applied laser pulses.

Table 3

Characteristic parameters of craters created on W/Cu FGM target.

Number of pulses	Spot diameter (mm)	Crater depth (μm)	Spot surface area (10^{-4} cm^2)	Crater volume (10^{-7} cm^3)	Ablated mass* (μg)
25	0.16	29	2.0	3.0	5.7
50	0.16	47	2.0	4.8	9.2
100	0.16	69	2.0	6.9	13
200	0.20	120	3.1	19	36

* Calculated using tungsten density of 19.28 g/cm^3 .

volume of the ablated material was calculated. Characteristic parameters of craters used to estimate the ablated volume and mass of the ablated material are given in [Table 3](#).

LIBS spectra of a W/Cu target irradiated by an increasing number of laser pulses applied to the same target spot are shown in [Fig. 12](#). As the figure shows, the intensity of a copper spectral line at 521.82 nm decreases with the increasing number of applied laser pulses, suggesting copper content gradually reduces from the top. The line disappeared from the spectra after 200 laser shots, indicating the complete removal of a layer containing a gradient concentration of Cu. Based on the obtained results, we estimated the depth of inbound copper into tungsten to $\sim 120 \mu\text{m}$. The copper concentrations at different depths were estimated from the calibration curve ([Fig. 9 b](#)) using a measured Cu I 521.82 nm and W I 522.46 nm line intensity ratios. The results are shown in [Table 4](#).

4. Conclusion

The results have shown that a standard LIBS setup based on Nd:YAG laser using a medium spectral resolution spectrometer can be successfully applied to quantitative analysis of W/Cu functionally graded materials relevant to fusion technology.

For the W/Cu composite with Cu in the 10.9% - 35.3% concentration range, a linear relationship was found between Cu I 521.82 nm to W I 522.46 nm spectral line intensity ratio and Cu concentration. Under optimized experimental conditions (fluence, delay and gate time, number of accumulations), the selected W and Cu lines used to construct a calibration curve were optically thin.

It should be noted that the suitability of the W/Cu samples selected

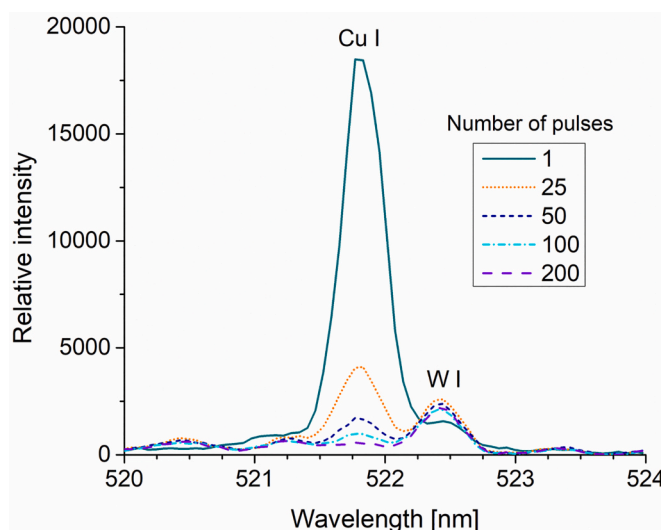


Fig. 12. LIBS spectra of a W/Cu-based gradient material. Laser energy 40 mJ; spot diameter 0.16 mm; delay 0.5 μs ; gate 2.5 μs ; 10 mbar argon.

Table 4

Copper content at different depths of the W/Cu FGM sample.

Number of laser shots	Depth (μm)	Intensity ratio Cu I 521.82/W I 522.46	Cu concentration (%)
1	0.9	12	30 ± 3
25	29	1.5	2.0 ± 0.2
50	47	0.7	0.39 ± 0.03
100	120	-	-

for the calibration technique should be carefully checked. Depending on the manufacturing processes, the grain size, shape of grains, distribution of additives inside the tungsten matrix, or other characteristics of W-based composites may influence the accuracy of LIBS analysis.

The copper concentration along the sample thickness direction was obtained by combining LIBS spectral analysis and optical profilometry results. The applied protocol may be suitable for depth profile analysis of tungsten-based composite in the fusion reactor, i.e., a transition layer between W tiles at the first wall of the reactor and cooling channels made of CuCrZr.

CRediT authorship contribution statement

M. Ivkovic: Conceptualization, Methodology, Supervision, Writing – original draft, Writing – review & editing. **J. Savovic:** Formal analysis, Visualization, Writing – review & editing. **B.D. Stankov:** Formal analysis, Investigation, Writing – review & editing. **M. Kuzmanovic:** Methodology, Validation, Writing – review & editing. **I. Traparic:** Formal analysis, Writing – review & editing.

Declaration of competing interest

The authors declare that they have no known competing financial interests or personal relationships that could have appeared to influence the work reported in this paper.

Data availability

Data will be made available on request.

Acknowledgements

The research was funded by the Ministry of Science, Technological Development and Innovation of the Republic of Serbia, Contract numbers: 451-03-47/2023-01/200024, 451-03-47/2023-01/200017 and 451-03-47/2023-01/200146, and supported by the Science Fund of the Republic Serbia, Grant no. 7753287.

Appendix A. Supplementary data

Supplementary data to this article can be found online at <https://doi.org/10.1016/j.sab.2024.106874>.

References

- [1] M. Niino, T. Hirai, R. Watanabe, Functionally gradient materials. In pursuit of super heat resisting materials for spacecraft, *J. Japan Soc. Compos. Mater.* 13 (1987) 257–264, <https://doi.org/10.6089/jscm.13.257>.
- [2] A. Kawasaki, R. Watanabe, Concept and P/M fabrication of functionally gradient materials, *Ceram. Int.* 23 (1997) 73–83, [https://doi.org/10.1016/0272-8842\(95\)00143-3](https://doi.org/10.1016/0272-8842(95)00143-3).
- [3] M. Naebe, K. Shirvanimoghadam, Functionally graded materials: a review of fabrication and properties, *Appl. Mater. Today* 5 (2016) 223–245, <https://doi.org/10.1016/j.apmt.2016.10.001>.
- [4] Y. Miyamoto, W.A. Kaysser, B.H. Rabin, A. Kawasaki, R.G. Ford (Eds.), Functionally Graded Materials, Springer US, Boston, MA, 1999, <https://doi.org/10.1007/978-1-4615-5301-4>.
- [5] K. Ichikawa (Ed.), Functionally Graded Materials in the 21st Century, Springer US, Boston, MA, 2001, <https://doi.org/10.1007/978-1-4615-4373-2>.
- [6] S. Suzuki, M. Akiba, M. Araki, K. Yokoyama, Thermal cycling experiments of Monoblock Divertor modules for fusion experimental reactors, *Fusion Technol.* 21 (1992) 1858–1862, <https://doi.org/10.13182/FST92-A29989>.
- [7] Y. Itoh, M. Takahashi, H. Takano, Design of tungsten/copper graded composite for high heat flux components, *Fusion Eng. Des.* 31 (1996) 279–289, [https://doi.org/10.1016/0920-3796\(95\)00432-7](https://doi.org/10.1016/0920-3796(95)00432-7).
- [8] G. He, K. Xu, S. Guo, X. Qian, Z. Yang, G. Liu, J. Li, Preparation of tungsten fiber reinforced-tungsten/copper composite for plasma facing component, *J. Nucl. Mater.* 455 (2014) 225–228, <https://doi.org/10.1016/j.jnucmat.2014.05.026>.
- [9] S. Wang, J. Li, Y. Wang, X. Zhang, R. Wang, Y. Wang, J. Cao, Thermal damage of tungsten-armored plasma-facing components under high heat flux loads, *Sci. Rep.* 10 (2020) 1359, <https://doi.org/10.1038/s41598-020-57852-8>.
- [10] A.V. Muller, D. Ewert, A. Galatantu, M. Milwlich, R. Neu, J.Y. Pastor, U. Siecken, E. Tejado, J.H. You, Melt infiltrated tungsten–copper composites as advanced heat sink materials for plasma facing components of future nuclear fusion devices, *Fusion Eng. Des.* 124 (2017) 455–459, <https://doi.org/10.1016/j.fusengdes.2017.01.042>.
- [11] R. Neu, J. Riesch, A.V. Müller, M. Balden, J.W. Coenen, H. Gietl, T. Höschken, M. Li, S. Wurster, J.-H. You, Tungsten fibre-reinforced composites for advanced plasma facing components, *Nucl. Mater. Energy.* 12 (2017) 1308–1313, <https://doi.org/10.1016/j.nme.2016.10.018>.
- [12] J.H. You, E. Visca, T. Barrett, B. Böswirth, F. Crescenzi, F. Domptail, M. Furdon, F. Gallay, B.-E. Ghidersa, H. Greuner, M. Li, A.V. Müller, J. Reiser, M. Richou, S. Roccella, C. Vorpahl, European divertor target concepts for DEMO: design rationales and high heat flux performance, *Nucl. Mater. Energy.* 16 (2018) 1–11, <https://doi.org/10.1016/j.nme.2018.05.012>.
- [13] Z.-J. Zhou, S.-X. Song, J. Du, Z.-H. Zhong, C.-C. Ge, Performance of W/cu FGM based plasma facing components under high heat load test, *J. Nucl. Mater.* 363–365 (2007) 1309–1314, <https://doi.org/10.1016/j.jnucmat.2007.01.184>.
- [14] E. Tejado, M. Dias, J.B. Correia, T. Palacios, P.A. Carvalho, E. Alves, J.Y. Pastor, New WC-cu thermal barriers for fusion applications: high temperature mechanical behaviour, *J. Nucl. Mater.* 498 (2018) 355–361, <https://doi.org/10.1016/j.jnucmat.2017.10.071>.
- [15] C. Li, D. Zhu, R. Ding, B. Wang, J. Chen, B. Gao, Y. Lei, Characterization on the melting failure of CuCrZr cooling tube of W/cu monoblocks during plasma operations in EAST, *Nucl. Mater. Energy.* 25 (2020) 100847, <https://doi.org/10.1016/j.nme.2020.100847>.
- [16] D.W. Hahn, N. Omenetto, Laser-induced breakdown spectroscopy (LIBS), part II: review of instrumental and methodological approaches to material analysis and applications to different fields, *Appl. Spectrosc.* 66 (2012) 347–419, <https://doi.org/10.1366/11-06574>.
- [17] S. Almaviva, L. Caneve, F. Colao, V. Lazic, G. Maddaluno, P. Mosetti, A. Palucci, A. Reale, P. Gasior, W. Gromelski, M. Kubkowska, LIBS measurements inside the FTU vessel mock-up by using a robotic arm, *Fusion Eng. Des.* 157 (2020) 111685, <https://doi.org/10.1016/j.fusengdes.2020.111685>.
- [18] A. Favre, V. Morel, A. Bultel, G. Godard, S. Idlaheen, A. Benyagoub, I. Monnet, A. Sémerok, M. Dinescu, S. Markelj, P. Magaud, C. Grisolia, Double pulse laser-induced plasmas on W and Al by ps-LIBS: focus on the plasma-second pulse interaction, *Fusion Eng. Des.* 168 (2021) 112364, <https://doi.org/10.1016/j.fusengdes.2021.112364>.
- [19] A. Marín Roldán, M. Pisarcík, M. Veis, M. Držík, P. Veis, Calibration-free analysis of a tungsten-based target for diagnostics of relevant fusion materials comparing picosecond and nanosecond LIBS, *Spectrochim. Acta - Part B at Spectrosc.* 177 (2021) 106055, <https://doi.org/10.1016/j.sab.2020.106055>.
- [20] P. Liu, D.Y. Zhao, L.Y. Sun, C.L. Fu, J.M. Liu, C. Li, R. Hai, C.F. Sang, Z.H. Hu, Z. Sun, J.S. Hu, L. Wang, J.L. Chen, Y.F. Liang, G.N. Luo, H. Ding, In situ diagnosis of Li-wall conditioning and H/D co-deposition on the first wall of EAST using laser-induced breakdown spectroscopy, *Plasma Phys. Control. Fusion.* 60 (2018) 085019, <https://doi.org/10.1088/1361-6587/aace83>.
- [21] F. Colao, S. Almaviva, L. Caneve, G. Maddaluno, T. Fornal, P. Gasior, M. Kubkowska, M. Rosinski, LIBS experiments for quantitative detection of retained fuel, *Nucl. Mater. Energy.* 12 (2017) 133–138, <https://doi.org/10.1016/j.nme.2017.05.010>.
- [22] C. Li, C.-L. Feng, H.Y. Oderji, G.-N. Luo, H.-B. Ding, Review of LIBS application in nuclear fusion technology, *Front. Phys.* 11 (2016) 114214, <https://doi.org/10.1007/s11467-016-0606-1>.
- [23] O.A. Waseem, H.J. Ryu, Tungsten-based composites for nuclear fusion applications, in: *Nucl. Mater. Perform.*, InTech, 2016, <https://doi.org/10.5772/62434>.
- [24] N. Farid, H. Wang, C. Li, X. Wu, H.Y. Oderji, H. Ding, G.-N. Luo, Effect of background gases at reduced pressures on the laser treated surface morphology, spectral emission and characteristics parameters of laser produced Mo plasmas, *J. Nucl. Mater.* 438 (2013) 183–189, <https://doi.org/10.1016/j.jnucmat.2013.03.022>.
- [25] G.S. Maurya, A. Marín-Roldán, P. Veis, A.K. Pathak, P. Sen, A review of the LIBS analysis for the plasma-facing components diagnostics, *J. Nucl. Mater.* 541 (2020) 152417, <https://doi.org/10.1016/j.jnucmat.2020.152417>.
- [26] P. Paris, J. Butikova, M. Laan, A. Hakola, I. Jögi, J. Likonen, E. Grigore, C. Ruset, Comparison of LIBS results on ITER-relevant samples obtained by nanosecond and picosecond lasers, *Nucl. Mater. Energy.* 18 (2019) 1–5, <https://doi.org/10.1016/j.nme.2018.11.018>.
- [27] D. Wu, L. Sun, J. Liu, Y. Lyu, H. Wu, S. Yuan, R. Hai, C. Li, C. Feng, D. Zhao, H. Ding, Parameter optimization of the spectral emission of laser-induced tungsten plasma for tokamak wall diagnosis at different pressures, *J. Anal. At. Spectrom.* 36 (2021) 1159–1169, <https://doi.org/10.1039/D1JA00009H>.
- [28] M.S. Seyam, P. Koshy, M.A. Elbestawi, Laser powder bed fusion of unalloyed tungsten: a review of process, structure, and properties relationships, *Metals (Basel).* 12 (2022) 274, <https://doi.org/10.3390/met12020274>.
- [29] H. Wu, C. Li, D. Wu, J. Liu, Z. He, Q. Li, S. Yuan, X. Cui, R. Hai, H. Ding, Characterization of laser-induced breakdown spectroscopy on tungsten at variable ablation angles using a coaxial system in a vacuum, *J. Anal. At. Spectrom.* 36 (2021) 2074–2084, <https://doi.org/10.1039/D1JA00196E>.
- [30] S.N. Andreev, S.V. Orlov, A.A. Samokhin, Simulation of pulsed-laser-induced explosive boiling, *Phys. Wave Phenom.* 15 (2007) 67–80, <https://doi.org/10.3103/S1541308X0702001X>.
- [31] K. Yahiaoui, T. Kerdja, S. Malek, Phase explosion in tungsten target under interaction with Nd:YAG laser tripled in frequency, *Surf. Interface Anal.* 42 (2010) 1299–1302, <https://doi.org/10.1002/sia.3300>.

- [32] H.Y. Oderji, N. Farid, L. Sun, C. Fu, H. Ding, Evaluation of explosive sublimation as the mechanism of nanosecond laser ablation of tungsten under vacuum conditions, *Spectrochim. Acta Part B At. Spectrosc.* 122 (2016) 1–8, <https://doi.org/10.1016/j.sab.2016.05.008>.
- [33] J. Hermann, C. Gerhard, E. Axente, C. Dutouquet, Comparative investigation of laser ablation plumes in air and argon by analysis of spectral line shapes: insights on calibration-free laser-induced breakdown spectroscopy, *Spectrochim. Acta Part B At. Spectrosc.* 100 (2014) 189–196, <https://doi.org/10.1016/j.sab.2014.08.014>.
- [34] J. Hermann, D. Grojo, E. Axente, C. Gerhard, M. Burger, V. Craciun, Ideal radiation source for plasma spectroscopy generated by laser ablation, *Phys. Rev. E* 96 (2017) 053210, <https://doi.org/10.1103/PhysRevE.96.053210>.
- [35] A. Kramida, Y. Ralchenko, J. Reader, NIST ASD Team, NIST Atomic Spectra Database (ver. 5.10), [Online], Available: <https://physics.nist.gov/asd>, 2022 [2023, May 30]. National Institute of Standards and Technology, Gaithersburg, MD., (n.d.). doi:doi:10.18434/T4W30F.
- [36] N. Konjević, M. Ivković, N. Sakan, Hydrogen Balmer lines for low electron number density plasma diagnostics, *Spectrochim. Acta - Part B At. Spectrosc.* 76 (2012) 16–26, <https://doi.org/10.1016/j.sab.2012.06.026>.
- [37] M.A. Gigosos, M.Á. González, V. Cardeñoso, Computer simulated Balmer-alpha, -beta and -gamma stark line profiles for non-equilibrium plasmas diagnostics, *Spectrochim. Acta Part B At. Spectrosc.* 58 (2003) 1489–1504, [https://doi.org/10.1016/S0584-8547\(03\)00097-1](https://doi.org/10.1016/S0584-8547(03)00097-1).
- [38] N. Konjević, M. Ivković, S. Jovićević, Spectroscopic diagnostics of laser-induced plasmas, *Spectrochim. Acta Part B At. Spectrosc.* 65 (2010) 593–602, <https://doi.org/10.1016/j.sab.2010.03.009>.
- [39] V. Dwivedi, D. Prochazka, D. Janíčković, P. Šperka, P. Švec, J. Kaiser, P. Veis, P. Porížka, LIBS protocol for the assessment of depth profile, homogeneity, and quantification of Fe/co - based bilayer ribbon, *Spectrochim. Acta Part B At. Spectrosc.* 196 (2022) 106509, <https://doi.org/10.1016/j.sab.2022.106509>.



Determination of austenitic steel alloys composition using laser-induced breakdown spectroscopy (LIBS) and machine learning algorithms

Ivan Traparić^a and Milivoje Ivković^b

Institute of Physics Belgrade, Pregrevica 118, Belgrade 11080, Serbia

Received 5 November 2022 / Accepted 1 February 2023

© The Author(s), under exclusive licence to EDP Sciences, SIF and Springer-Verlag GmbH Germany, part of Springer Nature 2023

Abstract. In this paper, the determination of composition of certified samples of austenitic steel alloys was done by combining laser-induced breakdown spectroscopy (LIBS) technique with machine learning algorithms. Isolation forest algorithm was applied to the MinMax scaled LIBS spectra in the spectral range form (200–500) nm to detect and eject possible outliers. Training dataset was then fitted with random forest regressor (RFR) and Gini importance criterion was used to identify the features that contribute the most to the final prediction. Optimal model parameters were found by using grid search cross-validation algorithm. This was followed by final RFR training. Results of RFR model were compared to the results obtained from linear regression with L^2 norm and deep neural network (DNN) by means of R^2 metrics and root-mean-square error. DNN showed the best predictive power, whereas random forest had good prediction results in the case of Cr, Mn and Ni, but in the case of Mo, it showed limited performance.

1 Introduction

The structural materials of fusion reactors are subjected to thermal, mechanical, chemical, and radiation loads. Due to their excellent manufacturability, good mechanical properties, welding ability, and corrosion resistance, austenitic stainless steels were chosen as structural reference material for ITER [1]. In addition, entire vacuum vessel of LHD stellarator in Japan is made of austenitic steel [2], and to diagnose the composition of the deposits on the fusion reactor's first wall, test targets made of austenitic steel (AISI 316 L) were settled at ten positions on the first wall [3]. Laser-induced breakdown spectroscopy (LIBS) is one of the emerging analytical technique that is non-destructive, easy to use and requires little to no preparation of the sample [4]. Therefore, it represents a great tool for the analysis of the composition of austenitic steel samples. There are two main approaches to the LIBS analysis, namely standard calibration method and calibration-free method [5]. In the method where calibration curve

is constructed, a connection between one integrated line intensity and known concentrations is established, thus enabling the determination of unknown concentration. This method is by far the most used one. Alternatively, one can assume local thermodynamic equilibrium (LTE) in plasma and use Saha–Boltzmann equation to obtain plasma temperature and density, and from this the unknown concentrations regardless of the matrix effect. Machine learning algorithms have been successfully applied in analysis of Raman spectra, NIR and THz spectroscopy, vibrational spectroscopy, fusion plasma spectroscopy, etc., just to name a few [6–10]. In recent years, to speed up the analysis of LIBS spectra, machine learning methods are being used intensively [11–14]. These methods involve the usage of principal component analysis (PCA) for dimensionality reduction, support vector machine (SVM) for classification purposes and partial least squares regression (PLS) for multivariate regression problems [15]. Also, for classification or regression problems, many authors applied back propagation neural networks (BPNN) or convolutional neural networks (CNN) to the LIBS spectra in order to perform quantitative analysis of different samples [16–20]. Other regression algorithms, like random forest regression (RFR), have also been widely used [21–24]. Random Forest was constructed and reported by Breiman [25], and it is based on the ensemble of decision trees, where the decision or prediction is made

Physics of Ionized Gases and Spectroscopy of Isolated Complex Systems: Fundamentals and Applications. Guest editors: Bratislav Obradović, Jovan Cvetić, Dragana Ilić, Vladimir Srećković, Sylwia Ptasińska.

^a e-mail: traparic@ipb.ac.rs (corresponding author)

^b e-mail: ivke@ipb.ac.rs

by the majority prediction. This algorithm was previously applied on steel spectra by Zhang et al. [26] where they showed that this regression could be applied for the determination of composition of steel alloys. Later, Zhang with his collaborators used BPNN combined with SelectKBest algorithm for feature selection to trace minor elements in steel samples [27]. Liu and his coworkers also used random forest, combined with permutation importance feature selection to train and predict the composition of steel alloys [28]. Gini importance criteria was also used previously in combination with random forest on classification problems [29, 30], but here we are applying it to regression problem.

In this paper, we will consider three algorithms, random forest, linear regression with \mathcal{L}^2 norm and deep neural network (DNN) to predict steel samples composition. Instead of making our own database, we will use the dataset published at the LIBS 2022 conference site [31] and record our own test dataset under similar conditions to check how much these small differences affect the final model performance. Idea to use RF algorithm is twofold. On the one end, it is able to catch nonlinear phenomena in the data, on the other end to see to what extent we can use already implemented Gini importance criteria within RF to make good regression model. Although simple neural networks have yielded good analytical prediction in the past, in general, they are hard to train (better said, it is not easy to find most favorable architecture), so we wanted to see how close RF predictions are going to be with respect to DNN.

The paper is organized as follows: In the first section, a brief introduction and overview of previous results is given. In Sect. 2, the experimental setup and sample preparation is described. Section 3 gives the detail description of applied methodology and data preprocessing, while the results are given in Sect. 4. Finally, we gave the conclusion of this work in Sect. 5.

2 Experimental setup and sample preparation

Experimental setup is shown in Fig. 1.

The setup is a classical LIBS setup consisting of Quantel Q switched neodymium-doped yttrium aluminum garnet (Nd:YAG) laser having pulse width of 6 ns, repetition rate of 10 Hz, pulse energy of 96 mJ and operated at fundamental wavelength $\lambda = 1064$ nm. Laser beam was reflected from 45° angle mirror M and focused via lens L onto a target mounted on a $x-y$ micrometric moving stage by a lens of focal length $f = 11$ cm. Light emitted from plasma was collected using a fiber optic cable with collimator having a focal length of $f_{fc} = 4.4$ cm and directed onto the $50 \mu\text{m}$ width entrance slit of Mechelle 5000 spectrograph that can record spectra from 200 to 950 nm. As a detector, we used Andor iStar ICCD camera (model DH734, 1024×1024 pixels) cooled to -15°C . Camera was triggered with a photodiode and gated by usage of Stan-

ford Research digital delay unit (model DG535). Delay from laser pulse was set to $0.6 \mu\text{s}$ and the gate width was set to $50 \mu\text{s}$.

Steel samples used in this work were AISI steels with certified composition from National Bureau of Standards (NBS, today NIST), whose elemental composition is given in Table 1.

Sample mentioned above, austenitic steel AISI 316 L lies in between these tested models (concentrations of main elements: Cr 17%, Ni 12%, Mo 2% and Mn 2%). Each sample was firstly polished by sandpaper 200, followed by polishing it with sandpaper 600. In front of laser beam, external shutter was placed, coupled with laser pulse counter. Counter was set to 16 counts, as it is a binary counter, and after 16 pulses, the shutter is closed for another 16 pulses. This represents one acquisition of the spectra. For each sample, we recorded 22 spectra from different places on the target, and each spectra is a result of averaging 20 acquisitions on the same place (this gives 320 individual laser shots per place on the target). To further improve and increase signal, electrical gain of the camera was set to 80 (on the scale of 0–255).

3 Methodology and data preprocessing

Database used in this paper was downloaded from LIBS 2022 website [31]. This database consists of a spectra of 42 different steel samples, and for each sample, a 50 single-shot spectra were taken. This gives in total a database of 2100 spectra samples divided into 40,002

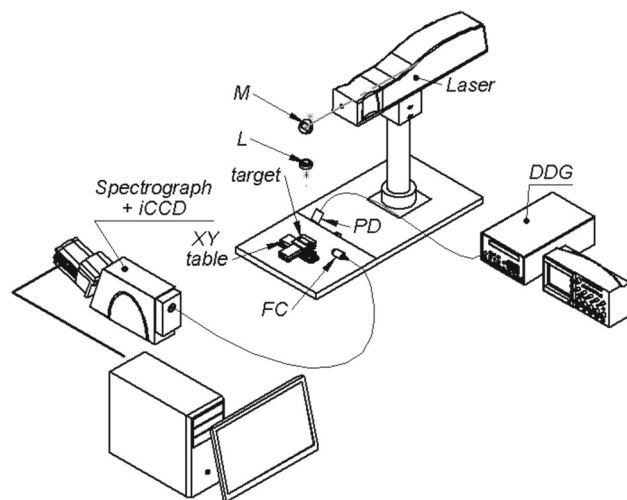
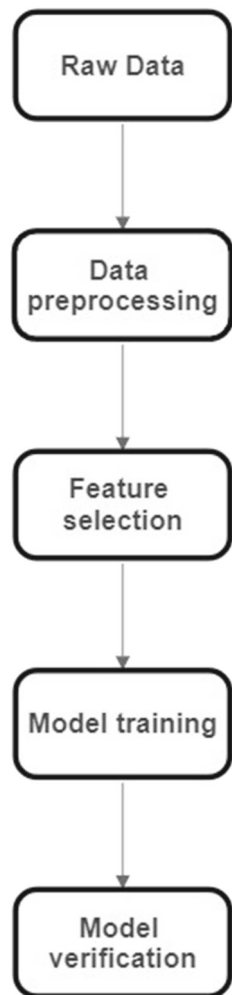


Fig. 1 Experimental setup. Laser (Quantel, $\lambda = 1064$ nm, pulse width 6 ns, peak energy 96 mJ) was focused via lens L onto the movable target and plasma spectrum was recorded by Andor iStar iCCD camera mounted on Echelle spectrograph. Camera gating was done by Stanford Research Digital Delay Generator (DDG, model 535) and triggered by photodiode (PD). Mirror M and lens L are integrated within a laser head, which was not drawn on this figure

Table 1 Steel alloy certified composition

Steel number	Steel type	Cr	Mn	Mo	Ni
443	Cr18.5–Ni9.5	18.5	3.38	0.12	9.4
445	AISI 410	13.31	0.77	0.92	0.28
446	AISI 321	18.35	0.53	0.43	9.11
447	AISI 309	23.72	0.23	0.053	13.26

**Fig. 2** Flowchart of procedures taken in this work

columns (each column corresponds to one wavelength). The flow diagram of our methodology is given in Fig. 2. For machine learning part of this work, we used python public repository scikit-learn.

3.1 Data preprocessing

Firstly, we restricted our dataset to the spectral range between 200 and 500 nm, as this is the spectral area where the most emission lines of metals of interest can be found. It is worth mentioning that all training dataset spectra were not intensity corrected. Therefore, no intensity correction was done on the test dataset.

In the spectra normalization step, two normalizations were tried to later adopt the best one, and those were total spectral area normalization, and standard normal variate (SNV) normalization. First one is clear, whereas SNV normalization represents a spectral normalization tool that mean centers the spectra and then divide each mean-centered intensity with its standard deviation [32]:

$$I_{\text{new}} = \frac{I_{\text{old}} - I_{\text{mean}}}{\sigma} \quad (1)$$

where I_{new} is the new intensity, I_{old} is the intensity that is being mean centered, I_{mean} is the mean intensity and σ is standard deviation of intensities. Besides these two, MinMax data scaling was also tried. MinMax scaling represents procedure where for each feature, we scale the values according to the formula below, so we have feature values between zero and one:

$$I_{\text{scaled}} = \frac{I - I_{\text{min}}}{I_{\text{max}} - I_{\text{min}}} \quad (2)$$

Proceeding further, we detected and ejected outliers with the help of Isolation Forest algorithm implemented in sci-kit learn. After the outliers have been removed, we fitted Random Forest regressor with aim to find features that give the most contribution to the final result. To achieve this, we actually trained four random forest models, one for each element, to have features that contribute to the each element prediction separately. Feature importances were calculated within random forest algorithm by usage of Gini importance. The higher the value, the more valuable this feature is to the final prediction.

3.2 Hyperparameters tuning and model selection

To find the optimal parameters of the model, we performed GridSearch cross-validation. This validation technique takes the given model parameters and initializes the model of interest with these parameters, splits provided dataset into training and test datasets, fits the model and reports the accuracy of the model through R^2 coefficient. This procedure is done five times in a row for each set of model parameters, where, at the end, for each model algorithm reports the best performance and with which parameters they were obtained. Used metrics to assess the predictive performance of the models were coefficient of determination R^2 and root-mean-square error (RMSE). With optimal parameters

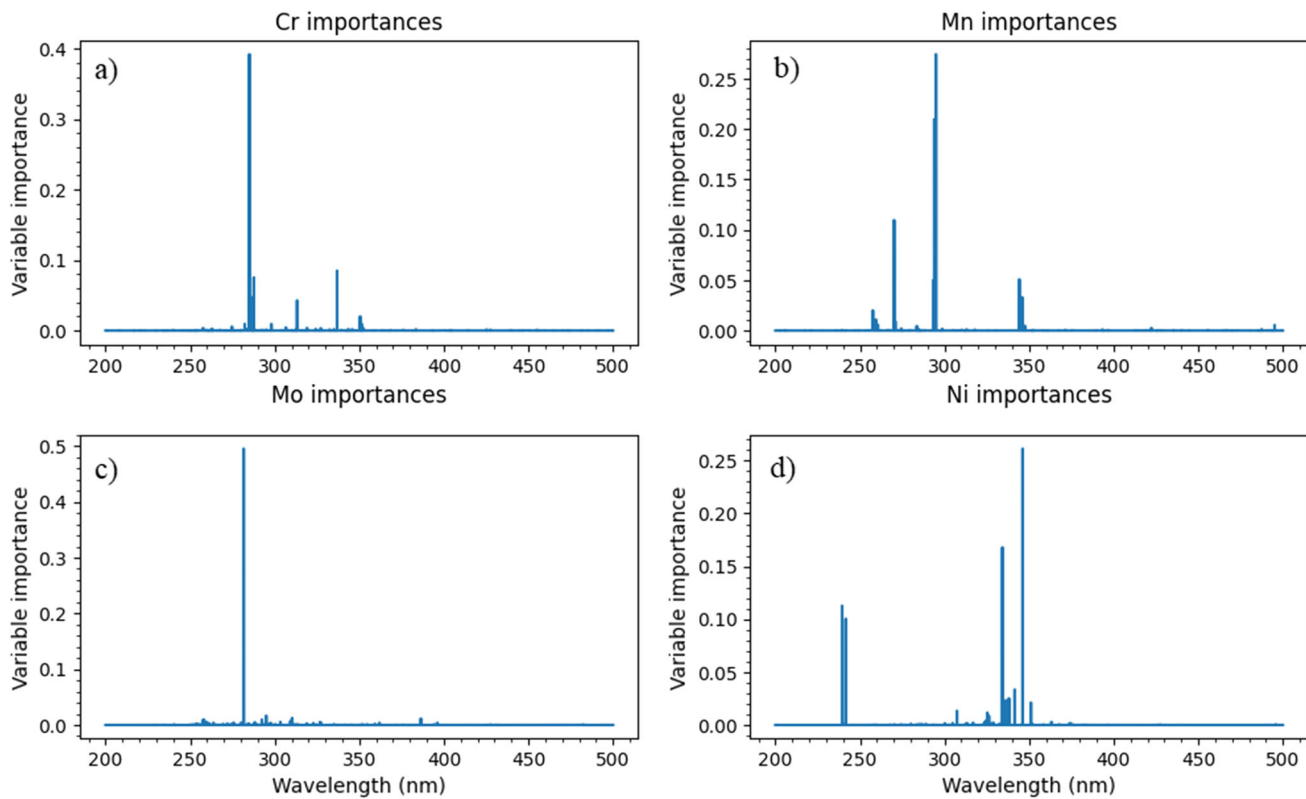


Fig. 3 Results for feature importance analysis for Cr and Mn (**a, b**) and Mo and Ni (**c, d**)

found, we proceeded to final model training and finally the prediction of steel samples composition.

4 Results

The results of feature importance analysis is given in Fig. 3. It is evident that the algorithm successfully recognized and selected persistent line of Mo II at 281.61 nm (see Fig. 3c)). Also in Fig. 3d), lines of Ni II at 239.45 nm and 241.6 nm were successfully identified. Great importance was also given for Cr II lines around 285, 286, 287, 313 nm, as well as to Cr II line at 336 nm (see Fig. 3a)). Unimportant features have value of zero or close to zero, so the condition threshold was set to 10^{-4} , 2×10^{-4} and 5×10^{-4} , while the best results were obtained for threshold 2×10^{-4} . Hence, the final dimensionality of dataset used to train the final model is given in Table 2.

In GridSearch cross-validation, parameters for random forest that were supplied to the algorithm were number of estimators (number of trees in forest) which was changed from 200 to 350 in the step of 50, and maximal depth of the individual tree which was varied from none to 4. None here means that the tree is going to expand until all leaves are pure. In the case of linear regression, the only parameter that could be changed is L^2 norm penalization coefficient α , and we have chosen the values of 0.5, 0.8 and 1. For DNN, considered

architectures were ones with one, two and three hidden layers [(100), (100, 100) and (100, 150, 50)]. Numbers in parentheses represent number of neurons in each hidden layer. Activation function was ReLU (Rectified Linear Unit). Best results reported for all models were ones with MinMax scaling. For RF, best results were the ones where number of trees was equal to 350 and maximum depth that was set to none. Best results with linear regression were reached for the α parameter equal to 0.8. Finally, for DNN, architecture with three hidden layers showed best performance. After dimensionality reduction via Gini importance, resulting dataset was divided into training and test datasets, keeping 20% of the data for testing. Validation of the models was done by using R^2 metrics and RMSE, and it is given in Table 3.

With model training finished, judging by the R^2 score, best overall performance is showed by deep neural network. The prediction precision for each element goes above 0.9, whereas the predicted values in the case of RF are little less. Results for linear regression are not given, since they are significantly worse than these, thus they were omitted. Prediction on recorded test dataset was done with RF as well as with DNN, and the predicted results are summed in Fig. 4. From Fig. 4a–d, it can be seen that DNN showed good performance on all elements, while the predictions made using RF are quite good for the case of Cr, Mn and Ni, but it showed bad overall performance regarding the prediction of Mo, see Fig. 4d. There was no difference when we tried to

Table 2 Dimensionality and number of samples in training dataset used for model training

Element	Number features	Number of samples
Cr	273	1608
Mn	129	1608
Mo	317	1608
Ni	120	1608

All useful information is contained in these selected features

predict Mo concentration with all features, where unimportant features were not removed.

5 Conclusion and future development

In this paper, the prediction of austenitic steel alloy samples was done using the random forest algorithm and deep neural network. Data preprocessing consisted of applying MinMax scaler on the raw data, followed by outliers removal with isolation forest algorithm. Feature

selection was performed by Gini importance criterion within random forest algorithm. It successfully isolated most important features, thus enabling the dimensionality reduction while keeping all the necessary information. This was preceded by final training of three models: random forest, linear regression with L^2 norm and deep neural network. Random forest and neural network showed better predictive power than linear regression; hence, they were used as selected models for prediction of the steel alloy composition. Trained random forest model showed good predictive power for

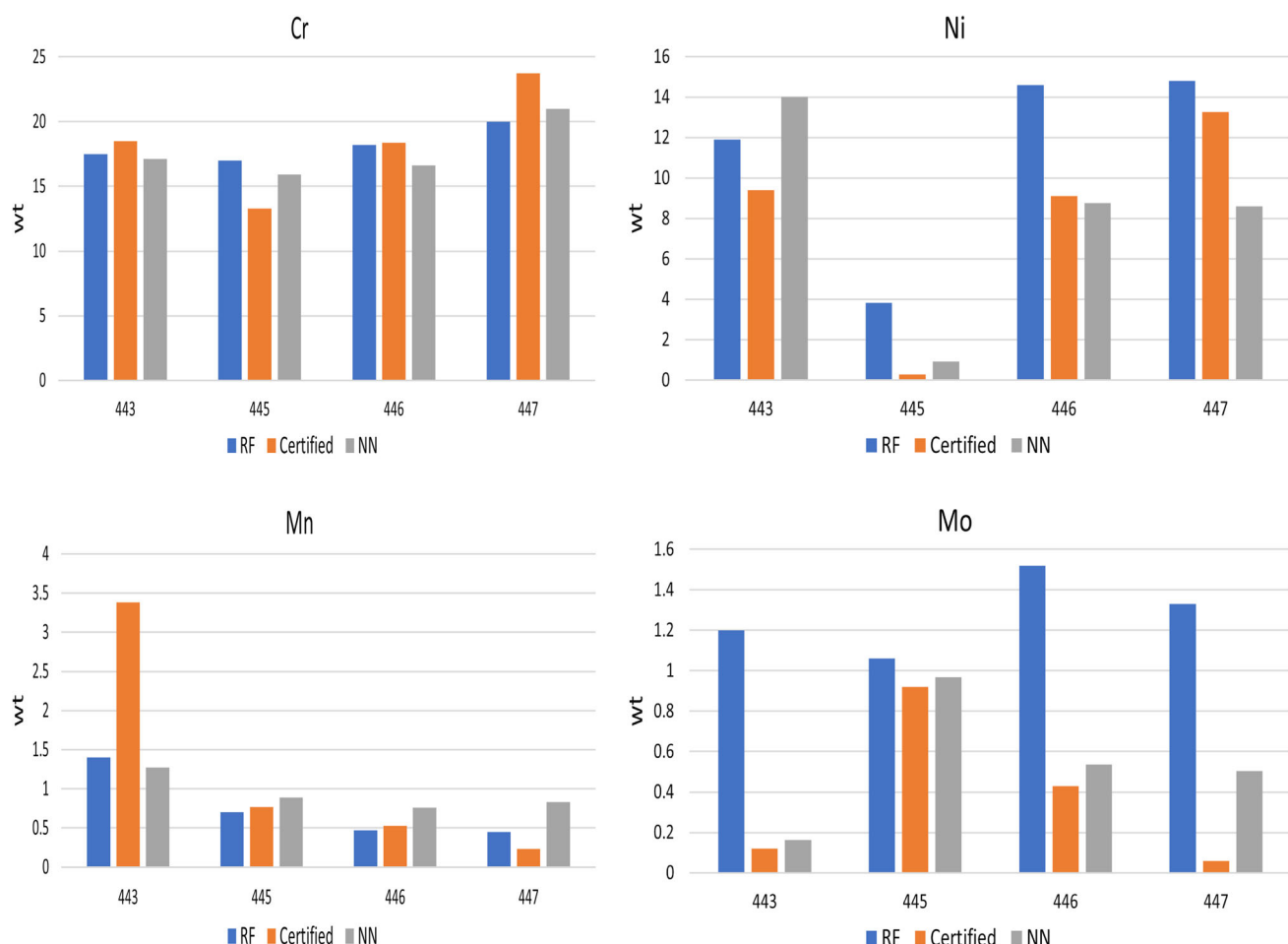


Fig. 4 RFR and DNN predicted results (denoted with RF and NN on the figure) and comparison with certified values. Numbers on x-axis denote the steel sample number given in Table 1. The figure indicates that the models learned and yielded good results in the case of Cr (a), Mn (c) and Ni (b), but on the other hand, RFR had rather poor performance in the case of Mo (d)

Table 3 R^2 and RMSE values for validation dataset

Element	R_{RFR}^2	R_{DNN}^2	RMSE_{RF}	RMSE_{NN}
Cr	0.88	0.97	3.68	1.84
Mn	0.89	0.93	0.397	0.313
Mo	0.85	0.96	0.511	0.263
Ni	0.97	0.98	1.77	1.21

Cr, Ni and Mn, but rather poor performance in the case of Mo. On the other hand, neural network showed good overall predictive power. Nevertheless, random forest algorithm, combined with the data preprocessing techniques, shows a good potential for application in austenitic steel alloy composition prediction, which was also confirmed by results from other authors. For future work, we tend to write a better feature extraction software that should improve the feature selection and hence the predictive power of a used regressor. Also, good overall results are obtained, although the training and test datasets were not intensity corrected. This work shows how useful it can be, to build a unique steel dataset for later usage by different authors, as they not need to every time record their own datasets. These results can be further improved, if one performs calibration transfer, as these spectra were recorded on different instruments. Here, this was not performed as we have not had any identical standard that was used on primary instrument.

Acknowledgements The research was funded by the Ministry of Science, Technological Development and Innovations of the Republic of Serbia, Contract Numbers: 451-03-68/2022-14/200024 and 451-03-68/2022-14/200146, and supported by the Science Fund of the Republic Serbia, Grant No. 3108/2021—NOVA2LIBS4fusion. Also we want to acknowledge the work of our technical associate Stanko Milanović for valuable assistance during the experimental setup. Finally, we want also to thank prof. Jelena Savović for providing us the test samples used in this work.

Author contributions

IT involved in methodology, software and original draft writing; MI involved in conceptualization, supervision and original draft editing.

Data Availability Statement This manuscript has associated data in a data repository. [Authors' comment: As we recorded the spectra of only four steel standard samples, we are of the opinion that scientific community will not have much use of this data, hence it is decided not to deposit it.]

Declarations

Conflict of interest Hereby, we want to state that these results should not be in any case compared to ones obtained by various authors at the LIBS 2022 conference benchmark-

ing competition, where this training dataset was first used. Best results from that competition will be published separately in special issue of Spectrochimica Acta B, and results from this paper have nothing to do with that competition. This paper was an extension of the work presented at SPIG 2022 conference.

References

1. R.J. Konings, R.E. Stoller (eds.), *Comprehensive Nuclear Materials* (Elsevier, Amsterdam, 2020)
2. N. Inoue, A. Komori, H. Hayashi, H. Yonezu, M. Iima, R. Sakamoto, Y. Kubota, A. Sagara, K. Akaishi, N. Noda, N. Ohyabu, O. Motojima, Design and construction of the LHD plasma vacuum vessel. Fus. Eng. Des. **41**(1), 331–336 (1998). [https://doi.org/10.1016/S0920-3796\(98\)00248-8](https://doi.org/10.1016/S0920-3796(98)00248-8)
3. V. Alimov, M. Yajima, S. Masuzaki, M. Tokitani, Analysis of mixed-material layers deposited on the toroidal array probes during the FY 2012 LHD plasma campaign. Fus. Eng. Des. **147**, 111228 (2019). <https://doi.org/10.1016/j.fusengdes.2019.06.001>
4. D.C.L.J. Radziemski, *Spectrochemical analysis using laser plasma excitation*, edited by D.C.L.J. Radziemski (Marcel Dekker Inc, New York, 1989)
5. E. Tognoni, G. Cristoforetti, S. Legnaioli, V. Palleschi, Calibration-free laser-induced breakdown spectroscopy: state of the art. Spectrochim. Acta Part B At. Spectrosc. **65**(1), 1–14 (2010). <https://doi.org/10.1016/j.sab.2009.11.006>
6. C.A.M. Ramirez, M. Greenop, L. Ashton, I. ur Rehman, Applications of machine learning in spectroscopy. Appl. Spectrosc. Rev **56**(810), 733–763 (2021). <https://doi.org/10.1080/05704928.2020.1859525>
7. N.M. Ralbovsky, I.K. Lednev, Towards development of a novel universal medical diagnostic method: Raman spectroscopy and machine learning. Chem. Soc. Rev. **49**, 7428–7453 (2020). <https://doi.org/10.1039/D0CS01019G>
8. W. Fu, W.S. Hopkins, Applying machine learning to vibrational spectroscopy. J. Phys. Chem. A **122**, 167–171 (2017). <https://doi.org/10.1021/acs.jpca.7b10303>
9. H. Park, J.-H. Son, Machine learning techniques for THz imaging and time-domain spectroscopy. Sensors (2021). <https://doi.org/10.3390/s21041186>
10. M. Koubiti, M. Kerebel, Application of deep learning to spectroscopic features of the Balmer-Alpha line for hydrogen isotopic ratio determination in tokamaks. Appl. Sci. (2022). <https://doi.org/10.3390/app12199891>
11. T. Chen, T. Zhang, H. Li, Applications of laser-induced breakdown spectroscopy (LIBS) combined with machine

- learning in geochemical and environmental resources exploration. *Trends Anal. Chem.* **133**, 116113 (2020). <https://doi.org/10.1016/j.trac.2020.116113>
- 12. C. Sun, Y. Tilan, L. Gao et al., Machine learning allows calibration models to predict trace element concentration in soils with generalized LIBS spectra. *Sci. Rep.* **9**, 11363 (2019). <https://doi.org/10.1038/s41598-019-47751-y>
 - 13. X. Zhang, F. Zhang, H.-T. Kung, P. Shi, A. Yushan-jiang, S. Zhu, Estimation of the Fe and Cu contents of the surface water in the Ebinur lake basin based on LIBS and a machine learning algorithm. *Int. J. Environ. Res. Public Health* (2018). <https://doi.org/10.3390/ijerph15112390>
 - 14. L. Sheng, T. Zhang, G. Niu, K. Wang, H. Tang, Y. Duan, H. Li, Classification of iron ores by laser-induced breakdown spectroscopy (LIBS) combined with random forest (RF). *J. Anal. At. Spectrom.* **30**, 453–458 (2015). <https://doi.org/10.1039/C4JA00352G>
 - 15. Y. Tian, Q. Chen, Y. Lin, Y. Lu, Y. Li, H. Lin, Quantitative determination of phosphorus in seafood using laser-induced breakdown spectroscopy combined with machine learning. *Spectrochim. Acta Part B At. Spectrosc.* **175**, 106027 (2021). <https://doi.org/10.1016/j.sab.2020.106027>
 - 16. M.S. Babu, T. Imai, R. Sarathi, Classification of aged epoxy micro-nanocomposites through PCA- and ANN-adopted LIBS analysis. *IEEE Trans. Plasma Sci.* **49**(3), 1088–1096 (2021). <https://doi.org/10.1109/TPS.2021.3061410>
 - 17. X. Cui, Q. Wang, Y. Zhao et al., Laser-induced breakdown spectroscopy (LIBS) for classification of wood species integrated with artificial neural network (ANN). *Appl. Phys. B* **125**, 12556 (2019). <https://doi.org/10.1007/s00340-019-7166-3>
 - 18. R. Junjuri, M.K. Gundawar, A low-cost LIBS detection system combined with chemometrics for rapid identification of plastic waste. *Waste Manag.* **117**, 48–57 (2020). <https://doi.org/10.1016/j.wasman.2020.07.046>
 - 19. L.-N. Li, X.-F. Liu, F. Yang, W.-M. Xu, J.-Y. Wang, R. Shu, A review of artificial neural network based chemometrics applied in laser-induced breakdown spectroscopy analysis. *Spectrochim. Acta Part B At. Spectrosc.* **180**, 106183 (2021). <https://doi.org/10.1016/j.sab.2021.106183>
 - 20. F. Poggialini, B. Campanella, S. Legnaioli, S. Pagnotta, S. Raneri, V. Palleschi, Improvement of the performances of a commercial hand-held laser-induced breakdown spectroscopy instrument for steel analysis using multiple artificial neural networks. *Rev. Sci. Instrum.* **91**(7), 073111 (2020). <https://doi.org/10.1063/5.0012669>
 - 21. H. Tang, T. Zhang, X. Yang, H. Li, Classification of different types of slag samples by laser-induced breakdown spectroscopy (LIBS) coupled with random forest based on variable importance (VIRF). *J. Anal. At. Spectrom.* **32**, 2194–2199 (2017). <https://doi.org/10.1039/C7JA00231A>
 - 22. F. Ruan, J. Qi, C. Yan, H. Tang, T. Zhang, H. Li, Quantitative detection of harmful elements in alloy steel by LIBS technique and sequential backward selection-random forest (SBS-RF). *Anal. Methods* **7**, 9171–9176 (2015). <https://doi.org/10.1039/C5AY02208H>
 - 23. J. Liang, M. Li, Y. Du, C. Yan, Y. Zhang, T. Zhang, X. Zheng, H. Li, Data fusion of laser induced breakdown spectroscopy (LIBS) and infrared spectroscopy (IR) coupled with random forest (RF) for the classification and discrimination of compound *Salvia miltiorrhiza*. *Chemom. Intell. Lab. Syst.* **207**, 104179 (2020). <https://doi.org/10.1016/j.chemolab.2020.104179>
 - 24. G. Yang et al., The basicity analysis of sintered ore using laser-induced breakdown spectroscopy (LIBS) combined with random forest regression (RFR). *Anal. Methods* **9**, 5365–5370 (2017). <https://doi.org/10.1039/C7AY01389B>
 - 25. L. Breiman, Random forests. *Mach. Learn.* **45**, 5–32 (2001). <https://doi.org/10.1023/A:1010933404324>
 - 26. T. Zhang et al., A novel approach for the quantitative analysis of multiple elements in steel based on laser-induced breakdown spectroscopy (LIBS) and random forest regression (RFR). *J. Anal. At. Spectrom.* **29**, 2323 (2014). <https://doi.org/10.1039/c4ja00217b>
 - 27. Y. Zhang, C. Sun, L. Gao, Z. Yue, S. Shabbir, W. Xu, M. Wu, J. Yu, Determination of minor metal elements in steel using laser-induced breakdown spectroscopy combined with machine learning algorithms. *Spectrochim. Acta Part B At. Spectrosc.* **166**, 105802 (2020). <https://doi.org/10.1016/j.sab.2020.105802>
 - 28. K. Liu et al., Quantitative analysis of toxic elements in polypropylene (PP) via laser-induced breakdown spectroscopy (LIBS) coupled with random forest regression based on variable importance (VI-RFR). *Anal. Methods* **11**, 4769 (2019). <https://doi.org/10.1039/c9ay01796h>
 - 29. K. Wei, Q. Wang, G. Teng, X. Xu, Z. Zhao, G. Chen, Application of laser-induced breakdown spectroscopy combined with chemometrics for identification of penicillin manufacturers. *Appl. Sci.* (2022). <https://doi.org/10.3390/app12104981>
 - 30. X. Jin, G. Yang, X. Sun, D. Qu, S. Li, G. Chen, C. Li, D. Tian, L. Yao, Discrimination of rocks by laser-induced breakdown spectroscopy combined with random forest (RF). *J. Anal. At. Spectrom.* **38**, 243–252 (2023). <https://doi.org/10.1039/D2JA00290F>
 - 31. E. Kepes. (2022) LIBS 2022 quantification contest. https://figshare.com/projects/LIBS2022_Quantification_Contest/142250
 - 32. T.W. Randolph, Scale-based normalization of spectral data. *Cancer Biomark.* **2**, 135–144 (2006). <https://doi.org/10.3233/CBM-2006-23-405>

Springer Nature or its licensor (e.g. a society or other partner) holds exclusive rights to this article under a publishing agreement with the author(s) or other rightsholder(s); author self-archiving of the accepted manuscript version of this article is solely governed by the terms of such publishing agreement and applicable law.

The usage of perceptron, feed and deep feed forward artificial neural networks on the spectroscopy data: astrophysical & fusion plasmas

N.M. Sakan^{ID}, I. Traparić, V.A. Srećković^{ID} and M. Ivković

Institute of Physics Belgrade, University of Belgrade, Pregrevica 118, 11080 Belgrade, Serbia (E-mail: nsakan@ipb.ac.rs)

Received: July 28, 2022; Accepted: October 1, 2022

Abstract. Artificial neural networks are gaining a momentum for solving complex problems in all sorts of data analysis and classification matters. As such, idea of determining their usability on complex plasma came up. The choice for the input data for the analysis is a set of stellar spectral data. It consists of complex composition plasma under vast variety of conditions, dependent on type of star, measured with calibrated standardized procedures and equipment. The results of the analysis has shown that even a simple type of perceptron artificial neural network could lead to results of acceptable quality for the analysis of spectra of complex composition. The analyzed ANNs performed good on a limited data set. The results can be interpreted as a figure of merit for further development of complex neural networks in various applications e.g. in astrophysical and fusion plasmas.

Key words: Atomic processes–Line: profiles–astrophysical & fusion plasmas

1. Introduction

The usage of machine learning algorithms is a growing field of research (D'Isanto et al., 2016; Baron, 2019; Kates-Harbeck et al., 2019). Since the computer power is constantly growing its usage is often found in a wide variety of applications: from determination of objects on a photograph all the way to expert systems capable to determine adequate states and predicted outcomes of complex systems; from difficult-to-maintain machines states and prediction of conditions, up to the assistance in human health monitoring.

Even the specific fields of spectroscopy rely deeply on artificial neural networks, as is the case for instance with medical spectroscopy application Wang et al. (2015), or for instance agricultural application Basile et al. (2022); Longin et al. (2019). The material recognition in extraterrestrial spectroscopic probing is also a very difficult task, since the limitations of the mass and resolving power of the onboard instruments are a very difficult limiting factor (Koujelev et al., 2010; Bornstein et al., 2005).

Usage of the artificial neural networks (ANN) fell into focus of our interest because of flexibility of their application, as well as a variety of complex problems that they have already solved.

All of the mentioned has been a factor for applying neural networks to the decision process of determining a stellar spectral type as an example of application on astrophysical data (Albert et al., 2020). Artificial neural networks are often used in astrophysics (e.g. for the integral field spectral analysis of galaxies in Hampton et al. 2017). There is an expectation of development of further focus on convolutional neural networks application on spectroscopic data (Castorena et al., 2021). Also, even more complex predictions based on back-propagation in neural networks as well as complex artificial neural networks structures in spectroscopic usage are known (Li et al., 2017). In order to have insight of applicability of the ANN usage we have limited our research on simplest case as a figure of merit.

Few random spectral curves from database Pickles (1998) are presented here in results. Entire database set consists of spectra for 12 types of stars, spectral type O normal; B normal; A normal; F normal; F Metal rich; F metal weak; G normal; G Metal rich; G metal weak; K normal; K Metal rich; K metal weak; and M normal. Our aim was to create test case as a method of determining a quality of specific ANN in various machine learning analysis, from stellar and fusion spectra analysis, material analysis, up to extremely specific cases as enhancing a low resolution instrument performance for specific applications (Marinković et al., 2019; Albert et al., 2020).

2. ANN basics and principles

The usage of systems related to the functions of neural networks has been in focus of investigation since mid-1940 McCulloch & Pitts (1943), but the real usage has evolved with the application of modern day digital computers, which enabled construction of networks of enlarged complexity. One of the simplest neural networks, that could be seen more as a test case of validity of operation of artificial intelligence systems, is perceptron (Rosenblatt, 1958). The prediction as well as sensitivity of the training data set is in favor of more complex networks. It is the primary goal of our investigation, along with their application on spectral data sets and measurements.

The choice for the dataset was made on open access data files for the 131 stellar spectra published by Pickles (1998) (available at accompanying reference appended to the bibliographical entry, as seen in May 2022). The results are promising and further research on the field is expected. The quality of the trained artificial neural network prediction is related to the data set as well as its structure. An effort of applying it on a large scale dataset or database should be carried out.

The problem of finding out a category of data subset is an inherent problem for any sort of machine learning and as such for the artificial neural networks also. The artificial neural network is a system of mathematical functions trying to resemble a simplified animal brain. The network consists of artificial neurons.

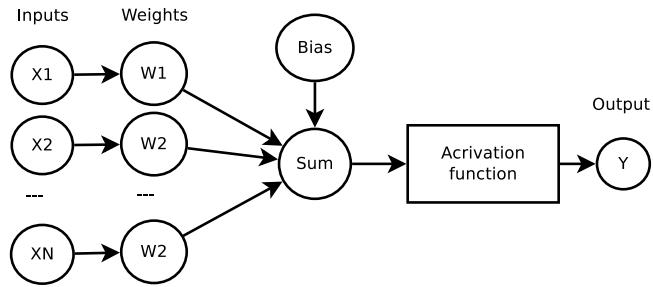


Figure 1. The concept of a neuron. Schematic presentation.

A neuron is described as a function that adopts output value based on its input values and bias value by the means of reaction function. The simplest neuron concept could be seen on a Figure 1. The neuron determines its output state as an output of activation function based on a weighted sum of input values and a bias value itself, and could be described by equation

$$y_{out} = f_{act} \left(Bias + \sum_{i=1}^N x_i w_i \right), \quad (1)$$

where f_{act} is a activation function, x_i and w_i are the i -th input value as well as adequate input weight.

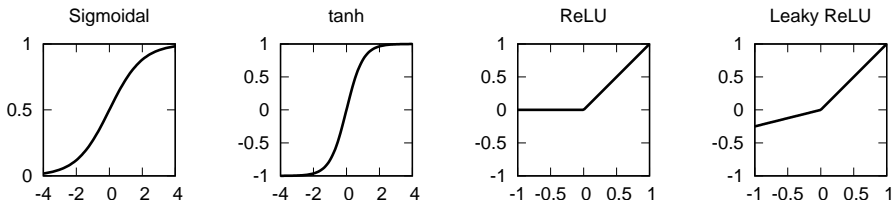


Figure 2. Four most common neuron reaction functions.

The neuron reaction on external stimulus is strongly dependent on its reaction function. In order to determine the neuron behavior on a micro scale, the reaction function as well as the method of adopting the weight values plays a determining role. Four most common reaction functions are shown on Figure 2.

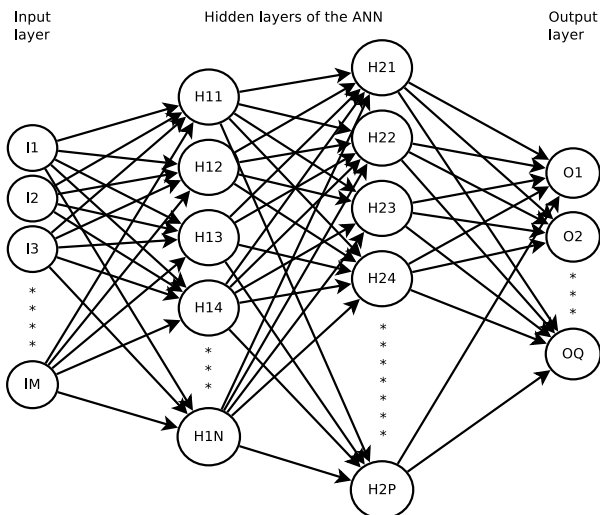


Figure 3. Concept of ANN of perceptron, feed forward and deep feed forward. The shown ANN consist of M input neurons, two hidden layers of N and P neurons and output layer of Q neurons.

A topology of the neural network as well as the learning method are determining the global reaction of the neural network. For the goal of usability analysis the simplest ANN topologies, perceptron, is chosen. The Feed Forward and Deep Feed Forward topologies are based upon fully connected dense layers of neurons, see Figure 3. The two specific layers, input and output, have the dimensionality of the input data and output states consequently and are the only limiting factors of the network. When there is more than one hidden layer, the neural network is considered to be the deep one.

3. Results and discussion

In Figure 4 several random spectral curves from database Pickles (1998) are presented. Entire dataset consists of spectra for 12 types of stars, spectral type O normal; B normal; A normal; F normal; F Metal rich; F metal weak; G normal; G Metal rich; G metal weak; K normal; K Metal rich; K metal weak; and M normal. Each epoch of the dataset was divided into 70% for training set and 30% for the test set.

As a test bench for the application of the ANN to the selection set of perceptron, Feed Forward and Deep Feed Forward networks are used. As a reaction function ReLU (rectified linear unit) was used, and the input data was normalized to unit using standardization

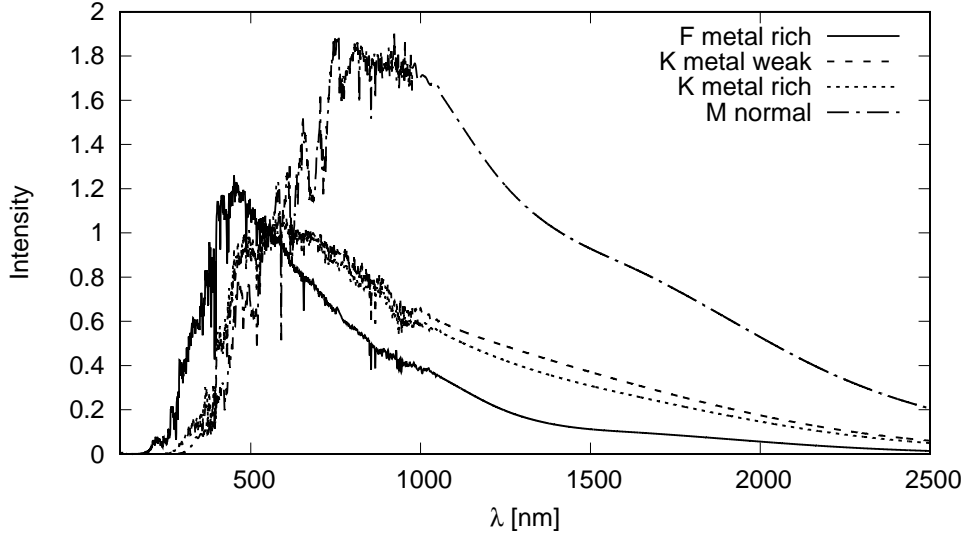


Figure 4. Several sample spectra. Spectra i.e. data is taken from [Pickles \(1998\)](#).

$$x' = \frac{x - \mu}{\sigma}, \quad \hat{\mu} = \frac{1}{N} \sum_{i=1}^N x_i, \quad \hat{\sigma} = \sqrt{\frac{1}{N-1} \sum_{i=1}^N (x_i - \hat{\mu})^2}. \quad (2)$$

No additional data preparation was imposed. The investigated neural network topologies were let to train on the set of data for 200 epochs. Input layer consisted of 4771 input values of available data, output layer consisted of 12 types of stars, spectral type O normal; B normal; A normal; F normal; F Metal rich; F metal weak; G normal; G Metal rich; G metal weak; K normal; K Metal rich; K metal weak; and M normal. The hidden layers consisted of 5000 neurons in first, 1000 in second and 512 neurons in third layer. They were included consequently in order to compare ANN behavior, see Figure 5.

It is obvious, by the analysis of calculated data presented in Figure 5, that the deeper ANNs are capable to learn faster and have better predictions after smaller epochs of learning. This capability is a winning solution in the case of complex spectra. The ANN could fall into pseudo stable states and produce a non-minimal error. Such falls into local minimum state could be avoided by several advanced methods one of which is providing an algorithm for forgetting of the learned state, e.g. algorithm that disturbs a learned state after each application.

Also, there are probably better methods for the input dataset preparation, from pure mathematical procedures up to convolutional ANN (CNN) incorporation. It is proven that, even in its simplest forms, ANN could be used for such

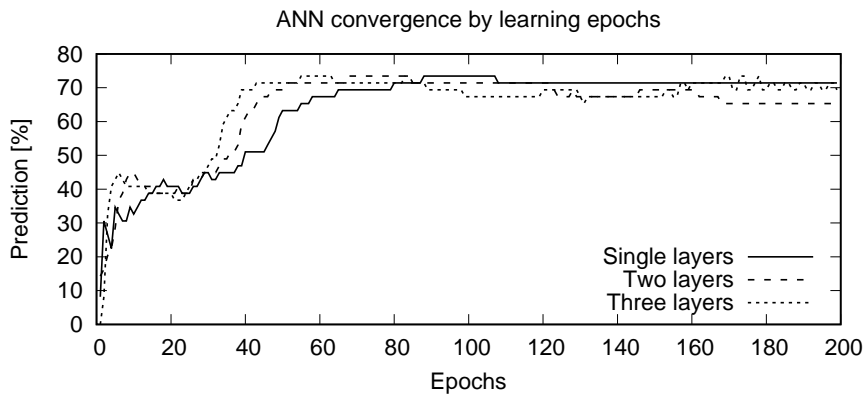


Figure 5. Convergence of ANN of perceptron, feed forward and deep feed forward, on analyzed dataset.

tasks. It is to expect that there are better ANN topologies for such a task, and this is a field for further investigation.

From the above it is obvious that even in its crudest form artificial neural networks are capable to successfully deal with the spectra classification. It is confirmed that this case could be used as a figure of merit for the further development of ANN and machine learning applications in general.

4. Conclusions and future possibilities

The results are promising and the further research on the field is expected. The first goal of analysis of a single set of complex spectral data recorded under similar conditions is achieved with reasonably good prediction. Concerning minute differences in comparison to each other it is considerable result for the basic ANN structure.

Since the quality of the trained artificial neural network prediction is related to its structure as well as the dataset quality and volume, an effort on a large-scale database collection should be carried out. One of the first steps should be inclusion of pre-trained convolutional ANN for the purpose of input data pre-processing before entering of selector ANN.

Commercial packages as well as some specific open-source solutions for the analysis of the spectra with the help of predefined ANN exist. Their application is usually very specific and does not allow the opportunity to fit the best ANN nor to perform unique mathematical procedures during input data preparation that could be best suited for the sought purpose. This possibility is the winning factor in each specific case. Such approach should enable systems for more specialized problem solutions, from stellar and fusion spectra analysis up to more

specific expert systems related to technical solutions. The further development in both ANN structures as well as data preparation should be carried out with the specified problem in mind.

Acknowledgements. The research was funded by the Ministry of Education, Science and Technological Development of the Republic of Serbia, Contract: 451-03-68/2022-14/200024 and supported by the Science Fund of the Republic Serbia, Grant no. 3108/2021.

References

- Albert, D., Antony, B. K., Ba, Y. A., et al., A Decade with VAMDC: Results and Ambitions. 2020, *Atoms*, **8**, 76, DOI: 10.3390/atoms8040076
- Baron, D., Machine Learning in Astronomy: a practical overview. 2019, *arXiv e-prints*, arXiv:1904.07248
- Basile, T., Marsico, A. D., & Perniola, R., Use of Artificial Neural Networks and NIR Spectroscopy for Non-Destructive Grape Texture Prediction. 2022, *Foods*, **11**, DOI: 10.3390/foods11030281
- Bornstein, B., Castano, R., Gilmore, M., Merrill, M., & Greenwood, J., Creation and testing of an artificial neural network based carbonate detector for Mars rovers. 2005, in *2005 IEEE Aerospace Conference*, 378–384
- Castorena, J., Oyen, D., Ollila, A., Legett, C., & Lanza, N., Deep spectral CNN for laser induced breakdown spectroscopy. 2021, *Spectrochimica Acta Part B: Atomic Spectroscopy*, **178**, 106125, DOI: <https://doi.org/10.1016/j.sab.2021.106125>
- D'Isanto, A., Cavuoti, S., Brescia, M., et al., An analysis of feature relevance in the classification of astronomical transients with machine learning methods. 2016, *Monthly Notices of the RAS*, **457**, 3119, DOI: 10.1093/mnras/stw157
- Hampton, E. J., Medling, A. M., Groves, B., et al., Using an artificial neural network to classify multicomponent emission lines with integral field spectroscopy from SAMI and S7. 2017, *Monthly Notices of the Royal Astronomical Society*, **470**, 3395, DOI: 10.1093/mnras/stx1413
- Kates-Harbeck, J., Svyatkovskiy, A., & Tang, W., Predicting disruptive instabilities in controlled fusion plasmas through deep learning. 2019, *Nature*, **568**, 526, DOI: 10.1038/s41586-019-1116-4
- Koujelev, A., Sabsabi, M., Motto-Ros, V., Laville, S., & Lui, S., Laser-induced breakdown spectroscopy with artificial neural network processing for material identification. 2010, *Planetary and Space Science*, **58**, 682, DOI: <https://doi.org/10.1016/j.pss.2009.06.022>, exploring other worlds by exploring our own: The role of terrestrial analogue studies in planetary exploration
- Li, Z., Zhang, X., Mohua, G. A., & Karanassios, V., Artificial Neural Networks (ANNs) for Spectral Interference Correction Using a Large-Size Spectrometer and ANN-Based Deep Learning for a Miniature One. 2017, in *Advanced Applications for Artificial Neural Networks*, ed. A. El-Shahat (Rijeka: IntechOpen)

- Longin, L., Tusek, A. J., Valinger, D., et al., Application of Artificial Neural Networks (ANN)Coupled with Near-InfraRed(NIR) Spectroscopy for Detection of Adulteration in Honey. 2019, *Biodiversity Information Science and Standards*, **3**, e38048, DOI: 10.3897/biss.3.38048
- Marinković, B., Srećković, V., Vujićić, V., et al., BEAMDB and MOLD—Databases at the Serbian Virtual Observatory for Collisional and Radiative Processes. 2019, *Atoms*, **7**, 11, DOI: 10.3390/atoms7010011
- McCulloch, W. S. & Pitts, W., A logical calculus of the ideas immanent in nervous activity. 1943, *The bulletin of mathematical biophysics*, **5**, 115, DOI: 10.1007/BF02478259
- Pickles, A. J., A Stellar Spectral Flux Library: 1150–25000 Å. 1998, *Publications of the ASP*, **110**, 863, DOI: 10.1086/316197
- Rosenblatt, F., The perceptron: A probabilistic model for information storage and organization in the brain. 1958, *Psychological Review*, **65**, 386, DOI: 10.1037/h0042519
- Wang, Q., Zheng, N., Li, Z., & Ma, Z., Quantitative analysis of glucose in whole blood using FT-Raman spectroscopy and artificial neural network. 2015, in *Proceedings of the 2015 International Conference on Computational Science and Engineering* (Atlantis Press), 471–475

New perspectives in the analysis of Stark width regularities and systematic trends

Z. Majlinger^{1,2,3} and I. Traparić⁴ 

¹ *Astronomical Observatory, Volgina 7, 11060 Belgrade, Serbia*

² *ES “I. G. Kovačić”, Kralja Tomislava 18, 51326 Vrbovsko, Croatia*

³ *ES “V. Gortan”, Prilaz Vladimira Gortana 2, 51000 Rijeka, Croatia*

⁴ *Institute of Physics Belgrade, Pregrevica 118, 11080, Belgrade, Serbia*

(E-mail: traparic@ipb.ac.rs)

Received: September 29, 2023; Accepted: October 20, 2023

Abstract. Regularities and systematic trends among the sample of Stark widths obtained by using modified semiempirical method from the STARK-B database were analysed. Two different approaches are independently used – multiple regression method combined with simple cluster analysis, and random forest (RF) machine learning algorithm. Predicted values of Stark widths calculated with estimate formulae obtained from multiple regression method, and those values predicted by using RF algorithm, were compared with already known corresponding experimental Stark widths published elsewhere. Results of this analysis indicate that both of these methods can mostly predict new Stark width values within the acceptable range of accuracy.

Key words: line profile — Stark broadening — atomic data — machine learning

1. Introduction

Stark broadening theory plays the important role in investigation of high temperature dense plasma, where the collisional processes between the charged particles contribute significantly to the spectral line broadening. From technological perspective, Stark widths and shifts of spectral lines in the spectra of neutral atoms and ions are of interest for a number of problems - for example, analysis and modelling of laboratory, laser produced, fusion or technological plasmas, accurate spectroscopic diagnostics and modelling, etc. Applications of Stark broadening theory are also various in research of astrophysical plasma as well - for example, for interpretation, synthesis and analysis of stellar spectral lines, determination of chemical abundances of elements from equivalent widths of absorption lines, opacity calculations, estimation of the radiative transfer through the stellar atmospheres and subphotospheric layers, radiative acceleration considerations, nucleosynthesis research, etc.

Calculation of Stark broadening parameters sometimes can be difficult, and it can take a time, especially if quantum theory is applied. If conditions to apply less accurate but faster quasistatic, unified, semiempirical or semiclassical methods are not satisfied, quick and simple estimates could become important, especially if we do not need a great accuracy, or there is no time for more complicated and more accurate calculations, or if we have a great number of Stark broadening parameters to calculate in very small period of time. This is very common case, for example, if astrophysical spectra are investigated. According to (Wiese, Konjević, 1982), regularities and systematic trends (RST) can be found among the Stark widths of atomic spectral lines, which can simplify the way of obtaining these estimates. This is especially significant when some atomic data, necessary to perform more accurate Stark broadening methods of calculations, are missing. For example, the lack of atomic data, such as energy levels or transition probabilities is usually noticed in the spectral data for rare-earth elements. Analysis based on RST is mostly the only way to determine Stark widths and shifts in sometimes very complex spectra of these elements, which become more and more important in spectral investigations of hot stars of spectral type A and B, and white dwarfs (Popović, Dimitrijević, 1998).

In this investigation, we focused on searching systematic trends among great amount of Stark widths from STARK-B database (Sahal-Bréchot et al., 2014b, 2015), obtained by modified semiempirical (MSE) method (Dimitrijević, Konjević, 1981) as a continuation of our previous work on determination of unknown MSE Stark widths and studying of RST among the MSE Stark broadening parameters (see, for example, Majlinger et al., 2015, 2017a,b, 2020a). Two different methods are used to analyse the sample – classical statistical regression method, which has already been used many times in previous investigations of regularities and systematic trends, and random forest (RF) algorithm from a group of machine learning methods, which become very popular methods more often used in these days whenever some classification or non-linear regression is needed to be performed. Unlikely to previous analyses of RST, here some new atomic parameters, which have not taken into consideration before, are included. We will shortly explain both of these methods and finally discuss and compare the obtained results.

2. Methods

2.1. Simple cluster and multiple regression analysis

Estimates of Stark widths can be divided into three main groups:

- approximations derived from the theory – e.g., Cowley's formula (Cowley, 1971) or MSE formula (Dimitrijević, Konjević, 1987)
- formulae based on statistical analysis on a large number of existing Stark widths (see e.g. Purić, Šćepanović, 1999; Purić et al., 1978).

- formulae based on systematic trends noticed without statistical analysis on corresponding examples ([Wiese, Konjević, 1982](#)).

Whether it is one type or another, the formula for estimating Stark widths for lines of multiple ionized atoms usually can be expressed as a non-linear function of atomic and plasma parameters:

$$\omega_E = f(\lambda, N_e, T, Z, E_{ion}, E_{upper}, E_{lower}) \quad (1)$$

Sometimes some of these parameters are included in the estimate implicitly, through the effective ionization potential χ_j for level j :

$$\chi_j = E_{ion} - E_j, \quad j = \text{upper, lower} \quad (2)$$

according to Purić, or effective principal quantum number of the upper (n_+) or lower (n_-) level, which has already been used, for example, in MSE theory of Dimitrijević and Konjević ([Dimitrijević, Konjević, 1981](#)):

$$n_+^2 = \frac{Z^2 E_H}{\chi_{upper}} \quad (3)$$

$$n_-^2 = \frac{Z^2 E_H}{\chi_{lower}} \quad (4)$$

Here $Z - 1$ is the charge of the ion, ω_E is the estimated Stark width in Å, λ is the wavelength in Å, N_e is the perturber density in cm^{-3} , E_H is the energy of the hydrogen atom (or Rydberg constant), E_{ion} is the ionization energy, and E_j is the energy of upper or lower levels in cm^{-1} ($j = \text{upper, lower}$).

Immediately after the first article on Stark broadening ([Holtsmark, 1919](#)), simple approximate formulas derived from the theory began to appear. Cowley's formula ([Cowley, 1971](#)) is probably the best known among them and it is still commonly used in astrophysics. Cowley (1971) specified three different formulas, one for neutral emitters, one for electrically charged emitters (which humble Cowley contributes to Griem), and one for estimating widths for temperatures close to 10000 K. The authors use different variants of Cowley's formula in addition to the original ones from the article ([Cowley, 1971](#)), and the difference is in the neglect or addition of the lower effective principal quantum number as a number and in the values of the numerical constant in the formula (see e.g. [Killian et al., 1991](#); [Alwadie et al., 2020](#)).

Jagoš Purić made a great effort in studying RST among the Stark width values. The first works on regularities were published by ([Purić, Ćirković, 1973](#)) and ([Purić et al., 1978](#)). Purić and his co-workers found the correlation between Stark width and difference between ionization energy and energy of the upper state (what he called the upper effective ionization potential) and a number of experimental and theoretical values of Stark widths, offering a set of different estimation formulae. In the following decades, a number of papers on this topic were published, where different correlation parameters were stated for different transitions, different charges and different homologous and isoelectronic

sequences (see e.g. Miller et al., 1980; Purić et al., 1978, 1993, 1997, 2008). This statistical research is also supported by some other authors (see e.g. Djeniže, 1999; Djeniže et al., 2001), with occasional attempts to generalize this approach for all different transitions, different elements and different charge values (Purić, Šćepanović, 1999; Scepanovic, Puric, 2013). Comparing the great amount of Stark width data from STARK-B database (Sahal-Bréchot et al., 2014b, 2015), Purić offered so-called “generalized” estimate (Purić, Šćepanović, 1999) which should be used, according to the authors, “to calculate Stark line widths of the multiply charged ion of different elements along the periodic table.” These scientific articles evolve over time, so Purić and co-workers later give up searching for a universal formula for all lines and focus their statistical analysis only on individual homologous or isoelectronic series (Dojčinović et al., 2011, 2012, 2013a,b; Tapalaga et al., 2011, 2018; Jevtić et al., 2012; Trklja et al., 2019b,a). However, the possibility to apply all of these estimates to predict new unknown Stark widths should be furtherly discussed (Majlinger et al., 2017a,b, 2020b).

The final purpose of this research was to find new general estimates accurate enough to approximately predict the unknown values of Stark widths. Our assumption is that these new estimates should be related on existing estimates, e.g. Cowley's from Cowley (1971) and Purić's from Purić and Šćepanović (1999). However, after investigation of accuracy in prediction of unknown Stark widths by using of these two estimates, in the cases of MSE calculated electron-impact widths for Lu III and Zr IV spectral lines, it was obvious that they don't offer enough accurate approximation (Majlinger et al., 2017a, 2020b). At least in the case of Zr IV Stark widths, several possible reasons were suggested to explain this discrepancy (Majlinger et al., 2017b):

- numerical coefficients in estimations are not properly adjusted
- some important parameters are neglected in equation (1) but significantly contribute to the result, and
- temperature functions used in previous estimates could be incorrect

According to statistical analysis of Stark widths calculated for 143 transitions from 26 multiply charged ions of 17 elements using the modified semiempirical method, (for example, most of them are elaborated by (Dimitrijević, Konjević, 1981), and previous assumptions, new estimates of Stark widths were found. After providing simple cluster analysis (Aggarwal, V., 2014) and multiple regression analysis (for example Chatterjee, Simonoff, 2014), we concluded that MSE Stark width sample has to be devided in three separate groups:

1. For a type I of transitions: $nl - nl'$, $L = l$, $L' = l'$ (for example, $2s^1S - 2p^1P^o$, $3s^3S - 3p^3P^o$, $3p^1P^o - 3d^1D$, $4s^3S - 4p^3P^o$, etc), proper estimate is Cowley-like:

$$\omega_{E1} = 3.438 \cdot 10^{-24} N_e \lambda^2 \frac{n_+^4 + n_-^4}{Z^2(2l_> - 1)^{-\frac{3}{4}}} f(T) \quad (5)$$

2. For a type II of transitions: $nl-n'l'$, $L = l$, $L' = l'$ (for example, $2p^3P^o-3s^3S$, $4p^2P^o-5d^2D$, $4d^2D-5f^2F^o$, $4d^2D-6f^2F^o$, etc), proper estimate is Purić-like:

$$\omega_{E2} = 0.808 \cdot 10^{-25} N_e \lambda^2 \frac{n_+^6 + n_-^6}{Z^2(2l_> - 1)^{-\frac{1}{5}}} f(T) \quad (6)$$

Here $f(T)$ is chosen temperature function (which will be explained later), while $l_> = \max(l_{upper}, l_{lower})$, where l_{upper} and l_{lower} are orbital quantum numbers for upper and lower level respectively.

3. For all other types of these simplest transitions (type III), like $nl-n'l'$, $L \neq l$, $L' \neq l'$ and $nl-n'l'$, $L \neq l$, $L' \neq l'$ (for example, $3s^1P^o-3p^1D$, $3s^4P^o-3p^4P$, $3p^5D^o-3d^5F$, $3d^1F^o-4p^1D$, etc.), a well known general expression, valid also for the first two types, can be used to obtain width for particular lines within a multiplet from an average width as a whole:

$$\omega_{E3} = \left(\frac{\lambda_{E3}}{\lambda_0} \right)^2 \omega_0 \quad (7)$$

where ω_{E3} and ω_0 are estimates of unknown Stark widths and a Stark width obtained with estimates (5) or (6), while λ_{E3} and λ_0 are corresponding wavelengths respectively.

After optimizing the number of parameters in these estimates according to minimum description length properties (see, for example, Grünwald, 2004), and keeping in mind that all models are uncertain, idealizing reality (Wit et al., 2012) and that sample is not equal to population, we rounded exponents in (5) and (6) on the closest integer or rational number, to avoid physically meaningless results (for example, $\lambda^{1.74}$ is replaced with λ^2 , $Z^{1.95}$ with Z^2 , etc.) and to approach enough to probable statistical model ideally concerning about population.

From interpolation of analysed data, new temperature function is suggested:

$$f(T) = \frac{1 - \beta}{\sqrt{T}} + \beta \frac{\ln T}{\sqrt{T}} \quad (8)$$

where β is the linear function of temperature defined as:

$$\beta = AT + B \quad (9)$$

Numerical constants A and B are estimated to be $A = 9.62 \cdot 10^{-7}$ and $B = -4.167 \cdot 10^{-2}$ from the values of lower temperature limit for all considered Stark widths. Lower temperature limit for most of considered Stark widths lies in a range 15000 – 70000 K which corresponds to range of distance between perturbing and perturbed levels used in all considered Stark width calculations around cca 7500 – 38500 cm⁻¹. It is easy to see that relation $0 \leq \beta \leq 1$ is mostly valid for such choice of A and B, and that temperature function approximately

simulates both lower and upper temperature limit conditions when β reach to its limits, which is in a good agreement with some previous analyses of behavior of Stark width values for highest and lowest value of temperature (for example [Sahal-Bréchot et al., 2014a](#)).

Correlation between new estimates of full Stark width at half maximum (FWHM) obtained by using relations (5), (6) and (7), and existing MSE values for transition type I, type II and type III with corresponding regression lines are displayed in Figs. 1-3 respectively. To calculate correlation parameters for each estimate, we used the general symbol ω_{EST} instead of ω_{E1} , ω_{E2} , and ω_{E3} . Correlation coefficients corresponding to each estimate WEST are presented in Table 1. In the most idealistic scenario, for log-log regression equation $\log \omega_{EST} = C_1 + C_2 \log \omega_{MSE}$, should be valid $C_1 = 0$, $C_2 = 1$ and therefore $\omega_{EST} = \omega_{MSE}$. As the additional attempt to confirm a validation of this method, predicted Stark widths with estimates from above are compared with corresponding experimental values from references ([Konjević et al., 1984, 2002](#)). Result of this comparison is presented in Fig. 4.

Table 1. Correlation parameters for log-log regression equation $\log \omega_{EST} = C_1 + C_2 \log \omega_{MSE}$, between results of estimates (5), (6) and (7) respectively, and MSE values of FWHM Stark widths from analysed sample.

Transition type	C_1	C_2	$ErrC_1$	$ErrC_2$	St. dev.	R_{corr}
I	-1.45E-5	0.9126	0.0325	0.0336	0.13	97.76
II	-.28E-5	1.0266	0.0473	0.0262	0.19	99.32
III	-0.0334	0.84	0.025	0.029	0.064	97.23

2.2. Machine learning methods and RF algorithm

As machine learning represents a very popular tool for different types of problems encountered in science, here it was applied on the study of regularities of Stark broadening. Machine learning model based on Random Forest algorithm was developed and described in detail in reference ([Tapalaga et al., 2022](#)), so here it would be briefly described for the sake of completeness. Before developing the model, we needed to develop and create a database for training and testing of the future models. This database was created as a combination of two databases, namely NIST atomic database ([Kramida et al., 2022](#)), from which we took atomic parameters of interest for every transition and Stark B database ([Sahal-Bréchot et al., 2015](#)) from which we took Stark width and plasma parameters for each calculated width. After the completion of this database, it contained around 53 000 lines. Features selected for this research were: Plasma electron density, electron temperature, atomic number, charge of the emitter, energies of both upper and lower levels, total angular momentum of both upper and lower levels, principal and orbital quantum numbers for initial and final of corresponding transitions.

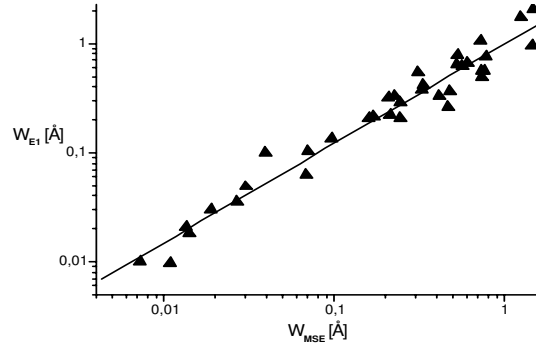


Figure 1. Log-log correlation between FWHM Stark width values obtained by using estimates from multiple regression analysis (ω_{E1}) and MSE values (ω_{MSE}), with corresponding regression line.

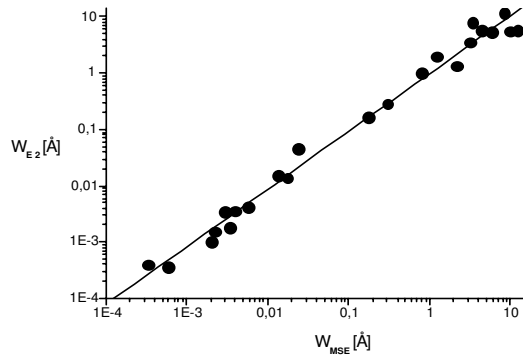


Figure 2. Log-log correlation between FWHM Stark width values obtained by using estimates from multiple regression analysis (ω_{E2}) and MSE values (ω_{MSE}), with corresponding regression line.

Additionally, ionization energy and quantity called upper level effective potential after (Purić, Šćepanović, 1999) were taken into a set of input parameters, which provides a label data comparison. Data outliers were removed as data having higher energy of lower level than upper level. Finally, the analysis was constrained to the following plasma parameters: $N \leq 10^{17} \text{ cm}^{-3}$, $T_e \leq 150\,000 \text{ K}$ and $E_{upper} \leq 500 \text{ eV}$. This restriction left us with around 32 000 available transitions for further analysis. To choose the best model and corresponding parameters, GridSearchCV (Grid Search Cross Validation) technique was applied. Here for every set of model parameters, model is trained and tested on

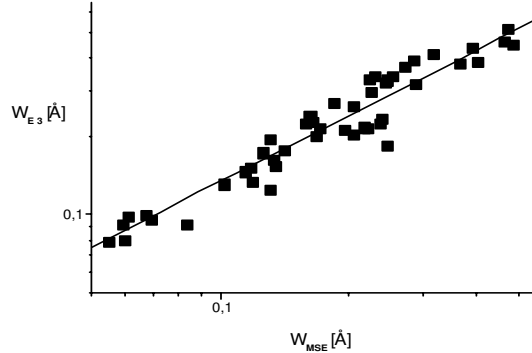


Figure 3. Log-log correlation between FWHM Stark width values obtained by using estimates from multiple regression analysis (ω_{E3}) and MSE values (ω_{MSE}), with corresponding regression line.

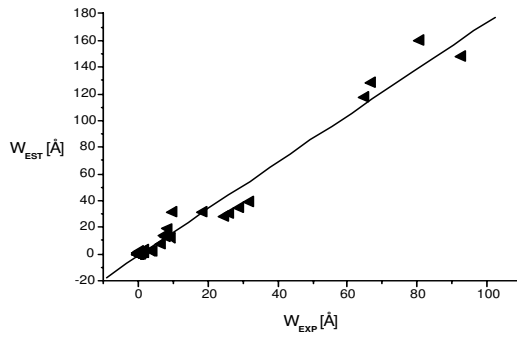


Figure 4. Linear correlation between FWHM Stark width values obtained by using estimates from multiple regression analysis (ω_{EST}) and corresponding experimental values (ω_{EXP}), with corresponding regression line.

given dataset, and best performance is reported. Along with best performance, algorithm reports with which parameters has been obtained. Three models were tested: Decission Tree, Random Forest and Gradient Boosting Regressor. Performances of the model are reported in table 2.

It can be seen that the best results were obtained with Random Forest for the following parameters: maximal depth of the tree equal to 10, minimal samples at one leaf set to 3 and number of estimators equal to 200. As in the case of multiple regression method, Stark widths predicted with using RF algorithm were compared with corresponding experimental widths from the same refer-

Table 2. Comparison of performances for three learning machine models used in analysis.

Model	Parameters	R^2 score
Decision tree	max_depth = 5	0.9
	max_depth = 10	
Random Forest	min_samples_leaf = 3	0.97
	n_estimators = 200	
Gradient Boosting Regressor	max_depth = 10	
	min_samples_leaf = 2	0.96
	n_estimators = 200	

ences as before (Konjević et al., 1984, 2002). Results of this comparison are shown in Fig. 5 and Fig. 6. As we can see on figure 5, RF model preforms well, except of few points that are estimated badly. Also, from the figure 6 it can be concluded that RF method performs better in visible part than in the ultra violet or infrared part of the spectrum.

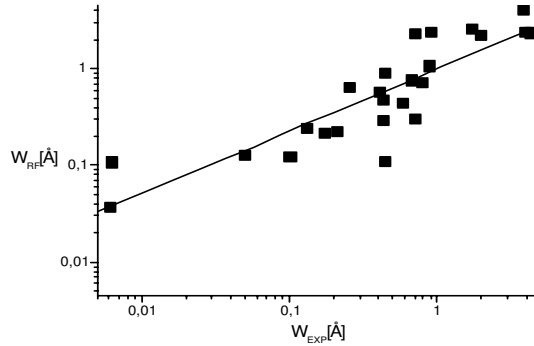


Figure 5. Log-log correlation between FWHM Stark width values obtained by using RF algorithm (ω_{RF}) and corresponding experimental values (ω_{EXP}), with corresponding regression line.

To improve the model and to test whether we could reduce the number of features in the dataset while keeping the accuracy of the model, permutation importance test was performed. This method permutes each feature randomly within dataset, and calculate the decrease in performance of the already trained model. Greater the decrease, more important is the feature. Results of this analysis are given in table 3.

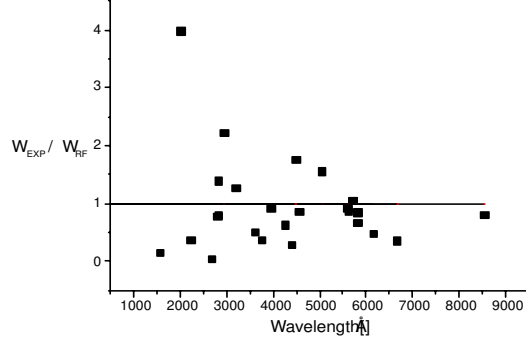


Figure 6. Dependence of ratio between experimental FWHM Stark widths (w_{EXP}) and corresponding values obtained by using RF algorithm (w_{RF}) on wavelength of spectral lines for which Stark widths are calculated.

Table 3. Feature importance test results for RF model.

Feature	Importance score
Electron density N_e	5.9 ± 0.2
Upper - level principal quantum number n_i	3.50 ± 0.12
Charge of emitter q	1.04 ± 0.04
Upper-level effective potential χ	0.37 ± 0.04
Emitter Z	0.31 ± 0.03
Upper-level orbital quantum number l_i	0.19 ± 0.02
Energy of upper level E_{upper}	0.11 ± 0.02
Lower-level principal quantum number n_f	0.11 ± 0.01
Energy of lower level E_{lower}	0.048 ± 0.005
Lower-level orbital quantum number l_f	0.029 ± 0.004
Lower-level total angular momentum quantum number J_{upper}	0.029 ± 0.007
Upper-level total angular momentum quantum number J_{lower}	0.021 ± 0.005
T_e	0.017 ± 0.003
E_i	0.002 ± 0.001

Results in table 3 indicate that electron density is most important feature as expected, while other important features are naturally emitter, its charge, principal and orbital quantum numbers of upper level and upper-level effective potential χ . Other parameters were removed from analysis, as upper level is included in definition of χ , and model was retrained. As expected, model gave very similar results as those reported in this work, which just confirms that model didn't got confused with some redundant data in initial run.

3. Discussion

For Type I, ratios between estimates and MSE values vary between 0.5 and 2.6, for type II between 0.4 and 1.7, and for type III between 0.7 and 2.0. so we can say that accuracy of our estimates according to MSE values are mostly between -50% and $+160\%$. Including predicted accuracy of MSE results, which is $\pm 50\%$, we expect that global accuracy of our estimates, according to statistical sample we used, should lie between $\pm 50\%$ and $\pm 100\%$ e.g. comparable with the old Griem's semiempirical theory (Griem, 1968).

Despite of several exceptions, ratio between most of new calculated estimates and corresponding experimental Stark widths from references (Konjević et al., 1984, 2002), lies between 0.2 and 2 (see Tab. 3), which leads to conclusion that our estimates are usually accurate in a range of $\pm 100\%$, in accordance with our expectations. On the other hand, average value of this ratio for comparison of estimates with experimental Stark widths is 1.38 ± 0.11 , resulting with accuracy in a range between $\pm 30\%$ and $\pm 50\%$, which is even better than theoretically predicted accuracy for modified semiempirical theory by Dimitrijević and Konjević (1981).

Ratios between Stark widths predicted by using RF algorithm and corresponding experimental Stark widths taken from the same references mentioned above (Konjević et al., 1984, 2002), with the exception of two extreme values 0.06 and 4, lie between 0.16 and 2.23, but average ratio of these values is 0.96 ± 0.16 , leading to an accuracy of around $\pm 20\%$, which is much better than accuracy of predicted results obtained by using classical statistical method. To express the accuracy for both methods, as it is usual in statistics, we used arithmetical mean as the average value of analysed data, while the standard deviation is used as a measure of data dispersion. As a final proof that both of presented methods could be valid, in Fig. 7 we presented results obtained from mutual comparison of Stark width values predicted with these two different approaches. Linear regression equation which expresses dependence between Stark widths predicted with RF method ω_{RF} and those predicted by using estimates WEST obtained by using formulae (5), (6) and (7) is found to be $\omega_{RF} = 0.0523 + 1.0563 \omega_{EST}$ with correlation coefficient $R_{CORR} = 91.05\%$. Figure 7 and values of correlation parameters show that both of these two methods are equivalent, e. g. the results of the estimates with RF model and classical multiple regression statistical method are almost the same. Although it is feeded with results obtained by using semiclassical perturbation method (see for example Sahal-Bréchot et al., 2014a), RF algorithm is shown to be a good predictor, despite of a theoretical method used to calculate analysed Stark width data, because it gives results comparable with estimates based on set of calculations obtained by using modified semiempirical method.

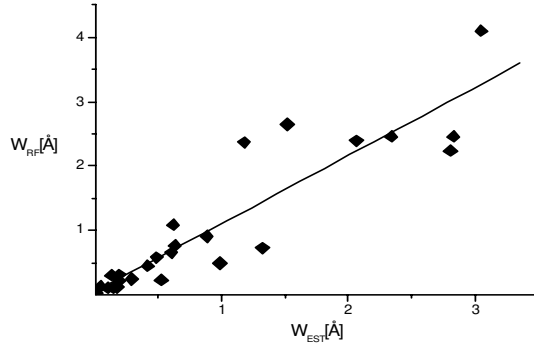


Figure 7. Linear correlation between FWHM Stark width values obtained by using estimates from multiple regression analysis (ω_{EST}) and corresponding values obtained by using RF algorithm (ω_{RF}), with corresponding regression line.

4. Conclusion

Both of the methods used in this study have some advantages and disadvantages. In general, the advantage of ML models is that they are faster and easier to perform with the proper knowledge of computer programming. On the other hand, any of ML algorithms is some kind of black box, e. g. we finally don't know how input and output parameters are connected. If we want to find out the relationship between Stark width values and atomic and plasma parameters presented in a form of simple formula, we have to continue to investigate regularities and systematic trends of Stark widths using the estimates as, for example, were obtained here (equations (5)-(7)). If we don't need to know this connection, using of some ML algorithm is probably the best solution. Results of predictions using RF model show that, if some general estimate really exists, according to previous vision of Jagoš Purić, it should be the function of 14 variables. In this case, number of input atomic and plasma parameters we used before in a group of equations (1) to find systematic trends among the Stark width value, should be enlarged. We proved that, with additional two parameters (upper and lower orbital quantum number) and considering transition type into analysis, strongly affect on result of estimate, as it is assumed, for example, in (Majlinger et al., 2017b).

However, it is very important to stress that the estimates obtained in this work should be valid under the assumption that they can be applied on simple type of spectra, as they have been analysed in this case (for example, where for all transitions in a whole spectrum parent term remains the same). For more complex spectra, these estimates should be improved, or some other methods are welcome to be used. Furthermore, although RF model shows very strong potential to be applied on RST analysis in future, it is tested only in the sample

of Stark broadening parameters related to simple spectra described here, and in the case of Li I spectral lines (Tapalaga et al., 2022), so it should also be confirmed in a greater sample to make us sure that this method can be applied generally in prediction of new Stark widths despite of complexity of a spectrum we investigate. For the application of these methods to study regularities and systematic trends among the Stark broadening parameters of lines in more complex spectra, additional investigations are needed, and development of both of these method are neccessary. Created database used in this and previous study is published online and it is available for use. It can be found on the link <https://github.com/ivantraparic/StarkBroadeningMLApproach>.

Acknowledgements. The research was funded by the Ministry of Science, Technological Development and Inovations of the Republic of Serbia, Contract numbers: 451-03-68/2022-14/200024 and 451-03-68/2022-14/200146. We are very grateful to Milan S. Dimitrijević on useful suggestions and comments during the writing of this paper.

References

- Aggarwal, C., V., R. C. 2014, *Data Clustering* (Taylor and Francis Group)
- Alwadie, N., Almodlej, A., Ben Nessib, N., Dimitrijević, M. 2020, *Contrib. Astron. Obs. Skalnaté Pleso*, **50**, 86
- Chatterjee, S., Simonoff, J. S. 2014, *Handbook of Regression Analysis* (John Wiley and Sons)
- Cowley, C. 1971, *The Observatory*, **91**, 139
- Dimitrijević, M., Konjević, N. 1987, *J. Quant. Spectrosc. Radiat. Transfer*, **20**, 223
- Dimitrijević, M. S., Konjević, N. 1981, *Spectral Line Shapes* (Walter de Gruyter and Co.), 211
- Djeniže, S. 1999, *J. Res. Phys.*, **28**, 231
- Djeniže, S., Srećković, A., Kalezić, S. 2001, *Serb. Astron. J.*, **164**, 21
- Dojčinović, I. P., Tapalaga, I., Purić, J. 2011, *Pub. Astron. Soc. Australia*, **28**, 281
- Dojčinović, I. P., Tapalaga, I., Purić, J. 2012, *Mon. Not. R. Astron. Soc.*, **419**, 904
- Dojčinović, I. P., Tapalaga, I., Purić, J. 2013a, *Bull. Astron. Soc. India*, **41**, 281
- Dojčinović, I. P., Tapalaga, I., Purić, J. 2013b, *Mon. Not. R. Astron. Soc.*, **429**, 2400
- Griem, H. R. 1968, *Phys. Rev.*, **165**, 258
- Grünwald, P. D., A tutorial introduction to the minimum description length principle. 2004, *ArXiv*, **math.ST/0406077**
- Holtsmark, J. 1919, *Annalen der Physik*, **363**, 577
- Jevtić, D., Dojčinović, I. P., Tapalaga, I., Purić, J. 2012, *Bull. Astron. Soc. India*, **40**, 151
- Killian, J., Montenbruck, O., Nissen, P. 1991, *Astron. Astrophys. Suppl.*, **88**, 101

- Konjević, N., Dimitrijević, M. S., Wiese, W. L. 1984, *J. Phys. Chem. Ref. Data*, **13**, 649
- Konjević, N., Lessage, A., Fuhr, J. R., Wiese, W. L. 2002, *J. Phys. Chem. Ref. Data*, **31**, 819
- Kramida, A., Ralchenko, Y., Reader, J., NIST ASD Team. 2022, NIST Atomic Spectra Database (version 5.10), <https://physics.nist.gov/asd>, accessed: September 2023
- Majlinger, Z., Dimitrijević, M. S., Srećković, V. A. 2020a, *Mon. Not. R. Astron. Soc.*, **496**, 5584
- Majlinger, Z., Dimitrijević, M. S., Srećković, V. A. 2020b, *Contrib. Astron. Obs. Skalnaté Pleso*, **50**, 164
- Majlinger, Z., Dimitrijević, M. S., Simić, Z. 2017a, *Atoms*, **5**, 49
- Majlinger, Z., Simić, Z., Dimitrijević, M. S. 2015, *Astron. Astrophys.*, **36**, 671
- Majlinger, Z., Simić, Z., Dimitrijević, M. S. 2017b, *Mon. Not. R. Astron. Soc.*, **470**, 1911
- Miller, M. H., Lessage, A., Purić, J. 1980, *Astrophys. J.*, **239**, 410
- Popović, L. C., Dimitrijević, M. S. 1998, *Contrib. Astron. Obs. Skalnaté Pleso*, **27**, 353
- Purić, J., Dimitrijević, M. S., Lakićević, I. S. 1978, *Physics Letters A*, **67**, 189
- Purić, J., Dojčinović, I. P., Nikolić, M., et al. 2008, *Astrophys. J.*, **680**, 803
- Purić, J., Šćepanović, M. 1999, *Astrophys. J.*, **521**, 490
- Purić, J., Šćepanović, M., Milosavljević, V., Ćuk, M., XXIII ICPIG (Toulouse, France). 1997, V – 48
- Purić, J., Ćirković, L., XI ICPIG. 1973, 398
- Purić, J., Miller, H., Lessage, A. 1993, *Astrophys. J.*, **416**, 825
- Sahal-Bréchot, S., Dimitrijević, M., Ben Nessib, N. 2014a, *Atoms*, **2**, 225
- Sahal-Bréchot, S., Dimitrijević, M. S., Moreau, N. 2015, STARK-B database, <http://stark-b.obspm.fr>, accessed: September 2023
- Sahal-Bréchot, S., Dimitrijević, M. S., Moreau, N., Ben Nessib, N., SF2A Conf. 2014b, 515
- Scepanovic, M., Puric, J. 2013, *Rom. Rep. Phys.*, **65**, 1275
- Tapalaga, I., Dojčinović, I. P., Purić, J. 2011, *Mon. Not. R. Astron. Soc.*, **415**, 503
- Tapalaga, I., Dojčinović, I. P., Purić, J. 2018, *Mon. Not. R. Astron. Soc.*, **474**, 5479
- Tapalaga, I., Traparić, I., Trklja Boca, N., et al. 2022, *Neural Comput. Applic.*, **34**, 6349
- Trklja, N., Dojčinović, I. P., Tapalaga, I., Purić, J. 2019a, *Atoms*, **7**, 99
- Trklja, N., Tapalaga, I., Dojčinović, I. P., Purić, J. 2019b, *New Astron.*, **59**, 54
- Wiese, W., Konjević, N. 1982, *J. Quant. Spectrosc. Radiat. Transfer*, **28**, 185
- Wit, E., van den Heuvel, E., Romeijn, J. 2012, *Statistica Neerlandica*, **66**, 217

UNIVERZITET U BEOGRADU
FIZIČKI FAKULTET



PRIMENA VEŠTAČKE INTELIGENCIJE I
MAŠINSKOG UCENJA U SPEKTROSKOPIJI
PLAZME

Ivan R. Traparić

Doktorska disertacija

Beograd, 2024

UNIVERSITY OF BELGRADE
FACULTY OF PHYSICS



**APPLICATION OF MACHINE LEARNING AND
ARTIFICIAL INTELLIGENCE IN PLASMA
SPECTROSCOPY**

Ivan R. Traparić

Doctoral dissertation

Belgrade, 2024

Mentor:

Doc. dr Marijana Gavrilović Božović,
Fakultet inženjerskih nauka Univerziteta u Kragujevcu

dr Milivoje Ivković,
Naučni savetnik Instituta za fiziku u Beogradu

Komisija za odbranu doktorske disertacije:

Prof. dr Bratislav Obradović,
Fizički fakultet Univerziteta u Beogradu

Prof. dr Ivan Dojčinović,
Fizički fakultet Univerziteta u Beogradu

dr Vladimir Srećković,
naučni savetnik Instituta za fiziku u Beogradu

Datum odbrane: _____

Ova disertacija urađena je u potpunosti u Laboratoriji za spektroskopiji plazme i lasere. Stoga bih se mnogo zahvalio svom mentoru dr Milivoju Ivkoviću za podršku, savete i svom znanju koje je nesebično podelio sa mnom tokom izrade ove teze. Takođe, zahvaljujem se i mentoru doc. dr Marijani Gavrilović Božović na vođenju teze i korisnim sugestijama vezanim za njen konačan izgled i koncepciju.

Mnogo sam zahvalan i kolegama iz laboratorije dr Biljani Stankov, dr Milici Vinić i Stanku Milanoviću na ogromnoj pomoći u eksperimentalnom delu ove teze, te za sve prijateljske razgovore i diskusije koje smo imali.

Veliku zahvalnost dugujem i svojoj porodici, koji su izdržali ovaj put dugačak četiri godine i za svu podršku koju su mi dali i strpljenje koje su imali za mene. Bez toga ne bi bilo ni ovog rada.

Mojoj supruzi Mariji i čerci Lari...

Rezime: U ovoj doktorskoj disertaciji ispitana je mogućnost primene mašinskog učenja i veštačke inteligencije za rešavanje nekih problema u oblasti optičke i ekstremne ultraljuči-časte emisione spektroskopije plazme.

Model slučajne šume, obučen je za modelovanje Stark-ove poluširine emitovane spektralne linije jer se za tu namenu pokazao kao najbolji od svih razmatranih modela. Napravljeni model uspešno je predvideo kvantnu prirodu atomske emisije i regularnosti duž izoelektronskog niza i spektralnih serija neutralnog atoma litijuma. Pokazano je da se ovaj model može koristiti za predviđanje novih Stark-ovih poluširina sa tačnošću od oko 20 %.

Zatim, pokazano je da se u slučaju kvantitativne analize korištenjem spektroskopije laserski indukovanih proba za obučavanje modela mašinskog učenja mogu iskoristiti baze koje nisu snimljene na vlastitoj aparaturi ponavljanjem istih eksperimentalnih uslova. Ovo je značajan rezultat jer dosta laboratorija nema sredstava da priušti dovoljan broj standardnih uzoraka za potrebe ovakvih analiza, i pruža mogućnost standardizacije snimanja ovih baza.

Konačno, primenom varijacionog autoenkodera modelovan je UTA (eng. Unresolved Transition Array) struktura emitovanog spektra volframa u ekstremnoj ultraljubičastoj oblasti spektra za tipične uslove u jezgru plazme heliotrona LHD u Japanu. Model je pokazao zadovoljavajuće poklapanje sa eksperimentalnim merenjima, i tačno predvideo temperaturne zavisnosti oblika emitovanog spektra. Model je pokazao i dodatni napredak u modelovanju, omogućava brzo predviđanje oblika emitovanog spektra za zadate uslove plazme u svega nekoliko stotina milisekundi, za razliku od trenutnih koliziono - radijativnih modela kojima za istu svrhu treba po nekoliko nedelja za račun.

Ključne reči: mašinsko učenje, veštačka inteligencija, fizika plazme, spektroskopija plazme, fuzija, LIBS.

Naučna oblast: Fizika

Uža naučna oblast: Fizika jonizovanog gasa i plazme

UDK broj:

Resume: In this doctoral thesis the possibility of application of machine learning and artificial intelligence for solving of some particular problems connected with plasma optical and extreme ultraviolet emission spectroscopy was investigated.

Random Forest model was trained for prediction of spectral line width due to Stark effect as it showed best performance of all considered models. Created model successfully predicted quantum nature of atomic emission and regularities along isoelectric sequence and spectral series of neutral lithium atom. It was also shown that the model can be used for prediction of new spectral line widths with the uncertainty of around 20 %.

Furthermore, it was shown that databases that weren't recorded inside one's own laboratory can be used for training of machine learning algorithms for the quantitative LIBS analysis by repeating the same experimental conditions. This is significant result, as many laboratories don't have the funds for enough standard samples for this kind of analysis, while at the same time this result provides the opportunity for standardisation of database recording process.

Finally, using the variational autoencoder the UTA (Unresolved Transition Array) structure of tungsten spectra in the extreme ultraviolet part of the spectrum for typical plasma parameters inside the plasma core of heliotron LHD was modeled. Model showed good agreement with experimental measurements, while also correctly modeling the temperature dependence of the shape of the emitted spectra. This model provides the opportunity for quick and accurate generation of new spectra for given plasma parameters in several hundreds of milliseconds, contrary to the developed collisional - radiative models for the same purpose, which need few weeks of computational time for same calculations.

Key words: machine learning, artificial intelligence, plasma physics, plasma spectroscopy, fusion, LIBS.

Scientific field: Physics

Research area: Physics of Ionised Gases and Plasma

UDC number:

Sadržaj

1	Uvod	1
2	Uvod u fiziku plazme i veštačku inteligenciju	4
2.1	Teorijske osnove fizike plazme	4
2.1.1	Kolektivne interakcije u plazmi	4
2.1.2	Sudarni procesi u plazmama	7
2.1.3	Kriterijum važenja plazmenog stanja	9
2.2	Dijagnostika plazme	9
2.2.1	Optička emisiona spektroskopija	9
2.2.1.1	Doppler-ovo širenje spektralne linije	10
2.2.1.2	Stark-ovo širenje spektralnih linija	10
2.2.1.3	Kvazistatičko širenje spektralnih linija	11
2.2.1.4	Sudarna aproksimacija	14
2.2.1.5	Semiklasična perturbaciona aproksimacija (SCP)	16
2.2.1.6	Regularnosti Stark-ovog širenja spektralnih linija	17
2.2.2	EUV spektroskopija plazme	18
2.3	Laserski indukovana plazma	19
2.3.1	Proces formiranja laserski indukovane plazme	20
2.3.2	Tipične vrednosti parametara laserski indukovanih plazmi	22
2.3.3	Spektroskopija laserski indukovanoog proboga (LIBS) kao analitička metoda	23
2.4	Visokotemperaturne plazme (fuzione plazme)	25
2.4.1	Načini konfiniranja visokotemperaturne plazme	27
2.4.2	Interakcija plazme sa zidom reaktora	32
2.4.2.1	Fizičko spaterovanje	32
2.4.2.2	Hemijsko spaterovanje	33
2.4.2.3	Termalno isparavanje	34
2.4.2.4	Pojava balončića (Blistering)	34
2.4.3	Problem akumulacije nečistoća sa velikim atomskim brojem Z	34
2.5	Mašinsko učenje i veštačka inteligencija	36
2.5.1	Ansamblerski nelinearni modeli	36
2.5.1.1	Prosta agregacija (<i>Bootstrap aggregation ili Bagging</i>)	37
2.5.1.2	CART (Classification and Regression Trees) algoritmi	37
2.5.1.3	Slučajna šuma	39
2.5.2	Neuronske mreže	39
2.5.2.1	Potpuno povezane neuronske mreže	39
2.5.2.2	Konvolucione neuronske mreže	42
2.5.3	Autoenkoderi	44
2.5.4	Varijacioni autoenkoder	45
2.5.5	Prevencija preprilagođavanja modela veštačke inteligencije	46
2.5.5.1	Regularizacija	46
2.5.5.2	Rano zaustavljanje	49

3 Primena mašinskog učenja za određivanje Stark-ovih poluširina linija	50
3.1 Pravljenje baze za obučavanje modela	50
3.2 Predpriprema podataka i izbor najboljeg modela	51
3.3 Analiza regularnosti Stark-ovog efekta za spektralne serije Li I	53
3.4 Procena važnosti atributa	56
3.5 Poređenje predikcija modela slučajne šume sa eksperimentalnim podacima	58
4 Primena mašinskog učenja u LIBS kvantitativnoj analizi	63
4.1 Opis eksperimenta	64
4.2 Predpriprema podataka	65
4.3 Rezultati	67
5 Primena veštačke inteligencije za modelovanje EUV spektra volframa	70
5.1 Opis eksperimenta	71
5.1.1 Thomson-ovo rasejanje	72
5.1.2 Tracer-Encapsulated Solid Pellet (TESPEL) sistem za ubacivanje čestica u plazmu	72
5.1.3 Soft X-Ray Multichannel Spectrometer (SOXMOS) EUV spektrometar	73
5.2 Predpriprema podataka za obučavanje modela	74
5.3 Pravljenje modela	75
5.4 Rezultati	79
6 Zaključak	84

1 Uvod

U ovom poglavlju dat je kratki uvod u mašinsko učenje i veštačku inteligenciju, te mogućnosti koje oni pružaju u savremenoj nauci. Nakon uvodnog dela, izložena su osnovna postignuća ove teze i data objašnjenja metoda veštačke inteligencije primenjenih u spektroskopiji plazme. U završnom delu poglavlja i dati su pregled strukture i organizacija teze.

Mašinsko učenje i veštačka inteligencija se odavno primenjuju u nauci, a ovde će biti navedene samo neke od primena i mogućnosti koje oni pružaju. Na primer, algoritmi veštačke inteligencije se uspešno koriste u molekularnoj biologiji za sekvenciranje DNA [1], ili u farmaciji gde se pomoću veštačke inteligencije otkrivaju novi lekovi [2]. Algoritmi veštačke inteligencije i mašinskog učenja našli su primenu u skoro svim granama fizike. U astrofizici se koristi za jako bitan zadatak klasifikacije zvdežda [3–5], koji omogućava dalje precizno izučavanje ovih objekata; u fizici čvrstog stanja veštačka inteligencija i mašinsko učenje se koriste u cilju predviđanja osobina novih materijala [6–8]; u kvantnoj mehanici, mogu se koristiti za rešavanje problema više tela [9, 10], pa i za pravljenje novih kvantnih eksperimenata [11, 12]. Veštačka inteligencija uspešno je primenjena i na računanje i modelovanje laserskog ubrzavanja jona [13], a često se koristi i u različitim vrstama spektroskopije: u kombinaciji sa Ramanovom spektroskopijom za identifikaciju različitih virusnih i bakteriološka oboljenja, klasifikaciju tumora itd [14]; u teraherznoj spektroskopiji u svrhu karakterizacije raznih bioloških uzoraka [15], kao i za određivanje izotopskog odnosa u divertoru tokamaka [16]. U spektroskopiji laserski indukovanih plazmi se najčešće koristi kao alat za kvantitativnu analizu [17, 18], ali ima dosta primene i klasifikacionih algoritama [19, 20]. U analizi visokotemperaturnih plazmi (ili obično fuzionih plazmi) veštačka inteligencija je primenjena za predviđanje upadnog topotnog fluksa na divertor tokamaka [21], kao i za predviđanje profila temperature i gustine elektrona [22]. Piccione i saradnici su u svom radu [23] koristili mašinsko učenje kako bi predvideli ravnotežne parametre fuzione plazme, dok su Li i saradnici [24] koristili neuronske mreže u kombinaciji sa fluidnim modelima kako bi predvidili dominantan tip turbulencije i transportne parametre. Dakle, uočljiv je jedan bogat spektar primena veštačke inteligencije u raznim oblastima fizike, unutar koje i ova teza treba da ostvari svoj doprinos.

Ova doktorska disertacija u potpunosti je urađena u laboratoriji za spektroskopiju plazme i lasere u Institutu za fiziku u Beogradu. Laboratorija ima višedecenijsku tradiciju u oblasti spektroskopije niskotemperaturnih plazmi i naširoko je poznata po merenju Stark-ovih parametara spektralnih linija emitovanih iz najrazličitijih izvora plazme za gustine elektrona u opsegu $10^{14} – 10^{18} \text{ cm}^{-3}$. Zbog svega ovoga, u svetu je poznata i kao deo Beogradske škole spektroskopije [25, 26]. Imajući u vidu dokazanu ekspertizu u polju emisione spektroskopije, i globalni trend primene novih metodologija veštačke inteligencije i mašinskog učenja u najrazličitijim oblastima nauke, oni su u ovoj tezi primenjeni kao poslednji alat tehnologije na analiziranje i obradu spektralnih linija emitovanih iz različitih vrsta plazme.

Različiti pravci istraživanja u laboratoriji za spektroskopiju plazme i lasere su umnogoči usmeravali i pravac istraživanja ove teze, koja posledično ima tri veće celine. Za sva tri dela ili celine je zajedničko da predstavljaju primenu novih tehnologija veštačke inteligencije i mašinskog učenja na dobro poznate oblasti spektroskopije plazme. Prvi deo teze bavi se primenom modela mašinskog učenja u cilju određivanja širine emitovane spektralne linije na

polovini njene visine¹. U tu svrhu napravljena je specijalna baza za trening modela mašinskog učenja nastala spajanjem Stark B i NIST baze atomskih podataka. U prvoj bazi sadržane su izračunate poluširine emitovanih spektralnih linija za razne jonske i neutralne emitere dobijene po semiklasičnoj perturbativnoj teoriji Sachal - Brechaut i Dimitrijevića [27, 28] i parametri plazme za koje je data poluširina izračunata. NIST baza atomskih parametara upotrebljena je kako bismo za svaku izračunatu poluširinu spektralne linije u Stark B bazi, našli atomske parametre od interesa za dati prelaz. Dobijena baza podataka korištena je za trening različitih modela mašinskog učenja. Trenirani model potom je iskorišten za analizu regularnosti Stark-ovog efekta duž spektralnih serija neutralnog litijuma, te su date predikcije poluširina linije usled Stark-ovog efekta za neke emiterе. Pored ovoga, ispitana je i eksperimentalno uočena regularnost Stark-ovog efekta za nanelekrisanje emitera, tj. regularnosti duž izoelektronskog niza. Na kraju, predikcije modela su upoređene sa eksperimentalno merenim poluširinama kako bi se proverila pouzdanost modela prilikom predikcije još neizračunatih Stark-ovih parametara.

Laboratorija za spektroskopiju plazme i lasere je dugo godina bila i centar razvoja lasera i laserskih sistema. Uporedo sa razvojem lasera, isti su korišteni i za stvaranje i spektroskopsko ispitivanje laserski indukovanih plazmi, kao prirodan spoj dve aktivnosti u kojima je laboratorija dala i daje veliki doprinos. U skladu sa ovim pravcem istraživanja, drugi deo teze fokusira se na primenu algoritama veštačke inteligencije za analizu spektra emitovanog iz plazme nastale interakcijom laserskog zračenja sa metom od čelika u cilju određivanja procenzualnog sastava elemenata. Po prvi put u ovoj tezi testirana je mogućnost da se obučavanja modela na već snimljenoj bazi podataka, pri čemu se u drugoj laboratoriji snimaju samo test spektri. Uobičajena praksa jeste da se napravi baza podataka od velikog broja standardnih uzoraka (tipično 50 uzoraka) čiji se spektri snime sa dostpunom aparaturom pod strogo kontrolisanim i reproducibilnim eksperimentalnim uslovima. Ovaj postupak je spor i naporan, te zahteva veliku koncentraciju eksperimentatora. Dodatno, većini laboratorija najčešće nije ni dostupan ovoliki broj standardnih uzoraka, a ni njihova cena nije zanemarljiva, te bi dokaz mogućnosti primene ovde predloženog pristupa bio značajan uspeh i pomak u oblasti. Baza za trening bila je ona snimljena za potrebe *benchmarking* takmičenja na konferenciji LIBS 2022 koja je javno dostupna online. U laboratoriji su snimljeni samo spektri trenutno dostupnih test uzoraka standarda i analizirana je uspešnost modela prilikom predikcije koncentracije nepoznatih uzoraka.

Treći deo ove teze je u tesnoj vezi sa trenutnim pravacem razvoja laboratorije, koja se u poslednje vreme bavi istraživanjima koja su relevantna za nuklearnu fuziju. Kako je krajem 2019. godine uspostavljena saradnja između Nacionalnog instituta za fuziona istraživanja (NIFS) u Japanu i Univerziteta u Beogradu, to je dalo priliku da se laboratorija dodatno približi ovoj tematiki. Treći deo ove teze bavi se primenom veštačke inteligencije za potrebe generisanja spektra volframa u ekstremno ultraljubičastoj oblasti, a u svrhu analize zračenja emitovanog iz plazme u heliontronu LHD u Japanu. Glavna ideja iza generisanja spektra jeste poređenje sa razvijenim koliziono - radijativnim modelima, te njihovo dalje usavršavanje za potrebe izučavanja akumulacije nečistoća sa velikim atomskim brojem Z u centru plazme, te ispitivanja transportnih osobina i vremena zadržavanja volframa prilikom ulaska u plazmu. Trenutno upotrebljeni model zasniva se na upotrebi varijacionog enkodera, koji se koristi za

¹još nazivano i poluširina linije, termin koji će se u nastavku ove teze intenzivno koristiti

generisanje nepoznatog spektra za zadatu temperaturu plazme T_e .

Teza je organizovana na sledeći način. U uvodu je dat pregled oblasti primena veštačke inteligencije u nauci generalno, ne samo u fizici, a zatim je u kratkim crtama opisan radni zadatak i ostvareni rezultati svakod og delova teze.

U poglavlju Uvod u fiziku plazme i veštačku inteligenciju uvedeni su osnovni pojmovi bitni za suštinsko razumevanje problematike koja se obrađuje u tezi, počevši od same fizike plazme, zatim metoda za spektroskopsku dijagnostiku primenjenu na različitim vrstama plazme koje su proučavane u tezi, zaključno sa modernim alatima i tehnikama veštačke inteligencije i mašinskog učenja koji su na inovativan način po prvi put upotrebljeni za rešavanje određenih problema objašnjениh u tezi. Pre svega, definisane su glavne veličine i teorijski koncepti koji se koriste u opisivanju i modelovanju plazme, nakon čega je opisana dijagnostika plazme metodom optičke emisione spektroskopije, gde su predstavljene teorije širenja spektralnih linija od značaja za ovu disertaciju (kvazistatička teorija širenja spektralnih linija i semiklasična perturbativna teorija). Dodatno, opisana je i teorija konkavne rešetke i opis rada EUV spektrometra koji je korišten za merenje spektara u trećem delu ove doktorske disertacije. Posle toga, opisana je teorija interakcije nanosekundnog laserskog impulsa sa materijalom i tehnika spektroskopije laserski indukovanih proba. Dalje, dat je kratak uvod u fiziku visokotemperaturnih plazmi, gde su opisani načini konfiniranja visokotemperaturne plazme i glavni procesi prilikom interakcije plazme sa zidom reaktora. Na kraju ovog poglavlja detaljno su opisani algoritmi veštačke inteligencije korišteni prilikom izrade ove teze, što uključuje nelinearne asamblerske modele poput slučajne šume i klasične neuronske mreže, a na kraju kao najnoviji pravac razvoja u veštačkoj inteligenciji, ukratko je objašnjen varijacioni autoenkoder kao jedan od generativnih modela koji se danas široko primenjuje.

U trećem poglavlju predstavljeni su rezultati dobijeni prilikom primene mašinskog učenja na određivanje Stark-ove poluširine emitovane spektralne linije, na izučavanje regularnosti Stark-ovog efekta i poređenje predviđenih i eksperimentalno merenih Stark-ovih poluširina. Detaljno je opisan postupak pravljenja baze za obučavanje, trening i optimizacija modela, kao i sam izbor najboljeg modela.

U četvrtom poglavlju izložena je primena mašinskog učenja u kvantitativnoj LIBS analizi. Prvo je dat opis eksperimenta korištenog za snimanje spektra laserski indukovane plazme. Potom sledi opis predpripreme ulaznih podataka i opis selekcije najbitnijih atributa, te redukcija dimenzionalnosti ulaznog skupa podataka. Dalje, opisani su dobijeni rezultati i dati su predlozi za moguće unapređenje modela.

Potom, u petom poglavlju izloženi su rezultati primene veštačke inteligencije u svrhu generisanja EUV spektra volframa. Poglavlje započinje opisom svih relevantnih sistema koji su korišteni prilikom prikupljanja eksperimentalnih podataka. Tu spadaju SOXMOS spektrometar za merenje u EUV oblasti spektra, TESPEL sistem za ubacivanje peleta sa nečistoćama u plazmu i na kraju sistem za Thomson-ovo rasejanje koji je korišten za merenje temperature elektrona. Zatim sledi opis modela kao i opis procedure predpripreme ulaznih podataka za obučavanje modela, nakon čega su dati ostvareni rezultati u ovom delu istraživanja.

Na kraju, u zaključku ove teze još jednom su predstavljeni svi rezultati dobijeni prilikom izrade ove doktorske disertacije i kako se do njih došlo. Takođe, u ovom delu su opisani u mogući pravci nastavka ovog istraživanja za svaki od tri dela doktorske disertacije.

2 Uvod u fiziku plazme i veštačku inteligenciju

U ovom poglavlju biće prvo izložene osnove teorije plazme koje su od značaja za ovu tezu, a koje se koriste u kasnjem delu rada. Posle teorijskih osnova, pažnja će potom biti usmerena na dijagnostiku plazme putem optičke emisione spektroskopije, te uz to objašnjena teorija širenja spektralnih linija u sudarnoj aproksimaciji, pošto se primenjeni model u ovoj tezi u velikoj meri oslanja na tu aproksimaciju. Posle objašnjenja osnovnih principa dijagnostike plazme spektroskopskim putem, biće objašnjeni osnove interakcije nanosekundnog laserskog impulsa sa materijalom, proces formiranja plazme, te metoda spektroskopije laserski indukovanih proba (eng. LIBS - *Laser Induced Breakdown Spectroscopy*) kao analitička metoda. Zatim će biti reči o visokotemperaturnim plazmama i procesu njihovog konfiniranja u laboratorijskim uslovima, da bi potom bila izložena teorija i osnovni procesi prilikom interakcije plazme sa materijalima zida reaktora. Posebno, biće reči o procesu akumulacije teških čestica u jezgru plazme kao procesu koji će biti analiziran u ovoj tezi. Na kraju, biće objašnjeni svi algoritmi veštačke inteligencije i mašinskog učenja korišteni prilikom izrade ove teze.

2.1 Teorijske osnove fizike plazme

Plazma kao stanje materije predstavlja četvрto agregatno stanje. U prirodi, plazma postoji u galaktičim objektima (zvezde, solarne oluje, korona, jonosfera), a na Zemlji tipičan primer je npr. munja. Munje i laboratorijske plazme (lukovi, fluoroscentne lampe, industrijske plazme za obradu materijala itd.) su uglavnom niskotemperaturne, što znači da je temperatura elektrona reda veličine nekoliko elektron volti, dok su jonske temperature čak niže, reda veličine sobne tempearture [29]. Za galaktičke objekte u stanju plazme, sem zvezda, temperature su reda veličine 1 - 100 eV i te plazme su često potpuno ionizovane. Kod zvezda, u jezgru temperature elektrona dostižu vrednosti od nekoliko keV, pa stoga te plazme zovemo visokotemperaturnim.

2.1.1 Kolektivne interakcije u plazmi

Tri osnovne osobine plazme koje proističu iz elektromagnetičnih kolektivnih interakcija između čestica jesu kvazineutralnost plazme, plazmene oscilacije i ekraniranje. Pod pojmom kvazineutralnosti, podrazumeva se da je ukupna zapreminska gustina nanelektrisanja plazme jednaka nuli. Ovo se može objasniti činjenicom da je svako lokalno nastajanje viška nanelektrisanih čestica usled termalnog kretanja unutar plazme praćeno uspostavljanjem veoma intenzivnih elektrostatičkih polja koja sprečavaju bilo kakvo dalje kretanje nanelektrisanih čestica [30]. Uslov makroskopske elektroneutralnosti plazme je ispunjen samo ako posmatrmo dovoljno velika rastojanja. Ovo se može ilustrovati jednostavnim izračunavanjem potencijala na površini sfere radiusa 1 cm uočenoj unutar plazme koja ima gustinu nanelektrisanih čestica 10^{19} m^{-3} i termalnu energiju kretanja od 6 eV po čestici. Uz pretpostavku da je 0.1 % elektrona napustilo uočenu sfernu zareminu, dobija se [30]:

$$\varphi = \frac{1}{4\pi\epsilon_0} \frac{Q}{R} = \frac{1}{4\pi\epsilon_0} \frac{e(n_i - n_e) \frac{4}{3} R^3 \pi}{R} = \frac{R^2}{3\epsilon_0} e \Delta n = 6000 \text{ V} \quad (1)$$

Dakle, da bi elektroni napustili ovu zapreminu, moraju imati srednju kinetičku energiju od 6 keV, a pri čemu oni imaju samo 6 eV. Međutim, ako bi posmatrana zapremina bila 0.01

mm, svi elektroni bi mogli napustiti uočenu zapreminu i uslov kvazineutralnosti više ne bi važio. Ovaj uslov može se kvantifikovati i drugačije, ukoliko se izračuna rad izvršen od strane elektrona da napuste posmatranu sferu [29]. Zbog sferne simetrije, električno polje preostalih jona mora imati radijalni pravac. Ovo polje, kada svi elektroni napuste sferu ima oblik [29]:

$$E_r = \frac{Q}{4\pi\varepsilon_0 r^2} = \frac{en_i \frac{4}{3}r^3\pi}{4\pi\varepsilon_0 r^2} = \frac{n_i e r}{3\varepsilon_0} \quad (2)$$

Energija elektrostatičkog polja unutar ove sfere je onda [29]:

$$W = \int \frac{\varepsilon_0 E^2}{2} dV = \int_0^{r_{max}} \frac{\epsilon_0 E_r^2}{2} 4\pi r^2 dr = \pi r_{max}^5 \frac{2n_i^2 e^2}{45\varepsilon_0} \quad (3)$$

Ukoliko ovu energiju izjednačimo sa termalnom energijom kretanja elektrona, dobićemo²:

$$\pi r_{max}^5 \frac{2n_e^2 e^2}{45\varepsilon_0} = \frac{3}{2} n_e k T_e \times \frac{4}{3} \pi r_{max}^3 \quad (4)$$

Odakle dobijamo [29]:

$$r_{max}^2 = 45 \frac{\varepsilon_0 k T_e}{n_e e^2} \Rightarrow r_{max} \simeq 7 r_D \quad (5)$$

Ovde je uvedena jedna karakteristična plazmena dužina koja se naziva Debye-ev radius, i data je izrazom:

$$r_D = \sqrt{\frac{\varepsilon_0 k T}{n e^2}} \quad (6)$$

Tako da se konačno može tvrditi da će plazma biti makroskopski elektroneutralna na rastojanjima koja su mnogo veća od Debye-evog radiusa.

Plazmene oscilacije javljaju se kao posledica jakih elektrostatičkih polja prilikom izlaska elektrona iz Debye-eve sfere [30]. Jako elektrostatičko polje koje se tada javlja, zaustavlja elektrone i usmerava ih nazad ka centru sfere gde se nalazi višak pozitivnih nanelektrisanja. Prilikom dolaska na površinu sfere, usled akumulirane kinetičke energije, elektron se neće zaustaviti na površini sfere već će nastaviti da se kreće ka centru. Zbog jakih odbojnih elektrostatičkih sila koje se javljaju usled viška negativnog nanelektrisanja, dolazi do ponovnog izlaska elektrona iz posmatrane sfere, pri čemu nastaju plazmene oscilacije [30]. Plazmene oscilacije elektrona imaju frekvenciju [30]:

$$\omega_e = \sqrt{\frac{e^2 n_e}{m_e \varepsilon_0}} \quad (7)$$

Primećuje se da elektronske plazmene oscilacije zavise samo od gustine elektrona u plazmi i reda su veličine od nekoliko MHz do nekoliko THz. Plazmene oscilacije mogu se definisati za sve vrste čestica prisutnih u plazmi. One predstavljaju brzinu reakcije plazme na promenu sopstvenog električnog mikropolja, a takođe i brzinu reakcije na pobudu spoljašnjim vremenjski promenljivim električnim poljem. Ovako definisana veličina omogućava formulisanje još

²Indeks i zamenjen je indeksom e jer prepostavljamo da su gustine elektrona i jona jednake

jednog uslova važenja kvazineutralnosti plazme. Može se reći da će makroskopska elektroneutralnost biti narušena i na većim rastojanjima od Debye-evog radiusa, ali samo u vremenskom intervalu koji odgovara periodu elektronskih plazmenih oscilacija koji je reda veličine 10^{-9} s. Zbog toga kažemo da uslov elektroneutralnosti ispoljava samo na vremenskim skalamama koje su mnogo veće od perioda plazmenih oscilacija [30].

Konačno, poslednja analizirana osobina plazme kao posledica kolektivnih interakcija u plazmi jeste Debye-evo ekraniranje plazme. Naime, zbog elektrostatičkog privlačenja jona i elektrona, svaki jon u plazmi biva okružen oblakom negativnog nanelektrisanja. Ovaj oblak ne može imati dimenzije veće od Debye-evog radiusa, jer je jedino unutar Debye-eve sfere elektroneutralnost plazme narušena [30]. Da bi se našao oblik potencijala jona okruženog oblakom elektrona, polazi se od pretpostavke da joni imaju uniformnu raspodelu i da postoji mala perturbacija elektronske gustine n_e . Sledeća pretpostavka jeste da su elektroni u termodinamičkoj ravnoteži, pa je njihova koncentracija data sa [31]:

$$n_e = n_0 e^{-\frac{qe\varphi}{kT_e}} = n_0 e^{\frac{e\varphi}{kT_e}} \quad (8)$$

U stanju termodinamičke ravnoteže srednja termalna energija elektrona je mnogo veća od elektrostatičke energije $kT_e \gg e\varphi$, pa možemo pisati [31]:

$$n_0 e^{\frac{e\varphi}{kT_e}} = n_0 (1 + \frac{e\varphi}{kT_e}) \quad (9)$$

Poisson-ova jednačina ima oblik [31]:

$$\nabla^2 \varphi(r) = -\frac{1}{\epsilon_0} e(n_e - n_0) \quad (10)$$

Zbog pretpostavljene sferne simetrije, operator ∇^2 ima oblik $\nabla^2 = \frac{1}{r} \frac{\partial}{\partial r} \left(\frac{\partial}{\partial r} r \right)$ te ubacivanjem (9) u (10) dobija se [31]:

$$\frac{\partial^2}{\partial r^2} \left(r \varphi(r) \right) - \frac{1}{r_D^2} r \varphi(r) = 0 \quad (11)$$

Rešavanjem ove diferencijalne jednačine dobijamo [30]:

$$\varphi(r) = C_1 \frac{e^{-\frac{r}{r_D}}}{r} + C_2 \frac{e^{\frac{r}{r_D}}}{r} \quad (12)$$

Zbog fizičkog smisla konačnog rešenja, odbacuje se drugi član, tj. $C_2 = 0$ jer potencijal ne može eksponencijalno da raste sa udaljavanjem od nanelektrisanе čestice. Konstanta C_1 određuje se tako da pri malim rastojanjima od jona, potencijal ima oblik Coulomb-ovog potencijala, tj za $r \rightarrow 0$ [30]:

$$\varphi(r \rightarrow 0) = \frac{1}{4\pi\epsilon_0 r} \frac{e}{r} \Rightarrow C_1 = \frac{1}{4\pi\epsilon_0} \quad (13)$$

Stoga je konačan oblik ekraniranog potencijala jona:

$$\varphi(r) = \frac{1}{4\pi\epsilon_0} \frac{e^{-\frac{r}{r_D}}}{r} \quad (14)$$

Ovaj rezultat nam govori da svaka nanelektrisana čestica u plazmi može da interguje samo sa drugim nanelektrisanim česticama koje se nalaze unutar Debye-eve sfere opisane oko te čestice, jer su na većim rastojanjima od Debye-vog radiusa, polja nanelektrisanih ekranirana i plazma se smatra makroskopski elektroneutralnom [30].

2.1.2 Sudarni procesi u plazmama

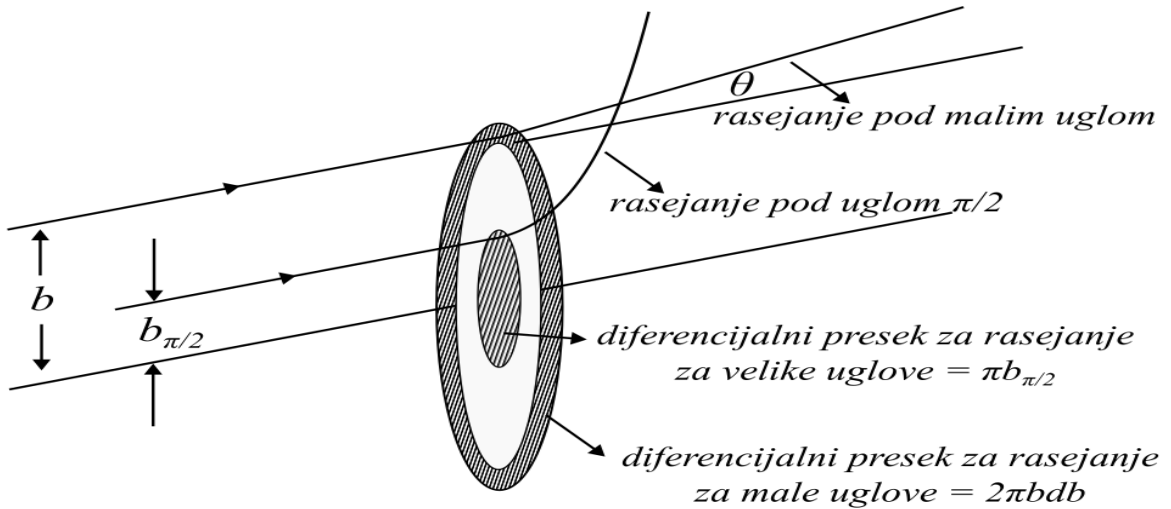
Sudarni procesi u plazmi biće razmatrani samo u binarnoj aproksimaciji. Pod pojmom sudar podrazumeva se rasejanje čestice vrste α na česticama vrste β pod nekim uglom rasejanja θ . Svako rasejanje se definiše veličinom koja se naziva diferencijalni presek za rasejanje. Prema definiciji, diferencijalni presek za rasejanje predstavlja verovatnoću da se čestica vrste α raseje nad česticom vrste β u jedinični prostorni ugao oko pravca određenim uglom θ [30]. Ugao rasejanja θ se u najopštijem slučaju može izračunati pomoću [30]:

$$\theta = \pi - 2 \int_{\rho_{min}}^{+\infty} \frac{b}{\rho^2} \frac{d\rho}{\sqrt{1 - \frac{b^2}{\rho^2} - 2 \frac{U(\rho)}{\mu v_r^2}}} \quad (15)$$

U gornjoj formuli b predstavlja parametar sudara, v_r relativnu brzinu čestice vrste α u odnosu na česticu vrste β , μ predstavlja relativnu masu ovih čestica a $U(\rho)$ prepostavljeni potencijal interakcije ovih čestica. Donja granica integracije ρ_{min} predstavlja najbliže rastojanje do kojeg čestica vrste α prilazi čestici vrste β . Ako prepostavimo da je oblik potencijala dat Coulomb-ovim potencijalom, dolazimo do čuvene Rutherford-ove formule za ugao rasejanja dve nanelektrisane čestice [29]:

$$\tan\left(\frac{\theta}{2}\right) = \frac{q_\alpha q_\beta}{4\pi\epsilon_0 b\mu v_r^2} \quad (16)$$

Moguća rasejanja dve čestice prikazani su na slici 1.



Slika 1: Rasejanje čestice vrste α na čestici vrste β . Moguća rasejanja predstavljaju rasejanja pod malim ugлом, gde je $\theta \ll \frac{\pi}{2}$ i rasejanja pod velikim uglovima gde je $\theta > \frac{\pi}{2}$.

Najčešći tipovi rasejanja u plazmama jesu rasejanja pod malim uglovima. Ako označimo sa $b_{\frac{\pi}{2}}$ parametar sudara za rasejanje pod ugлом od 90 stepeni, dobija se da je [29]:

$$b_{\frac{\pi}{2}} = \frac{q_\alpha q_\beta}{4\pi\epsilon_0 \mu v_r^2} \quad (17)$$

Totalni presek za rasejanje pod velikim uglovima onda predstavlja površinu kruga označenu na slici 1 i dat je sa [29]:

$$\sigma_v = \pi b_{\frac{\pi}{2}}^2 = \pi \left(\frac{q_\alpha q_\beta}{4\pi\epsilon_0\mu v_r^2} \right)^2 \quad (18)$$

Sa druge strane, rasejanja pod malim uglom data su za sve parametre sudara koji su van šrafiranoj krugi, što znači da se oni javljaju dosta češće. Pošto rasejanja pod malim uglom zavise od parametra sudara, ova površina se deli na prstenove radiusa b i debljine db . Tako se dobija diferencijalni presek za rasejanje pod malim uglom, koji je jednak $2\pi b db$ i ova površina predstavlja verovatnoću da čestica vrste α bude rasejana pod uglom θ , $\theta + d\theta$ nakon interakcije sa česticom vrste β [29]. Pošto su ovi sudari jako česti, mora se razmotriti kumulativni efekat ovih sudara. Može se pokazati da je presek za rasejanje koji odgovara tome da kumulativni efekat rasejanja pod malim uglom bude ekvivalentan jednom sudaru sa velikim uglom rasejanja dat sa [29]:

$$\sigma^* = 8 \ln \left(\frac{r_D}{b_{\frac{\pi}{2}}} \right) \sigma_v \quad (19)$$

Ubacivanjem (18) u (19) dobijamo [29]:

$$\sigma^* = \frac{1}{2\pi} \left(\frac{q_\alpha q_\beta}{\epsilon_0 \mu v_r^2} \right)^2 \ln \left(\frac{r_D}{b_{\frac{\pi}{2}}} \right) = \frac{1}{2\pi} \left(\frac{q_\alpha q_\beta}{\epsilon_0 \mu v_r^2} \right)^2 \ln \Lambda_{\alpha\beta} \quad (20)$$

Pošto presek za rasejanje opada kao $\sigma^* \sim v_r^{-4}$ zaključak je se da će za visokotemperaturne plazme Coulomb-ovi sudari biti zanemarljivi u odnosu na druge fenomene [29].

Kada je poznat totalni presek za dati sudar, može se definisati i koliziona frekvencija za sudare čestica vrste α sa česticama vrste β . Ona predstavlja broj sudara u jedinici vremena koje pretrpi jedna čestica vrste α sa česticama vrste β [30]. Definiše se kao [30]:

$$\nu_{\alpha\beta} = n_\beta \int \sigma_{\alpha\beta}(v_r) v_r dP_r^{\alpha\beta} = n_\beta \langle \sigma(v_r) v_r \rangle \quad (21)$$

U gornjoj formuli, $\sigma_{\alpha\beta}(v_r)$ predstavlja totalni presek za rasejanje, v_r je relativna brzina čestica, a $P_r^{\alpha\beta}$ predstavlja verovatnoću da jedan par čestica ima relativnu brzinu u intervalu $v_r, v_r + dv_r$. Ova raspodela može biti Maxwell-ova, ali ne i nužno. Ako se ipak prepostavi da ima oblik Maxwell-ove raspodele, onda se dobijaju tzv. Spitzer - Härm-ove formule za sudarne frekvencije. Totalna sudarna frekvencija za elektrone $\nu_e = \nu_{ee} + \nu_{ei} \simeq 2\nu_{ei}$, što daje [30]:

$$\nu_e = \frac{4}{3} \sqrt{\frac{2\pi}{m_e}} \left(\frac{ee_i}{4\pi\epsilon_0} \right)^2 \frac{n_e}{(kT_e)^{\frac{3}{2}}} \ln \Lambda_{ei} \quad (22)$$

Sudarna frekvencija za sudare elektron - elektron i elektron - jon je približno ista jer srednji slobodni put elektrona najviše zavisi od njegove energije. Totalna sudarna frekvencija za jone predstavlja ustvari kolizionu frekvenciju za sudare ion - ion jer joni sudare sa elektronima slabo osećaju zbog dosta veće mase. Ova frekvencija je [30]:

$$\nu_i = \nu_{ii} + \nu_{ie} \simeq \nu_{ii} = \frac{4}{3} \sqrt{\frac{\pi}{m_i}} \left(\frac{e_i^2}{4\pi\epsilon_0} \right)^2 \frac{n_i}{(kT_i)^{\frac{3}{2}}} \ln \Lambda_{ii} \quad (23)$$

Pošto kolizione frekvencije opadaju sa porastom temperature elektrona i jona, sudari su sve manje verovatni kako kinetička energija čestica raste. Ovo predstavlja veliko ograničenje omskog zagrevanja plazmi koji se koristi kod grejanja fuzionih plazmi.

2.1.3 Kriterijum važenja plazmenog stanja

Dakle, kao posledica gore navedenih kolektivnih interakcija u plazmi, sada se može formulisati i kvantitativni uslov važenja plazmenog stanja, odnosno kada se za materiju može reći da se nalazi u stanju plazme. Da bi materija bila u stanju plazme, moraju da budu zadovoljena dva uslova:

1. Da je zadovoljen uslov makroskopske elektroneutralnosti. Da bi ovaj uslov bio zadovoljen, dimenzije prostora koji zauzima plazma moraju biti mnogo veće od Debyeve sfere plazme. Ovaj uslov piše se tako da važi:

$$r_D^3 \ll V \quad (24)$$

2. Da bi se razvile oscilacije u plazmi, potrebno je da je uticaj sudara dosta mali. Iz ovoga proizilazi da mora da važi uslov:

$$\omega_{p\alpha} \gg \nu_\alpha \quad (25)$$

Gde je $\nu_\alpha = \sum_\beta \nu_{\alpha\beta}$ ukupna koliziona frekvencija čestica vrste α a $\omega_{p\alpha}$ je plazmenska frekvencija za tu vrstu čestica.

Ukoliko gas na nekoj temperaturi ispunjava oba gornja uslova, taj gas se može zvati plazmom.

2.2 Dijagnostika plazme

Za proučavanje i merenje parametara u plazmi razvijene su razne metode do danas. Prve metode uključuju sonde, a neki primjeri su Langmuir-ove sonde za merenje temperature i koncentracije elektrona u plazmi, te za merenje električnog polja u plazmi [32]. Kalem Rogowskog se koristi za merenje struje koja prolazi kroz plazmu [32], dok se Mirnov-ovi kalemovi koriste za merenje fluktuacija magnetnog polja u plazmi. Potom imamo laserske tehnike dijagnostike plazme koje uključuju Thomson-ovo rasejanje za merenje gustine elektrona i temperature elektrona, lasersku interferometriju za merenje gustine elektrona, lasersku reflektometriju za merenje profila koncentracije elektrona i fluktuacije gustine elektrona itd [32]. Pored lasera, u plazmu se mogu ubacivati i neutralne čestice koje služe kao probe za praćenje različitih procesa u plazmi. Konačno, jedna od najrasprostranjenijih tehnika za merenje parametara plazme jeste spektroskopija plazme. Spektroskopija se radi u skoro svim oblastima elektromagnetskog spektra (tvrdi i meki X - zraci, UV spektroskopija, optička emisiona spektroskopija) u zavisnosti od procesa koji se posmatra [32]. U ovoj tezi, akcenat je na optičkoj emisionoj spektroskopiji plazme i na spektroskopiju u ekstremnoj ultraljubičastoj (eng Extreme Ultraviolet - EUV) oblasti spektra. U daljem tekstu biće reči o optičkoj emisionoj spektroskopiji plazme, širenju spektralnih linija i o EUV spektroskopiji plazme. Za ostale dijagnostičke metode čitalac se upućuje na odgovarajuću literaturu [32, 33].

2.2.1 Optička emisiona spektroskopija

Kao posledica različitih procesa u plazmi, u svakom trenutku postoje pobuđene čestice plazme (jona ili neutrala) koje emituju zračenje iz optičkog dela spektra. Ovo zračenje se

putem sistema ogledala i sočiva dovodi na ulazni slit spektrometra i pomoću odgovarajućeg detektora na njegovom izlazu se ovo zračenje snima. Rezultujuće emitovane spektralne linije nisu beskonačno uske, nego su proširene usled različitih efekata vezanih za plazmu kao i sam instrument kojim se ovo zračenje posmatra. Na prvom mestu, postoji prirodno širenje spektralne linije kao posledica Heisenberg-ove relacije neodređenosti za energiju i vreme, ali o ovom širenju u ovoj tezi neće biti reči, ali se detalji mogu naći u odgovarajućoj literaturi (npr. [34]). Pored toga, sam instrument takođe uzrokuje određeno širenje linije, koje se naziva instrumentalno širenje i obično je opisano Gauss-ovom funkcijom.

2.2.1.1 Doppler-ovo širenje spektralne linije

Zbog relativnog kretanja emitera u odnosu na posmatrača (u našem slučaju merni instrument), dolazi do Doppler-ovog širenja spektralne linije. Doppler-ovo širenje ustvari predstavlja kumulativni efekat Doppler-ovog pomeraja pojedinačnih emisija svakog emitera usled Doppler-ovog efekta. Relativno jednostavno može se pokazati da ovaj profil spektralne linije ima Gauss-ovu raspodelu koja je oblika [34]:

$$I(\omega) = I_0 \exp \left[- \left(\frac{c(\omega - \omega_0)}{\omega_0 v_p} \right)^2 \right] \quad (26)$$

Gde je ω_0 centralna frekvencija na kojoj se emisija dešava, a $v_p = \sqrt{\frac{2kT}{m}}$ predstavlja najvekovatniju brzinu emitera. Ukoliko se zamene sve konstante, može se doći do poznatog izraza za poluširinu spektralne linije izazvane Doppler-ovim efektom:

$$\Delta\lambda = 7.16 \cdot 10^{-7} \lambda_0 \sqrt{\frac{T}{M}} \quad (27)$$

Pri čemu je M molarna masa emitera, a λ_0 centralna talasna dužina izražena u angstromima.

2.2.1.2 Stark-ovo širenje spektralnih linija

Još jedan mehanizam širenja spektralnih linija u plazmi predstavlja širenje usled pritiska. Ovo znači da zbog interakcije emitera sa okolnim česticama u plazmi dolazi do širenja i pomeranja spektralnih linija. Po tipu interakcije, može se govoriti o dva efekta. Ukoliko govorimo o interakciji emitera i električnog polja generisanog od strane slobodnih nelektrisanih čestica, onda se radi o Stark-ovom efektu [35]. Ako se radi o dipol - dipol interakciju između emitera i perturbera, onda je to van der Waals-ovo širenje spektralnih linija. U daljem toku teze, biće reči samo o Stark-ovom širenju spektralnih linija.

Stark-ovo širenje spektralne linije potiče od slobodnih nanelektrisanja koja okružuju emiter, koja svojim mikropoljima modifikuju proces emisije, što rezultira pomeranjem ili širenjem spektralne linije [35]. Pionirski radovi iz teorije Stark-ovog širenja potiču od Griem-a [36–38] i Baranger-a [39–41], a kasnije su razvijene različite teorije i matematički formalizmi od kojih se većina može naći u referenci [35]. U zavisnosti od toga da li su slobodna nanelektrisanja elektroni ili joni, razlikuje se matematički tretman. Elektroni se tretiraju u tzv. *sudarnoj* aproksimaciji (eng. *impact approximation*) u kojoj sudari elektrona sa emiterom uzrokuju promene u fazi emitovanog talasa što daje Lorentz-ov oblik spektralne linije [35]. Sa druge

strane, joni se tretiraju kvazistatički i njihov efekat se opisuje preko raspodele lokalnog mikropolja koju su dali Holtsmark [42], Mozer i Baranger [43], odnosno Hooper [44–46]. Uopšteno, profil linije se dobija iz Fourier-ovog transforma autokorelace funkcije operatora dipolnog momenta $C(t)$ [35]:

$$I(\omega) = \operatorname{Re} \frac{1}{\pi} \int_0^\infty dt \exp(-i\omega t)\{C(t)\} \quad (28)$$

Vitičaste zgrade predstavljaju usrednjavanje po svim mogućim konfiguracijama mikropolja. Ova funkcija ima oblik:

$$C(t) = \operatorname{tr}[D(0) \cdot D(t) \rho] \quad (29)$$

Gde je ρ matrica gustine, a $D(t)$ operator dipolnog momenta u Heisenberg-ovoj slici:

$$\mathbf{D}(t) = U^\dagger(t)\mathbf{D}(0)U(t) \quad (30)$$

A $U(t)$ predstavlja evolucioni operator koji zadovoljava Schrödinger-ovu jednačinu [35]:

$$i\hbar \frac{d}{dt}U(t) = H(t)U(t) = (H_0 + q\mathbf{E}(t) \cdot \mathbf{R})U(t) \quad (31)$$

Pri čemu je H_0 neperturbovani hamiltonijan, a član $q\mathbf{E}(t) \cdot \mathbf{R}$ predstavlja perturbaciju u dipolnoj aproksimaciji. U ovom izrazu, $\mathbf{E}(t)$ predstavlja vremensku zavisnost mikropolja koje generišu nanelektrisane čestice u plazmi.

2.2.1.3 Kvazistatičko širenje spektralnih linija

Ukoliko je polje statičko, onda evolucioni operator ima oblik:

$$U(t) = \exp\left(-\frac{i}{\hbar}Ht\right) = \exp\left(-\frac{i}{\hbar}(H_0 + q\mathbf{E} \cdot \mathbf{R})t\right) \quad (32)$$

Pri čemu je \mathbf{E} konstantan vektor električnog polja. Ukoliko napišemo da je ε svojstvena vrednost operatora H , onda u svojstvenom bazisu operatora H možemo pisati da je dipolni operator oblika [35]:

$$D_{ji}(t) = \exp\left(\frac{i}{\hbar}\varepsilon_j t\right)D_{ji}(0)\exp\left(-\frac{i}{\hbar}\varepsilon_i t\right) \quad (33)$$

Autokorelaciona funkcija se onda može napisati u obliku [35]:

$$C(t) = \sum_{ij} \exp\left(-\frac{i}{\hbar}(\varepsilon_i - \varepsilon_j)t\right)\mathbf{D}_{ij}\mathbf{D}_{ji}\rho_{ii} \quad (34)$$

Svojstvene vrednosti operatora H mogu se izraziti kao suma neperturbovanog dela koji potiče od operatora H_0 i interakcionog dela koji potiče od interakcije emitera sa poljem perturbera. Tako se dolazi do izraza [35]:

$$\varepsilon_k = \varepsilon_k^{(0)} + \Delta\varepsilon_k \quad (35)$$

Koristeći ovaj izraz, i uvodeći notaciju da je $\omega_{ij} = \frac{i}{\hbar}(\varepsilon_i - \varepsilon_j)$ iz jednačine (34) dobijamo [35]:

$$C(t) = \sum_{ij} \exp(-i(\omega_{ij} + \Delta\omega_{ij})t)\mathbf{D}_{ij}\mathbf{D}_{ji}\rho_{ii} = \sum_{ij} I_{ij} \exp(-i\omega_{ij}t) \quad (36)$$

Gde je I_{ij} intenzitet odgovarajuće spektralne komponente. Usrednjeno po svim konfiguracijama mikropolja, prema izrazu (28) dobiceemo na kraju [35]:

$$I(\omega) = \sum_{ij} \{ I_{ij} \operatorname{Re} \frac{1}{\pi} \int_0^\infty dt \exp(-i(\omega - \omega_{ij})t) \} = \sum_{ij} \{ I_{ij} \delta(\omega - \omega_{ij}) \} \quad (37)$$

Ovo usrednjavanje se može obaviti na sledeći način [35]:

$$I(\omega) = \sum_{ij} \int d^3\mathbf{E} W(\mathbf{E}) I_{ij}(\mathbf{E}) \delta(\omega - \omega_{ij}(\mathbf{E})) \quad (38)$$

U gornjem izrazu, $W(\mathbf{E})$ predstavlja verovatnoću da perturbujuće polje ima vrednost \mathbf{E} . Dakle, kako bi se izračunao konačan profil spektralne linije, moraju biti poznate svojstvene vrednosti i stanja operatora H , kao i raspodela verovatnoće mikropolja u plazmi. Prvu raspodelu verovatnoće mikropolja u plazmi je dobio Holtsmark [42], pod pretpostavkom da je plazma sastavljena od slobodnih i statistički nezavisnih čestica. Uz ovu pretpostavku, može se pokazati da je karakteristična funkcija funkcije raspodele oblika [35]:

$$A(\mathbf{k}) = \langle \exp(i\mathbf{k} \cdot \mathbf{E}) \rangle^n \quad (39)$$

Dodatno, Holtsmark je u [42] pretpostavio da je plazma homogena i izotropna, pa je funkcija raspodele onda $P(\mathbf{r})d^3\mathbf{r} = \frac{d^3r}{V}$. Ovde je V zapremina plazme, te se dobija konačan oblik karakteristične funkcije funkcije raspodele mikropolja [35]:

$$A(\mathbf{k}) = \left[\frac{4\pi}{V} \int_V dr r^2 \frac{\sin(kE(r))}{kE(r)} \right]^n \quad (40)$$

Ukoliko se dodatno pretpostavi da je polje dato kao Coulomb-ovo polje i uvede smena $x = \frac{kq}{4\pi\varepsilon_0 r^2}$, nakon rešavanja integrala dobija se [35]:

$$A(\mathbf{k}) = \left[1 - \frac{2\pi}{V} \left| \frac{qk}{4\pi\varepsilon_0} \right|^{3/2} \int_0^{+\infty} \frac{dx}{x^{5/2}} \left(1 - \frac{\sin x}{x} \right) \right]^n \quad (41)$$

U graničnom slučaju kada $n \rightarrow \infty$, pri čemu se gustina plazme drži konstantnom ($V \rightarrow \infty$ kada $n \rightarrow \infty$ tako da $N = \frac{n}{V}$ bude konstantno) dobija se na kraju [35]:

$$A(k) = \exp[-(kF_0)^{3/2}] \quad (42)$$

Pri čemu je F_0 tzv. Holtsmark-ovo polje dato sa [35]:

$$F_0 = \left(\frac{2}{5} \sqrt{2\pi} \right)^{2/3} \frac{q}{4\pi\varepsilon_0 r_0^2} \quad (43)$$

A $r_0 = \left(\frac{3}{4\pi N} \right)^{1/3}$ predstavlja karakteristično rastojanje između dve čestice unutar plazme. Pošto $A(\mathbf{k})$ zavisi samo od intenziteta vektora \mathbf{k} , inverznom Fourier-ovom transformacijom dobija se funkcija raspodele mikropolja unutar plazme [35]:

$$W(\mathbf{E}) = \frac{1}{8\pi^3} \int d^3\mathbf{k} \exp(-i\mathbf{k} \cdot \mathbf{E}) A(\mathbf{k}) = \frac{1}{2\pi^2} \int_0^{+\infty} dk k^2 A(k) \frac{\sin(kE)}{kE} \quad (44)$$

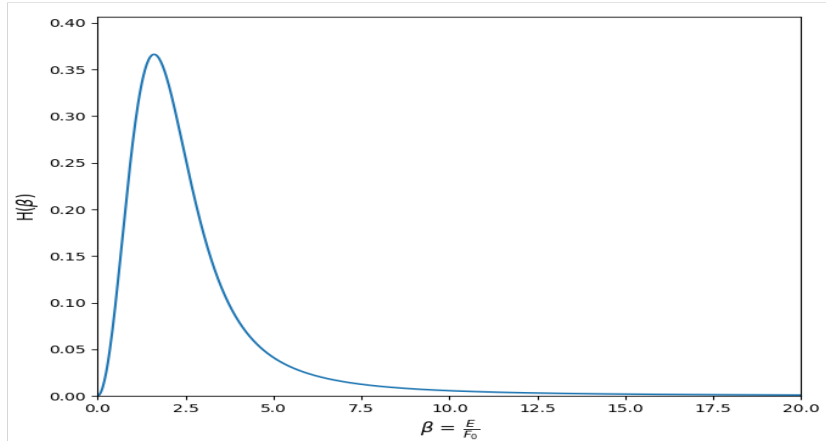
Korištenjem jednačina (42) i (44) dobijamo da je gustina verovatnoće $P(E)$ koja zavisi samo od intenziteta mikropolja, data sa [35]:

$$P(E) = 4\pi E^2 W(E) = \frac{2}{\pi} E \int_0^\infty dk k \exp[-(kF_0)^{3/2}] \sin(kE) \quad (45)$$

Konačno, ako se uvede normalizovano polje $\beta = \frac{E}{F_0}$ i $x = kF_0$ dobijamo konačan oblik Holtsmark-ove raspodele [35]:

$$H(\beta) = \frac{2}{\pi} \beta \int_0^{+\infty} dx \exp(-x^{3/2}) x \sin(\beta x) \quad (46)$$

Ova raspodela prikazana je na slici 2. Pošto je polazna pretpostavka Holtsmark-a o plazmi kao skupu slobodnih i statistički nezavisnih čestica bila jako gruba, kasnije su Ecker i Müller [47], Baranger i Mozer [43], kao i Hooper [44–46] razvili teoriju za kvazistatičko širenje koje uzima u obzir korelacije između nanelektrisanih čestica u plazmi.



Slika 2: Holtsmark-ova raspodela za različito normalizovano polje β

Prilaz koji su koristili Baranger i Mozer jeste klaster razvoj karakteristične funkcije funkcije raspodele koristeći Mayer - Ursell-ove funkcije [35], kao i uvođenje razlike u proračunu za visoko frekventna polja i nisko frekventna polja. Ova razlika je napravljena pomoću pretpostavke o različitim uzrocima postojanja niskofrekvenih i visokofrekvenih komponenti polja, gde se smatra da visoko frekventna komponenta električnog polja potiče od elektrona, a nisko frekventna komponenta polja potiče od superpozicije polja generisanog od strane jona i efekta ekraniranja od strane elektrona [35]. Autori su rezultate dali u obliku tabela za nekoliko vrednosti gustine elektrona N_e i temperature elektrona T_e . Hooper-ov pristup ima sličan matematički tretman kao kod Baranger-a i Mozer-a, ali uvođi dodatni parametar kako bi smanjio grešku odsecanja u Mayer - Ursell-ovom razvoju karakteristične funkcije [35]. Ovaj pristup, iako formalno drugačiji od Mozer-a i Baranger-a, daje poklapanje sa Holtsmark-ovim rezultatima. [35].

2.2.1.4 Sudarna aproksimacija

Sudarna aproksimacija je razvijena od strane Baranger-a u seriji radova [39–41]. Ukoliko nije drugačije naglašeno, u paragrafima 2.2.1.4 i 2.2.1.5 koristiće se CGS sistem jedinica. Sudarna aproksimacija predstavlja aproksimaciju gde emiter interaguje samo sa jednim perturberom u analiziranom vremenskom intervalu. Drugim rečima, vreme interakcije τ je mnogo manje od srednjeg vremena između dva sudara ΔT [48]:

$$\tau \ll \Delta T \quad (47)$$

Autokorelaciona funkcija ima oblik [48]:

$$C(t) = \text{tr}_E[\rho_E \text{tr}_p[\mathbf{D}U^\dagger(t)\mathbf{D}U(t)]] \quad (48)$$

Pri čemu je tr_E trag u prostoru stanja emitera, tr_P je trag po svim stanjima perturbera, dok je ρ_E je matrica gustine stanja emitera. Ukoliko je pretpostavka da se perturberi kreću po klasičnim putanjama, trag po stanjima perturbera može da se zameni statističkim usrednjavanjem po ansamblu, pa se dobija:

$$C(t) = \text{tr}_E[\rho_E \{\mathbf{D}U^\dagger(t)\mathbf{D}U(t)\}] \quad (49)$$

Još jedna aproksimacija koja se na ovom mestu uvodi jeste aproksimacija komplettnog sudara [48]. Pod komplettnim sudarom podrazumeva da se čitav proces interakcije završi pre emisije fotona. U tom slučaju, oblik spektralne linije može se izračunati primenom teorije atomskih sudara, tj. problem se svodi na traženje i izračunavanje matrica rasejanja S . Poslednja pretpostavka je da je spektralna linija izolovana, a to znači da nema degeneracije nivoa, odnosno nema preklapanja susednih atomskih nivoa. Tada, oblik spektralne linije $F(\omega)$ emitovane pri prelasku elektrona sa nivoa i ($\alpha_i J_i$) i f ($\alpha_f J_f$) opisan je Lorentz-ovom funkcijom i može se pisati [48]:

$$I(\omega) = \rho_E(\alpha_i J_i) \frac{4\omega^4}{3c^3} F(\omega) \quad (50)$$

$$F(\omega) = \frac{1}{\pi} \int_0^{+\infty} dt e^{i(\omega - \omega_{if})t} C(t) \quad (51)$$

$$C(t) = e^{-(\omega + id)t} \quad (52)$$

Što na kraju daje:

$$F(\omega) = \frac{\omega}{\pi[(\omega - \omega_{if} - d)^2 + \omega^2]} \quad (53)$$

U slučaju lokalne termodinamičke ravnoteže, gustina stanja predstavljena je Boltzmann-ovim faktorom:

$$\rho_E(\alpha_i J_i) = g_i \frac{1}{Z(T)} e^{-\frac{E_i}{k_B T}} \quad (54)$$

Gde je g_i statistička težina nivoa ($\alpha_i J_i$), E_i njegova energija, a $Z(T)$ particiona funkcija na temperaturi T . Poluširina na polovini visine (HWHM) i pomeraj spektralne linije opisane profilom datim jednačinom (51) može se dobiti iz:

$$\omega + id = \text{tr}_P \left(1 - S_{ii} S_{ff}^\dagger \right) \quad (55)$$

Trag po perturberima možemo pisati u sledećem obliku [48]:

$$tr_P = N_P \int_0^{+\infty} vf(v) dv \int_0^{+\infty} 2\pi\rho d\rho \oint \frac{d\Omega}{4\pi} \quad (56)$$

Gornja jednačina napisana je u semiklasičnoj aproksimaciji, gde se perturberi kreću po klasičnim putanjama sa parametrom sudara ρ . Perturberi, čija je gustina N_P se kreću relativnom brzinom v , sa raspodelom brzina $f(v)$ koja je opisana Maxwell-ovom funkcijom. Integral

$$\oint \frac{d\Omega}{4\pi}$$

predstavlja usrednjavanje po svim pravcima sudarajućih čestica. Prema tome, dobijamo [48]:

$$\omega + id = N_P \int_0^{+\infty} vf(v) dv \int_0^{+\infty} 2\pi\rho d\rho \langle 1 - S_{ii} S_{ff}^\dagger \rangle_{\text{angular average}} \quad (57)$$

Ugaono usrednjavanje može biti napisano kao linearna kombinacija $3j$ koeficijenata i inicijalnih i finalnih stanja S matrice. Finalna formula izgleda na sledeći način [48]:

$$\begin{aligned} \omega + id = N_P \int_0^{+\infty} vf(v) dv \int_0^{+\infty} 2\pi\rho d\rho & \times \left[\sum_{M_i} \frac{1}{2J_i + 1} \langle \alpha_i J_i M_i | T(\rho, v) | \alpha_i J_i M_i \rangle + \right. \\ & + \sum_{M_f} \frac{1}{2J_f + 1} \langle \alpha_f J_f M_f | T^\dagger(\rho, v) | \alpha_f J_f M_f \rangle - \\ & - \sum_{\substack{M_i M'_i \\ M_f M'_f \\ \mu}} (-1)^{2J_f + M_f + M'_f} \begin{pmatrix} J_i & 1 & J_f \\ -M_i & \mu & M_f \end{pmatrix} \begin{pmatrix} J_i & 1 & J_f \\ -M'_i & \mu & M'_f \end{pmatrix} \times \\ & \left. \times \langle \alpha_i J_i M_i | T(\rho, v) | \alpha_i J_i M'_i \rangle \langle \alpha_f J_f M_f | T^\dagger(\rho, v) | \alpha_f J_f M'_f \rangle \right] \end{aligned} \quad (58)$$

Gde je $T = 1 - S$. Konciznije zapisano, imamo da je [48]:

$$\begin{aligned} \omega + id = N_P \int_0^{+\infty} vf(v) dv & \times \left[\left(\sigma(\alpha_i J_i \rightarrow \alpha J, v) + \sigma(\alpha_f J_f \rightarrow \alpha' J', v) \right) - \right. \\ & - 2\text{Re} \int_0^{+\infty} 2\pi\rho d\rho \left[\sum_{\substack{M_i M'_i \\ M_f M'_f \\ \mu}} (-1)^{2J_f + M_f + M'_f} \begin{pmatrix} J_i & 1 & J_f \\ -M_i & \mu & M_f \end{pmatrix} \begin{pmatrix} J_i & 1 & J_f \\ -M'_i & \mu & M'_f \end{pmatrix} \times \right. \\ & \left. \left. \times \langle \alpha_i J_i M_i | T(\rho, v) | \alpha_i J_i M'_i \rangle \langle \alpha_f J_f M_f | T^\dagger(\rho, v) | \alpha_f J_f M'_f \rangle \right] \right] \end{aligned} \quad (59)$$

Gornja jednačina nam sada pruža mogućnost interpretacije članova. Prvi član u (59) predstavlja sumu svih preseka za neelastično rasejanje pri čemu se indukuju ekscitacioni i deeksitacioni prelazi sa gornjeg nivoa emitera $\alpha_i J_i$ ka svim nivoima perturbera αJ . Slično i za drugi član, koji predstavlja deeksitacije i ekscitacije sa donjem nivoem emitera $\alpha_f J_f$ ka svim nivoima perturbera $\alpha' J'$. Treći član predstavlja interferencijski član kojeg sačinjava linearna kombinacija nedijagonalnih elemenata T matrice.

2.2.1.5 Semiklasična perturbaciona aproksimacija (SCP)

Ova aproksimacija se zasniva na sudarnoj aproksimaciji iznesenoj u paragrafu 2.2.1.4. Prepostavka je da se perturberi kreću po klasičnim putanjama, pri čemu se uvodi aproksimacija da na oblik trajektorije perturbera ne utiče interakcija sa emiterom. Emiter se tretira kvantno - mehanički, a interakcija perturber - emiter se tretira pomoću vremenski zavisne perturbacione teorije. Ovaj prilaz razvila je Sylvie Sachal - Brechaut u svojim radovima [27, 28], a kasnije dodatno dopunjena u saradnji sa Milanom Dimitrijevićem [49].

Prilikom postavke simulacije, ukoliko je reč o neutralnim atomima, trajektorije perturbera su prave linije, dok su za jonske emitere te trajektorije hiperboličke [48]. Matrica T se računa tako što se matrica S , koja je oblika [48]:

$$S = \mathcal{T} \left(\exp \left(\frac{1}{i\hbar} \int_{-\infty}^{+\infty} \tilde{V}(t) dt \right) \right) \quad (60)$$

Razvije u Dyson-ov red do drugog člana. U jednačini, \mathcal{T} predstavlja hronološki operator, a $\tilde{V}(t)$ interakcioni potencijal za sistem emiter - perturber. Pod prepostavkom idealne plazme, interakcioni potencijal je zapravo elektrostatički potencijal oblika [48]:

$$\tilde{V}(t) = V = \frac{(Z_E + N) Z_P e^2}{r_P} - Z_P e^2 \sum_{i=1}^N \frac{1}{r_{iP}} \quad (61)$$

Ovde $(Z_E + N)$ predstavlja nanelektrisanje jezgra, a Z_P predstavlja nanelektrisanje perturbera. Rastojanje r_P je rastojanje između jezgra i perturbera, a r_{iP} je rastojanje između i -tog elektrona emitera i perturbera. Sledeći korak je razvoj $1/r_{iP}$ po multipolima, pri čemu se čuvaju samo članovi u aproksimaciji dugog dometa. Razvoj je oblika [48]:

$$V = \frac{Z_E Z_P e^2}{r_P} - \sum_{\lambda=1}^{+\infty} \frac{4\pi Z_P e^2}{2\lambda + 1} \frac{1}{r_P^{\lambda+1}} \sum_{\mu=-\lambda}^{+\lambda} \sum_{i=1}^N r_i^\lambda Y_{\lambda\mu}(r_P) Y_{\lambda\mu}^*(r_i) \quad (62)$$

Gde je $Y_{\lambda\mu}$ sferni harmonik. Zbog sferne simetrije, Coulomb-ov član je jedank nuli, pa dipolni i kvadrupolni član postaju bitni i oni se zadržavaju u računu. Sada se ovaj oblik potencijala vraća u Dyson-ov red i računa T matrica, pa potom se iz jednačine (59) dobija širina spektralne linije na polovini visine (FWHM) i pomeraj spektralne linije d .

Granica važenja semiklasične perturbacione aproksimacije jeste zapravo granica važenja sudarne aproksimacije. Ako se vratimo na jednačinu (47), srednje vreme između dva sudara možemo izraziti kao $\Delta T = N_P v_{typ} \rho_{typ}^2$ [48], dok se srednje vreme interakcije može proceniti sa $\tau = \rho_{typ}/v_{typ}$. Ovde je ρ_{typ} srednji parametar sudara, a v_{typ} tipična srednja relativna brzina perturbera. Kada se sve uzme u obzir dobija se uslov važenja udarne aproksimacije [48]:

$$\rho_{typ} \ll N_P^{-\frac{1}{3}} \quad (63)$$

Sve dok je zadovoljen gornji uslov, i SCP teorija daje dobre rezultate. Druga aproksimacija koja je krucijalna za teoriju jeste aproksimacija izolovane linije, tj. da ne dolazi do preklapanja perturbujućih i atomskih nivoa [48]. Ova aproksimacija postaje kritična ukoliko imamo prelaze sa visokih nivoa (sa visokim glavnim kvantnim brojem) ili na velikim gustinama, pa

srednja energija elektrona može postati uporediva sa energetskim razmakom između nivoa ΔE , što može dovesti do mešanja perturbovanih i atomskih stanja.

Tokom godina, poluširine linija i pomeraji su računati za različite emitere i različite prelaze, a svi podaci su upisani u Stark- - B bazu podataka [?], gde postoji pristup bilo kom računatom prelazu. Postojanje ovako velike baze podataka navodi na ideju da bi veštačka inteligencija i mašinsko učenje mogli da se upotrebe za novi pristup proučavanju spektralnih linija.

2.2.1.6 Regularnosti Stark-ovog širenja spektralnih linija

Kako Stark-ova poluširina zavisi od parametara plazme i atomske strukture, a atomska struktura emitera pokazuje razne regularnosti, za očekivati je da se to nekako manifestuje i u slučaju Stark-ovih poluširina [50]. Zbog jednostavnosti atomske strukture, alkalni i zemno - alkalni metali bi trebalo da pokazuju najizraženije regularnosti. Sa porastom složenosti atomske strukture, ove regularnosti postaju sve manje uočljive [50]. U svom preglednom radu, Wiese i Konjević [50] su podelili ove regularnosti u tri grupe:

1. regularnosti u okviru spektra emitera. Tu mogu biti regularnosti duž spektralne serije, te za kompleksnije spektre, regularnosti u okviru multipleta. Neki primeri se mogu naći u radovima [51–53]
2. regularnosti u okviru istih prelaza kod homolognih atoma [54, 55].
3. regularnosti duž izoelektronskog niza za posmatrani prelaz [56–58].

Purić zajedno sa svojim saradnicima je intenzivno proučavao regularnosti Stark-ovog efekta [59–63]. Prema tim radovima, moguće je uspostaviti vezu između Stak-ove poluširine linije ω i ionizacionog potencijala gornjeg nivoa $\chi = E_g - E_i$, pri čemu je E_g energija gornjeg nivoa, a E_i predstavlja ionizacionu energiju atoma. Purić i Šćepanović [64] su u svom radu predložili opštu formulu za određivanje Stark-ove poluširine jonskih emitera na osnovu uočenih regularnosti:

$$\omega = N_e f(T) Z^c a \chi^{-b} \quad (64)$$

U gornjoj formuli χ predstavlja potencijal jonizacije gornjeg nivoa, Z predstavlja nanelektrisanje jona koje vidi elektron koji vrši prelaz. Parametri a , b i c predstavljaju fit parametre koji ne zavise od temperature elektrona, gustine elektrona i ionizacionog potencijala. Funkcija $f(T)$ najčešće ima oblik:

$$f(T) = A + BT^{-C} \quad (65)$$

Gde je C još jedan fit parametar. Važenje formule (64) provereno je u nizu radova Purića i saradnika [65–68], ali univerzalni fit parametri do sada nisu utvrđeni. Regularnosti duž spektralnih serija neutralnog litijuma ispitane su i u ovoj tezi primenom mašinskog učenja, a rezultati ove analize su prikazani u delu 3.

2.2.2 EUV spektroskopija plazme

EUV spektroskopija podrazumeva merenje zračenja iz plazme u opsegu talasnih dužina od 5 do 100 nm. Zbog velike apsorpcije zračenja od strane atoma kiseonika u ovom spektralnom delu, sva merenja kao i spektrometar moraju da budu pod vakuumom. Dodatne poteškoće predstavlja skupljajuća i fokusirajuća optika, jer samo ograničen broj materijala ima nezanimarljivu refleksiju u ovom delu spektra. Iz tog razloga, koriste se sferne rešetke koje se ponašaju i kao disperzivni i kao fokusirajući element unutar VUV i EUV spektrometra. Što se samog spektrometra tiče, postoje dve konfiguracije: u jednoj konfiguraciji, ulazni slit je fiksiran tako da imamo veliki upadni ugao na rešetku zbog smanjenja gubitaka usled astigmatizama, dok se izlazni slit spektrometra pomera po krugu poluprečnika R . Ovaj krug se naziva Rowland-ov krug, a sama konfiguracija se naziva Paschen - Runge-ova konfiguracija. U drugoj konfiguraciji, ugao između upadnog i difraktovanog zraka sa rešetke je fiksiran, a umesto da se pomera izlazni slit, rešetka se rotira tako da se omogućuje jednostavniji dizajn spektrometra. Ovakva konfiguracija EUV spektrometra se naziva Seya - Namioka konfiguracija. U eksperimentalnom delu ovog rada korišten je spektrometar na bazi Rowland-ovog kruga, pa će o njemu biti više reči u nastavku, dok je druga konstrukcija detaljno prikazana u radu [69].

Rowland je u svom radu pokazao da ako se rešetka ureže na sfernem ogledalu, ona može služiti i kao sopstveni kolimator te se spektrometar svodi na tri elementa: slit, rešetku i detektor [70]. Dokaz ovog koncepta ogleda se u činjenici da ako rešetka i slit leže na krugu čiji je prečnik jednak poluprečniku krvine rešetke, pri čemu je rešetka tangenta na krug, spektralne linije su u fokusu na krugu. Jednačina rešetke u tom slučaju ista je kao i za ravnu rešetku, što je pokazano i u detaljnim teorijskim razmataranjima Beutler-a o konkavnoj rešetki izloženim u [71]. Dakle, jednačina rešetke postaje:

$$m\lambda = d(\sin \alpha + \sin \beta) \quad (66)$$

Gde je d konstanta rešetke, α predstavlja upadni ugao a β predstavlja difraktovani ugao. Ono što se menja u odnosu na slučaj ravne difrakcione rešetke jeste izraz za recipročnu disperziju, koji postaje [70]:

$$\frac{d\lambda}{dl} = \frac{1}{R} \frac{d\lambda}{d\beta} = \frac{d \cos \beta}{R} \quad (67)$$

Iz jednačine (67) da veći radius rešetke daje bolju rezoluciju spektrometra, a standardni prečnici kruga su 1, 3, 6 ili 6.6 m. Povećanje radijusa rešetke osim što otežava proces proizvodnje same rešetke, utiče i na povećanje gabarita, odnosno smanjenje svetlosne moći instrumenta, pa se danas kao kompromis koriste standardne dimenzije rešetki od 0.5, 1 i 3 m.

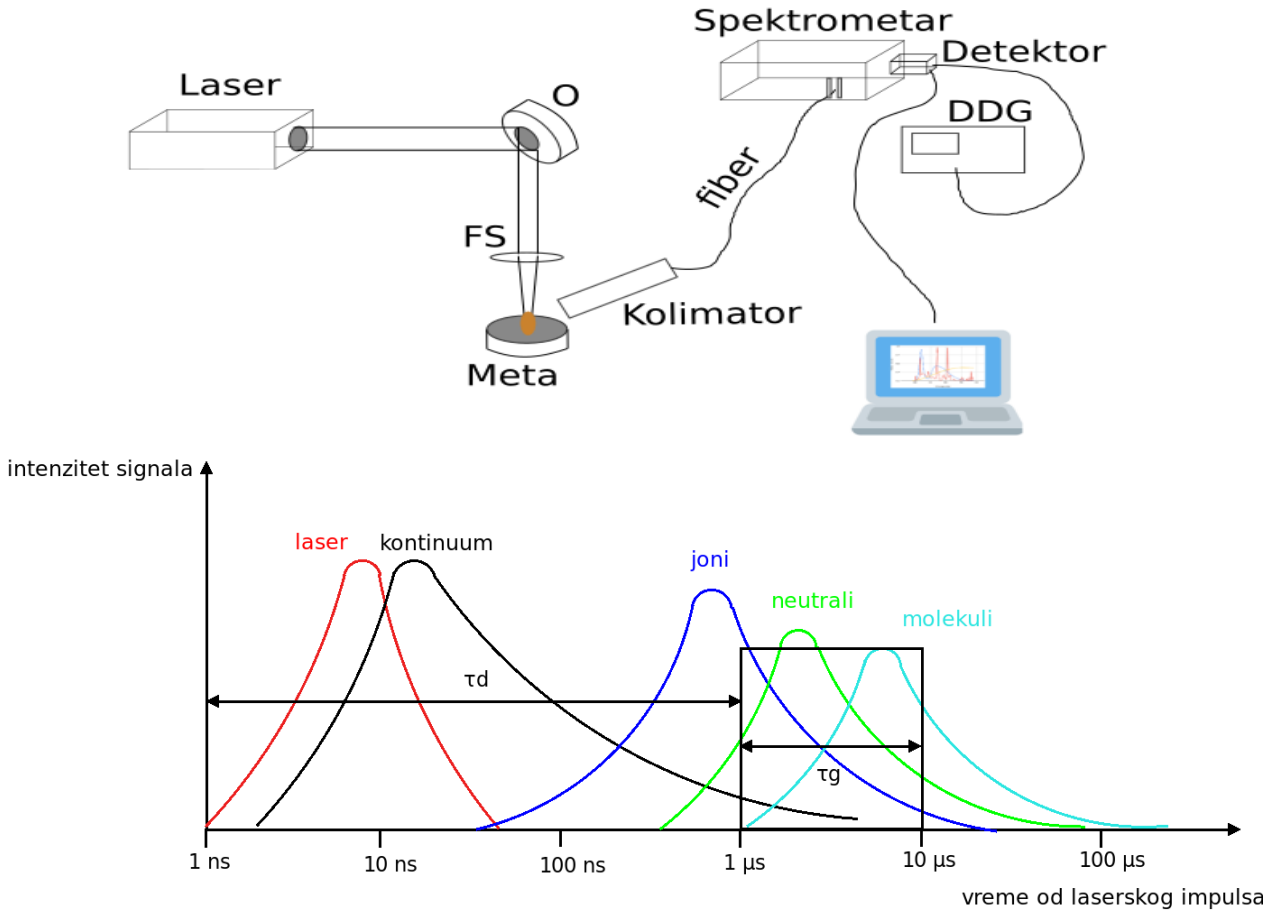
Astigmatizam predstavlja glavni izvor gubitaka kod sfernih difrakcionih rešetki, i prema Beutler-u, dat je izrazom [71]:

$$z' = l \left(\sin^2 \beta + \sin^2 \alpha \frac{\cos \beta}{\cos \alpha} \right) \quad (68)$$

Ovde z' predstavlja dužinu lika usled astigmatizma nakon fokusiranja tačkastog izvora, a l predstavlja visinu ureza na rešetci. Da bi ovi gubici bili manji, upadni ugao zraka mora biti manji.

2.3 Laserski indukovana plazma

Kako je u ovoj doktorskoj disertaciji korištena metoda laserski indukovanih probaja u svrhu kvantitativne analize uzorka čelika, u ovom poglavlju biće objašnjene osnove interakcije lasera sa materijalom i proces formiranja laserski indukovanih plazmi. Potom će biti date osnovne dijagnostičke metode laserski indukovanih plazmi, dok će na kraju biti opisana metoda laserski indukovanih probaja kao analitičke tehnike koja se može koristiti kao tehnika za kvantitativnu analizu.



Slika 3: Tipična eksperimentalna postavka spektroskopije laserski indukovanih probaja (gore) i vremenska zavisnost evolucije spektra i pojave emisionih linija u laserski indukovanoj plazmi (dole)

Laserski indukovane plazme se mogu proizvesti tako što se laserski impuls velike snage fokusira na ispitivanu metu. Nastala plazma se potom vrlo često analizira spektroskopskim putem, u cilju određivanja elementarnog sastava ispitivanog uzorka [72]. Dalje se na osnovu različitih hemometrijskih metoda mogu odrediti i relativne koncentracije elemenata u uzorku. Ova analitička metoda je dobila ime spektroskopija laserski indukovanih probaja (eng. Laser Induced Breakdown Spectroscopy (LIBS)). Tipična LIBS postavka prikazana je na slici 3 gore. Laserski impuls preko sistema ogledala O i sočiva FS se fokusira na metu, gde se usled interakcije jakog laserskog zračenja sa metom stvara plazma na površini mete. Svetlost emitovana iz plazme se potom pomoću sočiva projektuje na ulazni slit spektrometra, ili se vodi

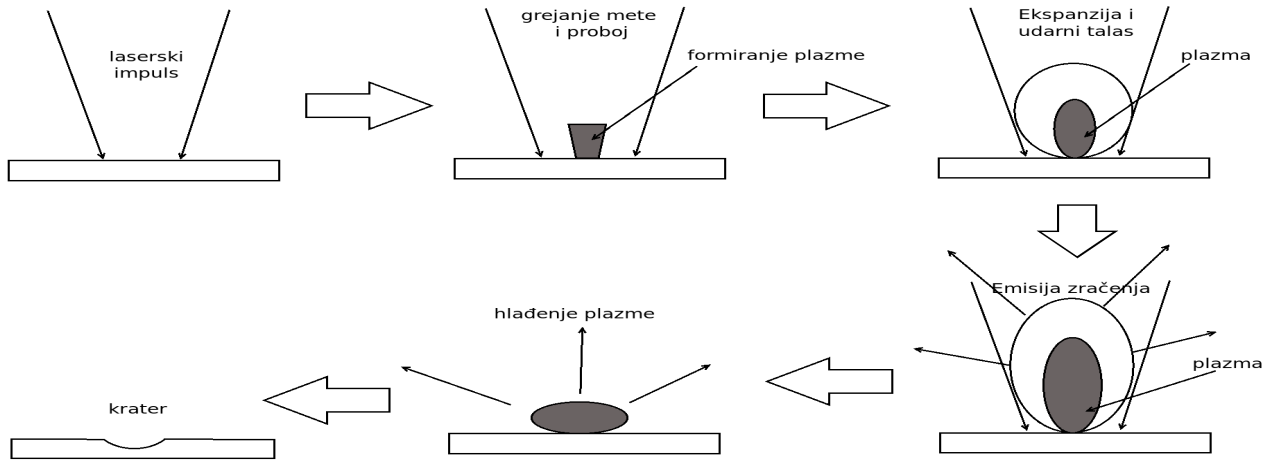
pomoću kolimatora i fiber optičkog kabla direktno na ulazni slit spektrometra kada prostorna raspodela emitovanog zračenja nije od interesa. Kao detektor se obično koristi iCCD ili CCD kamera često sinhronizovana pomoću elektronike za kašnjenje, označene sa DDG (eng. *Digital Delay Generator*) na slici postavke. Signal sa kamere se dalje preko kompjuterskog softvera snima i šalje se za dalju obradu.

Usled nehomogenosti uzorka i drugih faktora koji utiču na nereproducibilnost interakcije laser-meta, a u cilju dobijanja kvalitetnijeg signala u smislu odnosa signal-šum, često se signali dobijeni LIBS tehnikom akumuliraju ili usrednjavaju [72]. Pošto laserski indukovana plazma predstavlja impulsni izvor svetlosti, njena vremenska evolucija praćena je veoma brzim promenama svetlosnog signala čiji se intenzitet i trajanje hronološki može objasniti dominantnim uticajima pojedinačnih faktora, što je u pojednostavljenoj formi prikazano na slici 3 dole. U početnim vremenima, emisionim spektrom dominira kontinuum koji nastaje uslijed zakočnog zračenja i rekombinacionih procesa u plazmi [72]. Da ovaj kontinuum ne bi prekrio koristan signal koji dolazi od elemenata zastupljenih u tragovima, u LIBS merenjima je karakteristično da se radi početno kašnjenje od $1 \mu\text{s}$. Nakon što prođe par stotina nanosekundi, dolazi do pojave emisije jonskih linija, koje nestaju sa opadanjem temperature u plazmi, i posledično, dolazi do pojave emisije linija neutralnih elemenata na oko 5 do 10 μs od kraja laserskog impulsa. Na kraju, nakon što temperatura dovoljno opadne, dolazi do pojave molekulskih traka. Zbog opisane vremenske dinamike emisije laserski proizvedene plazme, za vremenski nerazložena merenja, tipično postoje dva vremena karakteristična za snimanje spektra. Prvo vreme, τ_d predstavlja vreme koje prođe od laserskog impulsa do aktiviranja senzora i početka snimanja spektra (eng. *delay time*) i τ_g (eng. *gate*) koje predstavlja vreme ekspozicije kamere i u zavisnosti od detektora može biti reda nekoliko mikrosekundi (iCCD kamere) do nekoliko milisekundi (obično CCD kamere).

2.3.1 Proces formiranja laserski indukovane plazme

Proces formiranja laserski indukovane plazme i dinamika njenog razvoja prikazani su na slici 4. Prilikom interakcije laserskog zračenja sa metom, slobodni elektroni koji nastaju u nelinearnim procesima interakcije lasera i okolnog gasa (npr. višefotonском apsorpcijom), interaguju sa laserskim zrakom i služe kao inicijalni absorberi energije [73]. Fotonska apsorpcija se najčešće vrši putem inverznog zakočnog zračenja [72]. Ovi elektroni se između dva sudara ubrzavaju pod dejstvom električnog polja laserskog zraka i u sudarima sa okolnim česticama kreiraju nove elektrone i jone, koji dalje mogu da interaguju sa električnim poljem i da budu ubrzani [72]. Ovo pravi lavinski efekat ubrzavanja i produkcije novih elektrona i jona koji su sposobni da dalje eksituju ili ionizuju konstituente plazme.

Nakon uspostavljanja plazme, dolazi do njene ekspanzije u radijalnom pravcu brzinama reda veličine nekoliko kilometara u sekundi. Najveću ekspanziju plazma ima u pravcu fokusirajućeg sočiva, pošto je najveći dotok energije u plazmu iz tog pravca [72]. Uspostavljanje plazme je obično praćeno jakim praskom uslijed prostirajućeg udarnog talasa koji dolazi iz fokalne zapremine. Upadni laserski zrak veoma brzo greje i topi materijal sa kojim interaguje, zatim materijal mete isparava u sloj odmah iznad površine mete gde ga dalje zagreva laserski zrak. Sa porastom gustine elektrona u plazmi, sve veći deo laserskog zraka ostaje apsorbovan u plazmi dok manji deo prolazi do površine mete. U jednom trenutku, čitav laserski snop je apsorbovan od strane plazme, meta je ekranirana a plazma se širi u pravcu laserskog snopa.

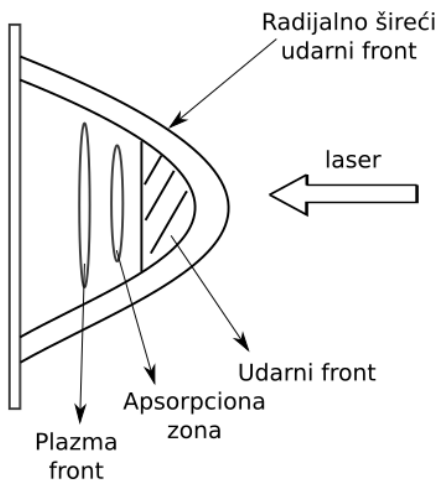


Slika 4: Vremenska zavisnost evolucije laserski indukovane plazme.

Kritična gustina za ovaj proces data je izrazom:

$$n_c \sim \left(\frac{10^{21}}{\lambda^2} \right) \text{ cm}^{-3} \quad (69)$$

Pri čemu je λ talasna dužina lasera izražena u mikronima. U procesu ekspanzije plazme bitne su tri oblasti: plazma front, udarni front i apsorpcioni front. Ove zone prikazane su na slici 5. Pri najmanjim intenzitetima, udarni front je ispred apsorpcionog i plazma fronta koji su kuplovani [73]. Akumulirana energija udarnog talasa odmah iza udarnog fronta kao i zračenje iz plazme su potrebni kako bi gurali apsorpcionu zonu ka laserskom zraku.



Slika 5: Dijagram ekspanzije plazme na čvrstim metama

rijom laserski podržanog detonacionog talasa, dok je pri većim iradijansama bolje opisana sa

modelom laserski podržanog radiacionog talasa. Okolni gas takođe ima uticaj na prostiranje i konfiniranje radijalno ekspandujuće plazme tako što usporava širenje plazme, a pritisak okolnog gasa utiče na veličinu plazme. Pri jako niskim pritiscima (vakuum), plazma ima jako male dimenzije, dok sa povećanjem pritiska raste i zapremina ekspandujuće plazme [73]. Posle nekog pritiska, veličina plazme opet kreće da opada kako se približavamo atmosferskom pritisku. Takođe, pritisak gase ima uticaj i na vreme trajanja emisije spektralnih linija iz plazme. Na atmosferskom pritisku, kao i u vakuumu, plazma traje kraće, dok na niskim pritiscima reda desetak mbar emisija spektralnih linija iz plazme može trajati i do $100 \mu\text{s}$.

2.3.2 Tipične vrednosti parametara laserski indukovanih plazmi

Laserski indukovane plazme se odlikuju sa relativno velikim gustinama elektrona i niskim temperaturama elektrona. Jedna od glavnih dijagnostičkih metoda za određivanje gustine elektrona u laserski indukovanim plazmama jeste optička emisiona spektroskopija. Najčešće korištene linije su vodonikove linije (najčešće H_α ili H_β) ili linije okolnog gasa, ukoliko se meta nalazi u kontrolisanoj atmosferi nekog pozadinskog gasa. To mogu biti npr. neke helijumove linije (kao što su He I 447.1 nm ili He II 468.6 nm). U nekim slučajevima može se koristiti i neka spektralna linija materijala mete, ukoliko sama meta poseduje linije pogodne za određivanje gustine elektrona spektroskopskim putem. Glavna prepreka određivanju gustine elektrona u plazmi spektroskopskim putem jeste samoapsorpcija spektralnih linija u plazmi, što je često slučaj za laserski indukovane plazme koje su optički debele za emitovanu svetlost. Provera optičke debljine plazme može se raditi eksperimentalno [74] korištenjem konkavnog ogledala postavljenog na rastojanju od dve žižne daljine od plazme. Poredi se intenzitet spektralne linije sa i bez ogledala i ukoliko je taj odnos konstantan i približno jednak 2, linija nije samoapsorbovana. Drugi način je teorijskim putem iz odnosa intenziteta linija unutar istog multipleta [75]. Ako su ti odnosi približno isti, plazma je optički tanka za datu spektralnu liniju. Često se samoapsorpcija primećuje i tako što su eksperimentalne linije u zasićenju i imaju tzv. *flat-top* profil. U izraženim slučajevima samoapsorpcije, spektralna linija može da ima i rupu u centru, pa kažemo da je linija samo obrnuta (eng. *self-reversed*). Tipične vrednosti gustine elektrona za laserski indukovani plazmu kreću se u intervalu od $N_e \sim 3 \cdot 10^{17} \text{ cm}^{-3}$ za mala vremena kašnjenja τ_d do $N_e \sim 1 \cdot 10^{16} \text{ cm}^{-3}$ za velika vremena kašnjenja.

Određivanje temperature elektrona u laserski indukovanim plazmama može se takođe vršiti spektroskopskim putem, a najčešće se koriste dve metode: Boltzmann plot metoda i korištenje odnosa intenziteta emitovanih spektralnih linija. Oba metoda zasnivaju se na osnovnoj prepostavci o postojanju lokalne termodinamičke ravnoteže (LTR). Intenzitet emitovane spektralne linije iz plazme koja nastaje prilikom prelaska elektrona sa nivoa i na nivo j možemo napisati u obliku:

$$I_{ij} = h\nu_{ij}n_iA_{ij} \quad (70)$$

Ovde je h Planck-ova konstanta, ν_{ij} frekvencija emitovanog fotona, n_i je populacija gornjeg energetskog nivoa a A_{ij} je Einstein-ov koeficijent za spontanu emisiju za posmatrani prelaz. Sada se iskoristi prepostavljeni uslov važenja LTR i uzme se da populacija nivoa i prati Boltzmann-ovu raspodelu po nivoima:

$$I_{ij} = h\frac{c}{\lambda_{ij}}\frac{g_i}{g_j}n_j e^{-\frac{E_i - E_j}{kT}} \quad (71)$$

Ako se posmatra naseljenost u odnosu na osnovni nivo, gornja jednačina postaje:

$$I_{ij} = h \frac{c}{\lambda_{ij}} n_0 \frac{g_i A_{ij}}{Z} e^{-\frac{E_i}{kT}} \quad (72)$$

Logaritmovanjem i sređivanjem jednačine dobija se:

$$\ln \frac{I_{ij} \lambda_{ij}}{g_i A_{ij}} = \ln \frac{h c n_0}{Z} - \frac{E_i}{kT} \quad (73)$$

Odakle se uočava da se merenjem relativnih intenziteta više linija, ukoliko je zadovoljena Boltzmann-ova raspodela, dobija linearna zavisnost $\ln \frac{I_{ij} \lambda_{ij}}{g_i A_{ij}}$ od E_i i moguće je odrediti temperaturu elektrona iz nagiba ove linije. Metoda je tačnija što su bolje određeni relativni intenziteti linija, što su bolje određeni ili izračunati Einstein-ovi koeficijenti i što je veći razmak između energija gornjih nivoa korištenih prelaza.

Druga metoda određivanja temperature elektrona predstavlja odnos intenziteta dve spektralne linije istog elementa. Ukoliko je zadovoljen uslov LTR i ako su populacije nivoa date Boltzmannovom raspodelom, onda je odnos intenziteta dat sa [73]:

$$\frac{I_{ij}}{I_{km}} = \frac{\lambda_{km} g_{ij} A_{ij}}{\lambda_{ij} g_{km} A_{km}} e^{-\frac{E_{ij} - E_{km}}{kT}} \quad (74)$$

Metoda je tačnija što je energijska razlika između ove dve linije veća. Upravo iz tog razloga, jako često se biraju linije koje predstavljaju isti prelaz za dva uspešivna jonska stanja. Još jedan metod procene, koji najčešće daje vibracionu ili rotacionu temperaturu sa periferije plazme jeste snimanje molekulske trake u kasnijim vremenima plazme. Ukoliko postoji LTR, sve tri merene temperature moraju da se slažu u razumnom opsegu greške. Tipične elektronske temperature za laserski indukovane plazme zavise od uslova. Prosečne elektronske temperature za laserski proizvedene plazme na atmosferskom pritisku su reda veličine od 8000 K do 12 000 K. Na sniženim pritiscima, u kontrolisanoj atmosferi sa pozadinskim gasom, temperature gasa se kreću od 20 000 K pri malim vremenima kašnjenja τ_d do par hiljada kelvina za kasnija vremena kašnjenja. Bitno je napomenuti da su navedene temperature zapravo aproksimacija temepeature elektrona eksitacionom temperaturom, a prava temperatura elektrona bi se dobila npr iz Thomson-ovog rasejanja.

2.3.3 Spektroskopija laserski indukovanih proba (LIBS) kao analitička metoda

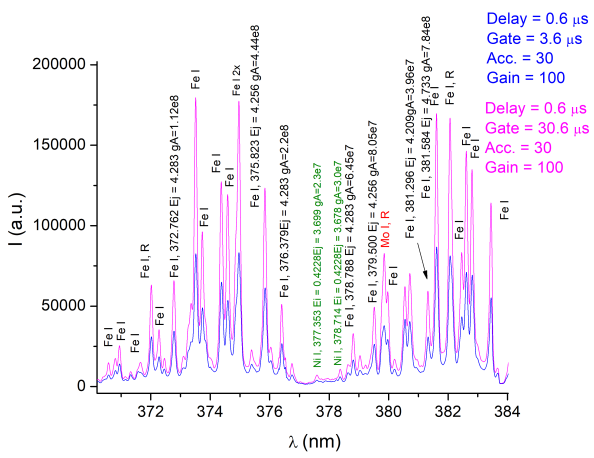
U poslednjih dvadesetak godina spektroskopija laserski indukovanih proba se jako često primenjuje kao analitička metoda kao potencijala zamena za složenije i skuplje metode (npr ICP - Masena spektroskopija). Koristi se kao kvalitativna ali i kao kvantitativna analitička metoda. Neke glavne prednosti LIBSa u odnosu na druge analitičke metode su [72]:

1. mogućnost detektovanja svih elemenata prisutnih u uzorku
2. jednostavnost
3. Brza analiza kao i analiza u realnom vremenu
4. minimalna priprema uzorka

5. *in-situ* analiza koja zahteva samo optički pristup uzorku

Prilikom evaluacije LIBSa kao analitičke metode, obično se procenjuju sledeći analitički parametri: granice detekcije, preciznost i tačnost, a u nekim slučajevima i selektivnost i osetljivost [73]. Prilikom snimanja spektra laserski indukovanih proba, određuju se talasne dužine analita i pripadajući intenziteti. Primer LIBS spektra dat je na slici 6. Posle identifikacije linija i izdvajanja linija pogodnih za kvantitativnu ili kvalitativnu analizu pristupa se istim nekom od narednih metoda.

Prva metoda predstavlja tzv. univarijantnu metodu ili metodu kalibracione krive. U ovom postupku, prvo se pristupa snimanju standardnih uzoraka i intenzitet jedne ili više spektralnih linija se povezuje sa koncentracijom analita ukoliko je slučaj o kvantitativnoj analizi. Ovo se ponavlja za svaki analit od interesa i prave se kalibracione krive koje kasnije služe za određivanje koncentracije analita u ispitivanom uzorku. U idealnom slučaju, ova kalibraciona kriva će ustvari biti prava linija koja prolazi kroz koordinatni početak [73].



Slika 6: Snimljeni LIBS spektar čelika, gde je vreme kašnjenja $\tau_d = 0.6 \mu s$ a vreme ekspozicije kamere u jednom slučaju iznosi $\tau_g = 3 \mu s$ a u drugom $\tau_g = 30 \mu s$. Ovako identifikovane spektralne linije analita se dalje koriste u analitičkim kvantitativnim i kvalitativnim metodama.

(jedan spektar LIBSa može sadržati hiljade kanala), analizu pravilnosti u podacima (eng. pattern analysis) itd. Mogućnost analiziranja više varijabli u istom trenutku omogućava ubrzavanje analiza i poboljšava kvalitet dobijenih rezultata [73]. Najčešće korišćene hemometrijske metode za kvantitativnu analizu jesu regresija analizom glavnih komponenti (eng. *Principal Component Regression* (PCR)), parcijalni metod najmanjih kvadrata (eng. *Partial Least Squares* (PLS)), metoda potpornih vektora (eng. *Support Vector Machine* (SVM)) itd.

Multivarijantne metode predstavljaju uvod u upotrebu alata mašinskog učenja i veštak-ke inteligencije koja je danas jako zastupljena u kvantitativnoj i kvalitativnoj analizi LIBS

spektara. Ključna ideja na kojoj se bazira primena alata mašinskog učenja i veštačke intelektualne logike u LIBS-u je snimanje velikog broja standardnih uzoraka sa različitim koncentracijama, i obučavanje modela na tako dobijenoj bazi podataka. Jednom obučeni modeli mogu se upotrebljavati za brzu analizu nepoznatih uzoraka bez potrebe preračunavanja koncentracije za svaki element posebno.

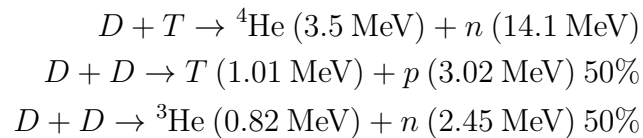
Mana ovog pristupa, jeste što je neophodno snimiti veliki broj spektara da bi se napravila dovoljno kvalitetna baza za obučavanje modela. Pošto i karakteristike instrumenta i sama merenja mogu da variraju od dana do dana [73], teško je i naporno praviti ovakve baze od nule za svako merenje. Ove poteškoće predstavljale su motivaciju da se u ovom radu ispita do koje mere se već snimljena baza može iskoristiti za obučavanje modela koji će kasnije biti korišten za ispitivanje nepoznatih uzoraka, a čiji je spektar snimljen sa sličnom aparatuiru u drugoj laboratoriji.

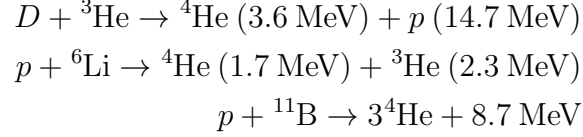
2.4 Visokotemperaturne plazme (fuzione plazme)

Visokotemperaturne plazme predstavljaju plazme u kojima temperature jona i elektrona dostižu i do nekoliko keV. Na Zemlji, to su jedino fuzione plazme. Pre nego što se dođe do plazmi na Zemlji, biće dat kratak uvod u reakcije fuzije koje se odvijaju u zvezdama. Kao glavni primer, biće uzeto Sunce koje je nama najbliža zvezda i predstavlja osnovnu pokretačku energiju svih bioloških procesa na Zemlji. Fuzija predstavlja reakciju spajanja dva lakša jezgra u teže jezgro, pri čemu se oslobađa energija jednakog vrednosti veze i postiže stabilnija konfiguracija. Da bi se desila reakcija fuzije, reaktanti (najčešće su to pozitivni joni) moraju da prevaziđu Coulomb-ovu barijeru da bi nuklearne sile počele da deluju. Ako uzmemo za primer deuterijum i tricijum koji će biti glavno gorivo u prvim fuzionim reaktorima, pri čemu je $r_m = 3.7 \times 10^{-15}$ m tipičan radius jezgra dobijemo vrednost potrebne energije:

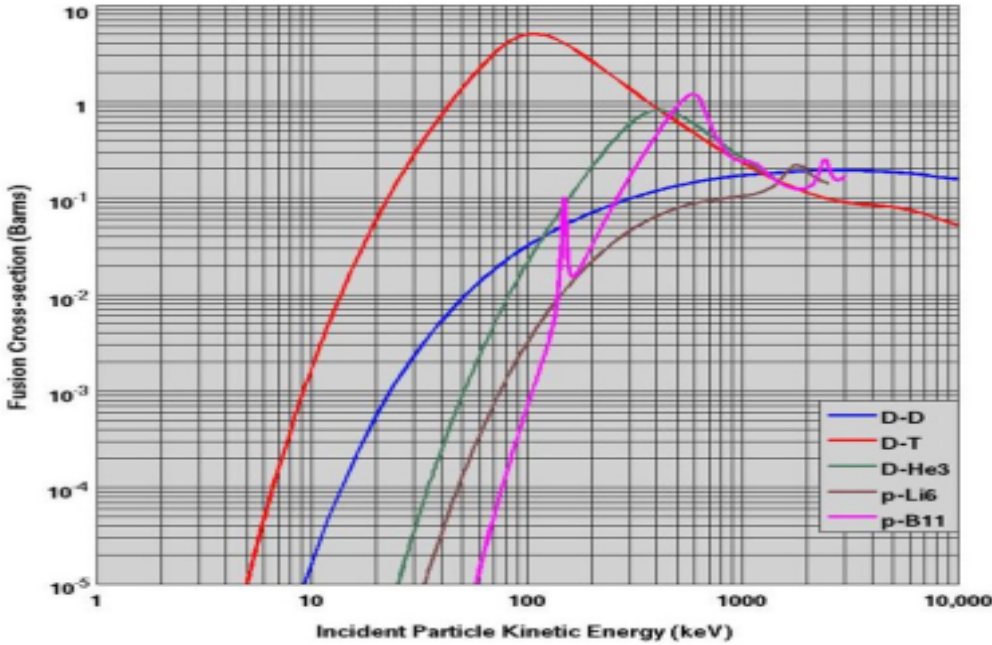
$$U = \frac{Z_1 Z_2 e^2}{4\pi\epsilon_0 r_m} = \frac{e^2}{4\pi\epsilon_0 r_m} = 0.4 \text{ MeV} \quad (75)$$

Ovo nije toliko velika energija i ostvariva je u većini modernih akceleratora. Međutim, kao što je naglašeno u poglavljju 2.1.2 videli smo da presek za sudar opada sa četvrtim stepenom relativne brzine, stoga ukoliko se ispalili snop visokoenergetskih čestica na metu, većina čestica iz snopa bi se samo elastično rasejala bez da stupe u reakciju fuzije [76]. Druga mogućnost za pokretanje reakcije fuzije jeste zagrevanje gasne smeše deuterijuma i tricijuma tako da sada svaka čestica mora da ima energiju od 0.25 MeV. To znači da temperatura gase mora da bude $E = kT \Rightarrow T = \frac{0.25 \text{ MeV}}{8.6 \times 10^{-5} \text{ eVK}^{-1}} \simeq 3 \times 10^9 \text{ K}$. Dakle, potrebno je dostići temperaturu od nekoliko milijardi stepeni celzijusa. Ova temperatura ostvariva je u Sunču zbog njegove ogromne mase, pa je plazma konfinirana gravitacionim poljem. Neke od razmatranih reakcija fuzije na Zemlji su sledeće [32]:





Odluka da se fuzija pokuša ostvariti u reakcijama koje uključuju deuterijum i tricijum (prva reakcija) doneta je na osnovu izračunatih preseka za reakciju prikazanih na slici 7. Vidi se da D - T reakcija ima maksimum na najnižoj temperaturi i takođe ima najveću verovatnoću od svih reakcija. Mana ove reakcije jeste što u svakoj reakciji nastaje neutron koji može da bude apsorbovan na površini zida reaktora. Apsorpcija neutrona negativno utiče na životni vek komponenti zida reaktora jer apsorpcijom neutrona metali postaju krči i radioaktivni [32]. Zbog toga, za drugu generaciju reaktora očekuje se da će raditi sa drugim tipovima reakcija koje ne uključuju neutrone. Ipak, mora se uzeti u obzir i nivo poteškoća u njihovom ostvarivanju.



Slika 7: Presek za reakcije za različite razmatrane fuzione reakcije. Verovatnoća za D - T reakciju dostiže maksimum pri najnižoj temperaturi. Slika preuzeta iz [32]

Pod pretpostavkom da reaktor radi sa D - T mešavinom u odnosu 50 % - 50 % Lawson [32] je izveo kriterijum za minimalnu temperaturu rada reaktora. Prvo se definiše dobitak u snazi iz fuzionih reakcija Q kao $Q = \frac{P_{fusion}}{P_{aux}}$. Kako bi fuzija bila komercijalno isplativa, minimalan uslov je $Q > 1$. Balans gubitaka i grejanja plazme daje [32]:

$$P_h = P_{aux} + P_\alpha - P_{Br} = P_{trans} + \frac{dW_p}{dt} \quad (76)$$

Pri čemu je P_{aux} grejanje plazme spoljašnjim metodama (ubrizgavanje neutralnih čestica, elektron - ciklotronsko grejanje itd.), P_α je grejanje plazme kroz sudare sa α česticama, P_{Br}

su gubici usled zakočnog zračenja, P_{trans} su gubici usled različitih transportnih procesa a $\frac{dW_p}{dt}$ predstavlja promenu termalne energije plazme. Dalje, P_{alpha} i P_{Br} možemo proceniti kao [32]:

$$P_\alpha = n_D n_T \langle \sigma v \rangle E_\alpha V_p = \frac{n_e^2 \langle \sigma v \rangle E_\alpha V_p}{4} \quad (77)$$

$$P_{Br} = C_B T_e^{\frac{1}{2}} n_e^2 V_p \quad (78)$$

Gde je pretpostavljeno da je $n_D = n_T = n_e$, a $\langle \sigma v \rangle$ predstavlja srednji presek za sudar reaktnata, E_α je energija α čestice, V_p je zapremina plazme, a $W_p = 3n_e k T_e V_p$ je termalna energija plazme. Transportni gubici procenjuje se kroz parametar vremena konfiniranja energije τ_E definisanim sa:

$$\tau_E = \frac{W_p}{(P_h - \frac{dW_p}{dt})} \quad (79)$$

Jednačina (76) sada se može napisati kao [32]:

$$n_e^2 \langle \sigma v \rangle E_\alpha \frac{Q+5}{4Q} - C_B T_e^{\frac{1}{2}} n_e^2 = \frac{3n_e k T_e}{\tau_E} + \frac{d}{dt}(3n_e k T_e) \quad (80)$$

U stacionarnom stanju, $d/dt = 0$, dobijamo da je [32]:

$$n_e \tau_E = \frac{3kT_e}{\frac{\langle \sigma v \rangle E_\alpha (Q+5)}{4Q} - C_B T_e^{\frac{1}{2}}} \quad (81)$$

Postavljanjem $Q = 1$, dobijamo Lawsonov kriterijum koji je dat sa:

$$n_e \tau_E = \frac{3kT_e}{\frac{3\langle \sigma v \rangle E_\alpha}{2} - C_B T_e^{\frac{1}{2}}} \quad (82)$$

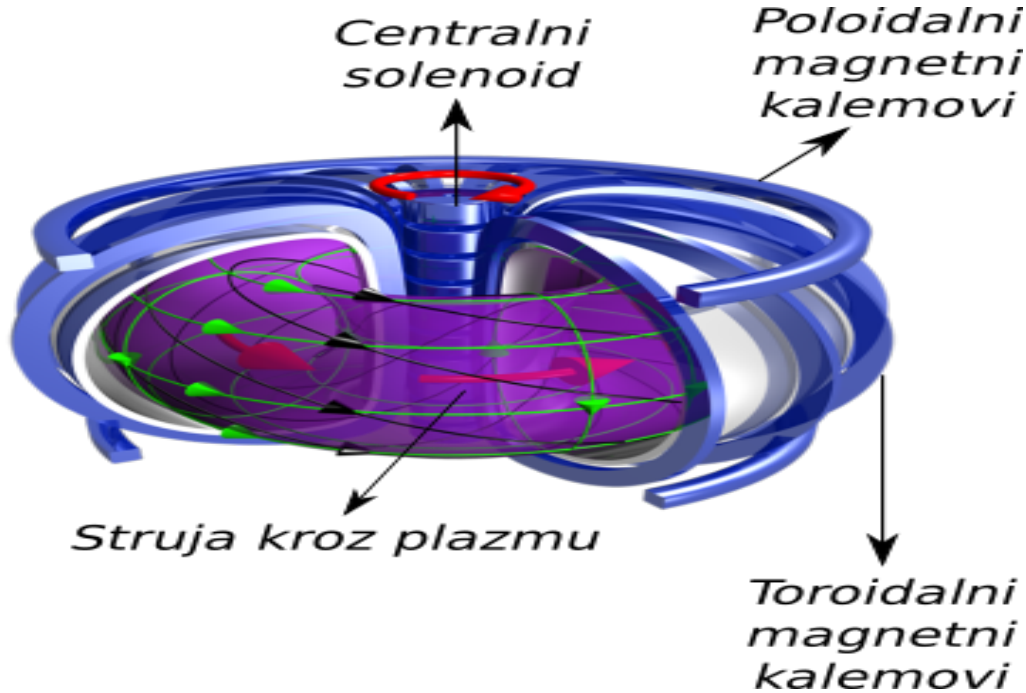
Za $T_e = 15keV$, pri čemu $\langle \sigma v \rangle \sim T_e^2$, Lawsonov kriterijum postaje:

$$n_e T_e \tau_E > 1.5 \times 10^{21} \text{ keV} \cdot \text{s} \cdot \text{m}^{-3} \quad (83)$$

Izraz (83) predstavlja uslov da fuzioni rektor proizvede istu količinu energije koja je uložena u njegov rad, pod pretpostavkom da su najdominantniji gubici oni usled zakočnog zračenja. U ostalim slučajevima, članovi koji uračunavaju ostale gubitke mogu se pojaviti u imeniocu jednačine (82) (npr. ciklotronska emisija) [32].

2.4.1 Načini konfiniranja visokotemperaturne plazme

U praktičnim pokušajima ostvarivanja fuzije na Zemlji, trenutno se razmatraju i u upotrebi su dva načina konfiniranja visokotemperaturne plazme. Jedan način konfiniranja je *magnetno konfiniranje plazme*, gde se plazma konfinira tako što se konfiguracijom magnetnog polja oko plazme postižu zatvorene trajektorije čestica i stabilne orbite. Drugi način konfiniranja je *inercijalno konfiniranje plazme*, gde se upotreboom snažnih laserskih zraka postiže implozija peleta sa gorivom i konfiniranje plazme. Podaci korišćeni u ovoj tezi dobijeni



Slika 8: Tokamak. Centralni solenoid indukuje struju kroz plazmu, koja potom konfinira plazmu svojim magnetnim poljem. Pošto magnetno polje indukovano protokom struje kroz plazmu nije dovoljno za stabilno konfiniranje plazme, dodatno se koriste toroidalni kalemovi kao i poloidalni magnetni kalemovi za pozicioniranje plazme.

su u uređaju koji radi na principu magnetnog konfiniranja plazme, pa će samo o ovom konfiniranju biti reči u nastavku teksta. Više o inercijalnom konfiniranju može se pročitati u predloženoj literaturi [32, 77].

Magnetno konfiniranje se može realizovati pomoću dva uređaja, *tokamak* i *stelerator*. Tokamak predstavlja uređaj koji suštinski funkcioniše kao transformator i prikazan je na slici 8. Oko centralnog solenoida, postavljen je torusni vakuumski sud u kojem se konfinira plazma. Puštanjem struje kroz centralni solenoid, što predstavlja primar transformatora, indukuje se struja kroz plazmu koja predstavlja sekundar transformatora. Struja kroz plazmu stvara pinč efekat, koji konfinira plazmu. Međutim, ovo polje samo po sebi nije dovoljno da bi plazma bila stabilno konfinirana, jer magnetno polje same struje kroz plazmu dovodi do razdvajanja pozitivnih i negativnih nanelektrisanja i pojave električnog polja koji potom uzrokuje $\mathbf{E} \times \mathbf{B}$ drift jona i elektrona ka zidu reaktora. Da bi se to sprečilo, kao i da bi se vršila korekcija oblika i pozicije plazme u reaktoru koriste se toroidalni i poloidalni magneti. Zajedničkim delovanjem ovih magneta postiže se spiralna trajektorija čestice zatvorene unutar mašine, odnosno postiže se konfiniranje čestica unutar uređaja [78]. Kao mera stabilnosti reaktora, uvedena je veličina koja se naziva faktor sigurnosti q_s čija nam vrednost govori koliko krugova čestica u plazmi napravi toroidalno dok se njena trajektorija ne zatvori poloidalno. Definisan je kao [79]:

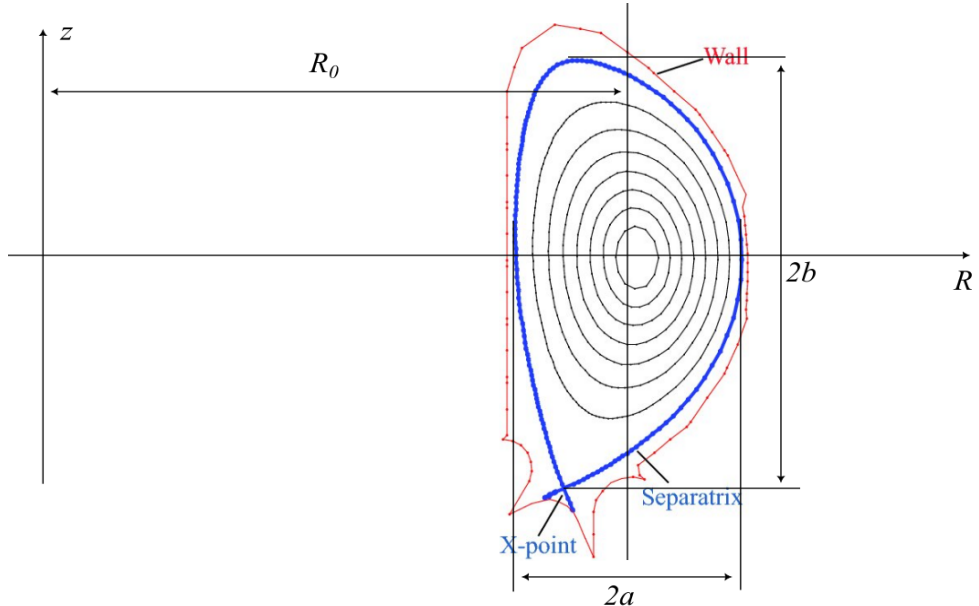
$$q_s = \frac{1}{\iota} = \frac{r B_\varphi}{R_0 B_\theta} \quad (84)$$

Ovde ι predstavlja rotacioni transform (eng. *rotational transform*), veličinu koja se koristi

češće u steleratorima, B_φ je toroidalno magnetno polje a B_θ predstavlja poloidalno magnetno polje. Rotacioni transform zapravo daje meru uvrnutosti magnetnog polja u stelerotoru kada se prati toroidalno. Može se reći da nam rotacioni transform ι daje broj poloidalnih rotacija po jednoj toroidalnoj rotaciji. Primećuje se da rotacioni transform zavisi od radikalne koordinate, i ta zavisnost tj. veličina promene rotacionog transforma se zove *magnetno smicanje* (eng. *magnetic shear*) [79]:

$$s = \frac{r}{q_s} \frac{dq_s}{dr} \quad (85)$$

Veća vrednost magnetnog smicanja je bolja za stabilan rad steleratora i tokamaka. Naime, ako imamo neke radikalne strukture ili nestabilnosti, pošto se čestice plazme kreću duž linija magnetnog polja, zbog postojanja smicanja postoji mogućnost da se ova nestabilnost "razmaže" u poloidalnom pravcu. Tada kažemo da je nestabilnost dekorelisana.



Slika 9: Poloidalni poprečni presek tokamaka [80]. Na slici su prikazane zatvorene magnetne površi i poslednja zatvorena linija magnetnog polja sa X - tačkom koja se naziva separatrix. Такође су oznaчени svi parametri koji ulaze u definiciju elongacije i trijangulariteta.

Eksperimentima je utvrđeno da je sa stanovišta nečistoća unetih u plazmu povoljnija konfiguracija sa divertorom nego sa limiterom, pa zbog toga oblik plazme više nije kružni nego izdužen i u obliku latiničnog slova D, kao na slici 9. Ovakvom konfiguracijom se postiže da otvorene linije magnetnog polja završavaju na divertoru čija je primarna uloga odvođenje čestica i viška toplice iz reaktora. Plazma se u divertorskoj konfiguraciji karakteriše sa dva parametra, a to su elongacija κ i trijangularitet δ . Elongacija κ definisana je kao odnos visine plazme i radiusa plazme a :

$$\kappa = \frac{z_{max} - z_{min}}{2a} = \frac{2b}{2a} \quad (86)$$

Dok je trijangularitet dat sa izrazom:

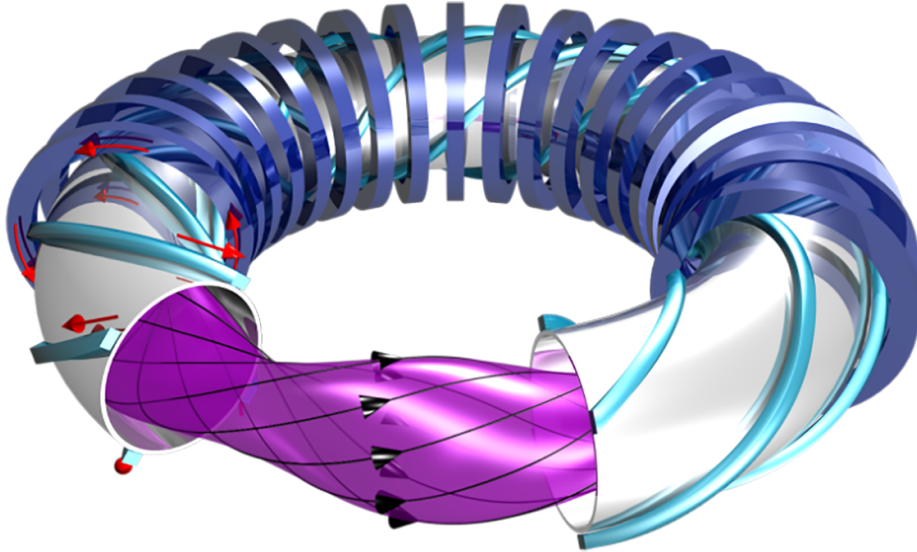
$$\delta = \frac{\delta_{upper} + \delta_{lower}}{2} \quad (87)$$

Pri čemu su δ_{upper} i δ_{lower} gornji i donji triunglaritet, dati sa izrazima [79]:

$$\delta_{upper} = \frac{R_0 - R(z = z_{max})}{a} \quad (88)$$

$$\delta_{lower} = \frac{R_0 - R(z = z_{min})}{a} \quad (89)$$

Linije magnetnog polja prolaze unutar ugnježdenih površi magnetnog fluksa, a poslednja zatvorena površ se naziva *separatrix* (eng. *separatrix*). Konfiniranje plazme u tokamaku nije lak zadatak, a eksperimentalno je utvrđeno da vreme konfinranja energije raste sa porastom veličine mašine, tj. važi da je $\tau \sim r_p$, gde je r_p radius plazme unutar tokamaka (rastojanje od centra vakuumske komore do zida reaktora) [78]. Takođe, vreme konfiniranja energije raste sa povećanjem struje kroz plazmu, a opada sa pritiskom plazme [78].

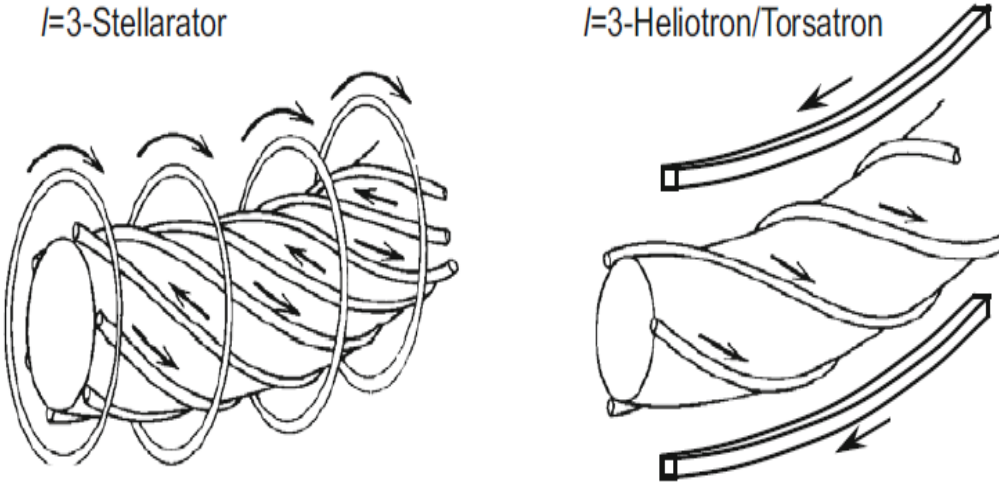


Slika 10: Klasični stelerator $l = 2$. Oblici i pozicije spoljašnjih magneta su takve da su linije sila magnetnog polja zatvorene bez potrebe za propuštanjem struje kroz plazmu.

Pošto je sam protok struje kroz plazmu u tokamacima izvor raznih nestabilnosti plazme i prepreka ka stabilnom radu reaktora, ispitivani su alternativni vidovi konfiniranja plazme pomoću spoljašnjih magnetnih polja. Jedna od najuspešnijih alternativa do kojih su naučnici uspeli da dođu jeste stelerator. Kod steleratora se zatvaranje linija magnetnog polja unutar uređaja i stabilne orbite postižu uvrтанjem spoljašnjih magneta tako da prave željeno magnetno polje [77]. S tim u vezi, za konfiniranje plazme nije potrebna struja koja prolazi kroz plazmu, već se konfiniranje vrši isključivo spoljašnjim magnetnim poljem. Prednost ovog dizajna jeste što se izbegavaju nestabilnosti koje nastaju unutar tokamaka, a čiji je uzrok upravo prolazak struje kroz plazmu [77].

Stelerator se može projektovati na tri načina, a glavni cilj je postizanje helikalnog magnetnog polja čije su linije sila zatvorene unutar torusa. Jedan način za postizanje helikalnog magnetnog polja je prikazan na slici 10. Kroz helikalne kalemove označene svetlo plavom bojom na slici propušta se struja u suprotnim pravcima, a na to polje se superponira jako

toroidalno polje nastalo dejstvovanjem toroidalnih kalemova označenih tamno plavom bojom na slici 10. Steleratori se karakterišu sa dva broja, koji se najčešće označavaju sa l i m . Broj l najčešće ukazuje na broj helikalnih kalemova. Za stelerator na slici 10 imamo 2 para od po 4 kalemova sa suprotnim strujama, što znači da ima broj $l = 2$. Kako se magnetne površi periodično ponavljaju u toroidalnom pravcu, broj tih toroidalnih segmenata označavamo sa m .



Slika 11: $l = 3$ stelerator (levo) i torsatron [79] (desno). Primetno je postojanje poloidalnih magneta kod torsatrona kako bi se dobilo helikalno magnetno polje. Struje kod torsatrona idu u istom pravcu, dok kod klasičnog steleratora struje susednih kalemova su antiparalelne.

Drugi način da se postigne sličan efekat uvrtanja magnetnog polja i rezultujuće helikalno magnetno polje jeste konstrukcija tzv. *heliontra* ili *torsatrona*. Kod heliontra, struja kroz helikalne kalemove teče u istom pravcu, pa broj l odgovara broju helikalnih kalemova. Kako bi se postiglo helikalno magnetno polje, pored helikalnih kalemova dodaju se i poloidalni kalemovi koji prave vertikalno magnetno polje kako bi se dobilo željeno rezutujuće magnetno polje. Slika ovog uređaja prikazana je na slici 11 desno, a primer jednog ovakvog uređaja je heliontron LHD (Large Helical Device) u Japanu koji je heliontron sa $l = 2$ i $m = 10$.

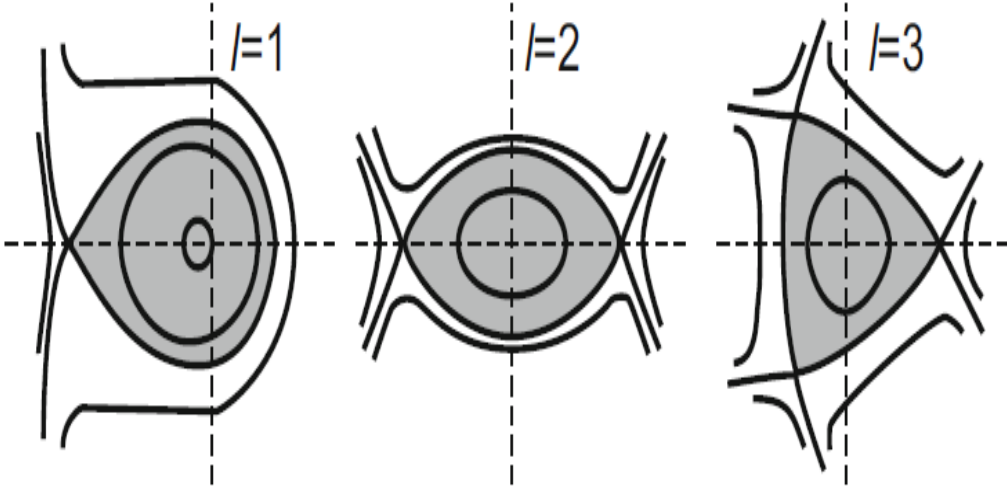
Treći način za kreiranje helikalnog magnetnog polja jeste da se spoljašnji kalemovi poređaju tako da prave helikalnu magnetnu osu. Ovi uređaji se još nazivaju *helijaci*. Taj dizajn koristi stelerator TJ - II u Madridu. Optimizovani steleratori, kao što je Wendelstein 7X u Greisfaldu koristi unapređeni dizajn helijaka. Njegovih 50 neplanarnih i 20 planarnih magneta su specijalno optimizovani i napravljeni kako bi uređaj postigao najbolje performanse u smislu magnetohidrodinamičke (MHD) stabilnosti, gustine plazme i dobrog konfiniranja visoko energetskih čestica (α čestica npr.). On je $m = 5$ stelerator.

Teorijski, pokazuje se da uvrtanje magnetnog polja prati uvrtanje magnetnih kalemova, međutim ovo uvrtanje po periodu toroidalnog obilaska ima jako mali doprinos jer se skalira kao [79]:

$$r \frac{d\theta}{dz} \propto \frac{1}{B_{z0}^2} \quad (90)$$

Gde je B_{z0} toroidalno magnetno polje. Dakle, kako bi steleratori postigli jako uvrtanje mag-

netnog polja (veliko ι), oni moraju imati veliki broj perioda ili segmenata sa magnetima, odnosno veliki odnos glavnog radiusa i radiusa plazme (*aspect ratio*). Veliko ι je povoljno za stabilnost reaktora kao i za efikasnost reaktora. Što se tiče magnetnih površi u steleratoru, one suštinski predstavljaju magnetne multipole, a na slici 12 prikazane su magnetne površi za $l = 1, 2$ i 3 steleratore. Vidimo da je u slučaju $l = 2$ poloidalni poprečni presek ima oblik



Slika 12: Izgled magnetnih površi za $l = 1, 2$ i 3 steleratore [79].

elipse, dok je za $l = 3$ poloidalni presek u obliku trougla.

2.4.2 Interakcija plazme sa zidom reaktora

Interakcija plazme sa zidom fuzionog reaktora je vrlo važan segment u istraživanju stabilnog rada reaktora, jer ukoliko čestice nečistoća sa zida udružuju se u plazmu, ona gubi energiju kroz zračenje te postaje nestabilna i gasi se. Takođe, čestice nečistoća mogu da izazovu i disruptcije, gde dolazi do naglog hlađenja ivice plazme [32]. Dva glavna problema do kojih interakcija vruće plazme sa zidom može dovesti je da se ošteti komponenta vakuumskog suda prvog zida reaktora, te kontaminacija plazme i nemogućnost ostvarivanja fuzionsih reakcija. Izvor čestica nečistoća jeste u raznim interakcijama plazme i materijala zida reaktora, procesima desorpcije kao i iz samih fuzionsih reakcija (tzv. helijumski "pepeo"). Kako bi spričeli desorpciju i otpuštanje *bulk* materijala iz zida reaktora, rade se različiti tretmani zida koji uključuju čišćenje zida tinjavim pražnjenjem ili odgrevanjem zidova. Pored gore navedenih procesa, na pojavu čestica nečistoća u plazmi utiču još i spaterovanje zida reaktora, hemijska erozija, isparavanje i formiranje balončića na površini zida (eng. *blistering*) [81].

2.4.2.1 Fizičko spaterovanje

Fizičko spaterovanje zida reaktora predstavlja proces transfera impulsa visokoenergetskog jona na atom mete u zidu koji se time oslobođa i odlazi u plazmu. Ovaj proces nastaje kada je energija upadnog jona veća od energije veze E_s atoma na površini mete. Za spaterovanje, definiše se tzv. *prinos spaterovanja* (eng. sputtering yield), koji predstavlja krucijalnu veličinu

za ovaj proces [81]:

$$Y = \frac{\text{broj emitovanih atoma mete}}{\text{broj upadnih čestica}} \quad (91)$$

Kako bi opisali koliko čestica mete sa energijom $E, E + dE$ biva spaterovano u jedinični prostorni ugao $d\Omega$ uvodi se diferencijalni prinos spaterovanja definisan relacijom [81]:

$$\frac{d^2Y}{dEd\Omega} \quad (92)$$

Obično se razlikuju tri režima spaterovanja: (1) režim nekoliko sudara, (2) kaskadni režim i (3) režim termalnog pika (eng. *thermal spike regime*) [81]. Prvi režim se javlja za luke projektila i za male energije projektila. Tu razlikujemo dva procesa a to su uzmicanje atoma mete prve i druge generacije, dok za manje energije dolazi i to rasejanja projektila unazad [81]. Sa povećanjem energije projektila i njihove mase, dešava se uzmicanje i emisija atoma mete nekoliko generacija. Tako se pravi kaskadni proces u kome atomi koji se nalaze dublje u meti mogu dobiti dovoljno energije da napuste metu, te ostaje krater na materijalu koji se primećuje u eksperimentima [81]. Prinos spaterovanja može se proceniti kao odnos upadne energije projektila E_{dep} na sloj debljine d i energije veze na površini mete E_s [81]:

$$Y = \frac{E_{dep}}{E_s} \quad (93)$$

Deponovana energija E_{dep} se može proceniti iz izraza [81]:

$$E_{dep} = n_0 S_n(E_0) d \quad (94)$$

Gde je n_0 gustina atoma u meti, $S_n(E_0)$ predstavlja presek za zaustavljanje projektila koji zavisi od upadne energije projektila E_0 , a d je debljina posmatranog sloja mete. Ovi preseci su dostupni u literaturi za razne vrste projektila. Bitno je reći da u procesima fizičkog spaterovanja čestice mete napuštaju metu prvenstveno kao neutralni, dok jako mali deo bude u obliku jona. Po pitanju koncentracija nečistoća, za luke čestice to je nekoliko procenata (npr. C i O) dok je za teške čestice ta koncentracija reda veličine nekoliko promila (npr. W i Mo) [77].

2.4.2.2 Hemijsko spaterovanje

Hemijska erozija zida reaktora nastaje kada se u interakciji upadnog projektila i atoma mete formiraju lako isparljivi molekuli koji napuštaju metu i ulaze u plazmu. Ovaj proces je jako važan za materijale od ugljenika, jer u reakcijama između upadnih atoma vodonika ili kiseonika dolazi do emisije različitih molekula ugljovodonika i oksida ugljenika [81]. Rešenje za uklanjanje ugljenikovih oksida CO i CO₂ jeste smanjenje koncentracije kiseonika u reaktoru.

Što se tiče ugljovodonika, istraživanja su pokazala da se grejanjem površine prvo isparava CH₃ molekul, a daljim povećanjem temperature rekombinacija vodonika u molekul H₂ postaje dominantan proces što smanjuje ukupan prinos hemijskog isparavanja [81]. Još jedan mehanizam hemijske erozije predstavlja tzv. jonsko - indukovana desorpcija. Pri ovom procesu, upadni jon ima dovoljno energije da sa površine izbaci ugljovodonične radikale sa niskom

energijom sublimacije putem raskidanja veze [81]. Hemijsko spaterovanje je jako teško opisati teorijski jer pored temperature površine mete, energije upadnih jona i upadnog fluksa, zavisi i od strukturalnih osobina same mete ugljenika i hemijskog sastava mete. Npr. primećeno je da se dodavanjem bora ili nekih metala (Ti) značajno menja i prinos nečistoća [81]. Dalje, primećeno je da ubacivanje plemenitih gasova u plazmu kako bi se povećalo zračenje plazme u okolini divertora značajno povećava hemijsko spaterovanje usled jako efikasnog raskidanja veze C-H u materijalu.

Pošto i dalje nedostaju simulacije koje bi dobro opisale ovaj tip spaterovanja (prvenstveno se rade simulacije molekularne dinamike) u drugim kodovima koji opisuju globalni prinos nečistoća u plazmu uvek se podrazumeva konstantran prinos od hemijskog spaterovanja koji iznosti negde oko 0.01 ili 0.02.

2.4.2.3 Termalno isparavanje

Porastom temperature površine mete, sve više atoma ima energiju da napusti površinu mete. Fluks nečistoća u plazmu može se proceniti na sledeći način [81]:

$$\Gamma_{subl} = s 2 \times 10^{24} \frac{p(T_s)}{\sqrt{MT_s}} \frac{\text{atoms}}{\text{m}^2\text{s}} \quad (95)$$

Gde je p napon pare koji zavisi od temperature površine mete, dok je s tzv. *sticking* koefficijent. Njegova vrednost za grafit je između 0.6 i 0.9 [81]. Za grafit, gornji izraz se može napisati i kao [81]:

$$\Gamma_{sub}^C = C_{sub} T_s^g e^{-\frac{E_s}{k_B T_s}} \quad (96)$$

Pri čemu je $C_{sub} = 2 \times 10^{20} \text{K}^{3.25}/\text{s}$, $g = 3.25$ i $E_s = 7.42 \text{ eV}$.

Ovi procesi su neizbežni na takozvanim vodećim ivicama divertora, gde linije sila magnetnog polja padaju normalno na divertorsku ploču.

2.4.2.4 Pojava balončića (Blistering)

Pojava balončića predstavlja proces do kojeg dolazi blizu površine mete zbog loše rastvorenih gasova. U eksperimentima prilikom bombardovanja mete sa atomima vodonika i helijuma, dolazi do ove reakcije pri velikim energijama po jediničnoj površini mete [81]. Helijum i vodonik se talože unutar pora uzorka jer je to energetski povoljnije nego ugradnja samog atoma u rešetku mete. Eksperimentima je pronađeno da je kritična vrednost za formiranje balončića helijuma u volframu reda $0.5 \times 10^{22} \text{He/m}^2$ pri čemu je prosečni dijmetar balončića oko $130 \mu\text{m}$ [81].

2.4.3 Problem akumulacije nečistoća sa velikim atomskim brojem Z

Ono što je primećeno u eksperimentima na TEXTOR tokamaku od strane Tokar-a i saradnika [82, 83] i potvrđeno u mnogim kasnijim studijama jeste akumulacija nečistoća u jezgru plazme koje je praćeno masivnim zračenjem energije iz centra plazme i zaravnavanjem profila elektronske temperature. Najčešće se ova nestabilnost objašnjava neoklasičnim transportom [83].

Naime, kada nečistoće putem nekog od gore navedenih procesa uđu u plazmu, dešava se

da usled sudara čestica nečistoća nanelektrisanja Z sa pozadinskom plazmom imamo profil gustine nečistoća koji ima izraženiji maksimum (pik) od profila gustine glavnih jona u plazmi. Pošto neki atomi dospeju u jezgro plazme, član u neoklasičnoj brzini proporcionalan sa $\frac{\partial T}{\partial r}$ usmeren ka ivici plazme se smanjuje. Kao posledica toga, javlja se ukupni fluks čestica usmeren ka centru plazme koji dalje nagomilava čestice nečistoća u plazmi i smanjuje temperaturu plazme. Ova akumulacija se može izbeći tako što se npr. izbegavaju profili gustine koji imaju izražen centralni maksimum [81].

Eksperimentalno je uviđeno da postoji određena korelacija između akumulacije nečistoća u jezgru plazme i gustine elektrona u plazmi. Ova korelacija je uočena i u tokamaku TEXTOR [82] i u heliontronu LHD. Naime, što je gustina elektrona veća, čestice nečistoća se duže zadržavaju u plazmi i imaju dugačka vremena poluživota (i do nekoliko sekundi) dok za manje gustine vreme poluživota nečistoća u plazmi se dosta smanjuje. Radijalni fluks nečistoća Z dat je sa izrazom [83]:

$$\Gamma_Z = -D_{\perp}^Z \frac{dn_Z}{dr} + v_{\perp}^Z n_z \quad (97)$$

i predstavlja sumu difuzionog i konvektivnog člana. Konvekcija se opisuje neoklasičnom transportnom teorijom, gde je brzina određena gradijentima gustine i temperature pozadinskih jona (najčešće deuterijuma) [83]:

$$v_{\perp}^Z = D_{neo} \left(\eta \frac{d \ln n_i}{dr} + \theta \frac{d \ln T_i}{dr} \right) \quad (98)$$

U gornjem izrazu D_{neo} je neoklasični koeficijent difuzije, a n_i i T_i su gustina i temperatura jona u plazmi. Parametri η , θ kao i koeficijent difuzije D_{neo} određeni su sa n_i , T_i , faktorom sigurnosti q i vrednošću toroidalnog magnetnog polja B_t . U konvencionalnim fuzionim uređajima, član proporcionalan gradijentu gustine jona usmeren je ka centru plazme i odgovoran je za pik u gustini nečistoća, dok drugi član teži da izbalansira ovaj transport [83]. Pad temperature u centru, iz bilo kog razloga, dakle smanjuje član koji sprečava konvektivni transport ka centru plazme i kreće akumulacija nečistoća. Kako čestice nečistoća uđu u centar plazme, zračenjem temperatura plazme u centru dalje opada, što dalje dovodi do smanjenja člana $\frac{d \ln T_i}{dr}$ i dalje akumulacije, pa se tako razvija nestabilnost plazme [83]. Tokar i saradnici su takođe dali predlog izraza za kritičnu vrednost gustine elektrona u jezgru plazme pri kojoj dolazi do pojave akumulacije nečistoća u centru plazme [83]:

$$n(0)_c = \frac{8D_{\perp}\kappa_{\perp}T(0)}{r_{max}^2 D_{neo}^{PS} Z_I n_I(0) L_I} \quad (99)$$

U gornjem izrazu, κ_{\perp} predstavlja koeficijent topotne provodnosti plazme, D_{neo}^{PS} predstavlja koeficijent neoklasične difuzije u Pfirsch - Schlüter režimu (režim male kolizionalnosti), $Z_I = \sum \frac{Z n_z}{n_I}$ predstavlja srednje nanelektrisanje nečistoća u plazmi, n_I predstavlja ukupnu gustinu nečistoća u plazmi, L_I je tzv. koeficijent brzine hlađenja (eng. *cooling rate coefficient*) nečistoće u plazmi, a r_{max} je parametar dat sa izrazom [83]:

$$r_{max} = \frac{1}{\sqrt{\frac{32D_{\perp}^2}{D_{neo}^{PS} Z_I \omega_{rad}} + \frac{1}{a^2}}} \quad (100)$$

Gde je a radius plazme, a $\omega_{rad} = \frac{L_I n_I}{3T}$ u cgs sistemu jedinica.

2.5 Mašinsko učenje i veštačka inteligencija

Mašinsko učenje predstavlja skup metoda koje mogu da otkriju šablove i relacije između ulaznih podataka u toku treninga, te da korištenjem nađenih relacija predvide nove vrednosti za ulazne parametre koje model do tada nije video.

Većina algoritama mašinskog učenja mogu se podeliti u dve grupe: regresioni modeli, koji kao izlaz daju numerički rezultat i klasifikacione modele, koji kao izlaz najčešće daju verovatnoću da neki objekat pripada određenoj klasi. Kako bi uspeli u ovome, oni moraju da budu obučeni na nekoj bazi podataka koja sadrži reprezentativne uzorke posmatranog problema. Postoje generalno dva načina treninga: *nadgledano učenje* i *nенадгледано учење*. Nadgledano učenje je najčešći oblik upotrebe, a pod njim se podrazumeva da model nauči funkciju preslikavanja sa ulaznih podataka \mathbf{x} ili atributa, koji su u određenom trenutku bili obeleženi ili obrađeni od strane čoveka na izlazne podatke y ili ciljne varijable tako što se obučava na parovima ulazno - izlaznih podataka $\mathcal{D} = \{(\mathbf{x}, y)\}_{i=1}^N$ [84]. Kako bi procenili veličinu odstupanja predikcije modela od tačne vrednosti ciljne varijable uvodi se *funkcija greške* $L(y, f(x))$. Za svaki model može se definisati njegova funkcija greške, pa samim tim nije jedinstvena. Pod obeležavanjem podataka se misli npr. da u svrhu klasifikacije često čovek mora da označi tačnu klasu svakog objekta, kako bi modeli bili u mogućnosti da kasnije predvide klasu za objekte koji nisu označeni. Isti je slučaj i u regresionej analizi, gde model treba da predviđa neku numeričku vrednost na osnovu ulaznih podataka. Ovde često čovek obrađuje sirove podatke dobijene na neki način (merene u nekom eksperimentu, podaci sa interneta itd.) te tako prilagođava podatke kako bi ih model što bolje naučio i imao bolji performans. Sa druge strane, u slučaju nенадгледаног учења, čovek nema nikakvog kontakta sa sirovim podacima koji služe kao ulazni podaci za model. Ovi algoritmi najčešće služe kao modeli za klasterovanje, tj. grupaciju sličnih tačaka jednih drugima. Na ovaj način mogu se detektovati pravilnosti u podacima i eventualno naći odudarajući podaci koji bi inače pokvarili performans modela ako bi bili ostavljeni u bazi za trening.

Duboko učenje sa druge strane predstavlja upotrebu neuronskih mreža kako bi one uspele da donesu dobre zaključke bez intervencija čoveka. Termin duboko učenje potiče od toga da se vrlo često koriste neuronske mreže sa više od jednog sloja. Neuronske mreže mogu se obučavati kako za zadatke regresije, tako i za zadatke klasifikacije. Razne su podele neuronskih mreža, npr. prema načinu obučavanja, prema arhitekturi, prema načinu prostiranja informacija kroz mrežu itd. Kako su u ovom radu korišteni samo regresioni modeli, kao i generativni modeli, u nastavku će reći biti samo o njima, a o klasifikacionim algoritmima čitalac se upućuje na odgovarajuću literaturu [85]. Takođe, neće biti reči o prostim linarnim modelima mašinskog učenja jer nisu korišteni u ovom radu. Biće obrađeni samo nelinearni modeli mašinskog učenja i to ansamblji, kao i neuronske mreže i generativni modeli.

2.5.1 Ansamblerski nelinearni modeli

Ansambli predstavljaju skup više modela koji zajednički donose neku odluku. Ključna pretpostavka kod ovih modela jeste ta, da ukoliko imamo veći skup modela, oni mogu dati mnogo veću preciznost u odnosu na jedan model, ukoliko su pravilno konstruisani [84]. Ova pretpostavka zasniva se na činjenici da ćemo usrednjavanjem pojedinačnih predikcija N nezavisnih modela dobiti vrednost koja je jako bliska pravoj, jer će se nezavisne slučajne greške koje ovi modeli prave u mnogome poništiti.

2.5.1.1 Prosta agregacija (*Bootstrap aggregation* ili *Bagging*)

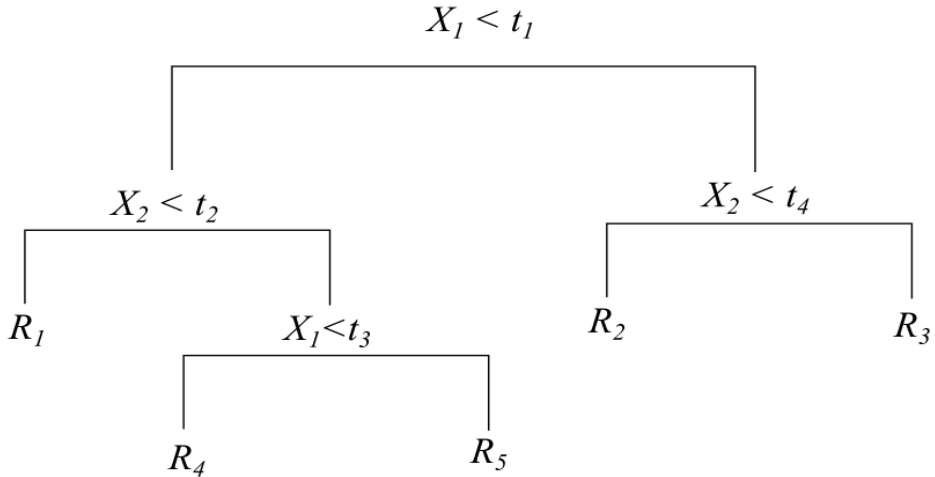
Prosta agregacija je postupak u kome se obučava veći broj modela čije predikcije moraju nužno da budu precizne, ali je bitno da su im greške nezavisne [84]. U slučaju regresije, modeli daju svoju vrednost koja se kasnije usrednjava kako bi se dobila konačna vrednost predikcije. U slučaju klasifikacije, vrši se glasanje. U slučaju regresije, koji je od interesa u ovoj tezi, ukoliko modele posmatramo kao m slučajnih nezavisnih promenljivih X_1, X_2, \dots, X_m od kojih svi imaju istu raspodelu opisanu sa srednjom vrednosću μ i varijansom σ^2 , onda na osnovu centralne granične teoreme važi [84]:

$$\sqrt{m} \left(\frac{1}{m} \sum_{i=1}^m X_i - \mu \right) \rightarrow \mathcal{N}(0, \sigma^2) \quad (101)$$

Dakle, važi da model ima očekivanu vrednost μ i varijansu σ/m . Ukoliko je μ tačna vrednost koju model treba da proceni, onda modeli proste agregacije nude smanjenje varijanse bez povećanja sistemskog odsupanja [84]. Jedan od najrasprostranjenijih ansambl modela jeste slučajna šuma, klasa CART (Classification and Regression Trees) algoritama.

2.5.1.2 CART (Classification and Regression Trees) algoritmi

CART algoritmi predstavljaju grupu algoritama koji se koriste za klasifikaciju i regresiju. Osnovni model, nad kojim se kasnije gradi ansambl, predstavlja *stablo odlučivanja* ili *drvo odlučivanja*. Jedno drvo odlučivanja predstavljeno je na slici 13.



Slika 13: stablo odlučivanja. Svaki čvor predstavlja uslov tipa if ... then, dok se u listovima nalaze vrednosti nakon obrade uslova u čvoru.

Svako drvo odlučivanja počinje od glavnog čvora ili korena stabla koji sadrži jedan test vrednosti odabranog atributa. Test može imati više rezultata, a svaki od rezultata čini granu koja vodi do sledećeg čvora u kome se nalazi novi test. Listovi predstavljaju predviđanje stabla za ulazni set vrednosti atributa. Na slici, vidimo da ako je ispunjen uslov glavnog čvora da je $X_1 < t_1$ tada granom dolazimo do drugog čvora u kome testiramo vrednost drugog

atributa X_2 . Ukoliko je uslov ispunjen dolazimo do lista u kome je predviđena vrednost R_1 . Ovaj pristup dalje važi za svaki od krajnjih listova sa predviđanjima modela.

Postavlja se pitanje, kako odabratи najbolji atribut koji će biti u glavnom čvorу stablu odlučivanja? Najlakše je ovaj postupak opisati za slučaj problema klasifikacije, a lako se prenosi i na problem regresije. Atribut koji se nalazi u glavnom čvoru mora biti takav da što bolje razdvaja ulazne podatke na podgrupe sa što homogenijim uzorkom u njima [84]. Kako bi ovo bilo moguće, definiše se stepen čistoće izevedene podgrupe nakon razdvajanja. Postoje dva testa: entropija i Gini-jev indeks. I entropija i Gini-jev indeks u osnovi počivaju na udelu u kome učestvuju instance različitih klasa. Entropija se za C klasa definiše kao:

$$H(p_1, \dots, p_C) = - \sum_{i=1}^C p_i \log p_i \quad (102)$$

Gde je p_i udeo klase i u podgrupi. Gornji izraz je jednak nuli kada je udio instance neke klase u podgrupi $p_i = 1$. To znači da je ta podgrupa homogena i entropija je jednak nuli. Dakle, entropija po sebi, shodno i definiciji u fizici predstavlja meru nehomogenosti podgrupe nakon razdvajanja te je cilj da bude što niža. Gini-jev indeks, sa druge strane, se definiše kao:

$$G(p_1, \dots, p_C) = 1 - \sum_{i=1}^C p_i^2 \quad (103)$$

Vidi se da Gini-jev indeks ima vrednost nula kada podgrupa nakon podele ima samo instance jedne klase. Na osnovu nekog od ova dva kriterijuma, računa se smanjenje nehomogenosti podgrupe u odnosu na polazu grupu [84]:

$$H(\mathcal{D}) - \sum_i \frac{|\mathcal{D}_i|}{|\mathcal{D}|} H(\mathcal{D}_i) \quad (104)$$

Ovde skup \mathcal{D}_i predstavlja skup svih instanci gde je vrednost atributa A jednaka i . Ideja jeste da se izračuna razlika nehomogenosti polaznog skupa i prosečne nehomogenosti svih njegovih podskupova dobijenih particionisanjem po vrednostima datog atributa.

Nakon određivanja polaznog glavnog čvora, ostaje još da se odredi i kriterijum zaustavljanja u stablu odluke, tj. potrebno je odrediti kolika će biti dubina stabla ili koliki može biti minimalan broj uzoraka prisutnih u svakom listu. Dubina stabla direktno može uticati na preprilagođavanje i podprilagođavanje modela podacima. Naime, duboka stabla teže da se preprilagode podacima na kojima se obučavaju i da zbog primene velikog broja testova uhvate i neke nebitne specifičnosti u podacima, dok su plitka stabla obično sklona podprilagođavanju podataka na kojima se obučavaju [84]. Što se tiče broja instanci u listu modela, obično je za slučaj regresije bolje imati nešto više uzoraka radi efekta usrednjavanja, kako model ne bi uradio preprilagođavanje podacima ako imamo samo jednu vrednost u listu.

Generalno, model stabla odlučivanja se ne smatra preciznim modelom. Pored gore opisanih problema preprilagođavanja i podprilagođavanja, razlog za to je i visoka varijansa modela koja je delom direktna posledica prirode obučavanja [84]. Sa druge strane, dobre osobine ovog modela jesu njegova interpretabilnost, mogućnost kombinovanja različitih vrsta atributa (numeričkih i kategoričkih) i jako velika efikasnost u vremenu predviđanja.

2.5.1.3 Slučajna šuma

Jedan od načina na koji se može smanjiti varijansa osnovnog modela jeste usrednjavanje vrednosti predviđanja više modela. To se jednostavno postiže obučavanjem M stabala odlučivanja na različitim podskupovima osnovne baze za obučavanje, što za konačan rezultat predikcije daje [86]:

$$f(\mathbf{x}) = \sum_{m=1}^M \frac{1}{M} f_m(\mathbf{x}) \quad (105)$$

Gde je $f_m(\mathbf{x})$ predikcija m -tog stabla odlučivanja za skup ulaznih atributa \mathbf{x} . Iako se koriste nasumični podskupovi podataka, algoritam obučavanja je isti i onda kao rezultat možemo dobiti visoko korelisane prediktore, što u konačnici daje ograničeno smanjenje varijanse [86]. Kako bi se ovo sprečilo, Breiman [87] je u svom radu predložio model slučajnih šuma koje ovaj problem prevazilaze tako što je stabla odlučivanja obučavaju na različitim ulaznim atributima i na nasumično izabranim podskupovima ulaznih podataka. Ova kombinacija čini slučajne šume jako dobrom modelom mašinskog učenja sa visokom tačnošću, pri čemu je i relativno lak za obučavanje. Mana modela jeste nedostatak interpretabilnost, što nadomešćuje brzinom predviđanja i lakoćom obučavanja. Parametri koji mogu da se menjaju za vreme obučavanja model jesu broj stabala m i veličina podskupova instanci i atributa [84].

2.5.2 Neuronske mreže

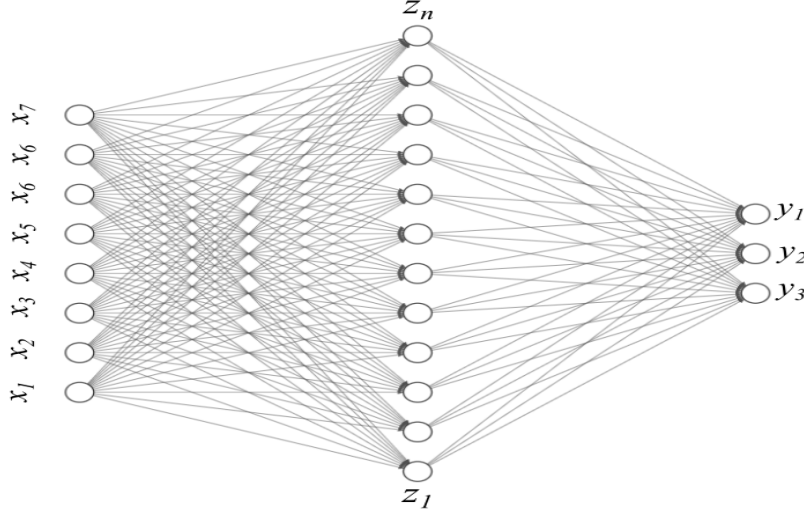
Neuronske mreže predstavljaju klasu metoda veštačke inteligencije koje imaju jako široku upotrebu. Najčešće se ovi algoritmi koriste za konstrukciju modela koji se treniraju na jako velikim bazama podataka i mogu biti jako robusni modeli. Neke od njihovih primena su kompjutersko prepoznavanje objekata, autonomna vožnja, medicinska dijagnostika, obrada teksta itd. [84]. Generalno, neuronske mreže mogu se podeliti na potpuno povezane neuronske mreže, konvolucione neuronske mreže, rekurentne neuronske mreže i grafovske neuronske mreže. Bitno je naglasiti da za trening neuronske mreže mora biti dostupan veliki broj sirovih podataka. Ukoliko je uzorak mali, obučavanje neuronske mreže vrlo lako vodi preprilagođvanju. Međutim, glavna prednost neuronskih mreža jeste da imaju mogućnost da konstruišu nove atrubute prilikom obučavanja na sirovim podacima [84]. Ovde će kratko biti opisane potpuno povezane neuronske mreže i konolutivne neuronske mreže jer su samo one i korištene prilikom izrade ove doktorske disertacije.

2.5.2.1 Potpuno povezane neuronske mreže

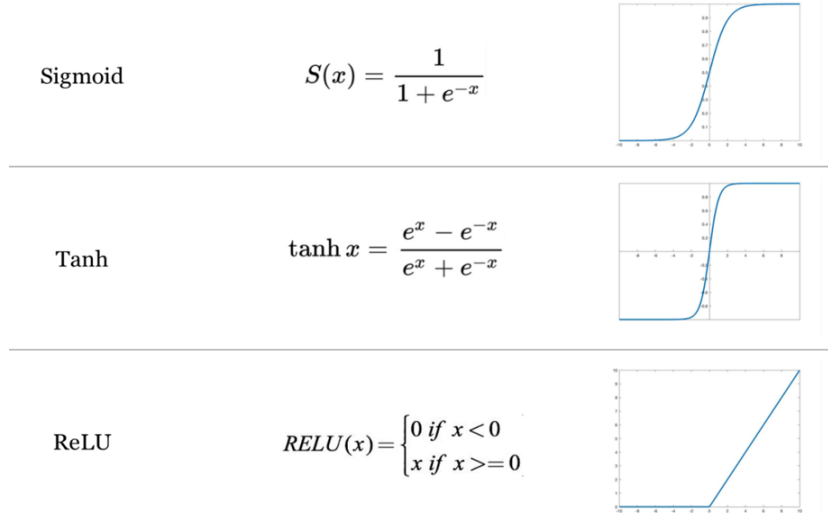
Osnovna gradivna jedinica potpuno povezane neuronske mreže jeste neuron. Tipično, ove neuronske mreže sastoje se od ulaznog sloja, skrivenog sloja i izlaznog sloja. Skrivenih slojeva može biti jedan ili više, čime se razlikuju *plitke* i *duboke* neuronske mreže. Tipična plitka neuronska mreža prikazana je na slici 14. Vidimo da ima ulazni sloj sa 8 neurona, skriveni sloj sa 12 neurona i izlazni sloj sa 3 neurona čija numerička vrednost predstavlja ujedno i rezultat predikcije neuronske mreže. Obično, vrednosti koje uzimaju neuroni u skrivenom sloju date su sledećom jednačinom [88]:

$$z_n = f\left(\sum_{j=1}^N \omega_{jn}^{(1)} x_j + \omega_{j0}^{(0)}\right) \quad (106)$$

Funkcija f u gornjem slučaju naziva se *aktivaciona funkcija* i služi da unese nelinearnost u model. Koeficijenti u linearnej kombinaciji $\omega_{jn}^{(1)}$ predstavljaju težinske vrednosti svakog ulaznog neurona (eng. *weights*) a $\omega_0^{(0)}$ predstavljaju slobodne članove (eng. *bias*).



Slika 14: Prosta potpuno povezana neuronska mreža sa 3 sloja (ulazni, skriveni i izlazni)



Slika 15: Aktivacione funkcije koje se najčešće koriste prilikom obučavanja neuronske mreže

Najčešće aktivacione funkcije koje se koriste u praksi jesu sigmoidna funkcija, hiperbolički tangens, ispravljačka linearna jedinica (ReLU - Rectified Linear Unit). One imaju oblik:

$$\sigma(x) = \frac{1}{1 + e^{-x}}$$

$$\tanh(x) = \frac{e^{2x} - 1}{e^{2x} + 1}$$

$$relu(x) = \max(0, x)$$

Ove funkcije prikazane su na slici 15. Arhitektura potpuno povezanih neuronskih mreža jedna je od najčešće korištenih u veštačkoj inteligenciji. Obučavanje neuronske mreže ovakve arhitekture tipično ide u dva koraka. Prvi korak predstavlja propagaciju unapred, gde se prema jednačini (107) od datih ulaznih vrednosti računa aktivacija za svaki skriveni i izlazni neuron. Drugi korak predstavlja propagaciju unazad, gde modelu saopštavamo grešku te opet postavljamo težinske faktore i slobodne članove na nove vrednosti i ponovo se kreće unapred. Što se tiče propagacije unazad, u opštem slučaju svaki neuron računa otežnjenu sumu svih svojih ulaza [88]:

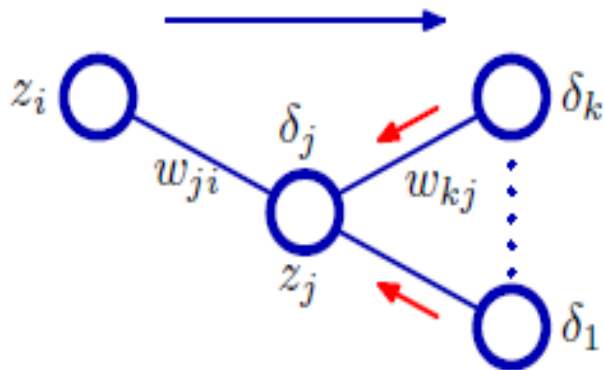
$$a_j = \sum_i \omega_{ji} z_i \quad (107)$$

Na ovu vrednost se onda primenjuje aktivaciona funkcija. Prepostavimo da grešku predviđanja možemo opisati metrikom E_n . Polazna tačka propagacije unazad jeste evaluacija izvoda E_n po težinskim faktorima ω_{ji} . Pošto E_n zavisi od težinskih faktora preko aktivacija a_j onda se može primeniti lančano pravilo i dobiti [88]:

$$\frac{\partial E_n}{\partial \omega_{ji}} = \frac{\partial E_n}{\partial a_j} \frac{\partial a_j}{\partial \omega_{ji}} \quad (108)$$

Ukoliko se uvede notacija $\frac{\partial E_n}{\partial a_j} \equiv \delta_j$ i koristeći činjenicu da je $\frac{\partial a_j}{\partial \omega_{ji}} = z_i$, dobićemo [88]:

$$\frac{\partial E_n}{\partial \omega_{ji}} = \delta_j z_i \quad (109)$$



Slika 16: Ilustracija propagacije unapred i unazad. Plava strelica ilustruje protok informacija napred, dok crvene strelice objašnjavaju proceduru propagacije unazad. Promene težinskih faktora i slobodnih članova jednog sloja dolaze računom greške δ za sloj ispred. Slika je preuzeta iz [88].

Dakle, traženi izvod dobija se tako što se pomnože vrednost δ za neuron na izlaznom kraju sa vrednošću z koja se nalazi na ulazu u neuron [88]. Kako bi izračunali greške za skrivenе slojeve, takođe koristimo lančano pravilo, te imamo [88]:

$$\delta_j = \frac{\partial E_n}{\partial a_j} = \sum_k \frac{\partial E_n}{\partial a_k} \frac{\partial a_k}{\partial a_j} \quad (110)$$

Suma ide po k neurona koji šalju impulse j -tom neuronu. Propagacija unazad prikazana je na slici 16. Vidi se da se greška j tog neurona koji šalje impulse ka k neurona, dobija tako što se evaluiraju greške k -tog sloja koji je ispred j -tog sloja. Znajući da se na aktivaciju a_j primenjuje aktivaciona funkcija $h(\cdot)$ kako bi dobili konačnu vrednost j tog neurona, tj. $z_j = h(a_j)$. Onda izraz (110) možemo pisati kao:

$$\delta_j = \sum_k \frac{\partial E_n}{\partial a_k} \frac{\partial a_k}{\partial a_j} = \sum_k \delta_k \frac{\partial}{\partial a_j} (\omega_{kj} z_j) = \sum_k \delta_k \frac{\partial}{\partial a_j} (\omega_{kj} h(a_j)) = h'(a_j) \sum_k \delta_k \omega_{kj} \quad (111)$$

Gornji rezultat daje konačnu formulu za evaluaciju algoritma propagacije unazad. Dakle, propagacija unazad se sastoji iz četiri koraka. Prvi korak jeste propagacija unapred gde nalazimo sve težinske faktore, slobodne članove i aktivacije koje povezuju ulazni vektor \mathbf{x} sa izlaznim slojem \mathbf{t} . Potom se nalaze greške izlaznog sloja [88]:

$$\delta_k = y_k - t_k \quad (112)$$

Gde je y_k vrednost ciljne promenljive a t_k predstavlja vrednost koju je predvideo model. Onda se korištenjem jednačine (111) nalaze greške za svaki skriveni sloj j , i na kraju pomoću jednačine (109) izračunaju potrebni izvodi te se završava propagacija unazad i ponovo kreće propagacija unapred.

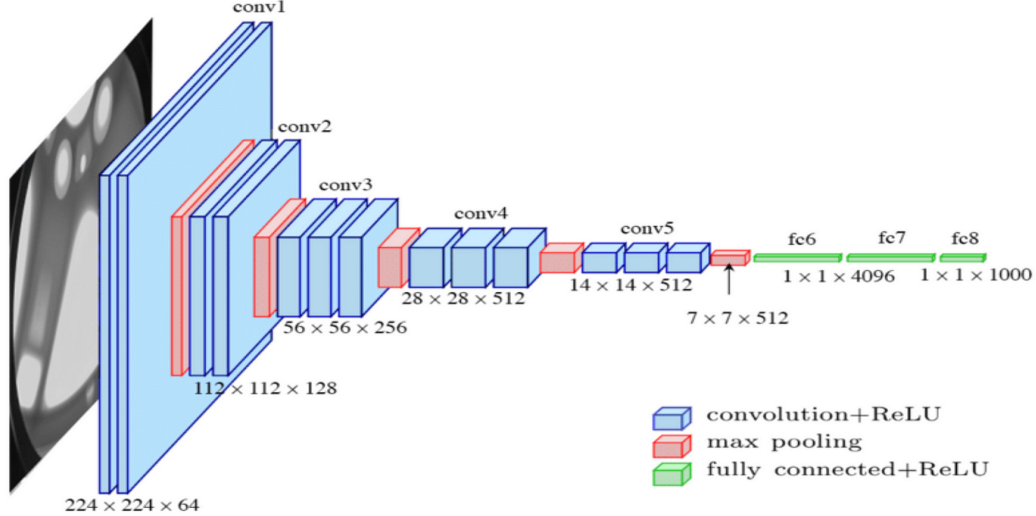
2.5.2.2 Konvolucione neuronske mreže

Konvolucione neuronske mreže predstavljaju tip neuronskih mreža koje se najintenzivnije koriste prilikom obrade slika, zvuka ili teksta [84]. Prednost konvolucionih neuronskih mreža jeste što imaju mogućnost da iz sirovih podataka koji su im dati konstruišu nove atributе na kojima zasnivaju predikcije. Ovo im omogućava činjenica da umesto da uče težinske faktore i slobodne članove, one uče filtere. Naime, filter ne predstavlja ništa drugo nego matricu koja je u mogućnosti da detektuje određenu osobinu ili svojstvo u signalu. Npr. to može biti filter za detekciju ivica na slici ili filter za detekciju karakterističnih oblika u nekom vremenski zavisnom signalu. Oblici ovih filtera su danas dorbo poznati jer je veliki broj njih razvijen kroz godine prakse u obradi slika, ali prednost konvolucionih neuronskih mreža jeste što se ovi filteri sami otkrivaju, te nema potrebe da ih korisnik unapred definiše. Ovime one zapravo same izdvajaju bitne karakteristike iz signala kroz filtere koje uče, te kroz tu osobinu daju optimalne rezultate. Zbog načina na koji funkcionišu, za njihovo obučavanje potrebna je dobra optimizacija i veliki broj podataka za obučavanje [84].

Sama arhitektura konvolucionih neuronskih mreža gotovo uvek podrazumeva duboke neuronske mreže jer je potrebno naučiti što više sitnih detalja u ulaznom signalu kako bi se dobili što bolji rezultati. To obično podrazumeva smenjivanje dva tipa slojeva, konvolucionih i agregacionih (eng. *pooling*) [84]. Izlazi iz konvolucionih slojeva se transformišu pomoću nelinearnih aktivacionih funkcija, a na kraj poslednjeg konvolucionog ili agregacionog sloja se nadovezuje potpuno povezani sloj, koji se obučava na atributima koje je konvolucioni sloj konstruisao. Primer proizvoljno kreirane konvolucione neuronske mreže prikazan je na slici 17.

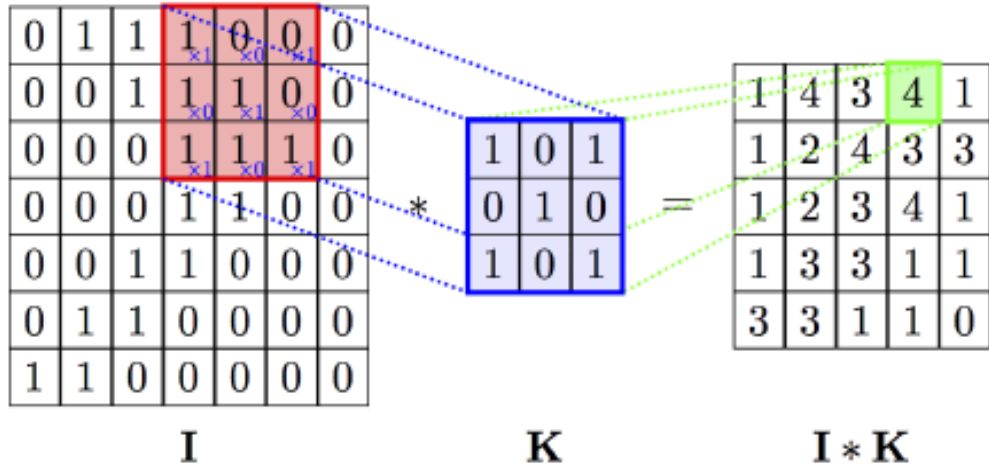
Matematički, operaciju konvolucije možemo zapisati kao [84]:

$$(f * g)_{ij} = \sum_{k=0}^{p-1} \sum_{l=0}^{q-1} f_{i-k, j-l} g_{k, l} \quad (113)$$



Slika 17: Arhitektura VGG16 konvolucione mreže. Sa slike se vide naizmenični konvolucijski i agregacioni slojevi, kao i tri potpuno povezana sloja na kraju. Slika je preuzeta kao javno dostupna, jer je VGG16 javno dostupna pretrenirana mreža čija se arhitektura može koristiti za različit niz problema.

Matrica I predstavlja ulaznu matricu ili signal, a matrica K predstavlja filter koji neuronska mreža uči i koji izdvaja neku korisnu osobinu signala. Primer funkcionisanja konvolucionne neuronske mreže prikazan je na slici 18.



Slika 18: Princip funkcionisanja konvolucionne neuronske mreže. Preko ulazne matrice prelazi tzv. filter i kao rezultat nastaje konvoluirani signal sa desne strane. Korak za koji se filter pomera udesno je parametar koji se zadaje neuronskoj mreži. Slika preuzeta iz [84]

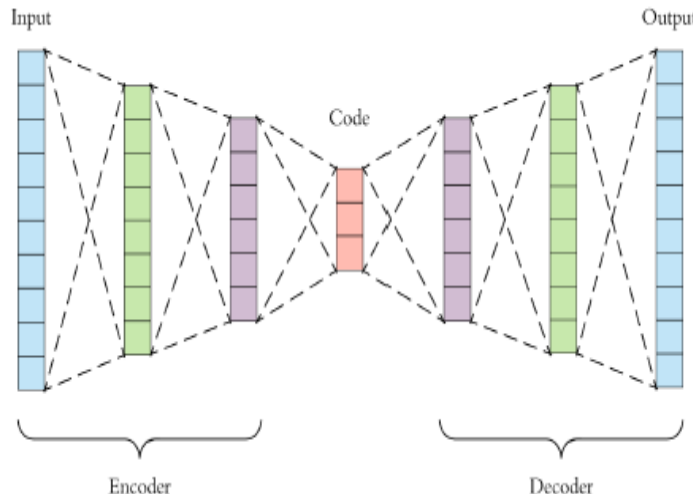
Dakle, sa slike se vidi da imamo ulaznu matricu koja predstavlja npr. sliku, gde su vrednosti u poljima intenzitet piksela, a matrica K predstavlja filter koji se primenjuje radi ekstrakcije nekog atributa sa slike. Rezultujuća matrica $I * K$ ne mora nužno da ima istu dimenziju kao ulazna matrica I što nekad nije povoljno, pa se radi *proširivanje* ili *padding*.

Ovo znači da se ulazna matrica proširi za isti broj mesta sa leve i desne strane, kako bi se dimenzije ulaza i izlaza poklopile. Proširivanje može da se radi sa nulama sa obe strane ili sa vrednostima kolone koja je na levom odnosno desnom kraju.

Agregacija predstavlja ukrupnjivanje informacija koje se dobijaju iz konvolucionog sloja, tako što se primenjuje neka jednostavna funkcija agregacije na susjedne jedinice [84]. Ta funkcija može biti prosti maksimum ili srednja vrednost obuhvaćenih jedinica. Ako se agregacija vrši na 3×3 piksela iz prethodnog sloja, onda je izlaz iz agregacionog sloja 9 puta manje dimenzije nego ulazni sloj. Suštinski, agregacijom konvolucionog sloja zanemarujemo informacije gde je tačno nađena neka osobina na slici ili u signalu, ali ih ne gubimo, tj. ostaje informacija da je ta osobina nađena. Glavna uloga koju agregacija ima jeste da smanji broj ulaza u potpuno povezani sloj, čime se u mnogome smanjuje računarsko vreme koje je potrebno za obučavanje mreže i olakšava njenu optimizaciju.

2.5.3 Autoenkoderi

Autoenkoderi predstavljaju neuronske mreže koje uče da na izlazu rekonstruišu ono što je dobijeno kao ulaz. Tipična arhitektura autoenkodera prikazana je na slici 19.



Slika 19: Tipična arhitektura autoenkodera. Sastoje od dve nezavisne neuronske mreže, enkodera i dekodera, koji su razdvojeni latentnim prostorom [84]

Vidimo da je autoenkoder sastavljen zapravo od dve neuronske mreže, enkodera i dekodera. Enkoder ima zadatku da ulazne podatke preslika u prostor manje dimenzionalnosti koji se naziva *latentni prostor*. Sa druge strane, dekoder ima zadatku da napravi preslikavanje iz latentnog prostora na ulazne varijable.

Latentni prostor je manje dimenzionalnosti u odnosu na ulazne podatke i tipično su podaci koji su bliski u prostoru atributa, bliski i u latentnom prostoru [84]. To znači da se interpolacijom između tačaka u latentnom prostoru mogu dobiti novi podaci. Poželjan je latentni prostor u kome su latentne varijable gusto spakovane i gde su prelazi između delova latentnog prostora glatki. Za proste autoenkodere često nije zadovoljen jedan od gornja dva kriterijuma. Naime, često se dešava da tačke koje su bliske jedna drugoj u latentnom prostoru

nisu bliske u prosotru atributa, ili da je latentni prostor takvog oblika da ne postoji glatki prelaz između njegovih delova. Pored ovoga, običan autoenkoder se ne može koristiti u svrhu generisanja novih podataka koji do tada nisu postojali, već se isključivo mogu generisati samo podaci koje je model video na ulazu. Kako bi se unapredile ove mane običnog autoenkodera, razvijen je model varijacionog autoenkodera, koji predstavlja model veštačke inteligencije sa Bayesovim zaključivanjem.

2.5.4 Varijacioni autoenkoder

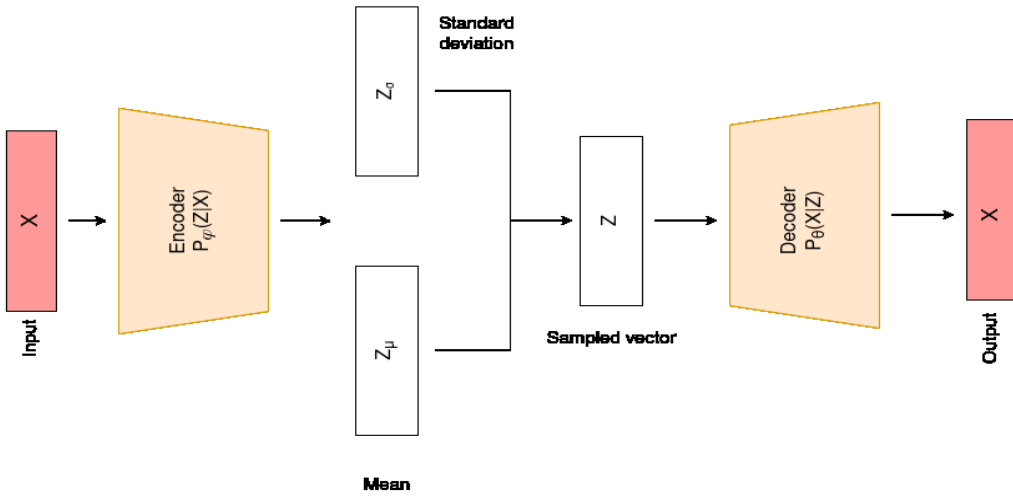
Kako bi se pravilno shvatio varijacioni autoenkoder, podesno je poći od Bayesove teoreme koja glasi [88]:

$$P(z|x) = \frac{P(x|z)P(z)}{P(x)} \quad (114)$$

U gornjoj jednačini $P(z|x)$ predstavlja novu uslovnu verovatnoću da će hipoteza z biti zadovoljena ako je dostupna informacija x , i u Bayesovojoj statistici naziva se aposteriori raspodela. Potom, $P(x|z)$ predstavlja verovatnoću da se desi događaj x pri čemu se desio događaj z i naziva se verodostojnost. $P(z)$ predstavlja prethodnu raspodelu (eng. *prior distribution*), odnosno verovatnoću opažanja događaja z pre nego što se desio događaj x , a $P(x)$ predstavlja tzv. graničnu verodostojnost i ista je za svako z . Stoga, u izračunavanju $P(z|x)$ ulogu igraju samo prethodna raspodela $P(z)$ i verodostojnosti $P(x|z)$.

Pošto je prostor pretrage latentnog prostora jako veliki, aposteriori raspodela $P(z|x)$ nikad nije unapred poznata, stoga se pribegava varijacionoj aproksimaciji, tj. zahtevu da $P(z|x) \simeq Q(z|x)$, pri čemu mora biti zadovoljeno da $Q(z|x)$ pripada klasi jednostavnijih raspodela od $P(z|x)$.

Arhitektura varijacionog autoenkodera prikazana je na slici 20.



Slika 20: Arhitektura varijacionog autoenkodera. Enkoder ima zadatak da nauči aposteriori raspodelu $p_\varphi(z|x)$, dok dekoder uči zajedničku raspodelu $p_\theta(x, z) = p(x|z)p(z)$.

Enkoder varijacionog autoenkodera ima zadatak da nauči raspodelu $p_\varphi(z|x)$. Kako je prethodno napomenuto, pošto je ova raspodela uglavnom nepoznata, njen oblik se prepostavlja,

tj. pokušava se dobiti da je raspodela $p_\varphi(z|x) \simeq q_\varphi(z|x)$, gde je $q_\varphi(z|x)$ poznata raspodela. Tipično, za varijacioni autoenkoder prepostavlja se da prethodna raspodela latentnih varijabli prati normalnu raspodelu $p(z) = \mathcal{N}(0, I)$, a potom se obučavanjem mreže postiže rezultat takav da je $q_\varphi(z|x) = \mathcal{N}(\mu, \sigma)$. Funkcija greške kod varijacionog autoenkodera se sastoji iz dva člana. Prvi član daje meru odstupanja generisanog izlaza od datog ulaza i često se naziva greška rekonstrukcije. Drugi član meri odstupanje $q_\varphi(z|x)$ od $p(z)$ i kod varijacionog enkodera se najčešće meri pomoću Kullback - Leibler divergencije. Ovaj član se još naziva i regularizacioni član jer se pomoću njega vrši regularizacija latentnog prostora sa ciljem da se slične varijable nađu što bliže u latentnom prostoru. Zbirno, funkcija gubitka varijacionog autoenkodera se naziva ELBO (eng. *Evidence Lower Bound*) i matematički se predstavlja kao:

$$ELBO = \mathbf{E}_{q_\varphi} \left[\log \left[\frac{p_\theta(x, z)}{q_\varphi(z|x)} \right] \right] + \mathbf{E}_{q_\varphi} \left[\log \left[\frac{q_\varphi(z|x)}{p(z)} \right] \right] \quad (115)$$

Greška rekonstrukcije je obično ili srednje kvadratno odstupanje ili srednje apsolutno odstupanje, dok KL divergencija za prepostavljenu normalnu raspodelu ima oblik:

$$D_{KL}(q_\varphi(z|x) || p(z)) = -\frac{1}{2} \left(1 + \log(\sigma^2 - \mu^2 - \sigma^2) \right) \quad (116)$$

U intuitivnom smislu, više se ne enkodira prost broj kao što je to slučaj kod običnih autoenkodera, već se enkodira raspodela. Kako bi bila moguća propagacija unazad, radi se reparametrizacija [89] i to:

$$z = \mu + \sigma \otimes \epsilon \quad (117)$$

Gde je ϵ generisani slučajni broj iz jedinične uniformne raspodele. Drugim rečima, očekivana vrednost μ predstavlja enkodiranu sliku sa ulaza, dok $\sigma \otimes \epsilon$ predstavlja varijaciju toga originalni podatak može biti perturbovan, a da još uvek postoji dobro prepoznavanje na ulazu [85].

2.5.5 Prevencija preprilagođavanja modela veštacke inteligencije

Problem preprilagođavanja modela trening podacima, pomenut nekoliko puta do sada u tezi, dovodi do loše generalizacije na nove podatke i tipično na test bazi podataka ima jako loše performanse. Postoje različite metode kojima se sprečava preprilagođavanje. Ovde će biti reči samo o dve koje se najčešće koriste, a to su regularizacija i rano zaustavljanje obučavanja.

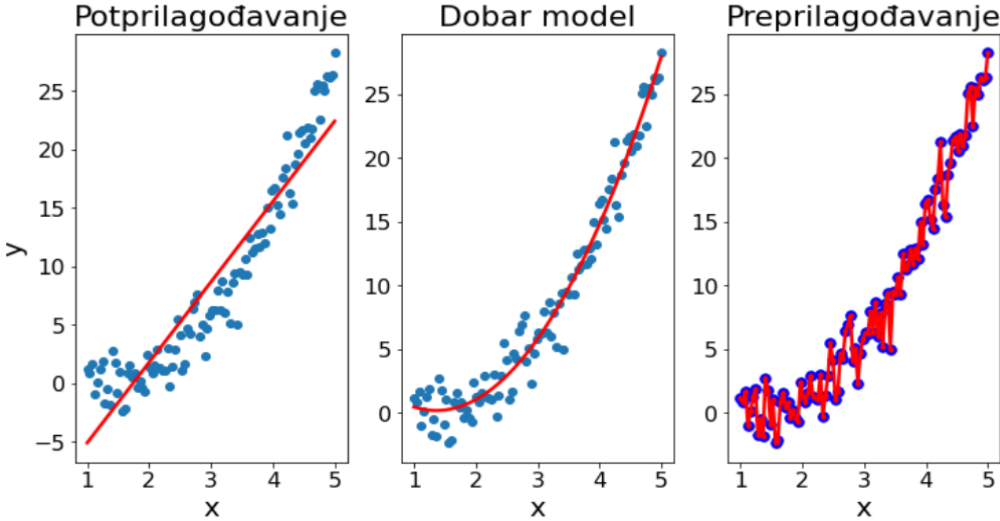
2.5.5.1 Regularizacija

Regularizacija kod modela mašinskog učenja predstavlja tehniku gde se na izabranu funkciju gubitka dodaje tzv. regularizacioni član čiji zadatak jeste da oteža preprilagođavanje modela i predstavlja kontratežu. Kako bi regularizacija bila iskontrolisana, dodaje se i koeficijent λ ispred, kako se ne bi u potpunosti sprečilo prilagođavanje modela podacima, što takođe nije cilj. Koeficijent λ dakle kontroliše koliko pažnje se usmerava na minimizaciju greške, a koliko na regularizacioni član [84]. Matematički, regularizaciju primenjujemo kao [84]:

$$\min \frac{1}{N} \sum_{i=1}^N L(y_i, f_\omega(x_i)) + \lambda \Omega(\omega) \quad (118)$$

Tipično, regularizacioni član je l_2 norma vektora koeficijenata, pa se dobija sledeći izraz:

$$\min \frac{1}{N} \sum_{i=1}^N L(y_i, f_\omega(x_i)) + \lambda \|\omega\|_2^2 \quad (119)$$



Slika 21: Prepostavljeni model kojeg dobro opisuje kvadratna regresija. Na slici je prikazan slučaj potprilagodavanja modela (levo), dobar model (sredina) kao i model koji se preprilagodio podacima (desno)

Pored l_2 regularizacije, radi se i l_1 regularizacija koja podrazumeva prostu sumu svih težinskih faktora, a ne njihovih kvadrata. Takođe, mogu se raditi obe regularizacije istovremeno. Bitno je naglasiti da se minimizacija radi na čitavom zbiru, a ne da se na minimalnu funkciju greške dodaje regularizacioni član. Dobar primer regularizacije može se ilustrovati modelom kojeg dobro opisuje kvadratna funkcija. Ova situacija opisana je na slici 21. Prepostavimo da model može imati jedan od tri navedena oblika:

$$y = \omega_0 + \omega_1 x \quad (120)$$

$$y = \omega_0 + \omega_1 x + \omega_2 x^2 \quad (121)$$

$$y = \omega_0 + \omega_1 x + \omega_2 x^2 + \omega_3 x^3 + \omega_4 x^4 \quad (122)$$

Prvi model koji je ustvari linearna regresija, je prikazan na slici 21 levo. Ovaj model očigledno se potprilagodio podacima i ne može zadovoljavajuće da opiše vezu između ciljne promenljive i atributa, te se ne može iskoristiti za predviđanje novih rezultata. Treći model je prikazan na slici 21 desno³, gde očigledno vidimo da se model preprilagodio podacima. Model koji se dobro prilagodio podacima prikazan je na slici 21 u sredini. Ukoliko vrednosti koeficijenata ω_3 i ω_4 postanu jako bliske nuli, vidimo da se model koji se ranije preprilagodio podacima potencijalno može speciti u tome i iskoristiti za predviđanje.

³Nije egzaktan fit, ali ideja grafika je da ilustruje slučaj preprilagođavanja uzimanjem u razmatranje više koeficijenata nego što je potrebno

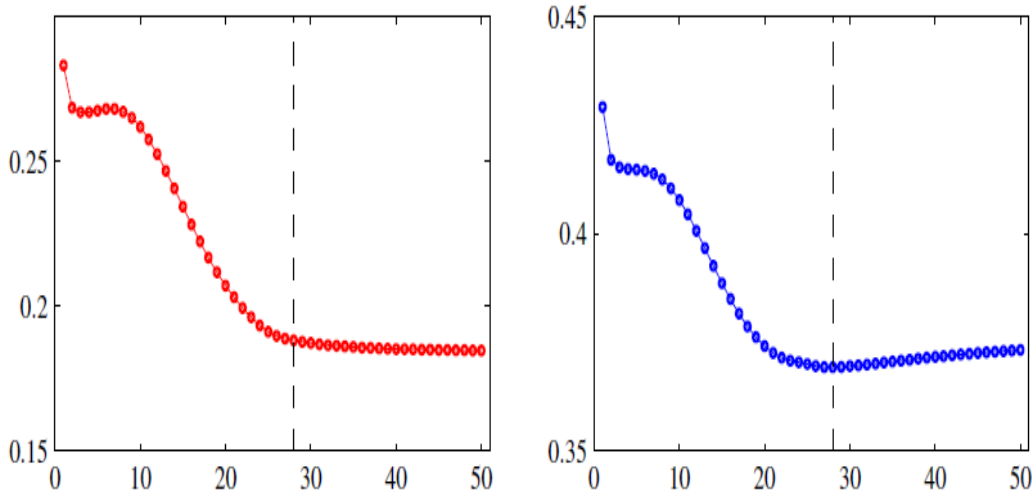
Na ovom primeru može se jasno uočiti uloga regularizacije. Ukoliko treći model u toku obučavanja poveća vrednosti ω_3 i ω_4 , to će se odraziti na sumu $\| \omega \|_2^2$ koja će se takođe povećati, a samim tim raste i ukupna funkcija greške. Povećanje funkcije greške sprečava konvergenciju modela, pa se dobija efekat "kažnjavanja" modela ukoliko se ovi koeficijenti povećavaju. Dakle, regularizacijom se postiže snižavanje vrednosti nepotrebnih koeficijenata, odnosno detekcija atributa koji su nepotrebni u analizi. Regularizacija kod neuronskih mreža podrazumeva dodavanje regularizationog člana na kraj aktivacije, tj:

$$a_j = \omega_0 + \sum_{i=1}^N \omega_i x_i + \lambda \| \omega \|^2 \quad (123)$$

Efekat je isti, ukoliko neki od članova ima veću vrednost od potrebne, regularizationi član povećava funkciju gubitka i sprečava neuronsku mrežu da konvergira.

2.5.5.2 Rano zaustavljanje

Alternativu regularizaciji predstavlja rano zaustavljanje treninga modela i ulgavnom se koristi prilikom treninga nelinearnih modela kao što su neuronske mreže. Prilikom obučavanja neuronskih mreža, funkcija gubitka je nerastuća funkcija broja iteracija u odnosu na podatke za obučavanje mreže [88]. Međutim, ako se prati trend funkcije gubitka u odnosu na validacionu ili test bazu, onda se prvo primećuje trend opadanja koji je nakon određenog broja iteracija praćen blagim porastom. Ovaj trend ilustrovan je na slici 22.



Slika 22: Obučavanje modela. Levo je funkcija gubitka za trening bazu koja je opadajuća funkcija interacija obučavanja, dok je desno funkcija gubitka validacione baze koja ima blagi rast nakon određenog broja iteracija. Slika je preuzeta iz [88]

Stoga je podesno zaustaviti obučavanje u trenutku kada funkcija gubitka na validacionoj bazi ne pokazuje dalje znake smanjivanja, odnosno zaustaviti obučavanje pre trenutka kada funkcija gubitka validacione baze kreće da raste.

Metod ranog zaustavljanja ima kvalitativno objašnjenje u sledećem. U trenutku započinjanja obučavanja mreže, broj stepeni slobode mreže je jako mali. Drugim rečima, kompleksnost modela je i dalje jako mala. Kako obučavanje napreduje, raste i kompleksnost mreže, a samim tim i sklonost ka preprilagodavanju podacima. Rano zaustavljanje u ovom smislu predstavlja efektivno ograničenje kompleksnosti mreže [88].

3 Primena mašinskog učenja za određivanje Stark-ovih poluširina linija

Prva od tri problematike primene alata mašinskog učenja u spektroskopiji i diagnostici plazme kojom se ova teza bavi predstavlja određivanje Stark-ove poluširine emitovanih atomskih linija, u okviru koje je nastala i studija regularnosti za neutralni atom litijuma. Teorijski proračuni Stark-ovih parametara se najčešće rade korišćenjem Griem-ove standardne teorije [90], Griem-ove semiempirijske formule [91], modifikovane semiempirijske formule Dimitrijevića i Konjevića [92], izloženom SCP teorijom Sahal - Brechaut i Dimitrijevića [27, 28]. Purić i saradnici su u nizu radova [54, 55, 62, 63, 65, 66, 68] ispitivali regularnosti Stark-ovog efekta, što duž izoelektronskih nizova, što duž određenog prelaza unutar atoma. Kako u ovoj iscrpnoj studiji i dalje nisu našli univerzalnu ili bar aproksimativnu formulu koja bi važila za veći broj emitera, napravljen je model mašinskog učenja i testirana je njegova preciznost i tačnost pri određivanju elektronske Stark-ove poluširine spektralne linije i ispitana je mogućnost utvrđivanja regularnosti duž atomskih prelaza. U ovoj sekciji opisan je način na koji je formirana baza za obučavanje modela, a zatim je obrazložen metod kojim je izabran najbolji model sa odgovarajućim parametrima i prikazani su postignuti rezultati koji su detalljno obrazloženi u radovima [93, 94]. Obučavanje modela i predikcije rađene su u programskom jeziku python pomoću open source biblioteke sci-kit learn [95].

Značaj dobijenih rezultata leži u tome što je napravljeni model uspešno uočio očekivane regularnosti Stark-ovog efekta, što prelaza duž spektralne serije, što duž izoelektronskog niza nekog emitera. U radu su proučavane regularnosti duž spektralnih serija neutralnog litijuma, ali model se može primeniti na bilo koji emiter. Pored toga, nema više potrebe za traženjem neke generalizovane formule koja bi pokrila svaki slučaj regularnosti, jer je model dobro generalizovao fizičku sliku iza fenomena Stark-ovog širenja. Takođe, model se može koristiti za brzu procenu elektronske poluširine emitovane spektralne linije usled Stark-ovog efekta, gde su dobijena odstupanja od eksperimentalnih rezultata koja iznose između 20 i 30 %.

3.1 Pravljenje baze za obučavanje modela

U svrhu formiranja baze podataka za određivanje Stark-ovih parametara, iskorištene su dve javno dostupne baze podataka koje se tiču atomskih parametara i Stark-ovih poluširina. Prva baza je Stark B baza podataka [96] gde su tabelirani Stark-ovi parametri za zadate parametere plazme. Atributi preuzeti iz ove baze podataka su: hemijski element (emiter), nanelektrisanje jona, elektronska temperatura i gustina elektrona. Za potrebe nalaženja parametara povezanih sa datim prelazom, uzete su i konfiguracije gornjeg i donjeg elektronskog nivoa. Druga baza, iz koje su dobijene informacije o svim atomskim prelazima od interesa jeste NIST baza atomskih podataka. Iz NIST baze atomskih podataka iskorišteni su: energija jonizacije, energije gornjeg i donjeg elektronskog nivoa, ukupan ugaoni moment gornjeg i donjeg nivoa kao i glavni i orbitalni kvantni broj za gornji i donji energetski nivo. Algoritam povezivanja ove dve baze i dobijanja konačne radi na sledeći način. Prvo, za određeni emiter iz Stark B baze podataka uzimaju se sve konfiguracije gornjeg i donjeg energetskog nivoa za koje je izračunata poluširina emitovane linije. Nakon toga, za svaku konfiguraciju iz Stark- B baze, traži se poklapanje sa konfiguracijom iz NIST baze atomskih podataka.

Kada se poklapanje pronađe, iz NIST atomske baze podataka uzima se energija tog nivoa, ukupan ugaoni moment za taj nivo, energija jonizacije, glavni i orbitalni kvantni broj za dati nivo. Energija jonizacije je potrebna za računanje efektivnog jonizacionog potencijala gornjeg nivoa χ , parametra kojeg je uveo Purić [64] u svojim radovima o regularnosti, a računa se kao razlika energije jonizacije i energije gornjeg nivoa:

$$\chi = E_{ion} - E_j \quad (124)$$

Zbog toga što algoritmi mašinskog učenja moraju da uzimaju brojevne vrednosti, hemijski simboli elemenata su zamjenjeni njihovim atomskim brojem Z . Radi boljeg razumevanja, pseudo algoritam je prikazan u algoritmu 1. Na kraju ovog postupka, uspešno je upareno 54236 prelaza za 53 različita emitera.

Nakon pravljenja baze, pristupljeno je čišćenju baze od odudarajućih podataka. Ovi odudarajući podaci nađeni su tako što je uočeno da za određeni broj prelaza ima tabelirane vrednosti energija donjeg nivoa veće od energija gornjeg nivoa, a kako je to fizički nemoguće, ovi prelazi su izbačeni iz baze podataka i nisu korišteni za trening. Takođe, kako su od interesa bile oblasti gustina elektrona $N_e < 10^{17} \text{ cm}^{-3}$, elektronskih temperatura do 150 000 K, iz baze su uklonjeni svi prelazi za koje se vrednosti gustine elektrona i elektronske temperature nalaze van ovih opsega. Nakon primenjenih ograničenja, za trening modela je ostalo 34973 prelaza za 53 emitera. Model uzima 14 ulaznih atributa, i na osnovu njih predviđa Stark-ovu elektronsku poluširinu ω_e koja je izražena u jedinicama rad/s jer se ispostavilo kao bolja opcija umesto da je data u nanometrima ili angstromima.

3.2 Predpriprema podataka i izbor najboljeg modela

Nakon kreiranja baze podataka, pristupljeno je predpripremi baze podataka kako bi modeli bili u stanju da što bolje nauče odnose između ulaznih atributa, a u cilju predviđanja ciljne varijable. Jedna od primetnih osobina napravljene baze podataka jesu različiti redovi veličina atributa. Na primer, gustine elektrona su reda 10^{17} cm^{-3} , temperature elektrona reda par desetina hiljada kelvina, dok su kvantni brojevi reda veličine 10 i manji. Ako bi model bio pušten da se obučava na ovakvoj bazi podataka, ne bi se dobili dobri rezultati jer bi model bio nestabilan i algoritmi minimizacije i optimizacije bi loše radili. Stoga su svi ulazni atributi skalirani tako da uzimaju vrednosti između 0 i 1, što je jako povoljno za rad svih modela mašinskog učenja. Postoji nekoliko metoda, a u ovom radu je korišten metod standardnog skaliranja. Standardno skaliranje podataka znači da se od vrednosti svakog atributa oduzima srednja vrednost atributa i deli sa standardnom devijacijom atributa. Drugim rečima, skaliranje se vrši tako da:

$$x_{new} = \frac{x_{old} - \mu}{\sigma} \quad (125)$$

Gde je x_{new} nova vrednost atributa, x_{old} predstavlja staru vrednost atributa, μ je srednja vrednost, a σ standardna devijacija atributa. Nakon skaliranja izabrani radni modeli bili su: linearna regresija, linearna regresija sa \mathcal{L}^2 normom, stablo odlučivanja, slučajna šuma i gradijentno pojačano stablo odlučivanja. Pošto svaki od ovih modela ima mnogo promenljivih parametara koji se mogu optimizovati, izbor vrednosti hiperparametara modela je rađen pomoću algoritma koji se zove *Grid Search Cross Validation*. Ova tehnika se zasniva na na nasumičnoj podeli baze za obučavanje u srazmeri 80% za trening i 20 % za test zadati

broj puta (u ovom radu 5 puta) za svaki model i svaki put nanovo trenira model za zadate hperparametre.

Algoritam 1 Pseudo kod generisanja baze podataka

```

for element in Stark-BElements do
    charge, Z ← OdrediNaelektrisanjeAtomskiBroj(element)
    elementNIST ← NađiElementUNISTu(element)
     $T_e \leftarrow$  Temperatura elektrona iz Stark- B
     $N_e \leftarrow$  Gustina elektrona iz Stark- B
     $\omega_e \leftarrow$  Stark-ova poluširina
    UpperLevels ← Konfiguracije gornjih energetskih nivoa iz Stark- B
    LowerLevels ← Konfiguracije donjih energetskih nivoa iz Stark- B
    Levels ← Konfiguracije svih energetskih nivoa iz NIST baze za elementNIST
    ionEnergy ← NađiEnergijuJonizacije(elementNIST)
    for lowerlevel in LowerLevels do
        for level in Levels do
            if lowerlevel == level then
                LowerBinEnergy, nf, lf, jf ← energija donjeg nivoa i kvantni brojevi vezani
                za dati prelaz
            end if
        end for
    end for
    for upperlevel in UpperLevels do
        for level in Levels do
            if upperlevel == level then
                UpperBinEnergy, ni, li, ji ← energija gornjeg nivoa i kvantni brojevi vezani
                za dati prelaz
             $\chi \leftarrow$  ionEnergy – UpperBinEnergy
            end if
        end for
    end for
    if length(LowerBinEnergy) != length(UpperBinEnergy) then
        Greška return
    else
        while i != length(LowerBinEnergy) do
            Z,  $T_e$ ,  $N_e$ , charge,  $\chi$ , ionEnergy, UpperBinEnergy, ji, LowerBinEnergy, jf, ni,
            li, nf, lf,  $\omega_e \leftarrow$  Upis u bazu za trening
        end while
    end if
end for

```

Za svaku podelu, model pamti rezultat i na kraju vraća najbolji rezultat modela u smislu R^2 koeficijenta determinacije i parametre za koji je ovaj rezultat postignut. Razmotreni parametri za sve modele dati su u tabeli 1.

Tabela 1: Razmotreni modeli i odgovarajući hiperparametri

Model	Hiperparametri
stablo odlučivanja	max_depth = 3,5,10
Slučajna šuma	max_depth = 3,5,10 min_samples_leaf = 3,4,5 n_estimators = 50,100,200
Gradijentno pojačano stablo odlučivanja	max_depth = 3,5,10 min_samples_leaf = 2,3,4 n_estimators = 50,100,200

Najbolji rezultati postignuti treningom za svaki model dati su u tabeli 2.

Tabela 2: Najbolji rezultati modela nakon treninga i odgovarajući koeficijent determinacije R^2

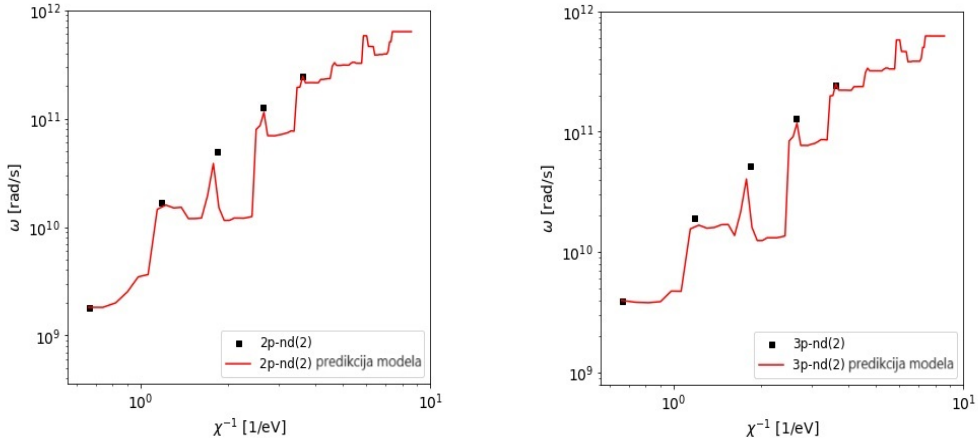
Model	Hiperparametri	R^2 koeficijent determinacije
stablo odlučivanja	max_depth = 5	0.9
Slučajna šuma	max_depth = 10 min_samples_leaf = 3 n_estimators = 200	0.97
Gradijentno pojačano stablo odlučivanja	max_depth = 10 min_samples_leaf = 2 n_estimators = 200	0.96

Zaključak Grid Search Cross Validation tehnike je da se najbolji rezultati dobijaju za model slučajne šume sa hiperparametrima koji su navedeni u tabeli 2. Preprilagođavanje nije problem ovde, a provereno je tako što su poređeni koeficijenti determinacije R^2 dobijeni za trening podatke i za test podatke. Pošto su istog reda većinie (trening $R^2 = 0.99$, a test $R^2 = 0.97$) zaključuje se da model nije preprilagodio podacima i da se može koristiti u analizi i predikciji Stark-ovih poluširina za različite emitere.

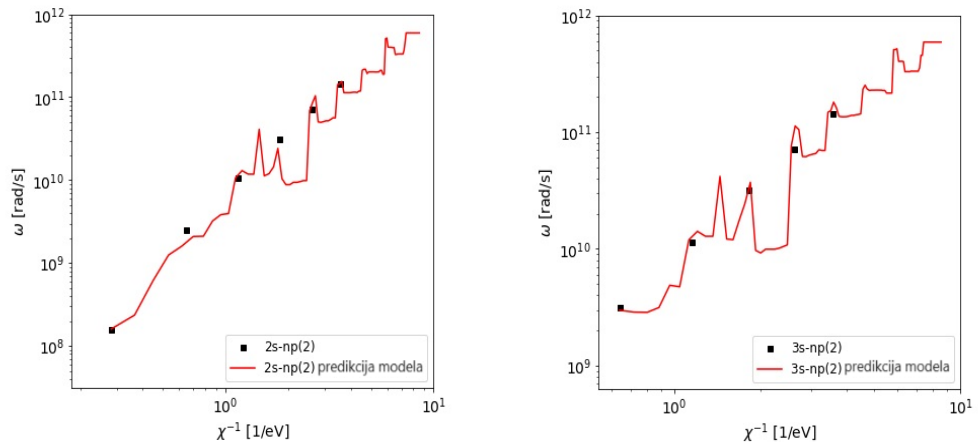
3.3 Analiza regularnosti Stark-ovog efekta za spektralne serije Li I

Model slučajne šume primjenjen je na izučavanje regularnosti duž spektralnih serija neutralnog litijuma. Na slikama 23, 24 i 25 prikazani su rezultati predikcije modela sa izračunatim Stark-ovim elektronskim poluširinama iz Stark- B baze. Predikcije su rađene i za necelobrojne glavne kvantne brojeve, stoga fizički smisao imaju samo skokovi prikazani crvenom linijom,

dok ostali rezultati nemaju fizičkog smisla. Vidi se da je model uspešno predvidio kvantnu prirodu emisije, te da daje u skladu sa greškom razumne rezultate za ovaj tip analize.



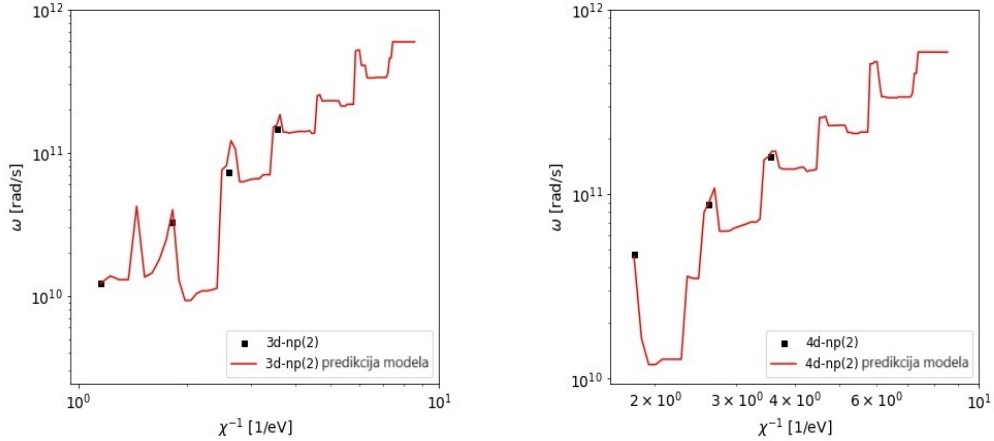
Slika 23: Predikcije modela za 2p - nd i 3p - nd spektralne serije Li I za $N_e = 10^{20} \text{ m}^{-3}$ i $T_e = 30000 \text{ K}$.



Slika 24: Predikcije modela za 2s - np i 3s - np spektralne serije Li I za $N_e = 10^{20} \text{ m}^{-3}$ i $T_e = 30000 \text{ K}$.

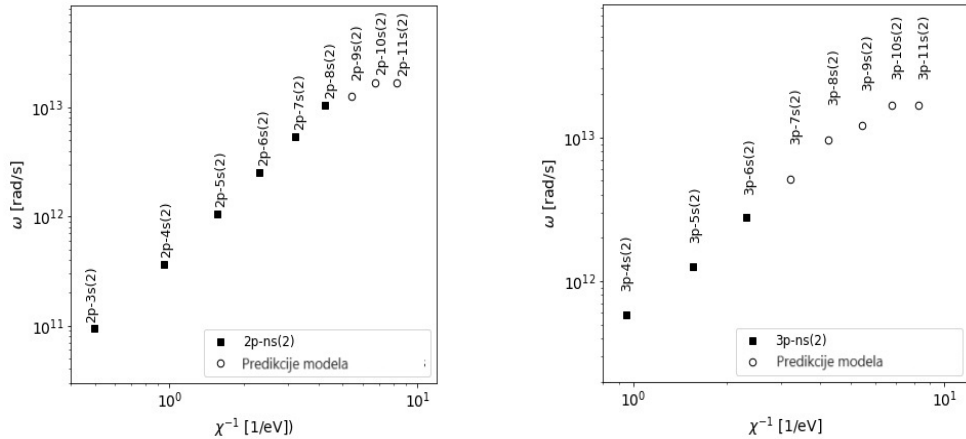
Sa slike 23 i 24 se primećuje da model nije na najbolji način predvideo energije na kojima se prelaz dešava, dok se na nekim mestima ni ne primećuje nagli skok u vrednosti. Ipak za većinu prelaza, ovo ponašanje je opaženo te se može reći da je model jasno uočio regularnosti duž spektralnih serija atoma Li I.

Od velikog interesa je bilo predvideti i elektronske Stark-ove polusirine za visoke energetske nivoe za koje ovi podaci još nisu izračunati. Predikcije su urađene za gustinu elektrona od $N_e = 10^{22} \text{ m}^{-3}$ i temperaturu elektrona $T_e = 30000 \text{ K}$. Ovi rezultati prikazani su na slici 26. Uočava se da model dobro prati linearni trend do određenog prelaza kada nastupa saturacija. Saturacija nije bila predviđena u ranijim studijama regularnosti Stark-ovog efekta [60,62,63] a najverovatnije objašnjenje njenog postojanja ove jeste Debye-ev efekat ekriranja emitera. Naime, pošto je reč o prelazima sa vrlo visokim energijama i visokim kvantnim brojevima,



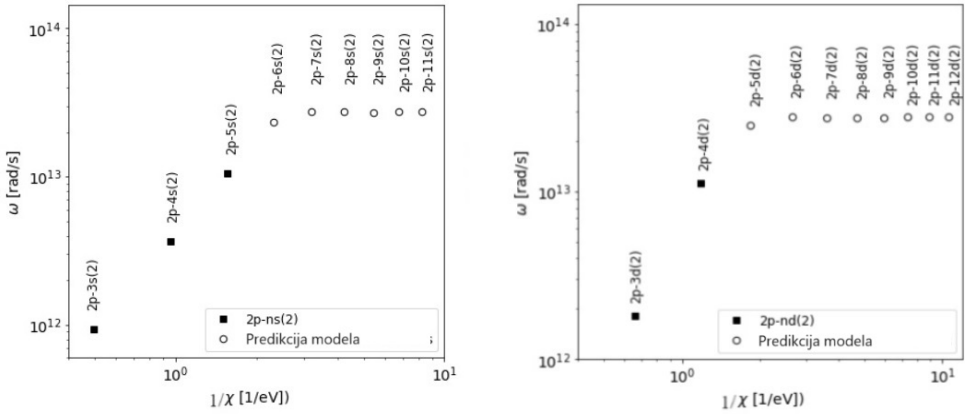
Slika 25: Predikcije modela za $3d - np$ i $4d - np$ spektralne serije Li I za $N_e = 10^{20} m^{-3}$ i $T_e = 30000 K$.

postoji verovatnoća da je emiter ekraniran i da ne vidi polje perturbujućih elektrona. Ovo predstavlja dobar primer fizičke slike koju je model uspeo da nauči iz podataka na kojima je obučavan, što znači da je postigao visok stepen generalizacije podataka.



Slika 26: Predikcije modela za $2p - ns$ i $3p - ns$ spektralne serije Li I za $N_e = 10^{22} m^{-3}$ i $T_e = 30000 K$.

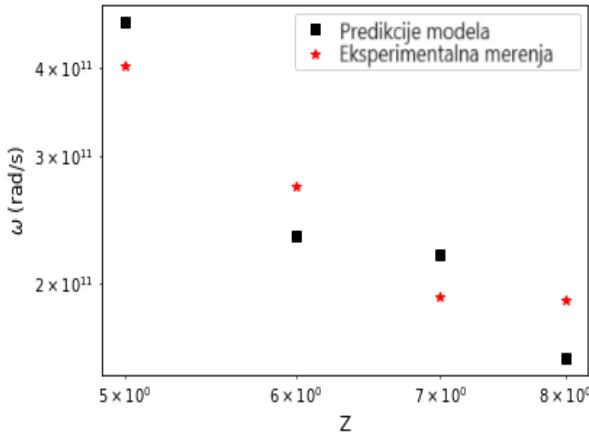
U cilju ispitivanja ove pretpostavke, urađena je i predikcija za veću elektronsku gustinu, za koju je Debye-ev radius manji, pa bi i saturacija trebalo da nastupi ranije, odnosno da bude uočljiva i na nižim glavnim kvantnim brojevima. Na slici 27 prikazana je predikcija modela za Stark-ove elektronske poluširine za spektralne serije $2p - ns$ i $2s - np$ za gustom elektrona od $N_e = 10^{23} m^{-3}$ i $T_e = 30000 K$. Kada se uporede slike 26 i 27 vidimo da se za spektralnu seriju $2p - ns$ saturacija javlja već kod glavnog kvantnog broja gornjeg energetskog nivoa $n_i = 7$, za razliku od gustine elektrona $N_e = 10^{22} m^{-3}$ gde se to dešava za $n_i = 10$. Ovaj rezultat predstavlja jak dokaz da je saturacija zapravo efekat Debye-vog ekraniranja. Pored regularnosti spektralnih serija, ispitana je i regularnost Stark-ovog efekta duž izoelektronskog niza atoma litijuma i rezultati su upoređeni sa eksperimentalnim podacima Blagojevića i



Slika 27: Predikcije modela za $2p - ns$ i $2s - np$ spektralne serije Li I za $N_e = 10^{23} m^{-3}$ i $T_e = 30000 K$.

saradnika [97]. Rezultati su dati za 3s-3p prelaze emitera B III, C IV, N V i O VI. Predikcije modela slučajne šume prikazani su na slici 28. Sa slike se vidi slaganje između predviđenih vrednosti Stark-ovih poluširina i eksperimentalno merenih.

Vidi se da je model uspešno predvideo regularnost Stark-ovog efekta duž izoelektronskog niza koja je i eksperimentalno potvrđena.



Slika 28: Studije regularnosti Stark-ovog efekta duž izoelektronskog niza litijuma. Posmatrani prelaz je $3s-3p$, a prelazi su u vidljivom delu spektra za proučavane emitere: B III, C IV, N V i O VI. Eksperimentalne i teorijski računate širine normirane na gustinu elektrona od $N_e = 10^{23} m^{-3}$.

3.4 Procena važnosti atributa

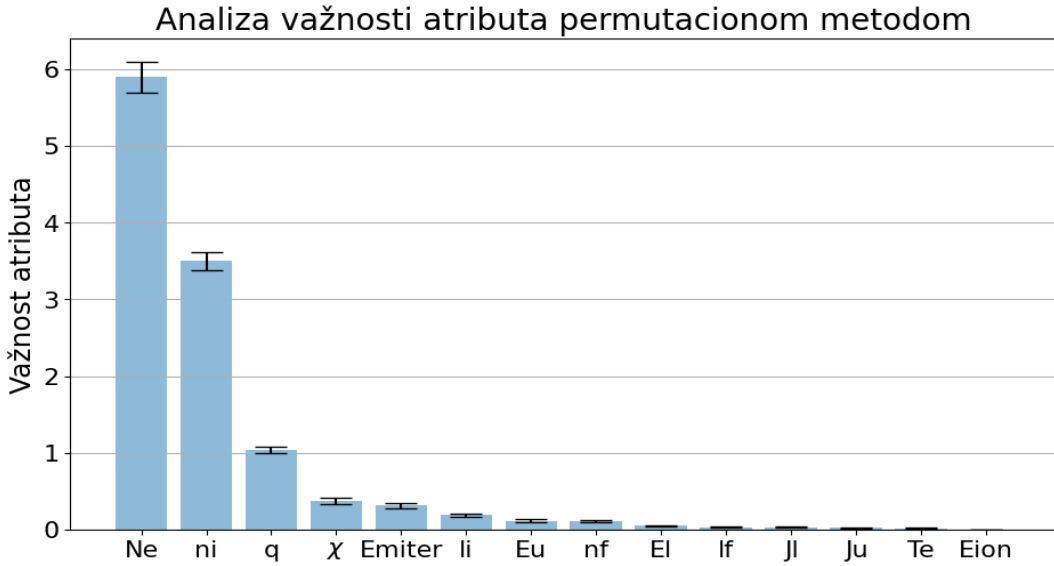
Pošto model uzima 14 ulaznih atributa na osnovu kojih se predviđa Stark-ova poluširina, može se ispitati koliko je svaki atribut pojedinačno bitan za finalnu predikciju modela. Odlučeno je da se važnost atributa za predikciju ispita korištenjem permutacione važnosti atributa (eng. *permutation feature importance*). Ovaj algoritam podrazumeava da se svaki atribut na-

izmenično permutuje sa nekim drugim atributom, pa se onda gleda opadanje performansi modela. Što je to opadanje izraženije, to je atribut bitniji za predikciju ciljne varijable. Neka je baza za obučavanje \mathcal{D} . Prvo se model obuči i izračuna referentni rezultat s . Potom se za svaki atribut $j \in \mathcal{D}$ radi k permutacija. Za svaku permutaciju k atribut se premešta na drugo mesto u odnosu na inicijalnu bazu podataka i tako se pravi nova baza za trening koja je zapravo loša kopija originalne (eng. *corrupted database*). Za ovu bazu se onda model nanovo obučava i računa se novi rezultat predikcije, a potom i važnost atributa j preko formule:

$$i_j = s - \frac{1}{K} \sum_{k=1}^K s_{k,j} \quad (126)$$

Analiza je važna sa stanovišta da li dati model može da ima manju dimenzionalnost od prvobitnog, ali tako da sačuva sve bitne informacije iz originalnog seta podataka. Takođe, u originalnoj bazi podataka postoje i redundantni podaci, npr. kada se definiše efektivni ionizacioni potencijal gornjeg nivoa preko formule (124) u njemu dalje figurišu i energija gornjeg nivoa i energija jonizacije. U originalnom modelu ovi atributi su ostavljeni, a sada treba ispitati i njihov uticaj.

Svaki atribut je permutovan 10 puta, i njegova važnost izračunata je po formuli (126). Rezultat analize prikazan je na slici 29.



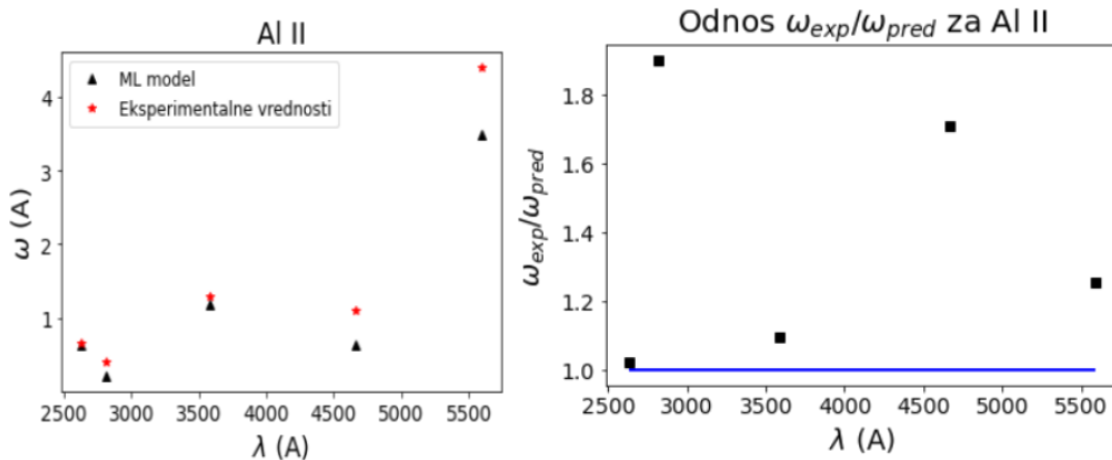
Slika 29: Analiza važnosti atributa korištenjem permutacione važnosti.

Očekivano, model smatra za najbitniji ulazni atribut gustinu elektrona što je i fizički opravdano, dok dalje imamo isključivo atomske parametre. Interesantno je da temperatura plazme jako slabo utiče na predikcije modela, što i jeste u skladu sa Stark-ovim efektom. Temperaturna zavisnost je mala, ali ipak postoji. Rezultat permutacione analize govori nam da možemo smanjiti dimenzionalnost ulaznih podataka, kako bi dobili još brži model sa istom moći predviđanja. Odbačeni atributi su energija gornjeg nivoa, ionizaciona energija, glavni kvantni broj donjeg nivoa i orbitalni kvantni broj donjeg nivoa. Ukupni orbitalni kvantni

broj oba nivoa zadržan je radi različitih multipleta, dok je temperatura elektrona ostavljena iz fizičkih razloga jer ipak ima malog uticaja na Stark-ovu poluširinu linije. Model je ponovo obučen, ali nije bilo mnogo boljeg rezultata. Koeficijent determinacije za iste parametre slučajne šume date u tabeli 2 sada je bio $R^2 = 0.98$, što predstavlja blago poboljšanje, ali je srednja relativna greška modela ostala u opsegu od 8 do 10 %. Dakle, zaključak je da u početnoj analizi redundantni podaci nisu imali veliki uticaj na generalizaciju modela, stoga je nastavljeno sa korišćenjem istog modela čije su predikcije sada upoređene sa eksperimentalnim merenjima.

3.5 Poređenje predikcija modela slučajne šume sa eksperimentalnim podacima

Kako bi se ispitala pouzdanost razvijenog modela slučajne šume, njegove predikcije upoređene su sa eksperimentalnim podacima raznih autora. Prvo poređenje je poređenje sa rezultatima Dojića i saradnika [98] za emitere Al II i Al III. Rezultati poređenja prikazani su na slici 30.



Slika 30: Poredjenje eksperimentalnih i predviđenih vrednosti za Al II. Prava linija na slici desno predstavlja slučaj kada je eksperimentalno merena poluširina jednaka predviđenoj poluširini

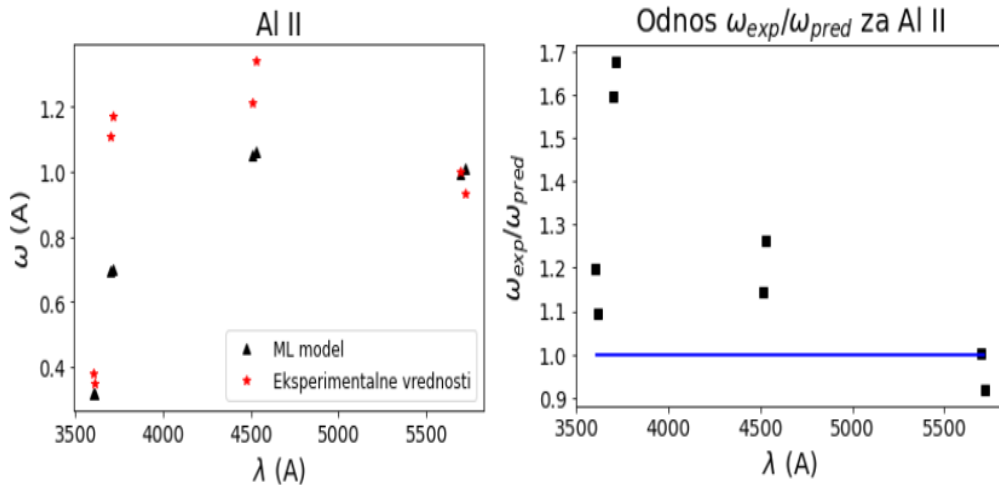
Pored slike 30 poređenje predviđenih vrednosti i eksperimentalnih vrednosti dano je u tabeli 3.

Tabela 3: Rezultati poređenja predviđenih Stark-ovih poluširina i eksperimentalno merenih vrednosti za Al II. Sve širine normirane su na gustinu elektrona od $N_e = 10^{23} \text{ m}^{-3}$

Talasna dužina [nm]	T_e [K]	ω_{exp} [A]	ω_{pred} [A]	$\omega_{exp}/\omega_{pred}$
263.154	26400	0.65	0.63	1.02
281.618	26400	0.40	0.21	1.89
358.66	26400	1.29	1.17	1.09
466.31	26400	1.09	0.64	1.70
559.33	26400	4.40	3.50	1.25

Sa slike 30 i iz tabele 3 može se zaključiti da je u slučaju emitera Al II srednja relativna greška predikcije modelom slučajne šume 24 %. Ova greška odgovara i SCP modelu čija usrednjena greška predikcije takođe iznosi oko 20 %.

Za Al III rezultati predikcije napravljenog modela dati su na slici 31 i u tabeli 4.

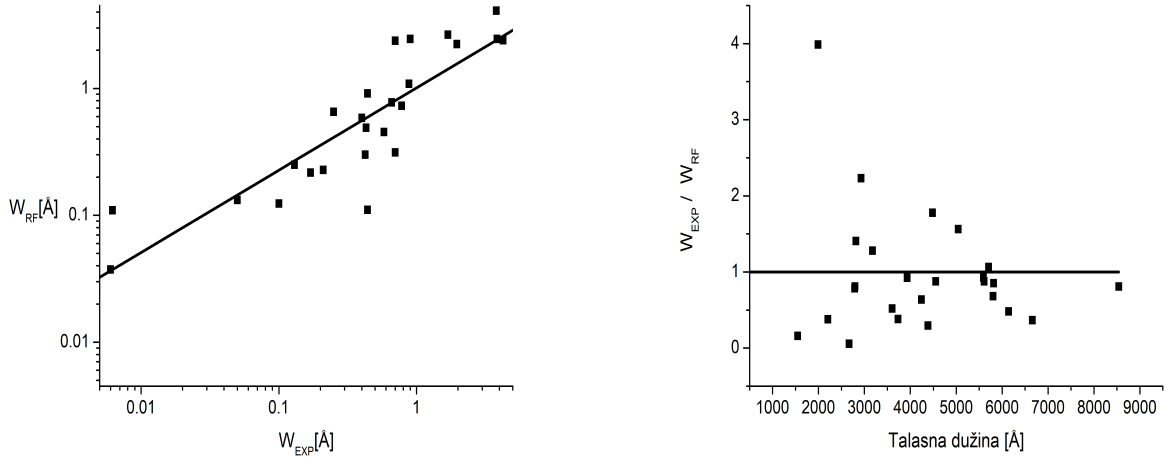


Slika 31: Poređenje eksperimentalnih i predviđenih vrednosti za Al III. Prava linija na slici desno predstavlja slučaj kada je eksperimentalno merena poluširina jednaka predviđenoj poluširini

Tabela 4: Rezultati poređenja predviđenih Stark-ovih poluširina i eksperimentalno merenih vrednosti za Al III. Sve širine normirane su na gustom elektrona od $N_e = 10^{23} m^{-3}$

Talasna dužina [nm]	T_e [K]	ω_{exp} [A]	ω_{pred} [A]	$\omega_{exp}/\omega_{pred}$
360.16	26400	0.38	0.32	1.18
361.24	26400	0.35	0.32	1.09
370.21	26400	1.11	0.70	1.59
371.31	26400	1.17	0.70	1.68
451.26	26400	1.21	1.05	1.14
452.92	26400	1.34	1.06	1.26
569.66	26400	1	0.99	1
572.27	26400	0.93	1.01	0.91

Iz tabele 4 zaključujemo da se srednja relativna greška modela za slučaj emitera Al III 18 %. Eksperimentalni podaci i predikcije modela upoređene su i za eksperimentalno određene širine iz radova [99, 100]. Rezultati ovog poređenja prikazani su na slici 32 i u tabeli 5.



Slika 32: Poređenje eksperimentalnih i predviđenih vrednosti za različite emitere date u tabeli 5. Prava linija na slici desno predstavlja slučaj kada je eksperimentalno merena poluširina jednaka predviđenoj poluširini

Tabela 5: Rezultati poređenja predviđenih Stark-ovih poluširina i eksperimentalno merenih vrednosti za različite emitere. Sve širine normirane su na gustinu elektrona od $N_e = 10^{23} \text{ m}^{-3}$

Emiter	Talasna dužina [nm]	T_e [K]	ω_{exp} [A]	ω_{pred} [A]	$\omega_{exp}/\omega_{pred}$
Al II	266.92	10500	0.0062	0.10	0.05
Al II	199.05	10500	0.44	0.11	3.98
Al III	360.52	50000	0.13	0.24	0.5
Al III	570.53	26400	0.78	0.73	0.06
Ba II	614.17	13000	0.44	0.91	0.48
Ba II	455.40	13000	0.49	0.43	0.87
Ca II	854.21	13000	0.88	1.08	0.80
Ca II	393.37	13000	0.23	0.21	0.92
Ca II	373.62	13000	0.25	0.65	0.38
Ca II	317.93	13000	0.58	0.45	1.27
Pb II	560.89	11600	1.96	2.23	0.87
Pb II	424.49	11600	1.69	2.64	0.63
Pb II	504.26	11600	3.84	2.45	1.56
Pb II	220.35	28000	0.05	0.13	0.05
Pb II	438.65	24000	0.70	2.37	0.29
Pb II	666.02	24000	0.90	2.45	0.36
Mg II	279.55	14300	0.12	0.10	0.80
Mg II	279.08	14300	0.17	0.21	0.78
Mg II	292.87	10000	0.70	0.31	2.23
Mg II	448.12	10000	4.26	2.39	1.78

Iz tabele 5 i sa slike 32 vidimo da model daje dobar red veličine Stark-ove poluširine emitovane spektralne linije sa tendencijom da uglavnom precenjuje njenu vrednost, što se jasno vidi sa grafika na slici 32 desno. Primetno je da model najveća odstupanja pravi u UV delu spektra, dok odstupanja teže manjim vrednostima u vidljivom delu spektra. Ukoliko izuzmemmo odudarajuće podatke iz analize, dobićemo da je prosečna relativna greška modela oko 38%, što je dovoljno dobro za kvalitativnu ocenu elektronske poluširine spektralne linije koja do sada nije eksperimentalno određena. Treba takođe biti svestan i toga da su najbolje eksperimentalno određenje Stark-ove poluširine i dalje date sa greškama reda veličine 15%

[99]. Ako se razmataju i analize date u tabelama 3 i 4 dolazi se do zaključka da je odstupanje modela prilikom poređenja sa eksperimentalnim vrednostima između 25 i 30 %.

4 Primena mašinskog učenja u LIBS kvantitativnoj analizi

Cilj istraživanja u ovom radu bio je ispitati mogućnost korištenja baze podataka za obučavanje modela snimljene pod kontrolisanim eksperimentalnim uslovima u jednoj laboratoriji, koji bi posle bio korišten za predviđanje sastava nepoznatih uzoraka iz spektara snimljenih u drugoj laboratoriji pod istim eksperimentalnim uslovima. Važnost rezultata dobijenih u ovom radu predstavlja i to da standardni uzorci nisu dostupni svim laboratorijama, skupi su, a i treba ih imati više desetina kako bi se postigla što bolja varijansa u bazi za obučavanje. Zbog toga što se zbog svojih osobina i dalje razmatraju kao referentni materijali za prvi zid reaktora [101], odlučeno je da ispitivani uzorci budu austenitni nerđajući čelici.

Što se tiče pristupa kvantitativnoj analizi u LIBSu, razlikuju se dve metode. Jedna je metoda univarijantne kalibracije, tj. pravljenje standardne kalibracione krive za intenzitet pogodno odabrane linije i određivanje nepoznate koncentracije prisutnog elementa iz ove kalibracione krive. Drugi način jeste da se iz Saha - Boltzmann-ove jednačine odrede gustina elektrona i elektronska temperatura, što dalje omogućava određivanje nepoznate koncentracije konstituenta metala nezavisno od efekta osnove. Za ovaj pristup neophodno je pretpostaviti važenje lokalne termodynamičke ravnoteže (LTR) u plazmi i on je poznat i kao bezkalibracioni metod (eng. *Calibration - Free LIBS*) [102]. Kako bi se ubrzala kvantitativna analiza uzorka, u LIBS zajednicu ušla je i primena mašinskog učenja i veštačke inteligencije [103–106]. Osnovni algoritmi koji se najčešće koriste pri analizi jesu analiza glavnih komponenti (PCA) za snižavanje dimenzionalnosti ulaznih parametara (to su najčešće merene talasne dužine), potom metoda potpornih vektora (SVM) za klasifikaciju po kategorijama ili metod parcijalnih najmanjih kvadrata za kvantitativnu analizu [107]. Pored ovih osnovnih algoritama mašinskog učenja, razni autori su primenili i proste duboke neuronske mreže ili konvolucionale neuronske mreže za klasifikaciju ili za kvantitativnu analizu različitih tipova uzorka [108–112].

Nelinearni modeli mašinskog učenja, poput slučajnih šuma, takođe su u širokoj upotrebi u analizi LIBS spektara [113–116]. Pre same konstrukcije modela, umesto metode glavnih komponenti koja traži pravce maksimalne varijanse u podacima, mogu se koristiti i neki drugi algoritmi kao što su već pomenuti metod permutacione važnosti atributa, potom Gini-jev kriterijum važnosti atributa, kao i drugi metodi napravljeni od strane autora direktno. Iako su glavne linije emitera koji se očekuju uglavnom poznate, poboljšanje automatske detekcije glavnih linija u spektru u mnogome ubrzava kvantitativnu analizu. U slučaju LIBS analize čelika, koji su od interesa i u ovom radu, Zhang i saradnici [117] su primenili metod slučajne šume za određivanje sastava nepoznatih čeličnih uzorka, dok su kasnije u radu [118] primenili i neuronsku mrežu kombinovanu sa predloženim algoritmom selekcije najvažnijih atributa koristeći sopstveni algoritam SelectKBest za određivanje koncentracije elemenata koji su prisutni u tragovima u meti. Dalje, za izbor najrelevantnijih atributa Liu i saradnici [119] su koristili metod permutacione važnosti atributa primenjen na model slučajne šume kako bi izvršili smanjenje dimenzionalnosti ulaznih podataka. Gini-jev kriterijum, koji je korišten i u ovom radu, korišten je u radovima [120, 121] u kombinaciji sa metodom slučajne šume za studiju klasifikacije, međutim ova kombinacija procene važnosti atributa i modela za predikciju nije bila do sada korištena za kvantitativne analize u LIBS zajednici i predstavljaju njen potencijalni originalni doprinos.

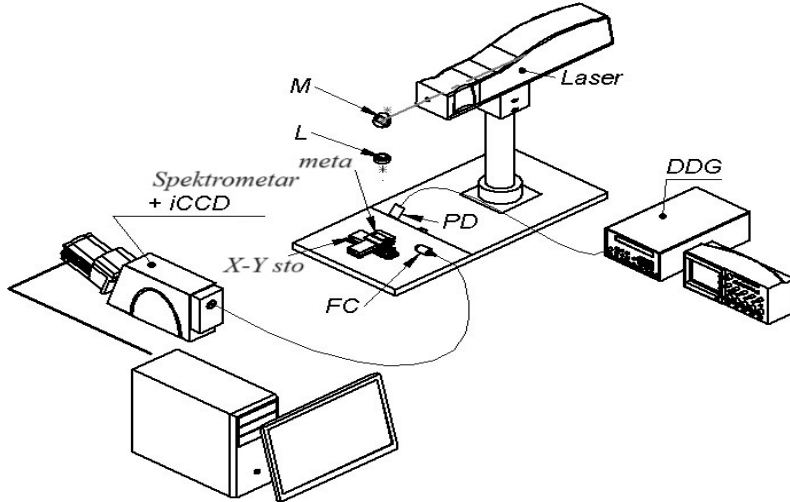
Jedan od problema koji se pojavljuje pri primeni veštačke inteligencije u LIBS zajednici jeste pravljenje dovoljno velike baze za obučavanje modela. To zahteva da eksperimentator poseduje veliki broj standardnih uzoraka (barem 50) koji su često i skupi te ih veliki broj laboratorijskih ne može priuštiti. Takođe, eksperimentator mora obezbediti i da se uslovi snimanja ne menjaju u toku akvizicije spektara, što značajno otežava rad. Jedne od samo pouzdanih baza podataka napravljene su za LIBS konferencije, u sklopu kojih se održava tradicionalno takmičenje uporedne procene (*benchmarking*) na temu primene veštačke inteligencije u LIBS-u. Na poslednjoj konferenciji LIBS 2022 u Bariju, rađena je LIBS kvantitativna analiza i određivanje koncentracije glavnih elemenata u čeliku, a baza za obučavanje je javno dostupna [122]. Postojanje javno dostupne i pouzdane baze podataka predstavlja idealnu priliku za testiranje mogućnosti obučavanja modela na već unapred pripremljenoj bazi za obučavanje, pri čemu se u laboratorijskom eksperimentatoru snimaju samo spektri nepoznatih test uzoraka. Ovo je bilo moguće izvesti jer u laboratorijskoj spektroskopiji plazme i lasera u Institutu za fiziku postoji sva neophodna oprema kako i potrebno iskustvo za postavljanje identičnog eksperimenta i postizanje približno istih uslova snimanja baze za obučavanje. Glavni cilj ovog rada je testiranje greške koja se inherentno uvodi u ovakvom procesu, kao i analiza metoda koje mogu da se preduzmu kako bi se iste mininizovale.

U nastavku, opisana je eksperimentalna postavka LIBS sistema za akviziciju. Nakon toga, objašnjen je postupak predpripreme baze za obučavanje i sam odabir modela, nakon čega su izloženi i rezultati. Celokupni rezultati ovog poglavlja predstavljeni su u radu [123], a sve analize rađene su u programskom jeziku python primenom sci-kit learn i keras biblioteka otvorenog koda [95].

4.1 Opis eksperimenta

Eksperimentalna postavka bila je identična kao ona opisana u propratnom fajlu koji je došao uz bazu za obučavanje i prikazan je na slici 33. Predstavlja klasičnu LIBS eksperimentalnu postavku gde se laserski zrak iz Nd:YAG lasera Quantel koji radi na osnovnom harmoniku $\lambda = 1064$ nm, ima vreme trajanja impulsa od 6 ns i repeticiju od 10 Hz fokusira na metu preko ogledala M i sočiva L žižne daljine $f = 15$ cm. Spektar generisane plazme se posmatra preko fokusirajućeg kolimatora žižne daljine $f = 4.4$ cm i fiber optičkim kablom se vodi do spektrometra Mechelle 5000 i detektuje preko Andor iStar ICCD kamere hlađene na -15°C . Kako bi se dobio što bolji odnos signal šum, korišteno je pojačanje kamere od 80 (mogući opseg 0-255). Kamera je okidana preko generatora kašnjenja Stanford Research Systems 535 (DDG generatora), kojim je kontrolisano kašnjenje kamere i njena ekspozicija. Sam DDG je okidan preko fotodiode PD koja je posmatrala plazmu. Meta je pomerana pomoću X-Y motorizovanog pomerača kako bi imali "sveže" mesto za novi pucanj. Akvizicija je rađena tako što se ispred laserskog zraka montirao opto - mehanički prekidač koji je povezan sa kontrolerom za brojanje impulsu. Na kontrolor je doveden sinhronizacioni signal iz lasera, koji vrši brojanje tih impulsu. Nakon izbrojanih 16 impulsu, prekidač se aktivira i laserski zrak se blokira. Ovo predstavlja jedno snimanje, a rađeno je usrednjavanje 20 ovakvih snimanja. To efektivno daje 320 laserskih pucnjeva u isto mesto. Rezultujući test spektar dobijen je kao zbir 5 ovako dobijenih spektara. Eksperiment je rađen u vazduhu, energija lasera bila je podešena na (96.1 ± 1.2) mJ, dok je kašnjenje bilo $0.6 \mu\text{s}$ a ekspozicija kamere $50 \mu\text{s}$. Diametar spota na meti bio je približno 0.2 mm, kako bi što bolje ponovili uslove snimanja.

Priprema uzorka za snimanje uključivala je brušenje uzorka sa brusnim papirom granulacije 200, pa potom sa brusnim papirom granulacije 600, te je na kraju površina uzorka obrisana sa etanolom.



Slika 33: Eksperimentalna postavka. Laserski impuls iz Nd:YAG lasera Quantel (6 ns, $\lambda = 1064 \text{ nm}$, 95 mJ) je preko ogledala M i sočiva L fokusiran na metu od čelika koja se nalazila na X-Y pomeraču.

Spektar svakog čelika snimljen je Mechelle 5000 spektrometrom za jedan pucanj Nd:YAG lasera, energije 95 mJ, talasne dužine $\lambda = 1064 \text{ nm}$ i dužine trajanja impulsa od 10 ns, dok je dijаметар laserskog spota na meti bio 0.2 mm. Ovo su uslovi koji su ponovljeni prilikom snimanja test spektara.

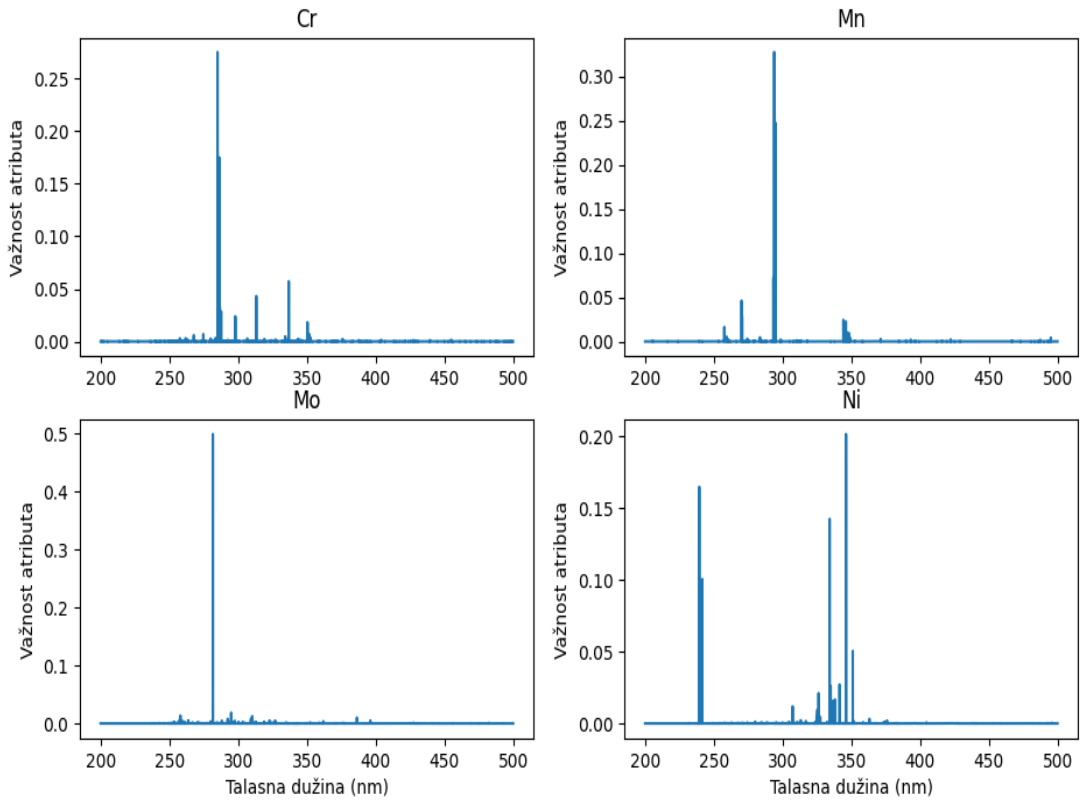
4.2 Predpriprema podataka

Snimljeni spektri u bazi za obučavanje su spektri 42 različite vrste čelika. Za svaki uzorak, u bazu je akumulirano 50 spektara. Ovo daje ukupno 2100 spektara u bazi za obučavanje, što predstavlja dovoljan broj kako bi se razvio dobar prediktivni model. Kako bi model što bolje naučio ulazne podatke, oni su normalizovani koristeći Standard Normal Variate (SNV) metodu normalizacije. Ova metoda podrazumeva da se od intenziteta svakog piksela oduzme srednja vrednost intenziteta svih piksela i podeli sa standardnom devijacijom snimljenog spektra [124]:

$$I_{new} = \frac{I_{old} - I_\mu}{\sigma} \quad (127)$$

Pri čemu je I_{new} vrednost intenziteta nakon normalizacije, I_{old} je merena vrednost intenziteta, I_μ predstavlja srednju vrednost intenziteta a σ standardnu devijaciju spektra. Nakon normalizacije, uklanjanje odudarajućih podataka urađeno je sa algoritmom izolacione šume (eng. *Isolation Forest*). Potom, urađeno je i skaliranje podataka koristeći MinMax skaliranje dato sa:

$$I_{new} = \frac{I - I_{min}}{I_{max} - I_{min}} \quad (128)$$



Slika 34: Važnost ulaznih atributa. Vidi se da su prepoznate neke od glavnih analitičkih linija elemenata od interesa. Na primer, prepoznanata je Mo II linija na 281.61 nm, a velika važnost je takođe data je i atributima jonskih linija Ni II na 239.45 nm i Ni II na 241.6 nm. Pored toga, za atom hroma veliku važnost imaju linije Cr II na oko 286 nm i 336 nm.

Ovo skaliranje dovodi vrednosti atributa na vrednosti između 0 i 1, što predstavlja stabilan opseg za većinu algoritama veštačke inteligencije i mašinskog učenja.

Pošto je ulazni set podataka velike dimenzionalnosti (40002 kolone), potrebno ga je smanjiti uz očuvanje najbitnijih informacija. Prvo smanjenje je jednostavno postignuto smanjenjem opsega emitovanog spektra na oblast talasnih dužina između 200 i 500 nm, jer u ovom opsegu leži većina analitičkih linija elemenata od interesa. Dimenzionalnost baze nakon ovog koraka iznosila je oko 15 000 kolonaje oko 15 000 kolona, što je i dalje prevelika brojka, pa je za dalju redukciju dimenzionalnosti iskorišten Gini-jev indeks. Biranjem atributa za koji je Gini-jev indeks najmanji, povećava se čistoća sledećih uzoraka, što rezultira time da algoritam na kraju teži da ostavi čiste uzorkе sa samo jednom vrednošću za date ulazne podatke. Algoritam mašinskog učenja koji ima implementiran ovaj algoritam jeste slučajna šuma, koja je korištена za dalju redukciju podataka. Za svaki element od interesa (Cr, Ni, Mo i Mn) formirana je slučajna šuma sa različitim hiperparametrima. Koristeći GridSearchCV algoritam opisan u prethodnom poglavlju, nađeni su optimalni hiperparametri. Broj stabala odlučivanja u slučajnoj šumi za svaki element postavljen je na 300, dok dubina drveta nije

ograničavana. Svi ostali parametri modela ostali su na svojim podrazumevanim vrednostima. Rezultat analize važnosti ulaznih atributa korišćenjem Gini-jevog indeksa prikazan je na slici 34. Na slici vidimo da su prepoznate neke od glavnih analitičkih linija elemenata od interesa. Prepoznata je Mo II linija na 281.61 nm, a velika važnost data je i atributima jonskih linija Ni II na 239.45 nm i Ni II na 241.6 nm. Takođe veliku važnost imaju i linije Cr II na oko 286 nm i 336 nm. Granica važnosti atributa je menjana, a najbolji rezultati dobijeni su za 2×10^{-4} .

4.3 Rezultati

Nakon smanjenja dimenzionalnosti baze za obučavanje, broj spektara korišten za obučavanje je dat u tabeli 6.

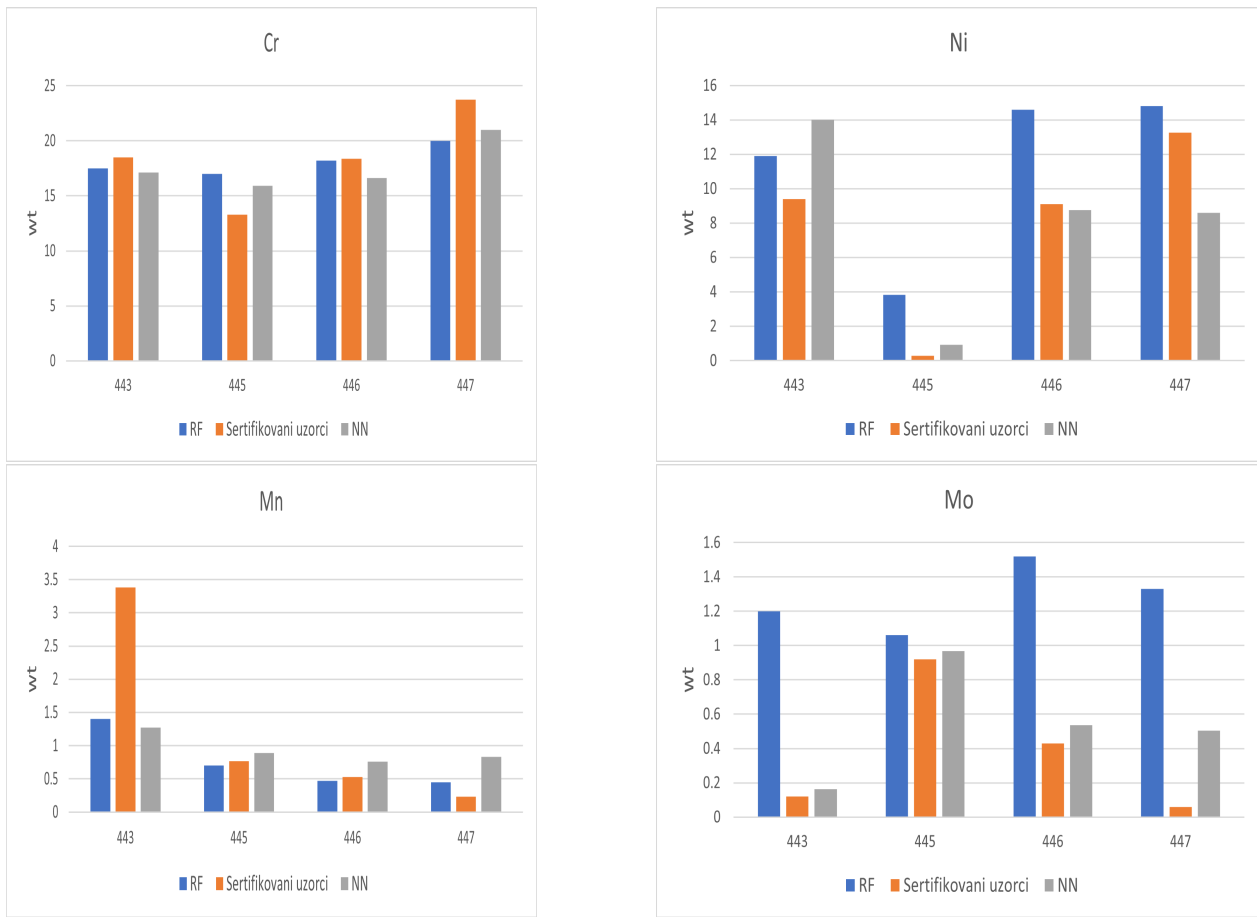
Tabela 6: Ukupna dimenzionalnost baze za obučavanje i broj uzoraka za obučavanje modela

Element	Broj ulaznih atributa	Broj spektara za trening	Broj spektara za validaciju
Cr	273	1608	492
Ni	120	1608	492
Mn	129	1608	492
Mo	317	1608	492

Instancirana su četiri modela, jedan za predikciju koncentracije svakog elementa od interesa. Korištena su dva različita prilaza, jedan je slučajna suma, a drugi je prosta potpuno povezana neuronska mreža. Dakle, to čini ukupno četiri instancirane slučajne šume i četiri instancirane neuronske mreže. Svaki instancirani model slučajne šume je imao 350 stabala odlučivanja, dok je arhitektura svake neuronske mreže bila sa tri skrivena sloja sa 100, 150 i 50 neurona respektivno. Aktivaciona funkcija je bila ReLU, a maksimalan broj iteracija postavljen na 1000. Kao što se iz tabele 6 može zaključiti, baza za obučavanje podeljena je u odnosu 80% prema 20% za trening i validaciju svakog modela. Rezultati predikcije modela poređeni su na dva načina: preko koeficijenta determinacije R^2 i preko korena iz srednjeg kvadratnog odstupanja RMSE (eng. *Root Mean Square Error*). Ovi rezultati prikazani su u tabeli 7.

Tabela 7: Rezultati predikcije modela slučajne šume (RF) i neuronske mreže (NN) na bazi za validaciju modela za elemente od interesa

Element	R^2_{RF}	R^2_{NN}	$RMSE_{RF}$	$RMSE_{NN}$
Cr	0.88	0.97	3.68	1.84
Ni	0.97	0.98	1.77	1.21
Mn	0.89	0.93	0.39	0.31
Mo	0.85	0.96	0.51	0.26



Slika 35: Predviđene koncentracije korišćenjem RF i NN modela i njihovo poređenje sa sertifikovanim vrednostima. Brojevi na x - osi označavaju laboratorijski broj uzorka. Slika sugerisce da je model postigao dobre rezultate za Cr, Mn i Ni, ali sa druge strane RF model je imao loš performans za slučaj molibdena Mo.

Na osnovu tabele 7 može se videti da je na osnovu oba parametra, neuronska mreža dala bolje rezultate za sve elemente od interesa.

Tabela 8: Koncentracije elemenata od interesa za laboratorijske uzorke čiji je spektar izmeren u ovom radu

Element	443 (Cr18.5-Ni9.5)	445 (AISI 410)	446 (AISI 321)	447 (AISI 309)
Cr	18.5	13.31	18.35	23.72
Ni	9.4	0.28	9.11	13.26
Mn	3.38	0.77	0.53	0.23
Mo	0.12	0.92	0.43	0.053

Međutim, cilj ovog rada bio je ispitati da li je moguće nakon obučavanja modela na

već dostupnoj bazi podataka koristiti isti model za predviđanje koncentracije nepoznatih uzoraka snimljenih pod istim uslovima u drugoj laboratoriji. Zbog toga je snimljen spektar 4 austenitna čelika laboratorijskih oznaka 443, 445, 446 i 447 čije su koncentracije elemenata od interesa unapred poznate i date su u tabeli 8. Koncentracije dobijene sa oba prilaza prikazane su na slici 35. Izloženi rezultati ukazuju da je moguće istrenirati model, a potom model koristiti za predviđanje test uzorka snimljenih u sopstvenoj laboratoriji. Treba takođe naglasiti da je u ovom slučaju posao bio otežan činjenicom da ulazni spektri u bazi za obuku nisu bili korigovani na intenzitet, stoga ni ulazni test spektri nisu bili korigovani na intenzitet. Može se videti da neuronska mreža daje dobre rezultate za sve elemente, slučajn šuma (RF) nešto lošije, pa je u slučaju molibdena došlo i do preprilagođavanja modela trening podacima. Model za predikciju molibdena je još jednom obučen, pri čemu su korišteni svi ulazni atributi bez ikakve redukcije, međutim rezultati predikcija na validacionom skupu podataka kao i na test skupu su ostali isti.

5 Primena veštačke inteligencije za modelovanje EUV spektra volframa

Kako je wolfram izabran za materijal prvog zida budućih fuzionih reaktora, sprovedene su intenzivne studije emitovanog elektromagnetskog spektra wolframa u različitim tokamacima i steleratorima [125–130], ili u joniskim zamkama elektronskog snopa [131, 132] (EBIT). Joni sa najgornjom N ljuškom ($n = 4$) predstavljaju dominantnu vrstu u plazama sa elektronskim temperaturama reda 0.6 do 4 keV. Emitovane spektralne linije većinom leže u oblasti ekstremnog ultraljubičastog zračenja i mekog X zračenja. Zbog veoma kompleksne strukture energetskih nivoa jona sa parcijalno popunjrenom 4d ili 4f podljuškom, jako veliki broj emitovanih linija se stapa u veoma uskom intervalu talasnih dužina. Ovo stapanje dovodi do pojave kvazikontinuumskog spektra koji se naziva UTA (eng. za *Unresolved Transition Array*) spektar. Tipičan primer jeste UTA spektar wolframa koji nastaje $n = 4$ -4 prelazima jona wolframa različitih stepena ionizacije koji se međusobno stapaju na oko 5 nm, pa se dobija nešto nalik kvazikontinuumskoj traci [128]. Prvi pokušaji modelovanja ovakvog tipa spektra korištenjem CR modela nije u potpunosti uspeло delimično usled numeričkih ograničenja proračuna, a delom i zbog nemogućnosti da se uključe komplikovane pobuđene elektronske konfiguracije različitih emitera [126–129]. Dugi niz godina, spektri wolframa proučavaju se na heliotronu LHD u Japanu pomoću različitih spektrometara [128–130]. Ova mašina pokazala se kao dobra za snimanje spektara wolframa zbog visoke temperature jezgra plazme, intenziteta spektralnih linija koje su emitovane i robustnosti prilikom ubacivanja nečistoća. Kao rezultat ovih istraživanja, formirana je velika baza emitovanih spektara wolframa. Stoga se prirodno nameće upotreba veštačke inteligencije kao rešenja za modelovanje ovog tipa spektra.

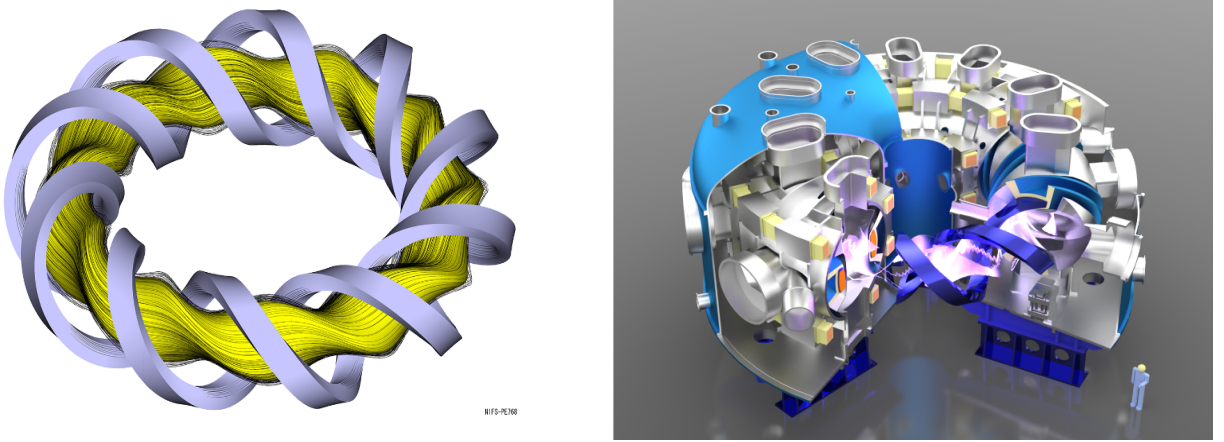
Za te svrhe, iskorišten je varijacioni autoenkoder (VAE), čija je arhitektura i princip rada objašnjen ranije u sekciji 2.5.4. Što se tiče primene varijacionih autoenkodera u fizici, najčešće se koriste za pravljenje kombinovanih modela, gde se koriste samo enkoder ili dekoder. Naprimer, Streeter i saradnici [133] su koristili VAE kako bi enkodirali profile gustine elektrona i profila rasejanja laserskog zraka, čije su latentne reprezentacije zajedno sa vrednostima laserske energije iskorištene za pravljenje drugog modela koji daje finalne predikcije. U niskotemperaturnoj plazmi, Daly i saradnici [134] su iskoristili VAE za modelovanje spektra ICP plazmi, tako što su konstruisali neuronsku mrežu koja je za unapred zadate parametere plazme naučila latentnu reprezentaciju spektara, odakle su pomoću dekodera rekonstruisali nove spekture.

Veštačka inteligencija i mašinsko učenje široko su rasprostanjeni i u fizici fuzionih plazmi. Piccione i saradnici [23] su iskoristili model slučajne šume i različite vrste neuronskih mreža kako bi proučavali MHD stabilnost tokamaka na bazi podataka dobijenoj merenjima na NSTX tokamaku. Li i saradnici [24] su iskoristili fluidne modele u kombinaciji sa potpuno povezanim neuronskim mrežama kako bi predvideli dominantne tip turbulencije kao i transportne osobine. Sa druge strane, Fu i saradnici [135] su koristili slučajnu šumu za predviđanje modova cepanja (eng. *tear-nig modes*) i disruptacija sa jako velikom tačnošću. Slučajna šuma je takođe korištena i u modelima Brenzkea i saradnika [21] kako bi predvideli snagu deponovanu na divertor na ASDEX-U tokamaku. Takođe, nedavno su Wei i saradnici [136] pokazali da veštačka inteligencija može uspešno biti primenjena i na rekonstrukciju profila faktora sigurnosti u tokamaku. Što se tiče varijacionog enkodera, on je iskorišten u radu Ferreira

i saradnika [137] kako bi detektovali anomalije u bolometarskoj tomografiji i te anomalije koristili kao perkurzore za disruptije. Pored toga, Wei i njegovi saradnici [138] su iskoristili VAE kako bi našli oblasti stabilnosti tokamaka.

5.1 Opis eksperimenta

LHD predstavlja $l = 2, m = 10$ heliotron sa superprovodnim kalemovima koji se nalazi u Japanu, u Nacionalnom institutu za fuziona istraživanja. Ovaj heliotron prilazan je na slici 36.



Slika 36: Heliotron LHD u Japanu. Levo je prikazan oblik plazme u mašini, dok je desno prikazan sam uređaj sa kriostatom. Slike su preuzete sa zvaničnog sajta NIFSa i javno su dostupne

Parametri LHDa dati su u tabeli 9.

Tabela 9: Parametri LHDa

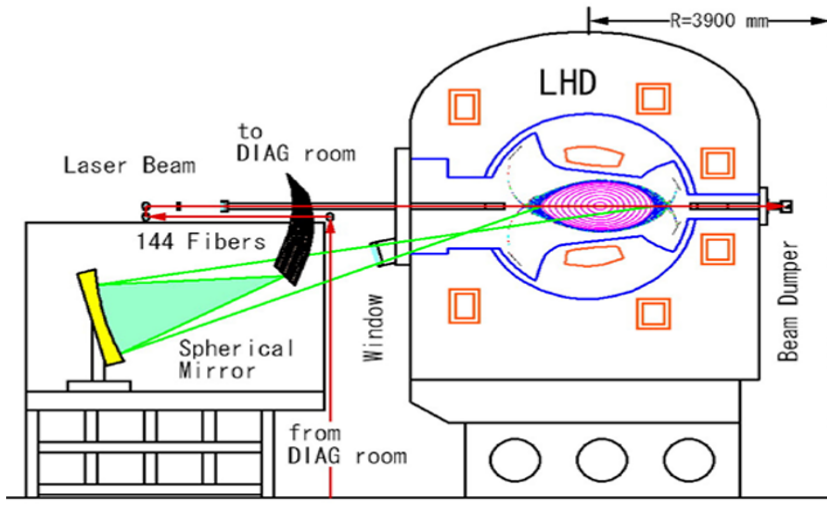
Veliki radius	3.9 m
Manji radius	0.6 m
Zapremina plazme	30 m ³
Jačina magnetnog polja	3.6 T
Ukupna snaga grejanja plazme	36 MW

Grejanje plazme ostvaruje se pomoću 5 NBI (eng. *Neutral Beam Injection*) modula ukupne snage 27 MW i instaliranih ECH (eng. *Electron Cyclotron Heating*) i ICRH (eng. *Ion Cyclotron Resonance Heating*) žirotrona. Za ECH antene mogu da isporuče 1.3 MW u kontinualnom modu ili oko 2 MW u toku od 2 s. Antene od ICRHa daju 1.3 MW u toku 6 s u opsegu frekvencija 25 do 100 MHz ili 0.8 MW kontinualno. LHD je opremljen raznim vrstama dijagnostičkih uređaja, a u ovom radu korišteni su sistemi za Thomson-ovo rasejanje, EUV

spektrometar SOXMOS (*Soft X-Ray Multichannel Spectrometer*) kao i sistem za ubacivanje čestica TESPEL (*Tracer-Encapsulated Solid Pellet*) i o ovim sistema će biti reči u nastavku.

5.1.1 Thomson-ovo rasejanje

Heliontron LHD opremljen je sistemom za detekciju Thomson-ovog rasejanja koji se sastoji od 4 Nd:YAG lasera (jedan Continuum DLS 9030 energije 1.6 J repeticije 30 Hz, dva Thales SAGA 230-10 energije 2 J i repeticije 10 Hz i jedan Continuum NY-8050 energije 0.55 J i repeticije 50 Hz), kolektorske optike i detektora. Ovaj sistem je prikazan na slici 37 i detaljno opisan u radu [139].



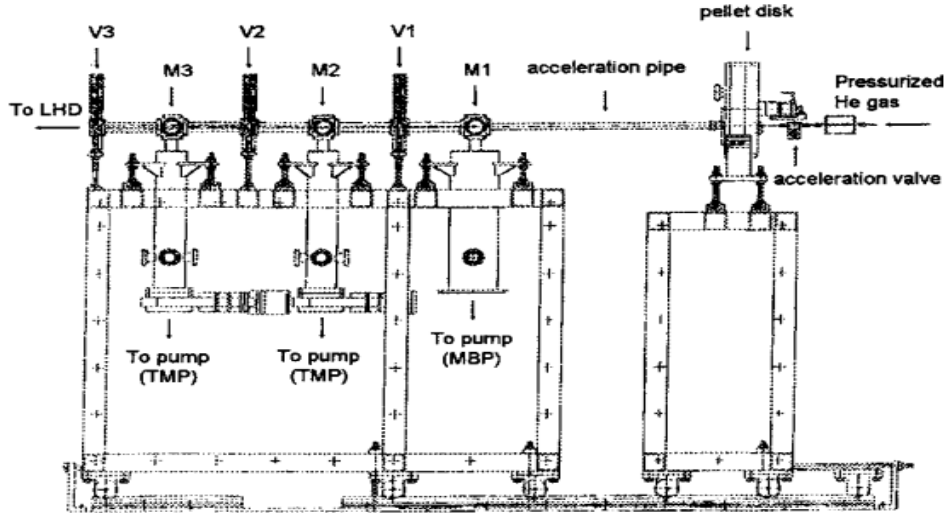
Slika 37: Shema Thomson-ovog rasejanja instalirana na LHDu.

Laserski zraci koji se vode iz dijagnostičke sobe dolaze do ogledala preko kojih se usmeravaju u plazmu duž glavnog radiusa u delu sa horizontalno izduženom plazmom. Rasejni zraci prolaze kroz prozor za posmatranje i kolimišu se preko zlatom prevučenog sfernog ogledala na 144 fibera koji vode svetlosni signal do detektora. Maksimalna vremenska rezolucija sistema je 10 ms. Opseg elektronskih temperatura koje sistem može da meri je između 5 eV i 20 keV. Elektronske koncentracije koje sistem može da meri su one iznad 10^{18} m^{-3} .

5.1.2 Tracer-Encapsulated Solid Pellet (TESPEL) sistem za ubacivanje čestica u plazmu

Tracer-Encapsulated Solid Pellet (TESPEL) sistem za ubacivanje čestica na LHDu koji se sastoji od tri sistema diferencijalnog pumpanja sa tri brzo zatvarajuća ventila prikazan je na slici 38 i detaljno je opisan u radovima [140–142]. Ubrzanje se vrši pomoću helijuma koji se nalazi pod pritiskom od od 6 do 20 atmosfere. Portovi M1, M2 i M3 služe za dijagnostiku peleta, a ventili V1, V2 i V3 imaju prosečno vreme zatvaranja od 5 ms što sprečava curenje helijuma u LHD. Komora M1 se vakumira mehaničkom pumpom, a komore M2 i M3 se vakumiraju turbo molekularnim pumpama i pritisak koji se postiže u komori M3 je reda veličine 10^{-9} torr.

Peleti se prave u tri oblika: sfera, hemisfera i cilindar. Sistem postiže brzine peleta reda veličine 200 m s^{-1} . Primećeno je u eksperimentima da najbolji oblik što se tiče samog lansiranja bilo lakših bilo težih nečistoća predstavlja hemisfera.

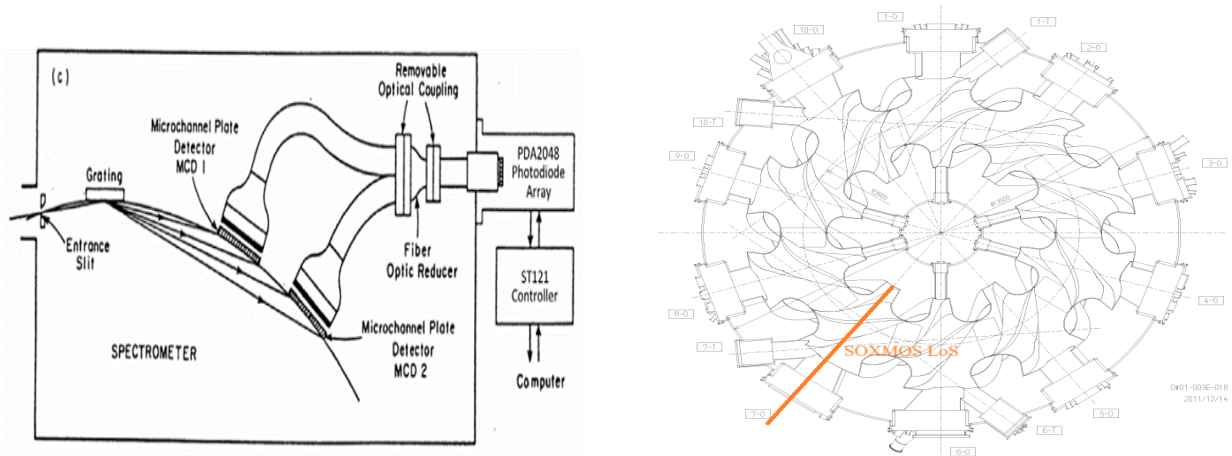


Slika 38: Shema TESPEL uređaja za ubacivanje nečistoća u plazmu [140]. 100 peleta koji staju u rotirajući nosač se lansiraju kroz cev za ubrzavanje dužine 1 m koristeći He pod pritiskom od 20 atmosfера.

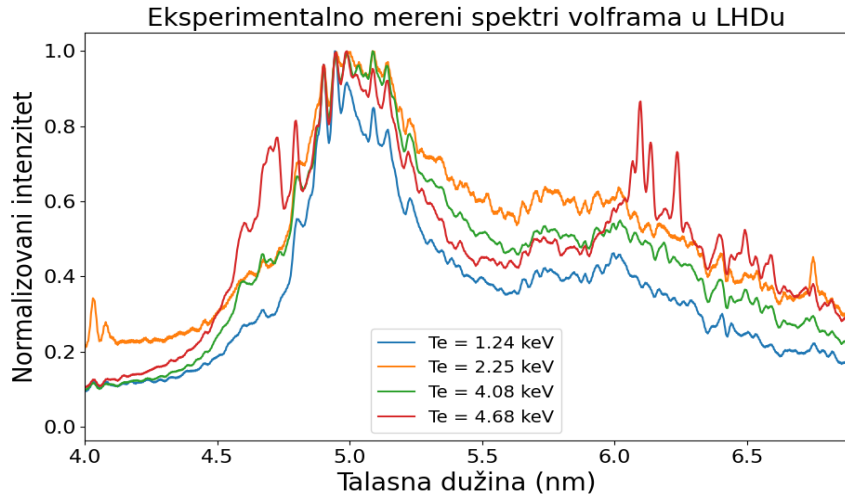
Ovaj oblik peleta omogućava velike lansirne brzine za teže nečistoće, dok istovremeno omogućava sporije lansiranje lakših nečistoća ako se eksperimentni rade na ivici plazme. Takođe, primećeno je da za pritiske veće od 16 atmosfera, brzina peleta na lansiranju postiže saturaciju [140], stoga je ta vrednost izabrana kao optimalna vrednost pritiska helijuma prilikom lansiranja.

5.1.3 Soft X-Ray Multichannel Spectrometer (SOXMOS) EUV spektrometar

Sistem se sastoji od VUV spektrometra sa velikim upadnim ugлом (eng. grazing incidence spectrometer) sa Rolandovim krugom radiusa 2 m, koji ima upadni ugao od 88° i prikazan je na slici 39. Ovaj tip spektrometra je detaljno opisan u radu [143]. Kao disperzionalni element mogu se koristiti dve difrakcione rešetke, jedna od 600 zareza po milimetru i druga od 133 zareza po milimetru. Rezolucija spektrometra se kreće od 0.01 nm za rešetku od 600 zareza po milimetru, dok je rezolucija 0.06 nm za rešetku od 133 zareza po milimetru. Spektrometar pokriva oblast talasnih dužina od 2 nm do 130 nm. Pre detektora, postoje dve multikanalne ploče, posle kojih dolazi fosforni element koji emituje svetlost koja se vodi putem fiber optičkih kablova na detektor, koji je u ovom slučaju niz od 2048 fotodioda. Instrument u ovoj konfiguraciji u svakom trenutku može da posmatra dve oblasti talasnih dužina. Vremenska rezolucija ovog spektrometra je 100 ms. Elektronska temperatura se donekle može kontrolisati spoljašnjim sistemima grejanja plazme (npr. ECH) te se tako mogu dobiti spektri volframa za različite temperature elektrona. Tipičan izgled spektra snimljen SOXMOS sistemom je prikazan na slici 40.



Slika 39: SOXMOS EUV spektrometar na LHDu. Levo je shema instrumenta, a desno je linija pogleda koju ima instrument. Linija pogleda je jedna linija kroz čitav horizontalno izdužen deo plazme.



Slika 40: Tipičan izgled spektra volframa snimljenog SOXMOS spektrometrom. Vidi se i UTA struktura spektra na 5 nm modelovana u ovom radu

5.2 Predpriprema podataka za obučavanje modela

Za potrebe ovog istraživanja, korišteni su spektri volframa u oblasti talasnih dužina između 3 i 7 nm koji su snimljeni u prethodnim kampanjama rađenim na LHD helitronu. Analizirano je ukupno 133 pražnjenja, od kojih kada se oduzmu neuspešna ubacivanja nečistoća u plazmu ostaje 99. Redni brojevi pražnjenja koja su razmotrena u ovom radu su: #181116 - 181198, #164695-164704, #151814-151847, #147567-147573. Od parametara plazme koji su od interesa, u razmatranje je uzeta samo temperatura elektrona. To je zbog toga što intenzitet spektralnih linija volframa jako slabo zavisi od gustine elektrona. To je diskutovano i u radu [126], gde kako autori navode, emisivnost spektralne linije volframa u prvom redu zavisi od temperature elektrona i od frakcione zastupljenosti posmatranog jona u plazmi. Ono što je takođe interesantno, u istom radu je pokazano da su u akumulacionoj zoni

zaravnjenja temperaturnog profila transportni procesi zanemarljivi. Naime, autori su pokazali da kada se izračunaju frakcione zastupljenosti jona volframa za slučaj bez transporta čestica i sa transportom, nema vidljive razlike u zastupljenosti. Stoga je dalje odlučeno da jedini parametar plazme od interesa u našem slučaju bude elektronska temperatura plazme. Zbog samog zaravnjavanja temperaturnog profila u jezgru plazme odakle dolazi emisija visokoionizovanih atoma volframa (u ovom radu opažena ionizaciona stanja od W^{40+}) opravdano je pretpostaviti da je emisija dešava na jednoj temperaturi elektrona, te čitav emitovani spektar poistovetiti sa jednom temperaturom elektrona.

Vremenska zavisnost temperature elektrona uzeta je za svaki spektar iz rezultata dobijenih iz Thomson-ovog rasejanja, a da bi izbegli da neke odudarajuće tačke signal je obrađen Savitky - Golay filterom 4 reda sa prozorom od 11 tačaka. Isti filter je takođe korišten i na samom EUV spektru kako bi minimalizovali šum. Potom, kako bismo izbacili spektre koji sadrže čisti šum, samo spektri čija je srednja vrednost veća od empirijski postavljene granice od 600 odbroja po kanalu su uzeti u razmatranje za kreiranje baze za obučavanje modela koja je nakon prolaska kroz sve spektre brojala 1220 spektara. Takođe, kako bi VAE što bolje predvidio oblik spektra, spektri su normalizovani sa SNV koja uključuje oduzimanje srednje vrednosti spektra od vrednosti svakog piksela, te deljenje te vrednosti sa standardnom devijacijom spektra:

$$I_n = \frac{I_s - I_{sr}}{\sigma} \quad (129)$$

Gde je I_n nova vrednost spektra koja ulazi u bazu za obučavanje, I_{old} je merena vrednost, I_{sr} je srednja vrednost spektra a σ predstavlja standardnu devijaciju spektra. Odudarajući podaci su uklonjeni korištenjem Isolation Forest algoritma i na kraju je baza za obučavanje brojala 1125 spektara.

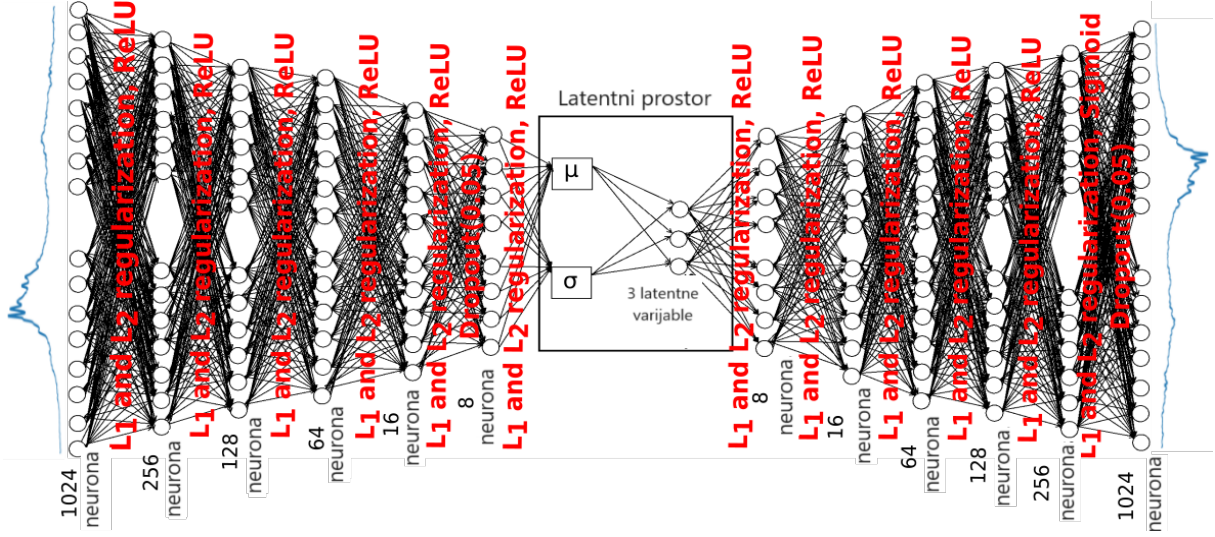
Od tog broja, proveravanjem je zaključeno da je samo 120 spektara za koje je centralna elektronska temperatura veća od 3 keV. Da bi izvršili balansiranje baze za obučavanje, odradena je augmentacija podataka. Augmentacija je rađena pomoću 2D grid interpolacije algoritmom najbližih suseda na sledeći način. Prvo je izdvojen podskup od 15 različitih spektara za prvih 15 elektronskih temperatura, između kojih je interpolacijom dodato još 100 spektara. Kako je ovih podskupova bilo 8, to znači da je augmentacijom podataka dodato 800 spektara, tako da je finalna baza za obučavanje modela imala 1727 spektara za obučavanje. Kako bi obučavanje išlo bolje i kako bi se izbegle nestabilnosti algoritma za trening poput eksplodirajućih gradijenata, urađeno je skaliranje ulaznih podataka koristeći MinMax skaliranje, gde je:

$$I_n = \frac{I_s - I_{min}}{I_{max} - I_{min}} \quad (130)$$

5.3 Pravljenje modela

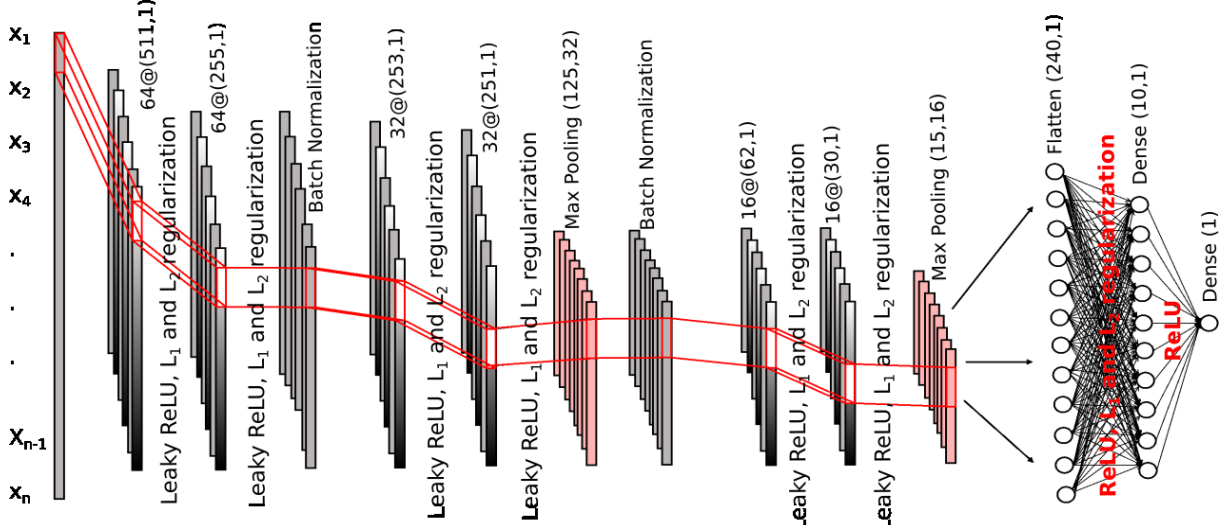
Nakon predpripreme podataka, započeto je sa pravljenjem radnih modela. Svi modeli napravljeni su korištenjem biblioteka otvorenog koda keras i tensorflow [144]. Enkoder varijacionog enkodera predstavlja potpuno povezanu neuronsku mrežu koja na ulazu ima 1024 jedinice, potom ima 5 skrivenih slojeva sa po 256, 128, 64, 16 i 8 neurona i na kraju, u latentnom prostoru ima 3 neurona. Korištena aktivaciona funkcija u ulaznom kao i u svim skrivenim slojevima je propuštajući ReLU (eng. *Leaky ReLU*) sa konstantom $\alpha = 0.3$. Pre

latentnog sloja, ubačen je Dropout sloj koji služi da nasumično izbací neke veze između neurona dva sloja kako bi se izbeglo preprilagođavanje neuronske mreže. Dropout layer ima faktor izbacivanja od 5 %. VAE korišten u ovom radu prikazan je na slici 41.



Slika 41: Arhitektura varijacionog autoenkodera korištenog u ovom radu

Dekoder je simetričan autoenkoderu, gde imamo latentni sloj, zatim 5 skrivenih slojeva sa po 8, 16, 64, 128 i 256 neurona i izlazni sloj od 1024 vrednosti što ustvari predstavlja rekonstruisani spektar. Aktivaciona funkcija svakog neurona bila je propuštajući ReLU sa koeficijentom $\alpha = 0.3$.



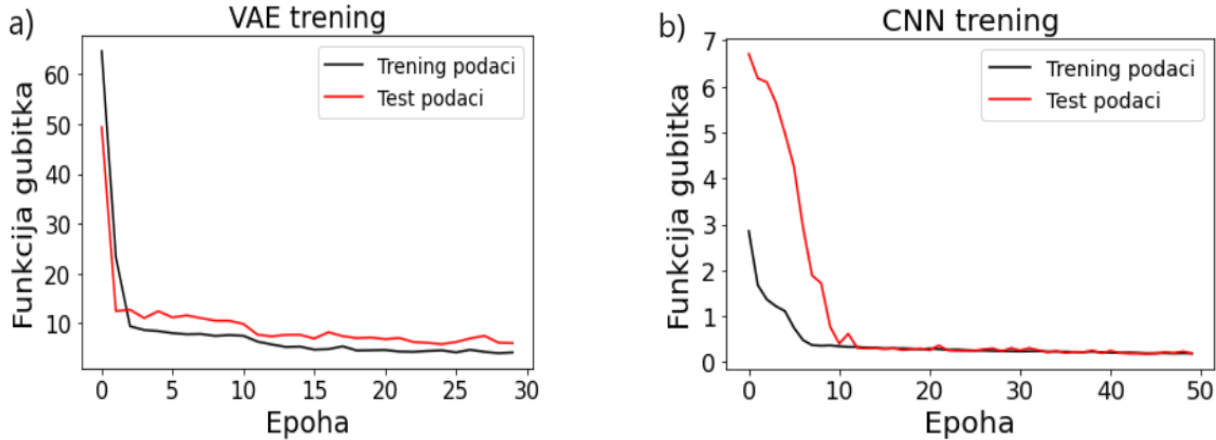
Slika 42: Arhitektura konvolucione neuronske mreže za određivanje temperature elektrona generisanog spektra

Aktivaciona funkcija poslednjeg izlaznog sloja dekodera bila je sigmoid funkcija. Takođe, Dropout sloj je postavljen između poslednjeg skrivenog sloja i izlaznog sloja dekodera sa faktorom izbacivanja od 5 %. Zbog jako malog uzorka na kome se model obučava, primenjene

su jake mere protiv preprilagođavanja modela podacima. Na prvom mestu, korištene su l_1 i l_2 regularizacije u svakom sloju enkodera pri čemu je koeficijent $l_1 = 10^{-4}$, dok je koeficijent $l_2 = 10^{-5}$. Brzina učenja η ostavljena je na vrednosti od $\eta = 0.001$. Takođe, kao još jedna mera protiv preprilagođavanja modela implementirano je rano zaustavljanje treninga. Obučavanje modela je zaustavljeno ako se funkcija gubitka modela ne poboljšava značajno u pet suksesivnih epoha. Rekonstruktivni deo funkcije gubitka ovde je modelovan sa srednjim kvadratnim odstupanjem, dok KL divergencija za pretpostavljeni oblik Gauss-ove raspodele ima oblik:

$$D_{KL} = -\frac{1}{2} \left(1 + \log(\sigma^2) - \mu^2 - \sigma^2 \right) \quad (131)$$

Kako bi znali kojoj temperaturi elektrona odgovara generisani spektar volframa, obučena je i jedna konvolucionna neuronska mreža. U suštini to je 1D konvolucionna neuronska mreža prikazana na slici 42 koja na početku ima dva konvolucionna bloka sa 64 filtera. Veličina jezgra je bila 3, a stride parametar je jednak 2. Aktivaciona funkcija u oba slučaja bila je propuštajuća ReLU funkcija sa $\alpha = 0.3$. Nakon ovog bloka sledi jedan Batch Normalisation sloj koji ima ulogu da spreči preprilagođavanje modela i ubrza obučavanje tako što ulazne težinske faktore recentrira i reskalira. Nakon ovog sloja idu još dva konvolucionna sloja sa po 32 filtera, veličinom jezgra jednakom 3 i sa stride parametrom jednakim jedinici. Dalje, nakon ovog bloka ide MaxPooling sloj i još jedan Batch Normalisation sloj. Konačno, još jedan konvolucijski blok od dva konvolucionna sloja sa 16 filtera, istom veličinom jezgra i stride parametrom jednakim 2. Posle trećeg konvolucionog bloka, MaxPooling je urađen i

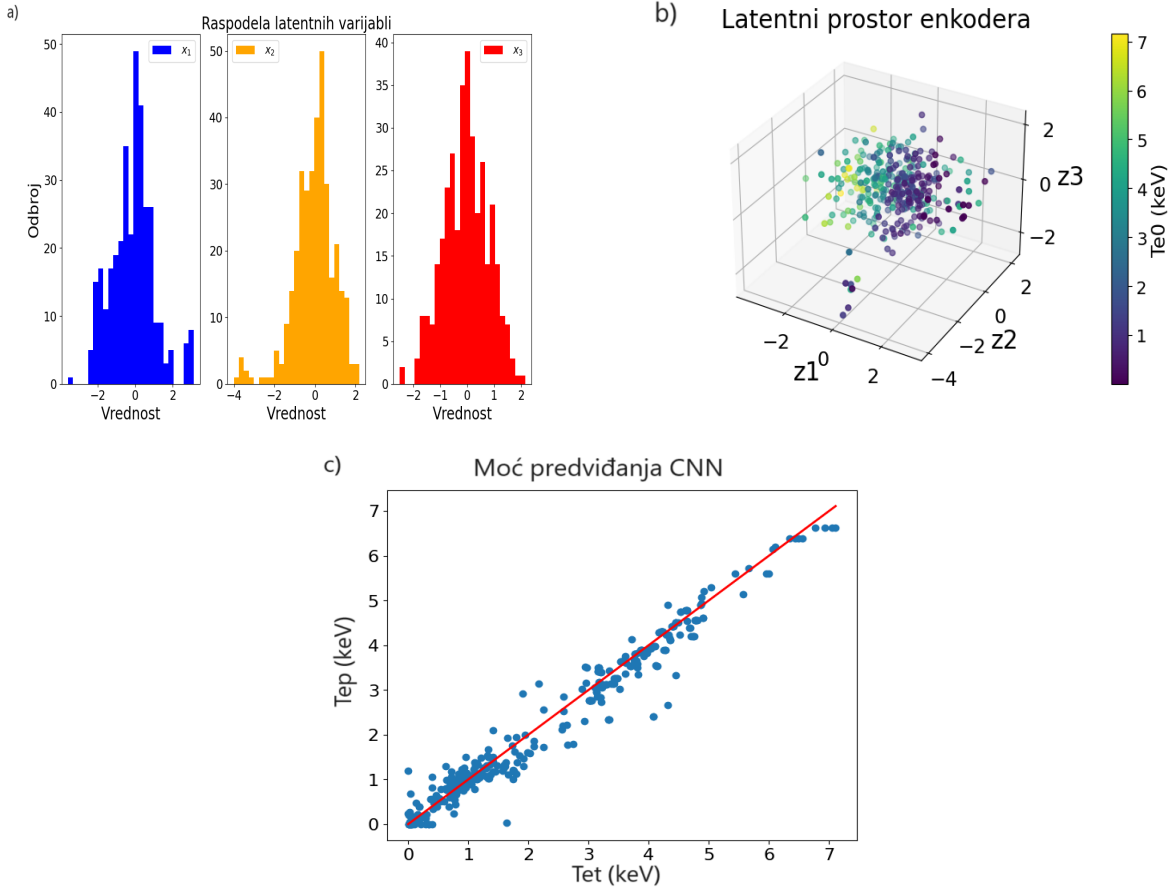


Slika 43: Rezultat obučavanja VAE (a) i CNN modela (b). VAE je postigao konvergenciju nakon 30 epoha, dok je CNN model konvergirao posle 50 epoha. Obučavanje je zaustavljeno od strane implementiranog ranog zaustavljanja,

izvršeno je pretvaranje 2D niza u 1D niz koji je imao 240 neurona, odakle sledi jedan sloj sa 10 neurona i konačno izlazni sloj sa jednim neuronom. Aktivaciona funkcija za guste slojeve je ReLU. Zbog malog uzorka i ovde su implementirane l_1 i l_2 regularizacije sa koeficijentima $l_1 = 10^{-5}$ i $l_2 = 10^{-6}$ i sa rano zaustavljanje gde je takođe implementirano da se obučavanje zaustavlja ukoliko nakon 5 epoha ne dođe do značajnog poboljšanja funkcije gubitka.

Optimizacija oba modela (VAE i CNN model) su rađeni sa optimizatorom Adam, s tim što je brzina učenja za CNN model bila $\eta = 10^{-4}$. Baza za obučavanje je podeljena na bazu

za obučavanje i bazu za testiranje u takvom omjeru da je 80 % podataka iskorišteno za obučavanje, a 20 % podataka za testiranje i validaciju modela. Rezultati obučavanja modela prikazani su na slici 43. VAE je postigao konvergenciju nakon 30 epoha, dok je CNN model konvergirao posle 50 epoha, a prva naznaka da model nije izvršio preprilagođavanje podacima jeste da su funkcije gubitka za trening i test bazu podataka istog reda veličine. Kako bi se stekao uvid u performans varijacionog autoenkodera, na slici 44 (b) prikazan je latentni prostor varijacionog enkodera i distribucija latentnih varijabli (a).



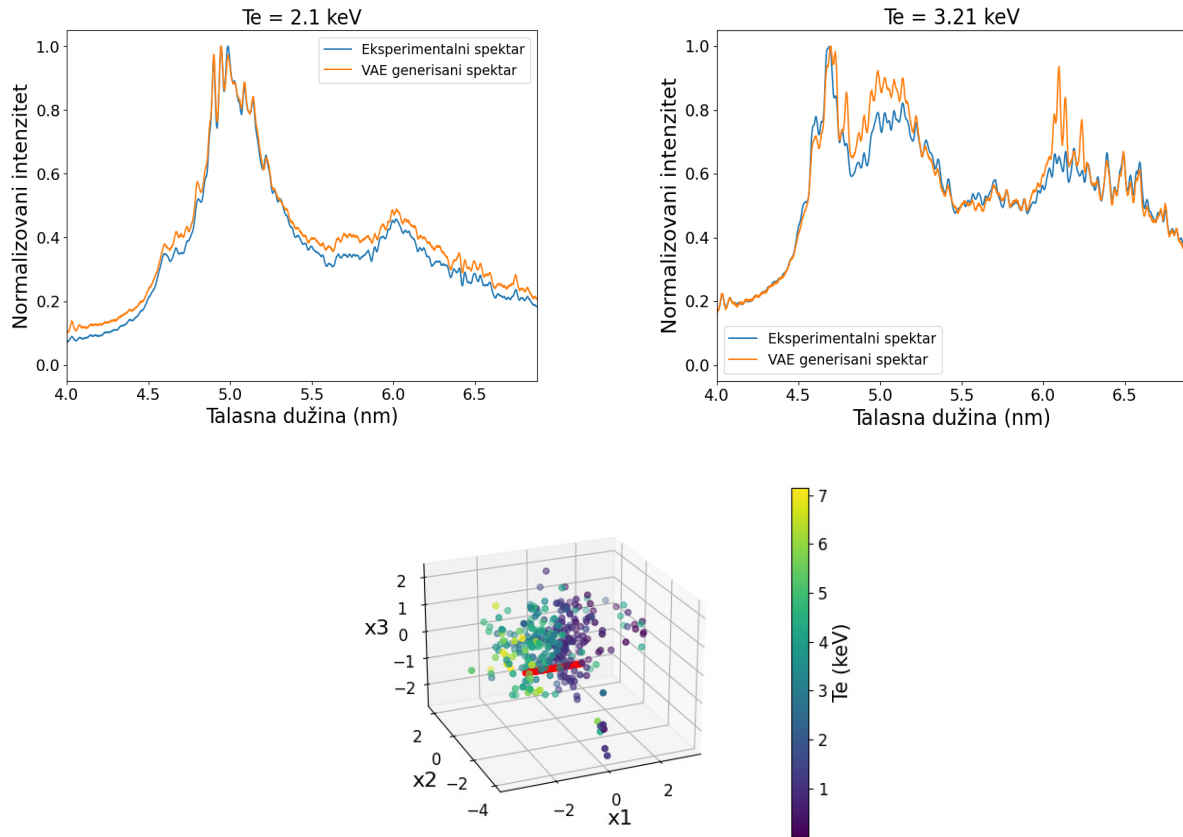
Slika 44: Raspodela latentnih varijabli (a), latentni prostor VAE (b) i predikciona moć konvolucione mreže (c). Primetno je da su tačke koje odgovaraju bliskim centralnim elektronskim temperaturama bliske, te da je svaka latentna varijabla približno opisana normalnom raspodelom. Ovo je dobar znak da je enkoder uspešno naučio reprezentaciju podataka te da je uspešno uradena redukcija dimenzionalnosti ulaznih podataka. Predikciona moć konvolucione neuronske mreže je najbolja između 1 keV i 5 keV i tu je greška predviđanja od 15 % i manje.

Primetno je da su sve tri latentne varijable odgovaraju normalnoj raspodeli, što je bio i polazni cilj, stoga možemo reći da je enkoder uspešno obavio posao. Takođe, vidi se i da postoji još par prisutnih odudarajućih tačaka u modelu, ali one ne kvare mnogo generalni performans modela. Sa druge strane, vidimo da su tačke u latentnom prostoru koje odgovaraju bliskoj centralnoj elektronskoj temperaturi, bliske i u latentnom prostoru. Stoga se može zaključiti da je enkoder uspešno generalizovao fizičku sliku iza samog signala, što dodatno

daje na snazi ovom modelu. Finalni performas VAE modela, zajedno sa dekoderom testiran je preko koeficijenta determinacije R^2 koji je iznosio 0.86 za finalni model, što je sasvim zadovoljavajuće za trenutne primene. Performas konvolucione neuronske mreže prikazan je na slici 44 (c). Neuronska mreža je optimizovana sa funkcijom gubitka srednje kvadratno odstupanje i iznosila je 0.24 keV, a određena je i srednja apsolutna greška odstupanja koja je iznosila 0.2 keV. Koeficijent determinacije R^2 iznosio je 0.96 i ovi parametri govore da u srednjem greška određivanja elektronske temperature koja se pridružuje generisanim spektru iznosi manje od 15 %.

5.4 Rezultati

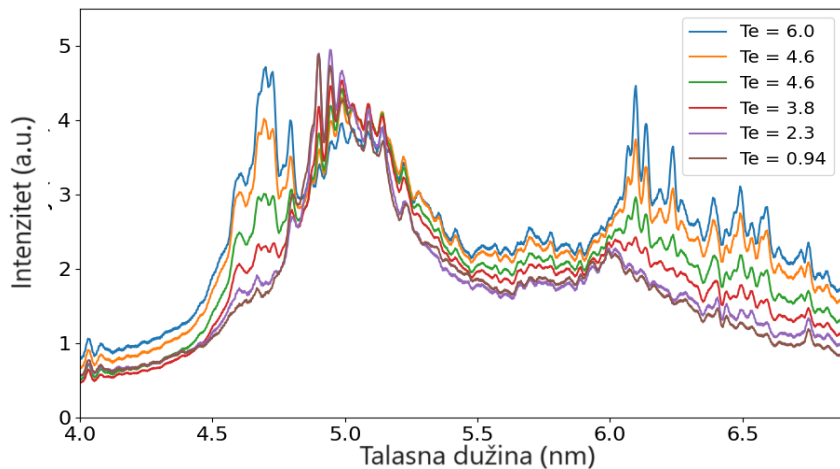
Kako bi proverili rad i predikcionu moć kreiranog modela, model je применjen na test spektre i rezultat generacije modela za dve temperature prikazan je na slici 45.



Slika 45: Generacija test spektara za temperaturu elektrona od 2.08 keV i 3.21 keV. Spektar za 2 keV je reprokuvan vrlo dobro i odlično se slaže sa eksperimentalnim spektrom, dok generisani spektar na 3.21 keV pokazuje spektralne linije na oko 6 nm koje nisu pristune u eksperimentalnom spektru, ali je poklapanje zadovoljavajuće. Treći grafik predstavlja odabrane tačke u latentnom prostoru za koje su generisani spektri pomoću dekodera.

Vidimo da model jako dobro opisuje spektor volframa i UTA strukturu za temperaturu od

2 keV na 5 nm nastalu od prelaza 4f - 4d i 4d - 4p W^{29+} - W^{34+} jona, te 4f - 4d prelaza W^{25+} - W^{28+} . Kako se temperatura povećava, raste i emisija jona na oko 4.5 nm koji odgovaraju jonima volframa W^{37+} - W^{42+} , dok se emisija na 5 nm smanjuje. Pikovi na oko 6 nm koji inače odgovaraju emisijama sa nivoa 4d - 4p prelazima W^{29+} do W^{34+} i W^{23+} - W^{28+} , 4f - 4d prelazima W^{23+} - W^{28+} i 5d - 4f prelazima W^{21+} - W^{23+} u ovom slučaju nisu dobro opisani, jer ih model predviđa a ne pojavljuju se u spektru na ovoj temperaturi. Sledeći korak bilo je iskoristiti mogućnost varijacionog enkodera da iz latentnog prostora generišemo pomoću dekodera nove spektre za različite temperature. U tu svrhu izabrano je 100 novih tačaka kroz latentni prostor i za generisane spektre određena je elektronska temperatura pomoću konvolucione neuronske mreže.



Slika 46: Generisani spektri volframa korištenjem dekodera za tačke iz latentnog prostora prikazane na slici 45

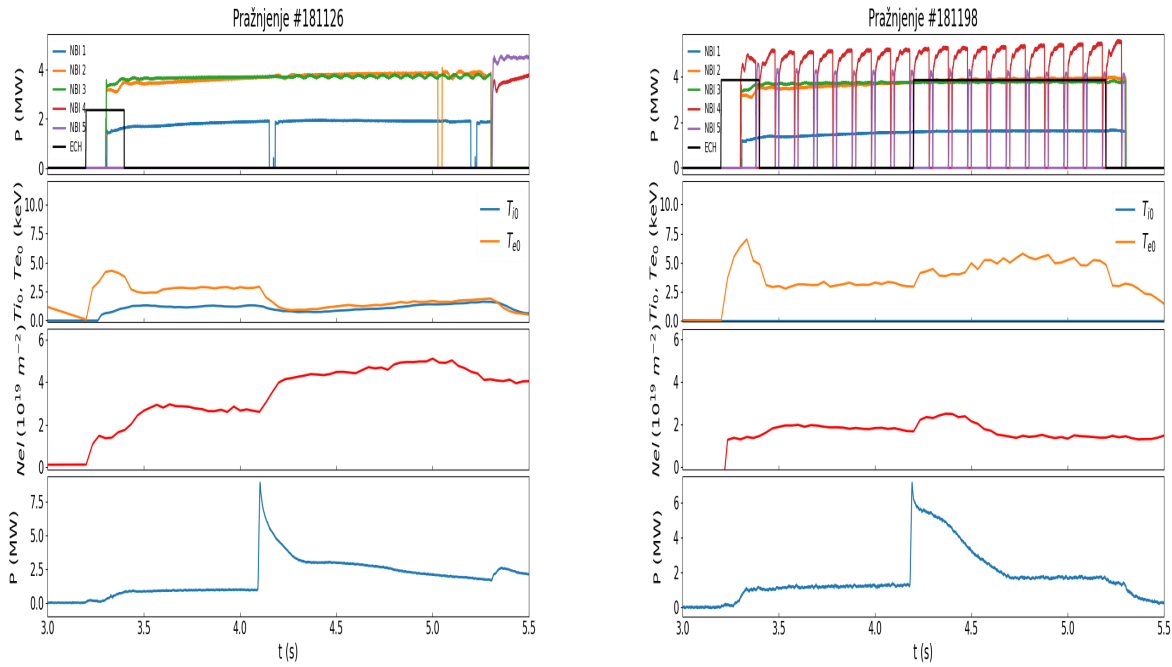
Tačke u latentnom prostoru za koje su generisani spekti prikazane su na slici 45 a generisani spekti prikazani su na slici 46.



Slika 47: Korelaciona mapa za spektre generisane za tačke sa slike 16, a koji su prikazani na slici 46

Vidi se sa slike da kako temperatura raste, tako nastaje i nagla promena u izgledu spektra. UTA struktura polako nestaje, a postaju izraženije spektralne linije koje odgovaraju visokojonizovanim stanjima volframa na 4.5 nm, kao i pikovi na 6 nm koji odgovaraju ionizacionim stanjima od $21+$ do $+34$. Da bi ovo dodatno potvrdili, za ove generisane spektre urađena je korelaciona mapa prikazana na slici 47. Korelaciona mapa nedvosmisleno ukazuje na to da prilikom porasta temperature jasno dolazi i do

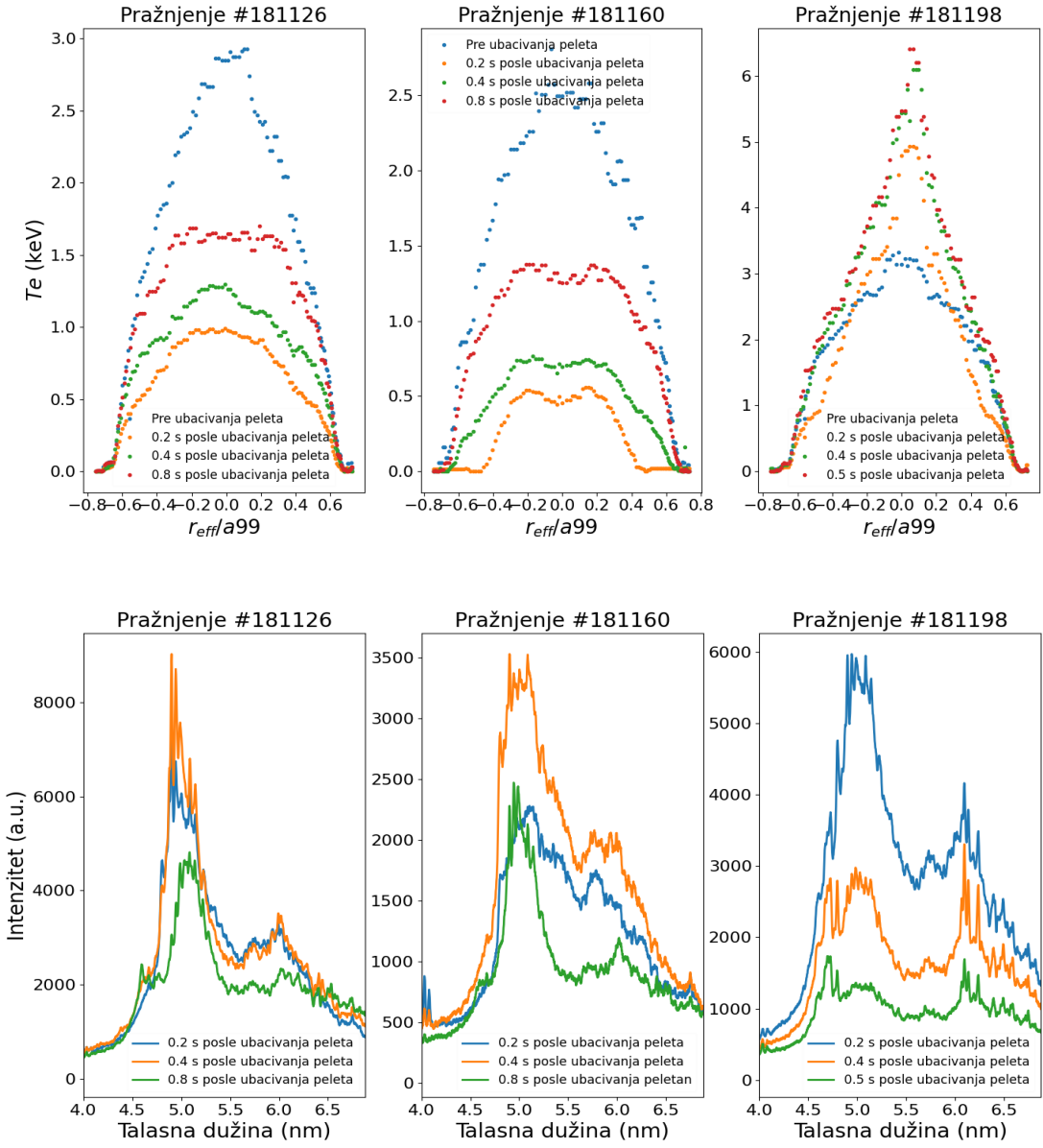
porasta emisije na talasnim dužinama od 4.5 nm i 6 nm dok se emisija UTA strukture na oko 5 nm smanjuje. Objasnjenje ove pojave jeste i ujedno i glavna slabost trenutnog modela, a to je prepostavka jedne elektronske temperature koja odgovara čitavom spektru. Naime, ova aproksimacija je dobra jer najčešće postoji zaravnjenje profila elektronske temperature duž linije posmatranja spektrometra, pa je i ova aproksimacija opravdana. Međutim, u slučajevima kada je ova aproksimacija narušena, dešava se da imamo emisiju spektralnih linija iz različitih delova plazme duž linije posmatranja koja se superponira u jedan spektar i model jedne elektronske temperature više nije dobar model. Kako bismo ovo ilustrovali, posmatraćemo tri pražnjenja razmatrana prilikom obučavanja ovog modela. Parametri ovih pražnjenja prikazani su na slici 48.



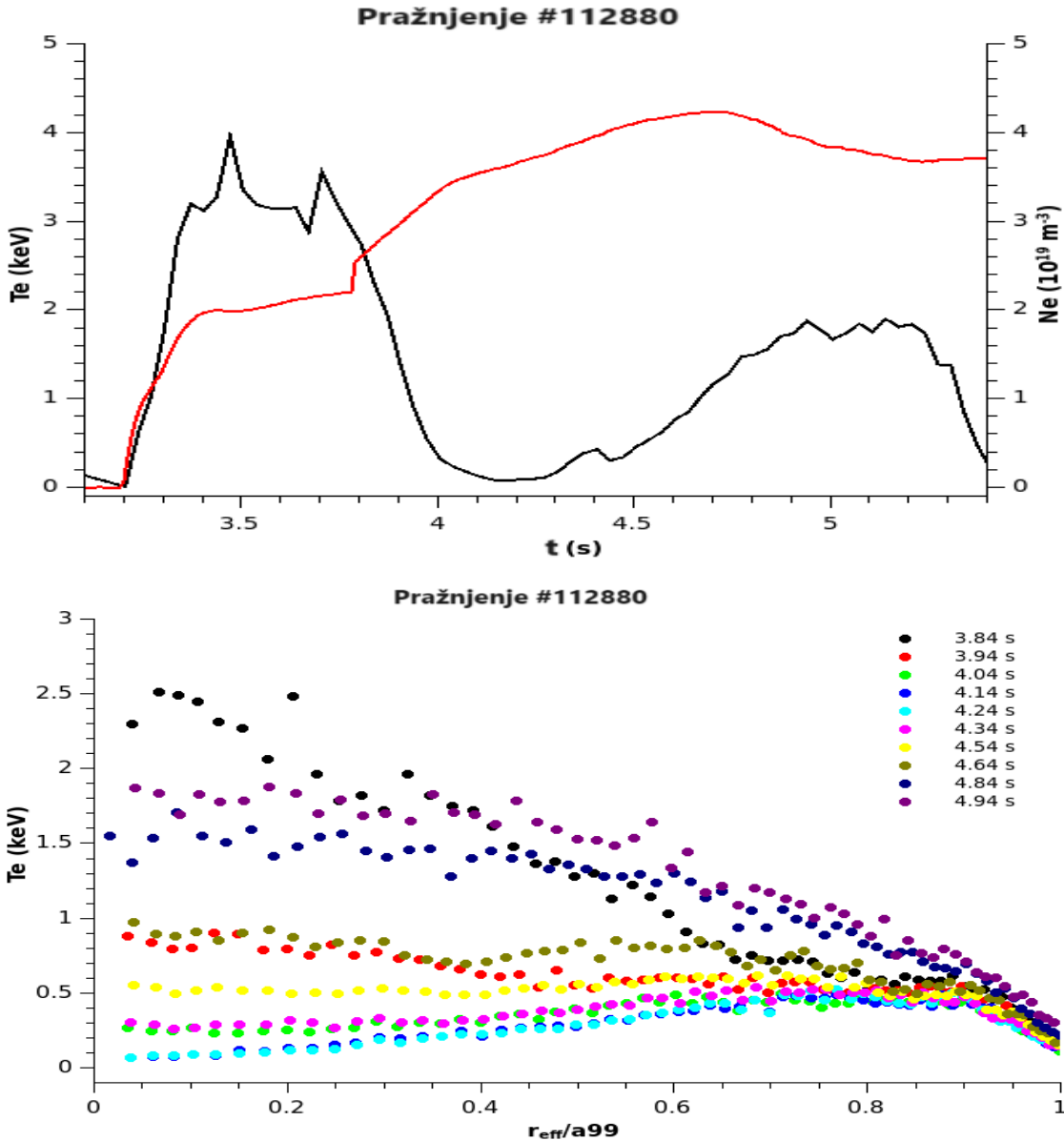
Slika 48: Parametri plazme za pražnjenja #181126 i #181198. Na prvom panelu oba grafika prikazana je aktivnost spoljašnjeg grejanja plazme. Na drugom panelu prikazane su centralna elektronska i jonska temperatura. Treći panel prikazuje linijsku gustinu elektrona dobijenu iz Thomsonovog rasejanja a četvrti panel prikazuje bolometarska merenja zračenja iz plazme.

Vremenski trenutak ubacivanja peleta u plazmu lako je prepoznati kao pik u bolometarskom merenju. Temperaturni profili koji odgovaraju ovim pražnjenjima prikazani su na slici 49 gore za neka vremena od interesa, a spektri koji su povezani sa njima na slici 49 dole. Primećuje se na slici 49 iznad da su u dva slučaja profili elektronske temperature ravni, te je prepostavka modela opravdana, međutim na trećem panelu, u slučaju pražnjenja broj #181198 vidimo da imamo pik u profilu elektronske temperature. Pik se javlja usled paljenja ECH grejanja velike snage u tom trenutku, stoga je primetna i nagla promena spektra prikazana na slici 49 dole na trećem panelu. Promena nastaje usled postojanja prostorne raspodele elektronske temperature, te prepostavka modela više ne važi i nije moguće poistovetiti čitav

emitovani spektar sa jednom temperaturom elektrona. Kao poslednji test modela, generisani su spektri za pražnjenje #112880 korišteno u ranijim studijama koje model nije video prilikom obučavanja i testiranja. Parametri pražnjenja prikazani su na slici 50 a), a profili temperature elektrona prikazani su na slici 50 b). Generisani su spektri za dve elektronske temperature, od 1.5 keV i od 0.9 keV i upoređeni su sa eksperimentalno merenim.

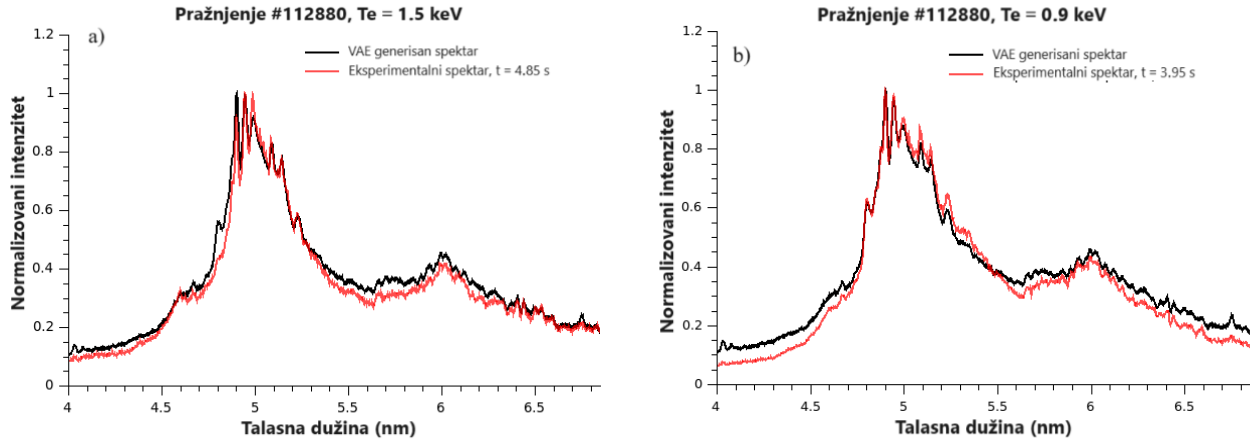


Slika 49: Temperaturni profili koji odgovaraju pražnjenjima prikazanim na slici 48. Primećujemo da je za dva analizirana pražnjenja prisutno zaravnjenje profila u jezgru plazme, dok je na trećem panelu primetan veliki pik profila temperature zbog aktivnog ECH grejanja te nagla promena odgovarajućeg emitovanog spektra u odnosu na druga dva analizirana pražnjenja.



Slika 50: Parametri plazme za pražnjenje #112880 kao i odgovarajući profili elektronske temperature. Vidi se da je prisutno zaravnjenje profila, stoga je opravdana prepostavka modela

Rezultati ovog poređenja prikazani su na slici 51. Vidimo da se model i eksperimentalni spektar odlično slažu, te da se ovaj model može koristiti za generisanje spektra volframa ali samo u slučajevima kada nastupi akumulacija nečistoća i dođe do zaravnjenja profila temperature elektrona. Model je dobro opisao sve karakteristike spektra u ovoj oblasti talasnih dužina, od UTA strukture na 5 nm, preko pojave spektralnih linija na 4.5 nm i 6 nm usled povećanja temperature ili usled odstupanja od aproksimacije učinjene prilikom pravljenja modela. Drugi modeli razvijani za istu primenu, uglavnom koliziono radijativni modeli [126,128], nisu bili u potpunosti uspešni prilikom opisivanja čitavog spektra. Još jedna prednost ovog modela jeste što je ekstremno brz, te nam omogućava generisanje više stotina spektara u svega nekoliko sekundi.



Slika 51: Generisani spektri volframa za temperature elektrona od 0.9 keV (a) i 1.5 keV (b). Slaganje sa eksperimentalnim merenjima je jako dobro.

6 Zaključak

Tema ove doktorske disertacije je primena veštačke inteligencije i mašinskog učenja u spektroskopiji niskotemperaturnih i visokotemperaturnih plazmi. Razmotreni su i analizirani različiti tipovi plazmi: laserski indukovane plazme, fuzione plazme itd. Prvi deo doktorske disertacije bavi se primenom mašinskog učenja za određivanje Stakovih poluširina emitovanih spektralnih linija u UV, optičkom i infracrvenom delu elektromagnetskog spektra. U ovom delu disertacije, uspešno je demonstrirana upotreba mašinskog učenja za predikcije Stark-ovog širenja spektralne linije, kao i predikcije regularnosti Stark-ovog efekta duž spektralnih serija i duž izoelektronskog niza. Napravljena je baza za obučavanje modela uspešnim spajanjem dve javno dostupne baze podataka NIST i Stark B. Na kraju, kreirana baza za obučavanje je sadržala oko 53235 upisanih atomskeh prelaza za koje je pri unapred zadata uslovima izračunata Stark-ova poluširina na osnovu semiklasične perturbativne teorije (SCP). Posle kreiranja, iz baze su izbačeni odudarajući podaci kao oni za koje je energija gornjeg nivoa manja od energije donjeg nivoa, a dodatno nisu razmatrani uslovi plazme gde gustina elektrona prelazi 10^{17} cm^{-3} i gde temperatura elektrona nije veća od 150 000 K. Zbog fizičke prirode ulaznih atributa i različitih redova veličine, vrednost atributa je skalirana tako da svaki atribut uzima vrednost između 0 i 1 putem algoritma standardnog skaliranja. Baza za obučavanje imala je 15 ulaznih atributa na osnovu čijih vrednosti je predviđana jedna ciljna varijabla. Probana su tri modela: stablo odlučivanja, slučajna šuma i gradijentno pojačano stablo odlučivanja. Za sva tri modela, upotrebom Grid Search CV algoritma pronađeni su parametri modela pri kojima daje najbolje predikcije. Najbolji rezultat postigla je slučajna šuma koja je imala koeficijent determinacije R^2 od 0.97 ostvaren na predikcijama na bazi za testiranje modela. Ovo je predstavljao dovoljan dokaz da model se nije preprilagodio podacima i da se može dalje koristiti u analizi Stark-ovog širenja spektralnih linija.

Prva analiza koja je u sklopu ove disertacije jeste proučavanje regularnosti Stark-ovog efekta. Testirane su regularnosti duž spektralnih serija neutralnog litijuma, kao i regularnosti duž izoelektronskog niza litijuma. Bitan rezultat postignut u ovom radu je da je model pokazao saturacioni efekat pri određivanju poluširine linije za prelaze sa visokim kvantnim brojem, što

raniji modeli koji su se bavili predviđanjem regularnosti Stark-ovog efekta nisu predvideli. Ovo je dobra naznaka da je model naučio fizičku sliku iza Debyevog ekraniranja emitera, što je dosta bolje nego da su rezultati ukazivali na konstantan porast širine spektralne linije. Dodatni dokaz za ovu tvrdnju jeste da se efekat saturacije javlja ranije za veće elektronske gustine, što je takođe u skladu sa teorijskim predviđanjima, jer Debye-ev radius opada sa porastom gustine elektrona. Pored regularnosti duž spektralnih serija, posmatrana je i regularnost duž izoelektronskog niza litijuma i rezultati su upoređeni sa eksperimentalnim rezultatima Blagojevića i saradnika. Pokazano je da model može uspešno da previdi i ovu vrstu regularnosti, što predstavlja dodatnu potvrdu da je model uspešno opisao ranije uočene regularnosti Stark-ovog efekta. Konačno, rezultati predikcije mdoela upoređeni su eksperimentalnim rezultatima iz radova Konjevića i saradnika. Dobijeni rezultati sugerisu na to da model daje bolje rezultate u vidljivoj oblasti spektra, dok u UV oblasti teži da podceni poluširinu linije skoro za faktor 2. Još jedan od zaključaka iz analize poređenja sa eksperimentalnim rezultatima jeste da model teži većim vrednostima Stark-ovih poluširina spektralne linije nego što je ona eksperimentalno izmerena. Prosečna greška koju model pravi određenja procenjena poređenjem eksperimentalnih i prediktovanih rezultata je između 25 i 30 %.

Na kraju, analize urađene u ovoj tezi sugerisu da mašinsko učenje može biti iskorišteno u modelovanju širenja spektralnih linija usled Stark-ovog efekta. Značaj ovog rezultata ogleda se u tome što model razvijen u ovoj tezi omogućava da se za jednostavan unos od 15 ulaznih parametara dobije procena Stark-ove poluširine jako brzo sa tačnošću od oko 30 %, što predstavlja jako dobru kvalitativnu procenu upotrebljivosti emitovane spektralne linije u svrhu dijagnostike plazme. Takođe, bitno je napomenuti da je model jako dobro generalizovao fizičku sliku iza Stark-ovog širenja spektralnih linija, na način da je uspešno predvideo očekivane regularnosti duž spektralnih serija i izoelektronskog niza, što je unapređenje u odnosu na formulu koju je predložio Purić u radu [64], gde ne postoji univerzalni fit parametri koji bi važili za svaki emiter.

Drugi deo ove doktorske disertacije bavi se primenom mašinskog učenja u kvanitativnoj analizi određivanja koncentracija glavnih konstituenata meta od čelika metodom spektroskopije laserski indukovanih proba. U sklopu ove disertacije pokazano je barem kvalitativno da postoji mogućnost korištenja prethodno snimljene baze podataka dobijene u jednoj laboratoriji koja je snimljena pod jasno definisanim i precizno kontrolisanim eksperimentalnim uslovima, a koja bi bila korištena za obučavanje modela koji bi posle bio korišten za predikciju nepoznatih uzoraka snimljenih u drugoj laboratoriji. Bitno je napomenuti da je važnost ove analize u tome što dovoljan broj standardnih uzoraka nije dostupan u svim laboratorijama. U cilju ispitivanja polazne pretpostavke, snimljeni su test spektri različitih standardnih uzoraka čelika pri istim uslovima i sa istom aparaturom kao i u originalnoj bazi za obučavanje. Nd:YAG laserki impuls koji radi na osnovnom harmoniku, trajanja impulsa od 6 ns i energije 95 mJ bio sočivom je fokusiran tako da dijmetar spota na meti bude približno 0.2 mm. Spektar je snimljen korištenjem Mechelle 5000 spektrometra i iCCD kamere, a rađeno je u vazduhu. Ovime su uspešno ponovljeni svi uslovi pri kojima je snimana originalna baza za obučavanje.

Kao predpriprema podataka korišten je MinMax algoritam skaliranja podataka, a procena važnosti ulaznih atributa rađena je na osnovu Gini-jevog kriterijuma. Takođe, ovo je prvi put da je ovaj način korišten za selekciju atributa za regresioni problem, jer je do sada uglavnom bio korišten za klasifikacione probleme. Obučena su četiri modela slučajne šume da

bi se procenila važnost atributa za svaki element ponaosob (Cr, Ni, Mo i Mn). Posle toga, najbolje rezultate redukcije dimenzionalnosti dala je empirijski određena granica od 2×10^{-4} kao granica iznad koje su svi bitni atributi. Tako je ulazna dimenzionalnost od 40002 talasne dužine, snižena na svega par stotina atributa što dosta olakšava obučavanje modela, a bez da su žrvtovane najbitnije informacije. Za konačne predikcije koncentracije glavnih konstituenata čelika obučena su dva modela, slučajna šuma i potpuno povezana neuronska mreža. Broj stabala odlučivanja u svakoj slučajnoj šumi bio je 350, dok dubina svakog drveta nije bila ograničena. Arhitektura neuronske mreže koja je korištena imala je 3 sakrivena sloja sa 100, 150 i 50 neurona. Neuronska mreža se u ovom slučaju pokazala kao bolji izbor modela, jer je za sva četiri elementa od interesa imala koeficijent determinacije R^2 veći od 0.9 i niži RMSE od modela slučajne šume.

Konačno u trećem delu ove doktorske disertacije, uspešno je demonstrirana mogućnost primene veštačke inteligencije za generisanje emitovanog spektra volframa u EUV oblasti spektra, u opsegu talasnih dužina od 4 do 7 nm. Nečistoće su unošene u plazmu pomoću TESPEL sistema za ubacivanje nečistoća, a spektar se snimao pomoću EUV spektrometra sa velikim upadnim uglom koji je postavljen u Paschenovoj konfiguraciji, gde je kao detektor korišten niz fotodioda. Temperatura elektrona ovom radu merena je Thomson-ovim rasejanjem, kao jedini relevantan parametar plazme za intenzitet emitovanih spektralnih linija. Urađena je predpriprema podataka kako bi ulazni podaci bili pogodni za obučavanje neuronskih mreža. Podaci su normalizovani korištenjem SNV normalizacije kako bi svi spektri imali istu srednju vrednost i standardnu devijaciju, što je pogodno za učenje oblika spektra i skalirani korištenjem MinMax algoritma skaliranja gde su vrednosti atributa dovedene između 0 i 1, što je pogodno za obučavanje modela. Kako bi se smanjio šum u eksperimentalno merenom signalu, podaci su filtrirani pomoću Savitzky - Golay filtera četvrtog reda sa prozorom od jedanaest tačaka. Nakon predpripreme podataka, podaci su podeljeni u odnosu 80 % - 20 % za obučavanje i testiranje modela. Napravljena su i obučena dva modela, jedan model je služio za generisanje spektra a drugi za određivanje elektronske temperature koja odgovara ovom generisanim spektru. Ključna pretpostavka ovog modela jeste da se emisija dešava efektivno na jednoj temperaturi elektrona, a opravdanje ove pretpostavke predstavlja činjenica da prilikom ulaska nečistoća u plazmu dolazi do zaravnjivanja profila temperature elektrona. Model obučen za generisanje spektra bio je variacioni autoenkoder, gde je arhitektura enkodera i dekodera takva da imaju po 5 skrivenih slojeva sa po 256, 128, 64, 16 i 8 neurona. Ulazni i izlani sloj autoenkodera imaju po 1024 neurona, dok latentni prostor autoenkodera ima tri tačke. Zbog malog broja podataka za obučavanje, primeće su mere protiv preprilagođavanja, a one su bile l_1 i l_2 regularizacija i rano zaustavljanje obučavanja. Dokazano je da latentne varijable prate normalnu raspodelu i da su tačke koje odgovaraju sličnim temperaturama elektrona bliske u latentnom prostoru. Ovo je dobar dokaz da se enkoder nije preprilagodio podacima, te da je uspešno naučio reprezentaciju podataka i dobro uradio smanjenje dimenzionalnosti ulaznih podataka. Da model nije izvršio preprilagođavanje ukazuje i to da su funkcije greške za trening i test faze jako bliske, kao i to da je koeficijent determinacije R^2 na test podacima 0.86. Konvolucionna neuronska mreža koja je obučena za određivanje temperature elektrona na osnovu ulaznog spektra volframa imala je takvu arhitekturu da se sastojala od tri konvolucionala bloka sa po dva konvolucionala sloja, dva Batch Normalisation sloja između svakog konvolucionog bloka i dva agregaciona sloja. Na kraju, iza konvolucionog bloka imala je tri potpuno povezana sloja sa 240, 10 i jednim izlaznim

neuronom. I za konvolucionu mrežu, zbog sprečavanja preprilagođavanja, urađena je l_1 i l_2 regularizacija kao i rano zaustavljanje. Model je postigao koeficijent determinacije od $R^2 = 0.96$ sa srednjim kvadratnim odstupanjem od 0.24 keV.

Obućeni modeli primjenjeni su na generisanje spektra volframa, tako što je u latentnom prostoru enkodera nasumično izabrano 100 tačaka za koje je pomoću dekodera generisan spektar. Dobijeni rezultati ukazuju na to da je na nižim temperaturama plazme (ispod 3 keV) dominantna UTA struktura na 5 nm koja potiče od emisije jona W^{29+} - W^{34+} i W^{25+} - W^{28+} . Porastom temperature, ova struktura polako nestaje, a pojavljuju se spektralne linije emtovane na oko 4.5 nm koje potiču od jona W^{37+} - W^{42+} i na 6 nm koje potiču od 4d - 4p prelaza W^{29+} - W^{34+} i W^{23+} - W^{28+} , te od 4f - 4d prelaza W^{23+} - W^{28+} i 5d - 4f prelaza W^{21+} - W^{23+} . Primećena je nagla promena oblika spektra volframa sa porastom temperature, a objašnjena je trenutnom slabošću modela i aproksimacije jedne elektronske temperature. Naime, u slučaju viših elektronskih temperatura, primećen je pik profila temperature umesto tipičnog zaravnjenja profila usled paljenja jakog ECH grejanja nakon ubacivanja peleta, pa se zapravo dobija efekat emisije spektralnih linija iz delova plazme sa različitim elektronskim temperaturama koje se superponiraju i mere integralno. Na kraju, kao finalni test, generisani su spektri za pražnjenje koje nije uključeno u pravljenje baze za obučavanje i trening radi potvrde validnosti modela. Model je dao dobra slaganja za dve odabранe elektronske temeprature od 1.5 keV i 0.9 keV. Iz toga se može zaključiti da trenutni model predstavlja dobar alat za dalju generaciju spektra i uvećanje baze za obučavanje zbog primene na dalje istraživanje. Glavna prednost varijacionog enkodera jeste što je pravilno naučio fizičku sliku procesa koji se odvijaju u plazmi i pored toga jako je kompjuterski efikasan, u smislu da možemo generisati nekoliko stotina spektara za nekoliko sekundi. Poređenja radi, trenutni CR modeli koje razvijaju kolege iz Japana rade tri nedelje račun samo jednog spektra jer moraju da uzmu u obzir jako veliki broj prelaza te raspodelu broja jonskih emitera u plazmi, kao i komplekse konfiguracione interakcije između različitih emitera.

Kao unapređenje i dalje istraživanje, u sklopu prvog dela doktorske disertacije moguće je proširiti model tako da opisuje i plazme koje imaju veću gustinu elektorna od 10^{17} cm^{-3} i temperaturu elektrona iznad 150 000 K. To bi u predviđanje modela uključilo i različite plazme koje se javljaju u svemiru, i relevantne su za astrofiziku. Kao finalni praktični proizvod ovog rada bi internet aplikacija za brzo računanje Stark-ove poluširine za unete atomske i plazmene parametre.

Što se tiče unapređenja koja se mogu uraditi u drugom delu disertacije kako bi ova procedura dobila na značaju i na dodatnoj preciznosti, jeste da se prvo uradi kalibracija po osetljivosti. Ona u slučaju originalne baze nije urađena kako bi se dodatno otežalo takmičarima koji su učestvovali. Pored toga, iako se uzorci snimaju sa istim instrumentom i pod istim eksperimentalnim uslovima, bilo bi potrebno i poželjno izvršiti i transfer kalibracije sa jednog uređaja na drugi. Naime, iako su to suštinski isti instrumenti, stanje komponentni u instrumentu kao i optike ne mora biti nužno isto, tako da su i drugačiji rezultati neminovni. U ovom radu, ovaj transfer nije bilo moguće uraditi jer u laboratoriji nije postojao nijedan isti uzorak kao onaj iz baze za obučavanje. Zbog toga bi uz ovako kvalitetne baze podataka trebalo dati i jedan standardni uzorak koji je lako dostupan svima kako bi druga laboratorija, odnosno eksperimentator ili korisnik, bio u mogućnosti da izvrši transfer kalibracije na svoj instrument. Takođe, ovaj rad podrazumeva i dostupnost iste opreme u obe laboratorije, što jako često nije slučaj, tako da bi mnogo ozbiljnija primena veštačke inteligencije podrazumevala i neku

vrstu standradizacije u pogledu eksperimentalnih procedura. Druga procedura koja je donekle ispitana, a mogla bi da ponudi alternativu transferu kalibracije, predstavlja mogućnosti primene metoda tzv. prenosa učenja (eng. *transfer learning*). Ovde se jedan dobro istrenirani model na nekoj velikoj bazi kao što je ona korištena u ovom radu, retrenira na manjoj bazi za obučavanje kako bi se prilagodio novom instrumentu i malo korigovao pretrenirane parametre.

Dalje istraživanje u sklopu trećeg dela teze predstavlja poboljšanje trenutnog modela tako da za ulazne parametre ima i profile elektronske temperature i gustine elektrona, kako bi se kasnije mogli izučavati i predviđati i neki atomski i transportni procesi u plazmi. Pored toga, uključivanjem gore pomenutih profila omogućio bi se i precizan i dobar test za izučavanje mehanizama uspostavljanja i prevencije akumulacije nečistoća u plazmi. Pored ovoga, bilo bi dobro i ispitati druge delove EUV spektra volframa i videti da li se u tim oblastima mogu naći neke korisne dijagnostičke linije.

Literatura

- [1] Yang, A. *et al.* *Frontiers in Bioengineering and Biotechnology* **8** (2020).
- [2] Vamathevan, J., Clark, D., Czodrowski, P. *et al.* *Nat Rev Drug Discov* **18**, 463–477 (2019).
- [3] Ball, N. M. and Brunner, R. J. *International Journal of Modern Physics D* **19**, 1049–1106 (2010).
- [4] Ishida, E. *et al.* *Monthly Notices of the Royal Astronomical Society* **483**, 2–18 (2019).
- [5] Rohde, D. J., Drinkwater, M. J., Gallagher, M. R., Downs, T. and Doyle, M. T. *Monthly Notices of the Royal Astronomical Society* **360**, 69–75 (2005).
- [6] A., G. *Topics in Current Chemistry* **32**, 1–32 (2012).
- [7] Carrasquilla, J. and Melko, R. *Nature Physics* **13**, 431–434 (2017).
- [8] Deringer, V. L., Caro, M. A. and Csányi, G. *Advanced Materials* **31**, 1902765 (2019).
- [9] Carleo, G. and Troyer, M. *Science* **355**, 602–606 (2017).
- [10] Hartmann, M. and Carleo, G. *Physical Review Letters* **122**, 250502 (2019).
- [11] Krenn, M., Malik, M., Fickler, R., Lapkiewicz, R. and Zeilinger, A. *Physical Review Letters* **116**, 090405 (2016).
- [12] Krenn, M., Gu, X. and Zeilinger, A. *Physical Review Letters* **119**, 240403 (2017).
- [13] Djordjević, B. Z. *et al.* *Physics of Plasmas* **28**, 043105 (2021).
- [14] Ralovsky, N. M. and Lednev, I. K. *Chemical Society Reviews* **49**, 7428–7453 (2020).
- [15] Park, H. and Son, J. *Sensors* **21** (2021).
- [16] Koubiti, M. and Kerebel, M. *Applied Sciences* **12** (2022).
- [17] Poggialini, F. *et al.* *Review of Scientific Instruments* **91**, 073111 (2020).
- [18] Li, L.-N. *et al.* *Spectrochimica Acta Part B: Atomic Spectroscopy* **180**, 106183 (2021).
- [19] Babu, M. S., Imai, T. and Sarathi, R. *IEEE Transactions on Plasma Science* **49**, 1088–1096 (2021).
- [20] Cui, X., Wang, Q., Zhao, Y. *et al.* *Appl. Phys. B* **125**, 56 (2019).
- [21] Brenzke, M. *et al.* *Nuclear Fusion* **61**, 046023 (2021).
- [22] Nieuwenhuizen, D. Modeling nuclear fusion reactors using variational auto-encoders (2021).

- [23] Piccione, A., Berkery, J., Sabbagh, S. and Andreopoulos, Y. *Nuclear Fusion* **60**, 046033 (2020).
- [24] Li, H., Fu, Y., Li, J. and Wang, Z. *Plasma Science and Technology* **23**, 115102 (2021).
- [25] NIKOLA KONJEVIĆ AND THE BELGRADE SCHOOL OF SPECTROSCOPY: 50 YEARS OF SCIENTIFIC LEADERSHIP AND CONTRIBUTIONS TO THE ADVANCEMENT OF PLASMA DIAGNOSTICS. *Spectrochimica Acta Part B: Atomic Spectroscopy* **131**, 139–140 (2017).
- [26] Ralchenko, Y., Griem, H. and Bray, I. *Journal of Quantitative Spectroscopy and Radiative Transfer* **81**, 371–384 (2003).
- [27] Sahal-Bréchot, S. *Astron. Astrophys* **1**, 91 (1969).
- [28] Sahal-Bréchot, S. *Astron. Astrophys* **2**, 322 (1969).
- [29] Bellan, P. M. *Fundamentals of Plasma Physics* (Cambridge University Press, 2006).
- [30] Milić, B. *Osnove fizike gasne plazme* (Gradivinska knjiga, 1989).
- [31] Miyamoto, K. *Plasma Physics for Controlled Fusion* 2 edn (Springer-Verlag Berlin, 2016).
- [32] *Fusion Physics* Non-serial Publications (International Atomic Energy Agency, Vienna, 2012).
- [33] Hutchinson, I. H. *Principles of Plasma Diagnostics* 2 edn (Cambridge University Press, 2002).
- [34] Demtröder, W. *Laser Spectroscopy, Vol. 1: Basic Principles* 4 edn (Springer-Verlag Berlin, 2008).
- [35] Gigosos, M. A. *Journal of Physics D: Applied Physics* **47**, 343001 (2014).
- [36] Griem, H. R. *Phys. Rev.* **128**, 515–523 (1962).
- [37] Griem, H. R. *Phys. Rev. Lett.* **17**, 509–513 (1966).
- [38] Griem, H. R. *Plasma Spectroscopy* 1 edn (McGraw-Hill, Inc., 1964).
- [39] Baranger, M. *Phys. Rev.* **111**, 481–493 (1958).
- [40] Baranger, M. *Phys. Rev.* **111**, 494–504 (1958).
- [41] Baranger, M. *Phys. Rev.* **112**, 855–865 (1958).
- [42] Holtsmark, J. *Annalen der Physik* **363**, 577–630 (1919).
- [43] Mozer, B. and Baranger, M. *Phys. Rev.* **118**, 626–631 (1960).
- [44] Hooper, C. F. *Phys. Rev.* **149**, 77–91 (1966).

- [45] Hooper, C. F. *Phys. Rev.* **165**, 215–222 (1968).
- [46] Hooper, C. F. *Phys. Rev.* **169**, 193–195 (1968).
- [47] Ecker, G. and Müller, K. *Z. Physik* **153**, 317–330 (1958).
- [48] Sahal-Bréchot, S., Dimitrijević, M. and Ben Nessib, N. *Atoms* **2**, 225 (2014).
- [49] Dimitrijević, M. and Sahal-Bréchot, S. *Journal of Quantitative Spectroscopy and Radiative Transfer* **31**, 301–313 (1984).
- [50] Wiese, W. and Konjević, N. *Journal of Quantitative Spectroscopy and Radiative Transfer* **28**, 185–198 (1982).
- [51] Kelleher, D. E. *Journal of Quantitative Spectroscopy and Radiative Transfer* **25**, 191–220 (1981).
- [52] Assous, R. *Journal of Quantitative Spectroscopy and Radiative Transfer* **10**, 975–990 (1970).
- [53] Jung, M. *Astron. Astrophys.* **58** (1963).
- [54] Purić, J., Labat, J., Ćirković, L., Lakićević, I. and Djeniže, S. *J. Phys. B.* **10**, 2375 (1977).
- [55] Miller, M. H., Lesage, A. and Purić, J. *Astrophys. J.* **239**, 410 (1980).
- [56] Platisa, M., Popovic, M., Dimitrijević, M. and Konjević, N. *Z. Natwforsch. a.* **212** (1975).
- [57] Platisa, M., Dimitrijević, M., Popovic, M. and Konjević, N. *Astron. Astmphys.* **54**, 837 (1977).
- [58] Bridges, J. M. and Wiese, W. L. *Phys. Rev.* **159**, 31–38 (1967).
- [59] Purić, J., Dimitrijević, M. S. and Lakićević, I. S. *Physics Letters A* **67**, 189 (1978).
- [60] Purić, J., Dojčinović, I. P., Nikolić, M. *et al.* *Astrophys. J.* **680**, 803 (2008).
- [61] Purić, J., Miller, H. and Lessage, A. *Astrophys. J.* **416**, 825 (1993).
- [62] Tapalaga, I., Dojčinović, I. P. and Purić, J. *Mon. Not. R. Astron. Soc.* **415**, 503 (2011).
- [63] Tapalaga, I., Dojčinović, I. P. and Purić, J. *Mon. Not. R. Astron. Soc.* **474**, 5479 (2018).
- [64] Purić, J. and Šćepanović, M. *Astrophys. J.* **521**, 490 (1999).
- [65] Trklja, N., Tapalaga, I., Dojčinović, I. P. and Purić, J. *New Astron* **59**, 54 (2019).
- [66] Trklja, N., Dojčinović, I. P., Tapalaga, I. and Purić, J. *Atoms* **7**, 99 (2019).

- [67] Jevtić, D., Dojčinović, I. P., Tapalaga, I. and Purić, J. *Bull. Astron. Soc. India* **40**, 151 (2012).
- [68] Scepanovic, M. and Puric, J. *Rom. Rep. Phys.* **65**, 1275–1280 (2013).
- [69] Namioka, T. *J. Opt. Soc. Am.* **49**, 951–961 (1959).
- [70] Thorne, A. P. *Spectrophysics* 1 edn (Springer Dordrecht, 1988).
- [71] Beutler, H. G. *J. Opt. Soc. Am.* **35**, 311–350 (1945).
- [72] Mizolek, A. W., Palleschi, V. and Schechter, I. *Laser Induced Breakdown Spectroscopy* (Cambridge University Press, 2006).
- [73] Cremers, D. A. and Radziemski, L. J. *Handbook of Laser-Induced Breakdown Spectroscopy* (Wiley, 2013).
- [74] Burger, M., Skočić, M. and Bukvić, S. *Spectrochimica Acta Part B: Atomic Spectroscopy* **101**, 51–56 (2014).
- [75] Konjević, N., Ivković, M. and Jovićević, S. *Spectrochimica Acta Part B: Atomic Spectroscopy* **65**, 593–602 (2010).
- [76] Martin, B. R. *Nuclear and Particle Physics* (John Wiley and Sons, 2006).
- [77] Schumacher, U. *Fusionforschung: eine Einführung* (Wiss. Buchges., 1993).
- [78] Wesson, J. *Tokamaks* (Oxford University Press, 2011).
- [79] Stroth, U. *Plasmaphysik: Phänomene, Grundlagen und Anwendungen* (Springer Spektrum Berlin, Heidelberg, 2018).
- [80] Adams, M. F. *et al.* *Journal of Physics: Conference Series* **180**, 012036 (2009).
- [81] Naujoks, D. *Plasma-Material Interaction in Controlled Fusion* (Springer Berlin, Heidelberg, 2006).
- [82] Tokar, M. Z. *et al.* *Plasma Physics and Controlled Fusion* **37**, A241 (1995).
- [83] Tokar, M. *et al.* *Nuclear Fusion* **37**, 1691 (1997).
- [84] Nikolić, M. and Zečević, A. *Mašinsko učenje* (Matematički fakultet, 2019).
- [85] Charniak, E. *Introduction to Deep Learning* (The MIT Press, 2018).
- [86] Murphy, K. P. *Machine Learning A Probabilistic Perspective* (The MIT Press, 2012).
- [87] Breiman, L. *Machine Learning* **45**, 5–32 (2001).
- [88] Bishop, C. M. *Pattern Recognition and Machine Learning* (Springer, 2006).

- [89] Kingma, D. P. and Welling, M. *Foundations and Trends in Machine Learning* **12**, 307–392 (2019).
- [90] Griem, H. R. *Spectral Line Broadening by Plasmas* (New York:Academic, 1974).
- [91] Griem, H. R. *Phys. Rev.* **165**, 258–266 (1968).
- [92] Dimitrijević, M. and Konjević, N. *Journal of Quantitative Spectroscopy and Radiative Transfer* **24**, 451–459 (1980).
- [93] Tapalaga, I., Traparić, I., Trklja Boca, N. *et al.* *Neural Comput. Applic.* **34**, 6349 (2022).
- [94] Majlinger, Z. and Traparić, I. *Contrib. Astron. Obs. Skalnaté Pleso* **53**, 58–71 (2023).
- [95] Pedregosa, F. *et al.* *Journal of Machine Learning Research* **12**, 2825–2830 (2011).
- [96] Sahal-Bréchot, S., Dimitrijević, M. S. and Moreau, N. Stark-b database. <http://stark-b.obspm.fr> (2015). Accessed: September 2023.
- [97] Blagojević, B., Popović, M., Konjević, N. and Dimitrijević, M. *Journal of Quantitative Spectroscopy and Radiative Transfer* **61**, 361–375 (1999).
- [98] Dojić, D., Skočić, M., Bukvić, S. and Djeniže, S. *Spectrochimica Acta Part B: Atomic Spectroscopy* **166**, 105816 (2020).
- [99] Konjević, N., Dimitrijević, M. S. and Wiese, W. L. *J. Phys. Chem. Ref. Data* **13**, 469 (1984).
- [100] Konjević, N., Lessage, A., Fuhr, J. R. and Wiese, W. L. *J. Phys. Chem. Ref. Data* **31**, 819 (2002).
- [101] Konings, R. J. M. and Stoller, R. E. (eds) *Comprehensive Nuclear Materials* (Elsevier, Amsterdam, 2020).
- [102] Tognoni, E., Cristoforetti, G., Legnaioli, S. and Palleschi, V. *Spectrochimica Acta Part B: Atomic Spectroscopy* **65**, 1–14 (2010).
- [103] Chen, T., Zhang, T. and Li, H. *Trends in Analytical Chemistry* **133**, 116113 (2020).
- [104] Sun, C., Tilan, Y., Gao, L. *et al.* *Scientific Reports* **9**, 11363 (2019).
- [105] Zhang, X. *et al.* *International Journal of Environmental Research and Public Health* **15** (2018).
- [106] Sheng, L. *et al.* *Journal of Analytical Atomic Spectrometry* **30**, 453–458 (2015).
- [107] Tian, Y. *et al.* *Spectrochimica Acta Part B: Atomic Spectroscopy* **175**, 106027 (2021).
- [108] Babu, M. S., Imai, T. and Sarathi, R. *IEEE Transactions on Plasma Science* **49**, 1088–1096 (2021).

- [109] Cui, X., Wang, Q., Zhao, Y. *et al.* *Applied Physics B* **125**, 12556 (2019).
- [110] Junjuri, R. and Gundawar, M. K. *Waste Management* **117**, 48–57 (2020).
- [111] Li, L.-N. *et al.* *Spectrochimica Acta Part B: Atomic Spectroscopy* **180**, 106183 (2021).
- [112] Poggialini, F. *et al.* *Review of Scientific Instruments* **91**, 073111 (2020).
- [113] Tang, H., Zhang, T., Yang, X. and Li, H. *Journal of Analytical Atomic Spectrometry* **32**, 2194–2199 (2017).
- [114] Ruan, F. *et al.* *Analytical Methods* **7**, 9171–9176 (2015).
- [115] Liang, J. *et al.* *Chemometrics and Intelligent Laboratory Systems* **207**, 104179 (2020).
- [116] Yang, G. *et al.* *Analytical Methods* **9**, 5365–5370 (2017).
- [117] Zhang, T. *et al.* *Journal of Analytical Atomic Spectrometry* **29**, 2323 (2014).
- [118] Zhang, Y. *et al.* *Spectrochimica Acta Part B: Atomic Spectroscopy* **166**, 105802 (2020).
- [119] Liu, K. *et al.* *Analytical Methods* **11**, 4769 (2019).
- [120] Wei, K. *et al.* *Applied Sciences* **12** (2022).
- [121] Jin, X. *et al.* *J. Anal. At. Spectrom.* **38**, 243–252 (2023).
- [122] Kepes, E. LIBS 2022 quantification contest (2022). URL <https://figshare.com/projects/LIBS2022QuantificationContest/142250>.
- [123] Traparić, I. and Ivković, M. *Eur. Phys. J. D* **77**, 30 (2023).
- [124] Randolph, T. W. *Cancer Biomarkers* **2**, 135–144 (2006).
- [125] Asmussen, K. *et al.* *Nuclear Fusion* **38**, 967–986 (1998).
- [126] Pütterich, T. *et al.* *Plasma Physics and Controlled Fusion* **50**, 085016 (2008).
- [127] Nakano, T., Asakura, N., Kubo, H., Yanagibayashi, J. and Ueda, Y. *Nuclear Fusion* **49**, 115024 (2009).
- [128] Murakami, I. *et al.* *Nuclear Fusion* **55**, 093016 (2015).
- [129] Murakami, I. *et al.* *Nuclear Materials and Energy* **26**, 100923 (2021).
- [130] Oishi, T. *et al.* *Atoms* **9**, 69 (2021).
- [131] Radtke, R., Biedermann, C., Schwob, J. L., Mandelbaum, P. and Doron, R. *Phys. Rev. A* **64**, 012720 (2001).
- [132] Utter, S. B., Beiersdorfer, P. and Träbert, E. *Canadian Journal of Physics* **80**, 1503 (2002).

- [133] Streeter, M. J. V. *et al.* *High Power Laser Science and Engineering* **11** (2023).
- [134] Daly, G. A., Fieldsend, J. E., Hassall, G. and Tabor, G. R. *Machine Learning: Science and Technology* **4**, 035035 (2023).
- [135] Fu, Y. *et al.* *Physics of Plasmas* **27**, 022501 (2020).
- [136] Wei, X. *et al.* *Nuclear Fusion* **63**, 086020 (2023).
- [137] Ferreira, D. R., Carvalho, P. J., Sozzi, C., Lomas, P. J. and JET Contributors. *Fusion Science and Technology* **76**, 901–911 (2020).
- [138] Wei, Y., Levesque, J., Hansen, C., Mauel, M. and Navratil, G. *Nuclear Fusion* **61**, 126063 (2021).
- [139] Narihara, K., Yamada, I., Hayashi, H. and Yamauchi, K. *Review of Scientific Instruments* **72**, 1122–1125 (2001).
- [140] Nozato, H., Morita, S., Goto, M., Ejiri, A. and Takase, Y. *Review of Scientific Instruments* **74**, 2032–2035 (2003).
- [141] Tamura, N. *et al.* *Review of Scientific Instruments* **79**, 10F541 (2008).
- [142] Sudo, S. and Tamura, N. *Review of Scientific Instruments* **83**, 023503 (2013).
- [143] Schwob, J. L., Wouters, A. W., Suckewer, S. and Finkenthal, M. *Review of Scientific Instruments* **58**, 1601–1615 (1987).
- [144] Chollet, F. *et al.* Keras (2015). URL <https://github.com/fchollet/keras>.

Biografija

Ivan Traparić rođen je u Trebinju, BiH, 14.9.1996. godine gde je završio osnovnu i srednju školu. Na osnovne studije Fizičkog fakulteta Univerziteta u Beogradu upisuje se 2015. godine na smer Primjenjena i kompjuterska fizika. Osnovne studije završava u redovnom roku 2019. godine sa srednjom prosečnom ocenom 9.43. Iste godine upisuje master studije na Fizičkom fakultetu Univerziteta u Beogradu na smeru Teorijska i eksperimentalna fizika. Master studije je završio sa srednjom prosečnom ocenom 10, a master rad odbranio sa ocenom 10. Master rad pod naslovom „Vakuum ultraljubičasta spektroskopija Lajmanove serije jonizovanog atoma helijuma“ je urađen u Laboratoriji za spektroskopiju plazme i lasere na Institutu za fiziku u Beogradu, pod rukovodstvom dr Milivoja Ivkovića.

Na Institutu za fiziku u Beogradu je zaposlen od aprila 2021. godine kao student doktorskih studija u zvanju istraživač pripravnik, a od novembra 2023. godine u zvanju istraživač saradnik. Tokom doktorskih studija, bavio se ili se bavi vakuum ultraljubičastom (VUV) spektroskopijom električnih gasnih pražnjenja, primenom mašinskog učenja i veštačke inteligencije u spektroskopiji plazme u optičkoj i VUV oblasti spektra, te unapređivanjem metoda i poboljšanja granica detekcije pojedinih elemenata u spektroskopiji laserski indukovanih proba.

Trenutno učestvuje kao član projektnog tima na projektu NOVA2LIBS4fusion koji se realizuje u okviru poziva IDEJE Fonda za nauku Republike Srbije. Kandidat je do sada publikovao 5 radova, od kojih su 3 objavljena u vodećim međunarodnim časopisima. Prema indeksnoj bazi Scopus ima h faktor 2, a radovi su citirani 5 puta bez autocitata. Održao je pozivno predavanje na međunarodnoj konferenciji *14th Serbian Conference on Spectral Line Shapes in Astrophysics* u sekciji *Spectral Line Research: New Frontiers*.

Spisak publikacija:

1. Tapalaga, I., Traparić, I., Trklja Boca, N. et al. Neural Comput Applic 34, 6349–6358 (2022).
<https://doi.org/10.1007/s00521-021-06763-4>.
2. Traparić, I., Ivković, M. Eur. Phys. J. D 77, 30 (2023). <https://doi.org/10.1140/epjd/s10053-023-00608-6>.
3. M Ivkovic, J Savovic, Biljana D Stankov, M Kuzmanovic, I Traparic, Spectrochim. Acta B 213 (2024) 106874, <https://doi.org/10.1016/j.sab.2024.106874>.
4. NM Sakan, I Traparic, VA Sreckovic, M Ivkovic, Contrib. Astron. Obs. Skalnaté Pleso 52, 97-104, 2022, <https://doi.org/10.31577/caosp.2022.52.3.97>.
5. Z Majlinger, I Traparic, Contrib. Astron. Obs. Skalnaté Pleso 53, 58-71, 2023, <https://doi.org/10.31577/caosp.2023.53.3.58>

ИЗЈАВА О АУТОРСТВУ

Име и презиме аутора: Иван Трапарић

Број индекса: 8009/2020

Изјављујем

Изјављујем да је докторска дисертација под насловом Примена машинског учења и вештачке интелигенције у спектроскопији плазме

- резултат сопственог истраживачког рада;
- да дисертација у целини ни у деловима није била предложена за стицање друге дипломе према студијском програмима других високошколских установа;
- да су резултати коректно наведени и
- да нисам кршио ауторска права и користио интелектуалну својину других лица.

У Београду,

Потпис аутора

**Изјава о истоветности штампане и електронске верзије докторског
рада**

Име и презиме аутора: Иван Трапарић

Број индекса: 8009/2020

Студијски програм: Физика јонизованог гаса и плазме

Наслов рада: Примена машинског учења и вештачке интелигенције у спектроскопији плазме

Ментор: доц. др Маријана Гавриловић Божовић и др Миливоје Ивковић

Изјављујем да је штампана верзија мог докторског рада истоветна електронској верзији коју сам предао ради похрањивања у **Дигиталном репозиторијуму** Универзитета у Београду.

Дозвољавам да се објаве моји лични подаци vezани за добијање академског назива доктора наука, као што су име и презиме, година и место рођења и датум одбране рада.

Ови лични подаци могу се објавити на мрежним страницама дигиталне библиотеке, у електронском каталогу и у публикацијама Универзитета у Београду.

У Београду,

Потпис аутора

Изјава о коришћењу

Овлашћујем Универзитетску библиотеку „Светозар Марковић“ да у Дигитални репозиторијум Универзитета у Београду унесе моју докторску дисертацију под насловом:

Примена машинског учења и вештачке интелигенције у спектроскопији плазме

која је моје ауторско дело.

Дисертацију са свим прилозима предао сам у електронском формату погодном за трајно архивирање.

Моју докторску дисертацију похрањену у Дигиталном репозиторијуму Универзитета у Београду и доступну у отвореном приступу могу да користе сви који поштују одредбе садржане у одабраном типу лиценце Креативне заједнице (Creative Commons) за коју сам се одлучио.

1. Ауторство (CC BY)
2. Ауторство – некомерцијално (CC BY-NC)
3. Ауторство – некомерцијално – без прерада (CC BY-NC-ND)
4. Ауторство – некомерцијално – делити под истим условима (CC BY-NC-SA)
5. Ауторство – без прерада (CC BY-ND)
6. Ауторство – делити под истим условима (CC BY-SA)

У Београду,

Потпис аутора

1. Ауторство. Дозвољавате умножавање, дистрибуцију и јавно саопштавање дела, и прераде, ако се наведе име аутора на начин одређен од стране аутора или даваоца лиценце, чак и у комерцијалне сврхе. Ово је најслободнија од свих лиценци.
2. Ауторство – некомерцијално. Дозвољавате умножавање, дистрибуцију и јавно саопштавање дела, и прераде, ако се наведе име аутора на начин одређен од стране аутора или даваоца лиценце. Ова лиценца не дозвољава комерцијалну употребу дела.
3. Ауторство – некомерцијално – без прерада. Дозвољавате умножавање, дистрибуцију и јавно саопштавање дела, без промена, преобликовања или употребе дела у свом делу, ако се наведе име аутора на начин одређен од стране аутора или даваоца лиценце. Ова лиценца не дозвољава комерцијалну употребу дела. У односу на све остале лиценце, овом лиценцом се ограничава највећи обим права коришћења дела.
4. Ауторство – некомерцијално – делити под истим условима. Дозвољавате умножавање, дистрибуцију и јавно саопштавање дела, и прераде, ако се наведе име аутора на начин одређен од стране аутора или даваоца лиценце и ако се прерада дистрибуира под истом или сличном лиценцом. Ова лиценца не дозвољава комерцијалну употребу дела и прерада.
5. Ауторство – без прерада. Дозвољавате умножавање, дистрибуцију и јавно саопштавање дела, без промена, преобликовања или употребе дела у свом делу, ако се наведе име аутора на начин одређен од стране аутора или даваоца лиценце. Ова лиценца дозвољава комерцијалну употребу дела.
6. Ауторство – делити под истим условима. Дозвољавате умножавање, дистрибуцију и јавно саопштавање дела, и прераде, ако се наведе име аутора на начин одређен од стране аутора или даваоца лиценце и ако се прерада дистрибуира под истом или сличном лиценцом. Ова лиценца дозвољава комерцијалну употребу дела и прерада. Слична је софтверским лиценцима, односно лиценцима отвореног кода.